Zeitabhängige Suche nach astrophysikalischen Neutrinos vom Mikroquasar Cygnus X-3 mittels IceCube und AMANDA

Diplomarbeit in Physik

vorgelegt dem

Fachbereich Physik

der Universität Hamburg

im

Dezember 2010

angefertigt am

Max-Planck-Institut für Kernphysik, Heidelberg

von

Markus Voge

aus Eutin

Erstgutachterin: Dr. Elisa Resconi
Zweitgutachterin: Prof. Dr. Caren Hagner

Time-dependent search for astrophysical neutrinos from microquasar Cygnus X-3 using IceCube and AMANDA

Diploma thesis in PHYSICS

submitted to the

DEPARTMENT OF PHYSICS

University of Hamburg

December 2010

carried out at the

Max Planck Institute for Nuclear Physics, Heidelberg

by

Markus Voge

from Eutin

First reviewer: Dr. Elisa Resconi
Second reviewer: Prof. Dr. Caren Hagner

Zusammenfassung

Woher stammt die kosmische Strahlung? Wie werden Teilchen der kosmischen Strahlung beschleunigt? Diese Fragen wurden bisher nicht zufriedenstellend beantwortet. Zwar gibt es genügend Modelle und Vermutungen und die theoretische Beschreibung hat große Fortschritte gemacht, jedoch fehlt es an Beweisen, um die Modelle bestätigen oder widerlegen zu können. Von der experimentellen Seite ist zu wenig über den Ursprung der kosmischen Strahlung bekannt. Kosmische Strahlungsteilchen erreichen uns nicht aus Richtung ihrer Quelle, sondern werden auf Grund ihrer Ladung von kosmischen Magnetfeldern abgelenkt und ihre Richtung ist somit willkürlich. Lediglich die ultra-hochenergetischen Teilchen lassen Rückschlüsse auf ihren Entstehungsort zu, doch da die Flüsse sehr gering sind, ist auch dies schwierig. Andererseits liefert uns γ-Strahlung einen faszinierenden Blick in den Komsos und zeigt auf, an welchen Orten hoch-energetische Teilchen produziert werden. Nur ist nicht klar, ob diese Quellen gleichzeitig kosmische Strahlung produzieren, weil wir nicht wissen, ob Hadronen beschleunigt werden. Ein eindeutiger experimenteller Nachweis steht noch aus.

Das IceCube Neutrino-Observatorium soll hier Abhilfe schaffen. Es wurde geplant mit dem Ziel, astrophysikalische Quellen hochenergetischer Neutrinos zu detektieren. Derlei Neutrinos können nur durch beschleunigte Hadronen, d.h. durch Wechselwirkung kosmischer Strahlung, entstehen. Sollte eine Neutrinopunktquelle gefunden werden, so wäre sie mit größter Wahrscheinlichkeit auch eine Quelle kosmischer Strahlung, welche Neutrinos in der Nähe ihres Beschleunigungsorts erzeugt.

Einer der vielversprechendsten Kandidaten, kosmische Strahlung zu produzieren, ist das Röntgenbinärsystem Cygnus X-3 in der auffälligen “Cygnus-Region” der Milchstraße. Schon in der Vergangenheit stand es unter Verdacht, einer der Hauptproduzenten der galaktischen kosmischen Strahlung zu sein. Dies konnte jedoch nie experimentell bestätigt werden. Beobachtungen weisen auf dichte Materie und starke Absorption hin – womöglich der Grund, warum die Detektion von γ-Strahlung lange nicht gelungen ist. Die Bedingungen für die Produktion von Neutrinos hingegen wären ideal und die starke Absorption stellte für die Neutrinos kein Hindernis dar.

Diese Arbeit setzt sich mit den Eigenschaften des Cygnus X-3 auseinander. Mit Hilfe von Informationen aus anderen Bereichen der Astrophysik, nämlich Radio- und Röntgendaten, wurde festgestellt, zu welchen Zeiten beim Cygnus X-3 hochenergetische Teilchen erzeugt werden könnten. Anschließend wurde damit eine zeitabhängige Suche nach Signalneutrinos vom Cygnus X-3 in den Daten der Detektoren IceCube und AMANDA vorgenommen. Die Analyse ist optimiert für ein weiches Neutrino-Emissionsspektrum und hat ein verglichen mit der zeitunabhängigen Suche erhöhtes Entdeckungspotential.

Es wurde kein signifikantes Signal von der Position des Cygnus X-3 während oder kurz vor oder nach möglichen Neutrinoemissionsphasen gefunden. Die Wahrscheinlichkeit, dass die Beobachtung einem Datensatz aus reinem Hintergrund entspricht, beträgt 57%. Eine obere Schranke auf die Fluenz (zeitintegrierter Fluss) von $\nu_\mu + \bar{\nu}_\mu$ von der Cygnus-X-3-Position während aller aktiven Phasen wurde auf $1.8 \cdot 10^{-3} \, (E/\mathrm{TeV})^{-3} \, \mathrm{TeV}^{-1} \, \mathrm{cm}^{-2} \, \mathrm{sr}^{-1}$ für ein E^{-3}-Spektrum und auf $2.5 \cdot 10^{-4} \, (E/\mathrm{TeV})^{-2} \, \mathrm{TeV}^{-1} \, \mathrm{cm}^{-2} \, \mathrm{sr}^{-1}$ für ein E^{-2}-Spektrum bei einem Konfidenzniveau von 90% festgesetzt.

Abstract

Where do cosmic rays originate? How are cosmic rays accelerated? These are questions that have still not been adequately answered. In spite of the existence of many models and hypotheses and significant advances of theoretical description, there is still no clear evidence supporting one model or ruling out another. The problem is that from experimental side, too little is known about the origin of cosmic rays. Cosmic ray particles do not point to their origins since—due to their charge—they are deflected in magnetic fields that exist throughout the universe and thus their direction is scrambled. Only at ultra-high energies pointing is possible, but the flux is so low that it is still difficult. On the other hand, γ-rays provide a fascinating view of the cosmos and reveal sources of high-energy particles. However, it is not clear if these sources also produce the cosmic rays observed at Earth because it is not known if hadron acceleration is involved. The experimental "smoking gun" is yet to come.

The IceCube Neutrino Observatory is being built to change this situation. It was designed to detect astrophysical sources of high-energy neutrinos which can only arise from accelerated hadrons and thus from interaction of cosmic rays. If a neutrino point source was found, then this would be most likely a source of cosmic rays that produce the neutrinos close to the site where they were accelerated.

One of the most promising cosmic ray source candidates is the X-ray binary system Cygnus X-3, residing in the prominent "Cygnus region" of our Galaxy. It has been suspected in the past to be a major contributor to Galactic cosmic rays, but that has never been confirmed by experiment. Observations show evidence for dense matter and strong absorption that might have hindered detection in γ-rays for a long time, however representing ideal conditions for production of high-energy neutrinos that escape from the absorptive material.

In this work, the properties of Cygnus X-3 were considered and information from other wavelengths, namely radio and X-ray data, was used to indicate phases of possible high-energy particle ejection. This information was used to perform a time-dependent search for a neutrino signal from the position of Cygnus X-3 in data from the IceCube and AMANDA detectors. The analysis is optimized for a soft emission spectrum and has increased potential for discovery compared to a time-integrated analysis.

No significant point source signal was found at the position of Cygnus X-3 during or near the times of possible neutrino emission. The probability for the observation to occur in a background only sample is 57%. An upper limit on the $\nu_\mu + \bar{\nu}_\mu$ fluence (time-integrated flux) from the Cygnus X-3 position during all active periods is set at $1.8 \cdot 10^{-3} \, (E/\mathrm{TeV})^{-3} \, \mathrm{cm}^{-2} \, \mathrm{sr}^{-1} \, \mathrm{TeV}^{-1}$ for an E^{-3} spectrum and at $2.5 \cdot 10^{-4} \, (E/\mathrm{TeV})^{-2} \, \mathrm{cm}^{-2} \, \mathrm{sr}^{-1} \, \mathrm{TeV}^{-1}$ for an E^{-2} spectrum at 90% confidence level.

Contents

List of Figures

List of Tables

CHAPTER I

An Overview of Astroparticle Physics

1.1 Cosmic Ray Physics

1.1.1 Historical development

The birth of cosmic ray physics can be dated back to an important discovery made in the early 20th century by Austrian physicist Victor F. Hess and others. In 1911 and 1912, Hess carried out seven balloon flights to heights up to 5,300 m with improved experimental techniques (e.g. an improved electroscope) in order to measure ionization of the atmosphere [1]. He found that up to 1 km, ionization decreases (this is the component that is caused by radioactive substances in the Earth's crust), but above it increases considerably and at 5 km it is several times more intense than at ground level [2]. Hess concluded that there must be an ionizing radiation that penetrates the atmosphere from outer space. Thus, "*cosmic rays*" were discovered.

Important discoveries followed that opened the field of particle physics, above all the identification of new particles like positrons [3], muons [4] and pions [5] in cosmic ray induced particle showers. Another milestone for the understanding of cosmic rays was the discovery of extensive air showers by Pierre Auger et al. in the late 1930s that enabled the study of the highest energy cosmic rays [6], see section 1.1.5 about air showers.

1.1.2 The energy spectrum of cosmic rays

Cosmic rays (CRs) are *charged particles* entering the Earth's atmosphere from outer space and from all directions [8]. They are mainly protons and heavier nuclei. The **energy spectrum** of cosmic rays is a nearly featureless power-law, except for features in the spectrum called 'knee' and 'ankle', i.e. kinks where the power law changes its exponent. The spectrum of CRs spans over ~ 10 orders of magnitude from few GeV to 10^{11} GeV, and the integrated flux above 100 GeV is higher than that above 10^{11} GeV by sixteen orders of magnitude [6].

The (differential) CR flux is: [8, 9]

$$\frac{d\Phi}{dE} = 1.8 \left(\frac{E}{\text{GeV}}\right)^{-\gamma} \frac{1}{\text{GeV}} \frac{\text{particles}}{\text{cm}^2 \cdot \text{s} \cdot \text{sr}}. \tag{1.1}$$

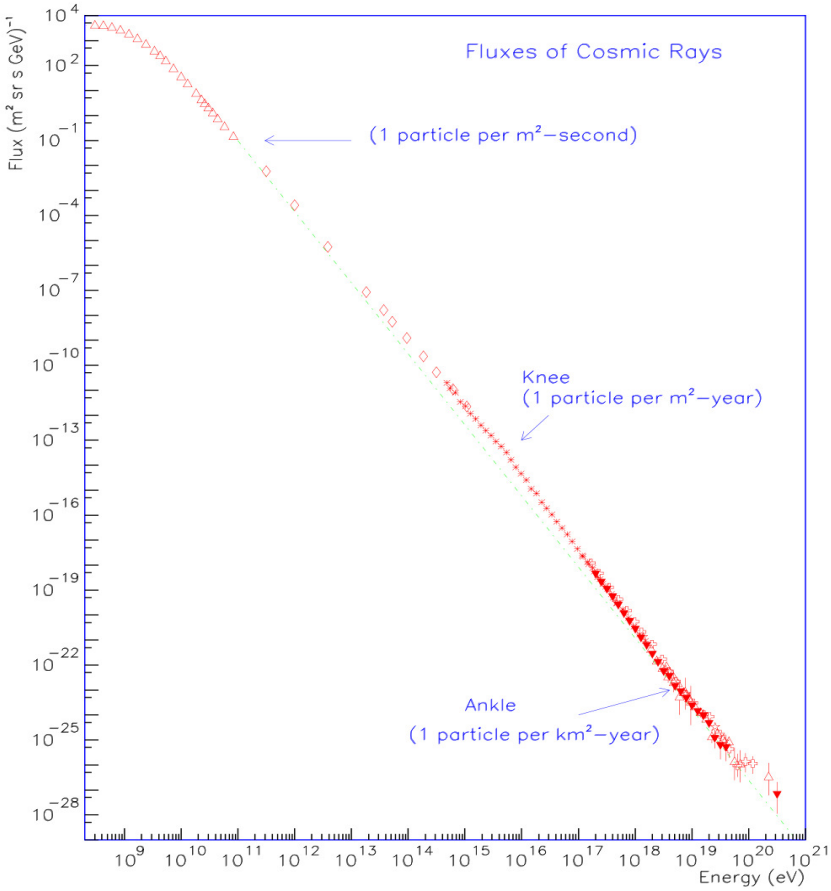

Figure 1.1 The cosmic ray particle energy spectrum including all particles. The labels indicate approximate integral fluxes. The data represent published results of the LEAP, Proton, Akeno, AGASA, Fly's Eye, Haverah Park, and Yakutsk experiments. From [7].

The exponent γ is called the *spectral index* and is:

$$\gamma \approx \begin{cases} 2.7 & \text{if } E < 10^{15} \text{ eV} \\ 3 & \text{if } 10^{15} \text{ eV} \leq E \leq 10^{19} \text{ eV} \\ 2.7 & \text{if } E > 10^{19} \text{ eV} \end{cases} \tag{1.2}$$

So, the spectrum softens (steepens) at the knee around 10^{15} eV and hardens (flattens) again at the ankle around 10^{18} eV.[1] The current understanding is that CRs below the knee are accelerated at supernova remnants (SNRs) in the Galaxy, those between knee and ankle come from other Galactic sources and those above the ankle are of extra-galactic origin [6]. However, the exact origin of the highest energy cosmic rays is still unknown. The shape of the cosmic ray spectrum as a power-law is one of their most striking features. It reveals that they acquire their energies in non-thermal processes. CRs are thus much different than the radiation studied in traditional astrophysics (like the one from stars, hot gas etc.), that is all produced thermally and following a black body spectrum [8].

Galactic CRs (GCRs) are characterised by intermediate energies of few GeV up to $\approx 10^{17}$ eV. They constitute the majority of cosmic rays and arrive at the Earth at a rather constant and isotropic flux which is however modulated and distorted due to the solar wind

[1] But the measurement and interpretation of the ankle is not very clear yet.

and solar magnetic field (the "heliospehre") [8, 10]. Above ≈100 GeV, the Sun's influence becomes negligible [8], but additional anisotropies are caused by deflections in the Earth's magnetic field: The *latitude effect* makes the CR event rate in the atmosphere dependent on geomagnetic latitude. This is simply because the particles are deflected according to the Lorentz force by the perpendicular component of the Earth's magnetic field which is greater at the equator [10]. The second effect is the so-called *east-west effect*. Because of the geomagnetic field, cosmic ray particles that are mainly positively charged are always bent to one direction. Those coming from west bend downwards, towards the surface of the Earth, those coming from east bend upwards, away from the Earth [6].

Extra-galactic CRs (ECRs) are the highest energy particles in the cosmic ray spectrum. They have energies starting at the ankle around 10^{18} eV up to the highest energies ever observed (few 10^{20} eV) [6]. These are also referred to as *ultra-high energy cosmic rays* (UHECR). The general understanding is that below $\sim 10^{18}$ eV, extra-galactic CRs are suppressed because of magnetic deflections that prevent them to reach our Galaxy[2]. Particles are confined to their host galaxy if their gyroradius is smaller than the size of the galaxy. This is probably the reason for the steepening of the CR spectrum at energies lower than the ankle: Sources in our own Galaxy reaching these high energies become rare, but the flux from powerful extra-galactic accelerators is suppressed. Above the ankle, the spectrum flattens, because particles from extra-galactic sources can reach us.

1.1.3 The GZK effect

Shortly after the discovery of cosmic microwave background radiation (CMB) in 1965 by Penzias & Wilson [11], it was predicted by Greisen, Zatsepin and Kuzmin that there should be an "end to the cosmic ray spectrum" due to the interaction of protons and nuclei with CMB photons [12, 13]. This effect is called the **GZK cut-off** after the authors mentioned above. The most important interactions are pion production (via the Δ-resonance) and production of e^+e^- pairs [12, 6]:

$$\begin{aligned} p + \gamma &\longrightarrow \Delta^+ \longrightarrow p + \pi^0 \\ p + \gamma &\longrightarrow \Delta^+ \longrightarrow n + \pi^+ \\ p + \gamma &\longrightarrow p + e^+ + e^- \end{aligned}$$

As soon as the center of mass energy is equal to the masses of all reaction products, a reaction is energetically possible. Thus, the threshold energy of a proton hitting a 2.725 Kelvin CMB photon to produce a π^0 can easily be estimated to be $\approx 10^{20}$ eV.[3] More detailed calculation gives a threshold energy of $\sim 6 \times 10^{19}$ eV. This means that CR particles above that energy can only travel limited distances (cf. fig. 1.11). Since sources of highest energy cosmic rays are expected to be rather far away, there should be a sharp suppression of CRs above the threshold energy.

In spite of the theoretically well understood GZK cut-off effect, there have been exper-

[2] The so-called "magnetic horizon" is the maximum distance from which we can receive CRs and becomes smaller and smaller for lower energies. [8]

[3] With the 4-vectors $\mathbf{p}_\gamma$ and $\mathbf{p}_\mathbf{p}$, the CM energy $\sqrt{s}$ obeys: $s = (\mathbf{p}_\gamma + \mathbf{p}_\mathbf{p})^2 = m_p^2 + 2\epsilon E_p(1 - \beta_p \cos\theta)$ with ϵ, the energy of the CMB photon (on average 6.34×10^{-4} eV [6]), and θ, the angle between photon and proton. For ultra-relativistic protons and head-on collision, $\beta_p \approx 1$ and $\cos\theta = -1$. Setting $\sqrt{s} = m_p + m_{\pi^0}$ gives $E_p \approx 10^{20}$ GeV.

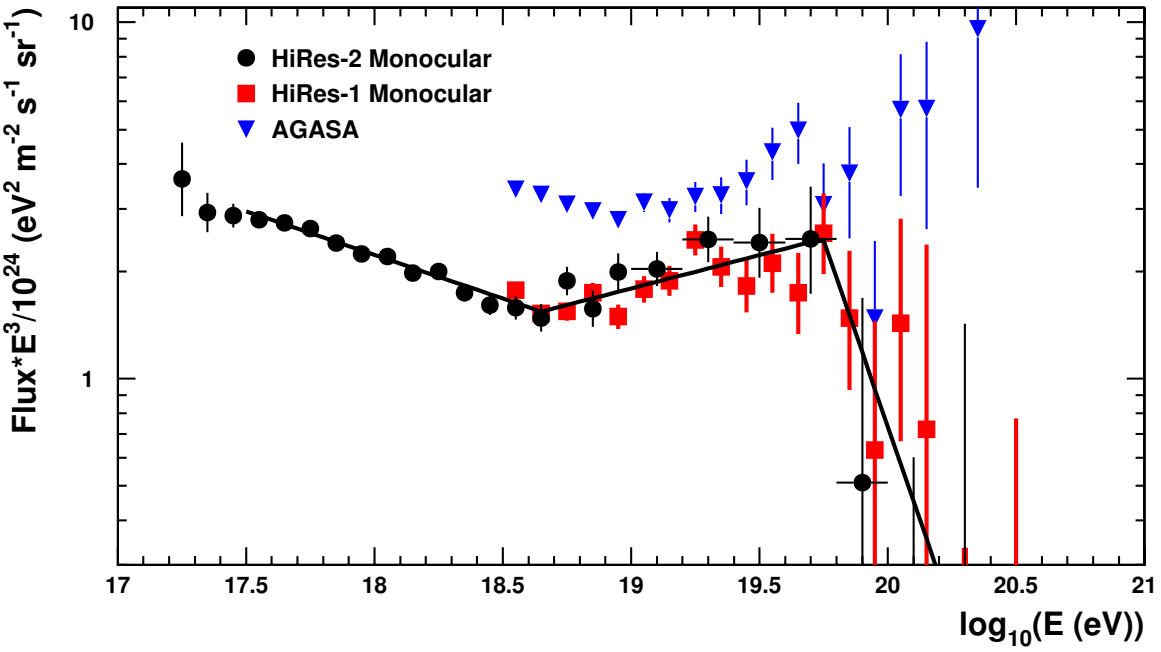

Figure 1.2 The end of the cosmic-ray energy spectrum measured by the AGASA and HiRes detectors. HiRes observed the GZK suppression that was not observed by AGASA. From [15].

imental observations of CR flux above the threshold, e.g. by the AGASA experiment in Akeno, Japan [14]. This would favour top-down scenarios of CR generation (particle decay), as opposed to bottom-up scenarios (acceleration) (see section 1.4). However, other experiments, e.g. HiRes, contrast this result by observing a suppression compatible with the GZK cut-off [15], see fig. 1.2. The Pierre Auger Observatory recently confirmed the suppression with a significance of more than 20σ [16].

1.1.4 Cosmic ray composition

The **composition** of cosmic rays is in general about 90% protons, $\sim 9\%$ α-particles (He-nuclei) and $\sim 1\%$ heavier nuclei [17]. The exact composition is not known to high accuracy, but it is believed that all stable nuclei are present in some extent [6]. In addition to the content mentioned above, there is also a steady flux of electrons ($\sim$0.9%), positrons ($\lesssim 0.1\%$) and anti-protons ($\lesssim 10^{-5}$) [6].[4] The chemical composition becomes heavier at higher energies because heavier nuclei have a flatter energy distribution than lighter nuclei or protons [17, 9]. The composition of CRs sheds light on their origin. Comparing the nuclear composition in greater detail with the one in our Solar System, one finds that they are relatively similar, with a few exceptions e.g. the abundance of Li, Be and B nuclei is higher in CRs than in the solar system (cf. fig. 1.3). This can be explained as a propagation effect: Li, Be and B are produced as secondary particles via interactions of primary CR particles with matter in the Galaxy [8, 17].

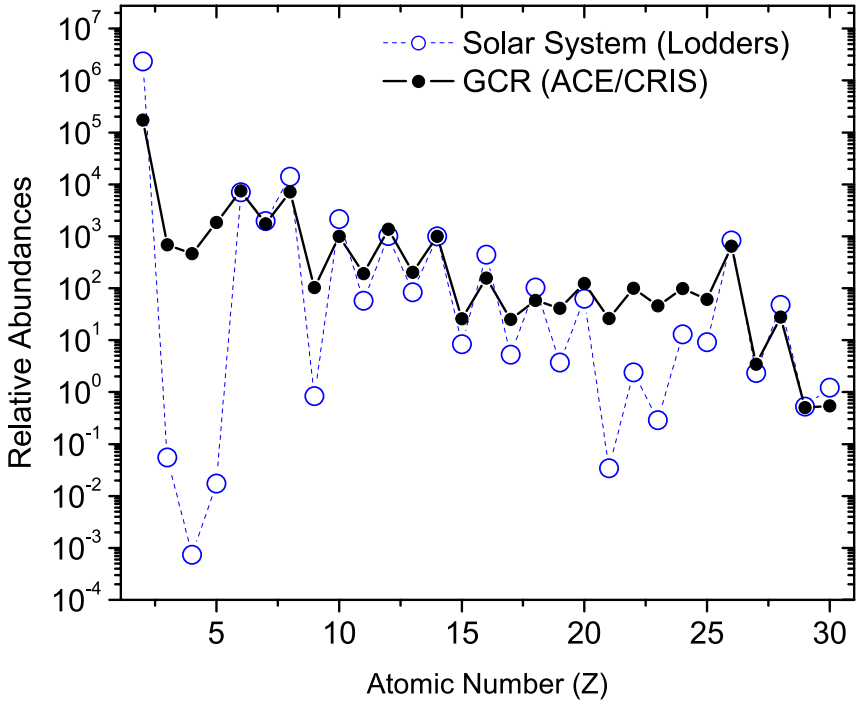

Figure 1.3 Abundances of nuclei observed in cosmic rays and Solar System abundances (normalized to 1000 for Si). From [21].

1.1.5 Air showers

Primary cosmic ray particles that hit the Earth's atmosphere interact with nuclei of air molecules. A cascade of particles forms and travels down the atmosphere. Typically, a cosmic ray hadron (e.g. proton) hitting a nucleus produces mesons such as pions (π^+, π^-, π^0) or kaons (K^+, K^-, K^0) together with the hadronic rest of the collided nuclei. The mesons receive a certain fraction of the primary energy and thus have the same energy spectrum $\propto E^{-2.7}$ as the CR primaries. The neutral pions decay almost immediately into two photons:

$$\pi^0 \longrightarrow \gamma + \gamma.$$

Charged mesons either interact with another nucleus of the air or they decay into a muon and a neutrino:

$$\begin{aligned} \pi^+(\pi^-) &\longrightarrow \mu^+(\mu^-) + \nu_\mu(\bar{\nu}_\mu) \\ K^+(K^-) &\longrightarrow \mu^+(\mu^-) + \nu_\mu(\bar{\nu}_\mu) \end{aligned}$$

The meson decay probability is suppressed by the meson's Lorentz factor and this suppression is $\propto E^{-1}$ at high energies. The result is that the energy spectrum of **atmospheric neutrinos and muons** is $\propto E^{-3.7}$ [23]. Additionally, the meson decay/interaction proba-

[4] If γ-rays were counted to cosmic rays, they would make up $\lesssim 2\%$ of the total particle flux at energies around 10^{19} eV [18] and much less at lower energies [19, 20].

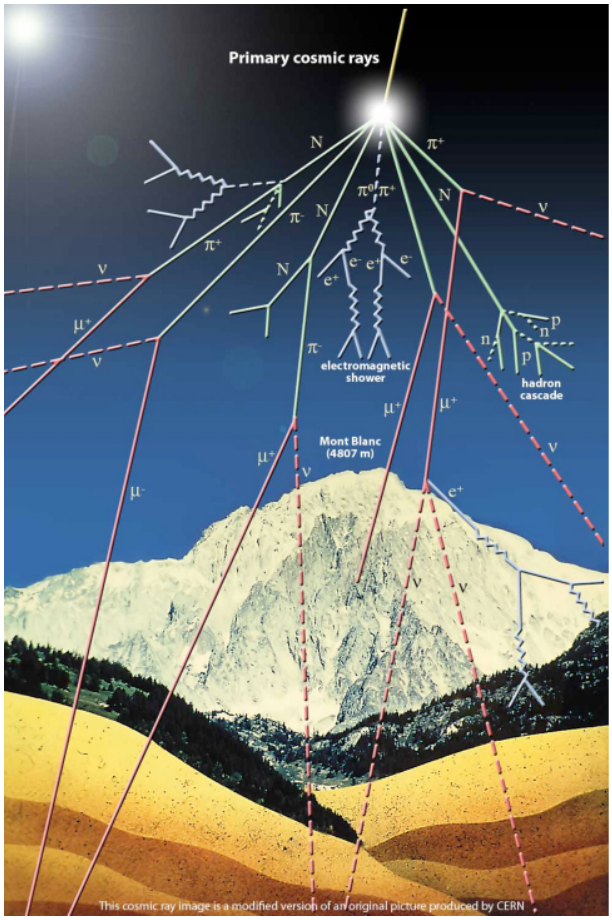

Figure 1.4 Schematic picture of a cosmic ray induced air shower. From [22].

bility is highly dependent on the density of air and thus on its temperature. A higher temperature results in lower density and decreases the interaction probability of the mesons. Their interaction length is therefore longer and they have a higher probability to decay before interacting with a nucleus. This is noticed as seasonal variation in the atmosperic muon flux, with a higher flux during summer [23]. Heavier mesons, including charmed mesons like D mesons, decay much quicker and have almost no chance to interact. They should provide an additional *prompt* component of the atmospheric neutrino and muon spectrum $\propto E^{-2.7}$ [23]. The magnitude of this charm component is uncertain and remains to be measured [24].

Neutrinos traverse the atmosphere mostly undisturbed and also muons can travel significant distances before they decay into an electron and neutrinos [23]. But energetic hadrons (e.g. nuclei or nucleons) create further hadronic cascades (with further production of mesons or nuclear reactions), whereas energetic photons (e.g. from π^0 decay) and electrons/positrons cause an electromagnetic cascade: e^+ and e^- above $\sim$100 MeV lose energy mainly through bremsstrahlung [23] and create photons, photons in turn lose energy mainly through creation of an e^+e^- pair. This leads to an avalanche-like increase in number of particles until after a certain atmospheric depth[5] $X_{\max}$ it reaches its maxi-

[5]Atmospheric depth X, measured in g/cm^2, is defined as the integral of air density ρ from a certain

mum and afterwards declines.[6] Fig. 1.4 shows a schematic picture of the whole air shower process.

High-energy CR primaries (energies $\sim 10^{15}$ eV and more) create huge atmospheric showers called **extensive air showers** (EAS). They were first detected by Pierre Auger et al. by recording coincident CR events [26]. The particles associated with a large shower can fill an area of the order of 10^4 m^2. This allows ground based experiments to have an effective area much larger than the instrumented one, needed for the study of highest energy cosmic rays that have fluxes of only 1 particle per km^2 and year [6, 7] or even 1 particle per km^2 and century [27, 28].

1.1.6 Cosmic ray experiments

There are in principle three types of experiments to detect cosmic rays: Space-based and balloon-based experiements, that can both be described as "direct detection" experiments, and ground-based experiments. Cosmic ray particles hitting the atmosphere interact with air nuclei (as described in section 1.1.5). This shielding effect of the atmosphere means that direct observation of CR primaries is only possible in space or at very high layers of the atmosphere [7]. This is done via **satellites** orbiting the Earth (e.g. PROTON satellites [29], SOKOL [30], PAMELA that is currently active [31] etc.) and via **balloons** that fly at altitudes of 40 km (e.g. JACEE [32], CREAM [33], ANITA [34] etc.). Balloon-borne CR detectors have the disadvantage of still flying within very thin layers of atmosphere, so that first interactions have already taken place. However, they are much cheaper than satellite missions [6]. Both satellite and balloon detectors are limited in size, leading to a limited amount of collected particles. As a consequence, direct observations run out of statistics typically around a few 100 TeV [7].

Ground-based detectors observe the particles from air showers instead of the primaries. Above $\sim$100 TeV the showers are extensive enough to be detectable from ground [7] and thus ground-based detectors are complementary to space-based. Using the atmosphere as target medium, the effective area becomes much larger than the mere detector area. Detector designs split in two general principles: *ground array* detectors and *optical* detectors. Ground array detectors consist of a large number of detector units (typically water Cherenkov detectors or scintillation detectors) and perhaps other devices to detect shower muons, electrons and hadrons. Examples are the Volcano Ranch in New Mexico, USA, and Haverah Park near Leeds, England, that started in the early 1960s [7] or AGASA near Tokyo, Japan [14, 7] and KASCADE in Karlsruhe, Germany [35, 6], both in the 1990s. Optical detectors use either Cherenkov light (see section 1.3.5) produced by relativistic shower particles moving faster than the speed of light in air, or fluores-

height h upwards:

$$X = \int_h^\infty \rho(h')dh'$$

Thus, it corresponds to the thickness of the atmospheric layers above h. The lower the height above ground level, the larger the atmospheric depth [6].

[6] The electromagnetic cascade process is nicely illustrated in the toy model by Heitler [25], in which after an interaction length X_0 the number of particles doubles (either by $\gamma \longrightarrow e^+e^-$ or by $e \longrightarrow e+\gamma$) and the energy per particle is halved. Thus, after n interaction lengths, one incident particle of energy E_0 has turned into 2^n particles, each with energy $E_0/2^n$. The shower reaches its maximum when the particle energy drops below particle production threshold energy $E_c = 2m_e$. From this follows $X_{\max} = X_0 \log_2(E_0/E_c)$. Typical values of X_0 (as atmospheric depth) in air are $\approx$37 g/cm^2 [6].

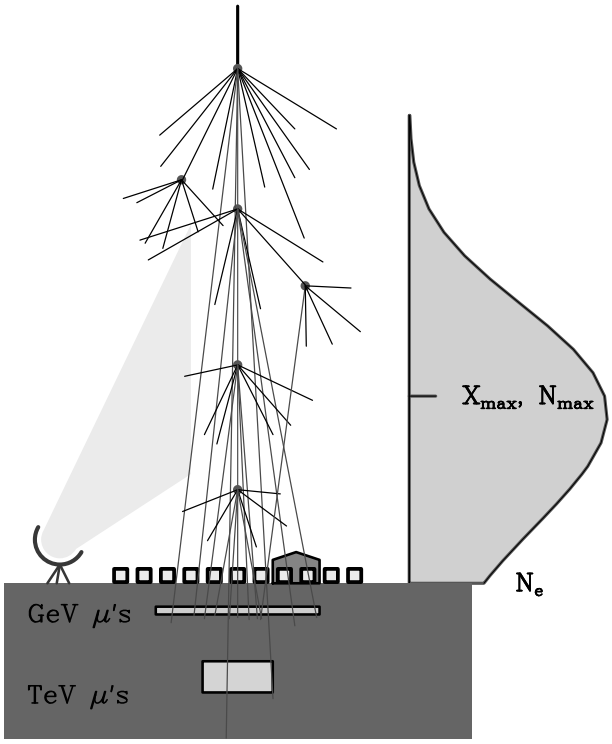

Figure 1.5 Schematic picture of different CR shower experiment setups. The optical technique is illustrated as telescope looking towards the shower maximum, the squares show a surface array and the house indicates a hadronic calorimeter. Underground muon detectors are also shown. On the right is the electron number as function of atmospheric depth with maximum at $X_{\max}$. From [6].

cence light emitted by atmospheric nitrogen atoms that are excited by the passing shower particles [7, 6]. This requires clear, moonless nights so that only in $\sim 10\%$ of the time, observation is possible. Examples are the Fly's Eye detector, the first CR fluorescence detector [7], and its successor HiRes on hilltops above the desert in Utah, USA [36, 6]. Ground-based CR experiments have to reconstruct the primary energy and type from the observed shower particles. This can often only be done on a statistical basis and with limited accuracy. E.g. the array detectors can derive the energy of the primary from the particle density at 600 m from the shower core. The atmospheric depth at shower maximum $X_{\max}$ yields information on the composition [7]. Fig. 1.5 illustrates the ground based techniques.

An advancement in EAS detector design is represented by the **Pierre Auger Observatory** (PAO) that started physics data-taking in 2004 [37] and is scheduled to run for 20 years [38, 39]. It is situated in the Argentinian pampa [39] and consists of a surface array of 1600 water-Cherenkov detectors with a spacing of 1.5 km covering an area of 3000 km^2. These are overlooked by 24 air fluorescence detectors distributed over four buildings [40]. The PAO is aimed at *ultra-high energy cosmic rays* (UHECR) with full efficiency for extensive air shower detection above 5×10^{18} eV, at the range of the ankle and the GZK cut-off, where supposedly the transition from Galactic to extra-galactic components takes place [40]. The 'hybrid' approach using both an array and fluorescence detectors allows a more reliable energy and direction measurement for events observed by both detector systems, with the array sampling the lateral particle density of the shower and the fluorescence detectors observing its longitudinal development [40].

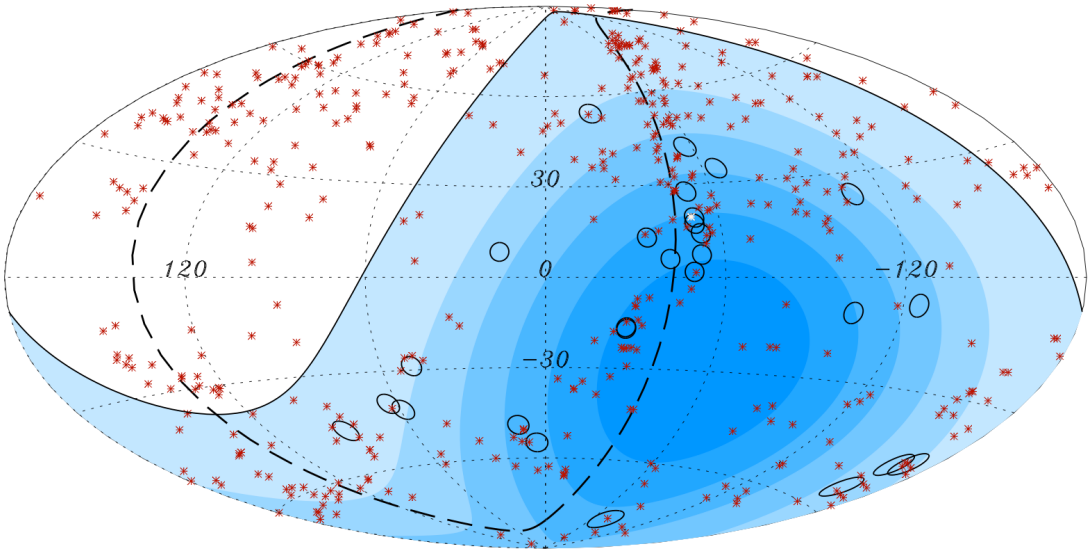

Figure 1.6 Map of the sky in galactic coordinates with circles of radius 3.1° centered at the arrival directions of the 27 events with energy > 57 EeV detected by the PAO between 1 January 2004 and 31 August 2007. The positions of 472 AGN with redshift $z < 0.018$ (distance $D < 75$ Mpc) are indicated by red asterisks. The solid line is the border of the field of view, darker color means larger exposure. The dashed line is the supergalactic plane. Centaurus A, one of the closest AGN, is marked in white. From [28].

It might be possible to do "charged particle astronomy" with UHECRs. At ultra-high energies, cosmic rays are less and less deflected by magnetic fields, so that they point to their acceleration sites within a certain angular uncertainty. This is an interesting option for the future and the PAO has done first steps in this direction, e.g. a correlation study of the arrival directions of highest-energy events with the position of active galactic nuclei (AGN) has been performed [28, 41]. It rejects the null hypothesis of an isotropic UHECR flux with at least 99% confidence level. Out of 27 events with energy above 57 EeV (5.7×10^{19} eV), 20 events correlate within 3.1° with positions of AGN with distance $D < 75$ Mpc. The probability of this occurring by chance if the flux were isotropic is $1.7 \cdot 10^{-3}$. A sky map with the event positions and the known locations of nearby AGN is given in fig. 1.6. The correlation implies a bottom-up scenario of particle acceleration at AGN (see section 1.4), which would be confirmed by the detection of neutrino point sources consistent with AGN. The Auger measurements can be used to estimate the corresponding neutrino flux from these sources: In [42], an expectation of $0.4 - 0.6$ events per year from Centaurus A, the nearest AGN, is calculated for a km^3 neutrino telescope like IceCube. According to [43] and assuming an E^{-2} spectrum, the diffuse neutrino flux from all AGN in the Northern hemisphere is $d\Phi/dE = 2 \cdot 10^{-12} \, (E/\mathrm{TeV})^{-2}$ TeV cm^{-2} s^{-1} sr^{-1} based on the Auger results, causing 19 events from the whole Northern sky in one year of IceCube operation.

1.2 Gamma-ray Astronomy

Gamma-ray astronomy is a term applied to observations of high energy photons above the X-ray region, starting e.g. around 0.1 MeV [17]. Within the last decades, this part of high energy astronomy has radically advanced thanks to technological breakthroughs.

Gamma-ray astronomy is one of the most exciting fields of high-energy astrophysics right now and reveals completely new aspects of the high-energy universe.

There are, in principle, two ways how high energy (> 30 MeV) and very high energy (> 30 GeV) γ-rays can be produced: via **hadronic** interactions, e.g. through interactions of accelerated protons or nuclei with matter that give rise to neutral pions which decay into two photons:

$$N + N' \longrightarrow \pi^0 + X \longrightarrow \gamma + \gamma + X \tag{1.3}$$

and via **leptonic** processes, e.g. synchrotron radiation of relativistic electrons, bremsstrahlung or inverse Compton scattering, which is scattering of relativistic leptons on low energy photons with an energy transfer from e to γ:

$$e_{\text{high E.}} + \gamma_{\text{low E.}} \longrightarrow e_{\text{low E.}} + \gamma_{\text{high E.}} \tag{1.4}$$

Very efficient is the combination of synchrotron radiation and inverse Compton scattering where low energy photons are produced as synchrotron radiation and then upscattered to high energy photons through inverse Compton effect [6].

γ-rays are produced as secondary particles by interactions of CRs and thus give us information about the propagation of CRs in the interstellar medium. They may also be produced directly at sites of CR acceleration and provide information about the sources of CRs [17, 44]. But because of the leptonic production channel, γ-rays are ambiguous: The existence of γ-rays is in general no proof for the existence of CRs. A big advantage of the use of photons as cosmic messengers is the fact that they are neutral and thus not deflected by Galactic or extra-galactic magnetic fields so that they point to the site of their origin. Additionally, γ-rays are in contrast to neutrinos much easier to detect due to their electromagnetic interactions that yield much higher cross-sections [45]. However, this reactiveness also leads to disadvantages, e.g. γ-rays can be absorbed in clouds so that sources may be γ-ray dark even though high-energy particles are present. Moreover, interaction of γ-rays with CMB photons sets an upper bound on the observation radius for highest energies (see section 1.3.1).

1.2.1 Space-based observations

Because the atmosphere is opaque to γ-rays, direct detection is only possible from space [8]. In the 1960s, first **satellites** (e.g. the OSO missions) were launched into space to detect extra-terrestrial γ-rays. The typical energies of γ-ray satellite missions lie between few MeVs and a few hundred GeVs [46]. Detection techniques include Compton scattering (dominant up to 10 MeV) and electron-positron pair production above 10 MeV, both allowing directional reconstruction and thus astronomy [46]. Early missions saw the discovery of diffuse γ-rays from the Galactic plane and high energy photons from solar flares [46]. Quite unexpectedly came the discovery of gamma ray bursts (GRBs) in 1967 by the Vela satellites [46]. First detected persistent γ-ray point sources were the Crab and Vela pulsars seen by COS-B in the 1970s [46]. A groundbreaking experiment was the Compton Gamma-ray Observatory (CGRO) in the 1990s that brought the proof that gamma ray bursts are isotropically distributed and thus extra-galactic [8]. Its instrument EGRET performed the first all-sky survey above 50 MeV. One of the most recent γ-ray satellite experiments is the *Fermi gamma-ray space telescope*, launched by NASA in June 2008, whose main instrument, the Large Area Telescope (LAT), allows γ-ray detection in

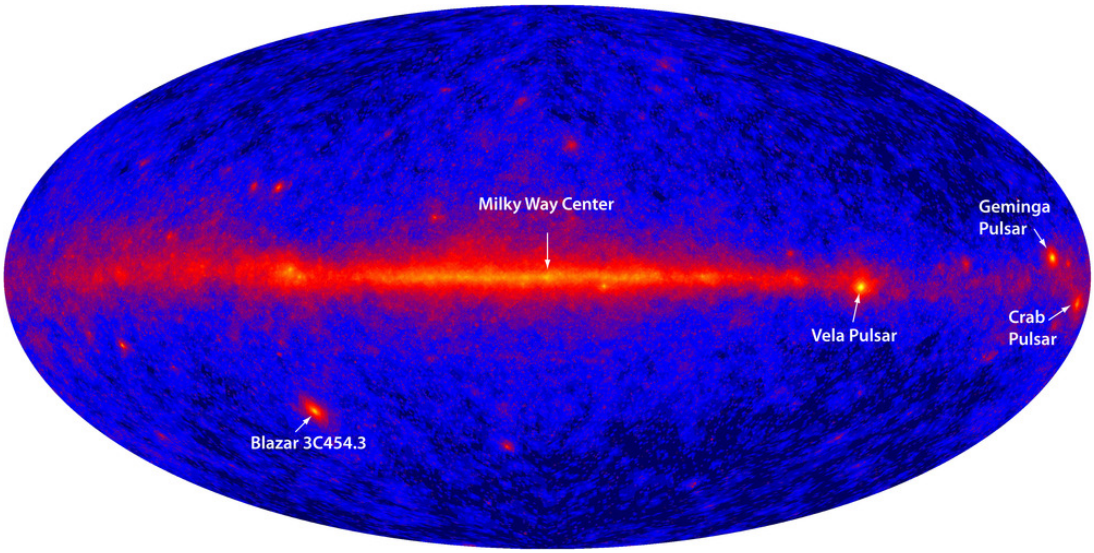

Figure 1.7 An all-sky view from the Fermi-LAT instrument that reveals bright emission in the plane of the Milky Way (center), bright pulsars and super-massive black holes (blazars). The map is in Galactic coordinates with the center of the Galaxy at the center of the map. The bright band of emission from the Milky Way is dominated by diffuse emission along the plane of the Galaxy. From [48], see also [49].

an energy range of 20 MeV–300 GeV [47]. Its main science goals include the identification of sources found by EGRET and the better understanding of GRBs, among many other topics [47]. The Fermi satellite constantly scans the entire sky for γ-rays. Its γ-ray view of the sky is shown in fig. 1.7.

1.2.2 Ground-based observations

In analogy to charged CRs, the γ-ray flux falls very steeply and conventional satellites, because of their limited size, fail to collect enough particles above ~ 100 GeV [8]. But around the same energy, air showers initiated by γ-rays start to become detectable from the ground. The cascade particles themselves reach the ground mainly at high altitudes and if the primary energy lies above 10 TeV. They can be detected with detector arrays like scintillators [50] or water Cherenkov tanks [51] (see also section 1.3.5). At lower energies, when the shower "dies out" in the atmosphere, the Cherenkov radiation emitted by the charged shower particles (mainly e^+e^-) in the higher atmosphere is still detectable on ground. This is used as detection method for energies between 100 GeV and 10 TeV [50, 52, 45]. The main problem of ground-based γ-ray observations is the overwhelming background of air showers induced by hadronic cosmic rays. While in a space detector a γ-ray is clearly identified by a pair of diverging tracks from pair production, the distinction between a γ-ray and hadron induced air shower on the ground is not that easy [52]. First ground-based γ-ray detectors recorded the uniform distribution of air showers due to cosmic rays and tried to see a narrow cluster in the direction of a gamma-ray source. But the sources are much too weak so that very high energy (VHE) gamma-ray astronomy was not feasible for many years until additional methods were found to reject the majority of hadronic showers [50, 52].

The **air shower array** type of gamma-ray observatories can use muon detectors to discriminate the hadronic showers [45]. One big advantage over the atmospheric Cherenkov

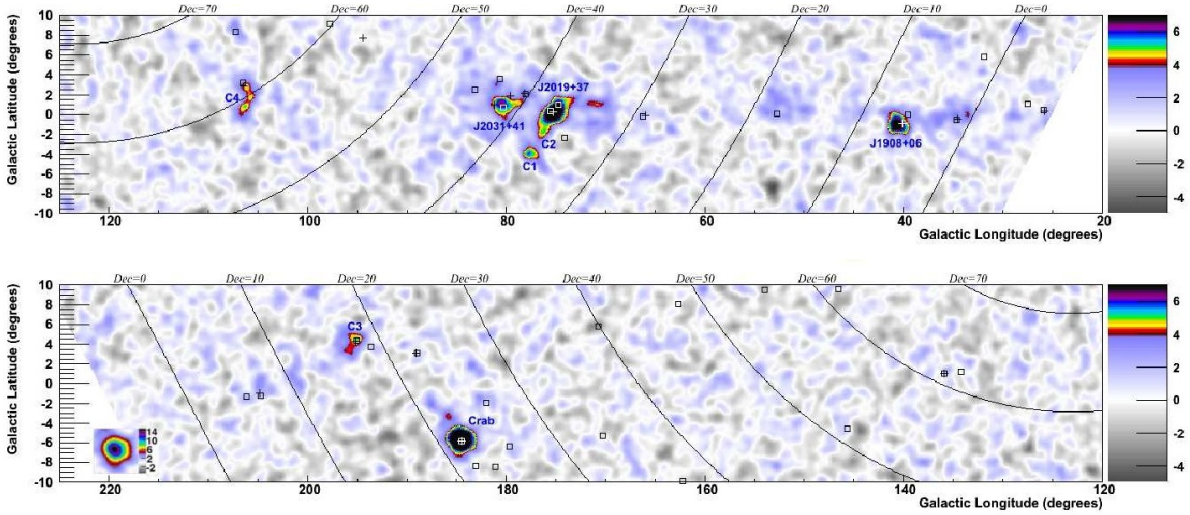

Figure 1.8 Milagro significance map of the Galactic plane from an analysis of Milagro data collected between 2000 and 2007. Color code reflects pre-trial significance. From [53].

technique is the high duty cycle of nearly 100% operation time, whereas Cherenkov telescopes need clear, moonless nights for operation. An important experiment was the *Milagro Observatory*, located at the Los Alamos National Laboratory, USA, that took data in the 2000s. Milagro consisted of a big 24-million-liter water reservoir that contained two layers of photomultiplier tubes (PMTs) of which the upper one was used for reconstruction and the lower one for background rejection via penetrating muons and hadrons [51, 53]. An important result of Milagro is the survey of the Galaxy visible from the Northern Hemisphere including the Cygnus region. Milagro has detected eight TeV γ-ray candidate sources at more than 5σ pre-trial significance of which three remained above 5σ after correction for trials (one of those is the Crab Nebula), see fig. 1.8. Milagro's successor is the HAWC (High Altitude Water Cherenkov) experiment on the Sierra Negra Mountain in Mexico at 4100 m elevation that will be 15 times more sensitive than Milagro [44].

Imaging atmospheric Cherenkov telescopes (IACTs) use the Chrenkov radiation emitted in flight by air shower particles to detect the γ-rays that started the shower. The Cherenkov light (see section 1.3.5) is collected by large mirrors and thrown on a camera with PMT modules that are fast enough to process the very short ($\sim$ns) flashes of light [54]. The crucial point of the method is the discrimination between showers initiated by cosmic ray hadrons and those initiated by γ-rays. After many years of research and development, significant advances were made in the 1980s and 1990s to overcome this problem [52, 50]. It was found that the shape and orientation of the Cherenkov images can be used to reject more than 99% of the background [50]. The basis for this is the different topology of a purely electromagnetic and a hadronic shower that consists of a nuclear core and several small hadronic and elecromagnetic showers: The former is more uniform and laterally narrower, the latter more ragged and has a broader lateral distribution [52, 50], see fig. 1.9. This imaging based background rejection works much better than the muon based one of air shower arrays ($\sim$91% for Milagro [51]). Also, the angular resolution of $\sim 0.1°$ [55] wins over the 0.75° of Milagro [51]. Disadvantages are the small fraction of observable time during clear, moonless nights ($\sim$10%) and the small field of view ($\sim 5°$) [55, 56].

Important IACTs are the H.E.S.S. telescope array (four 12 m diameter telescopes,

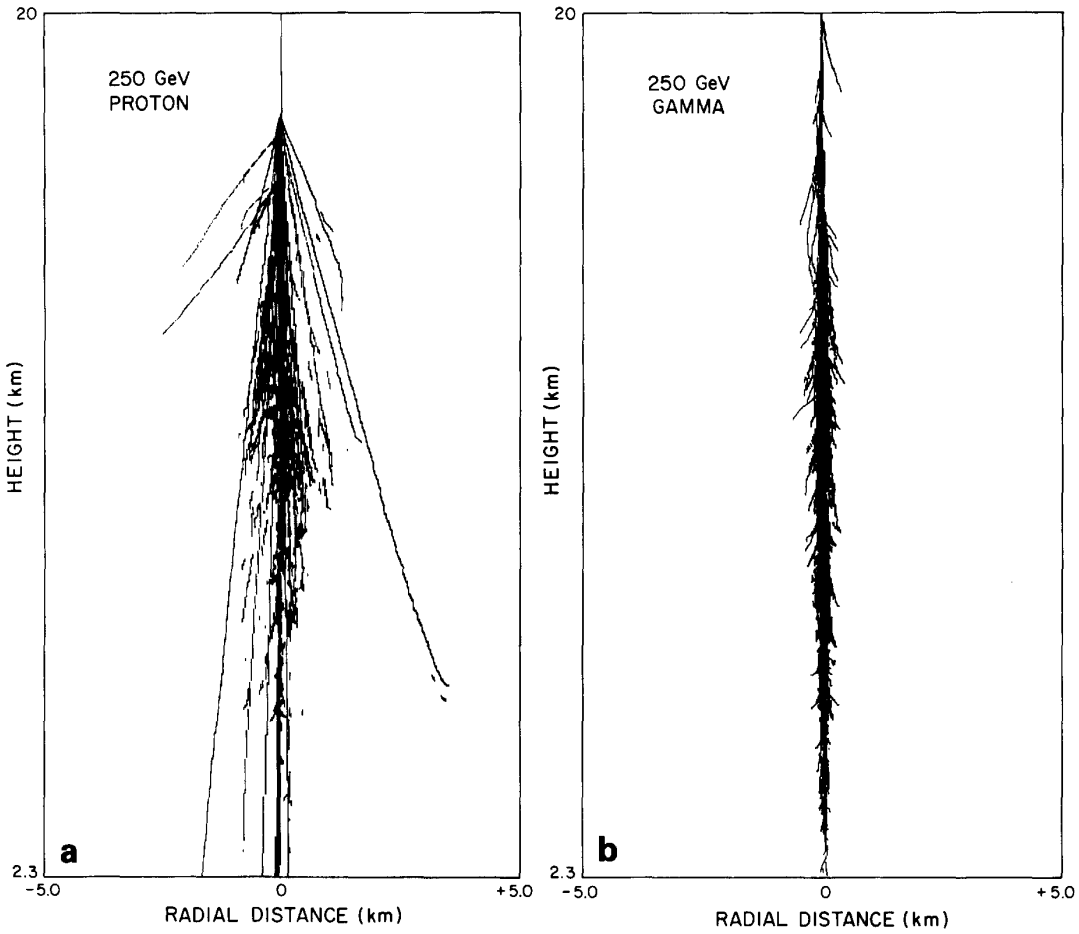

Figure 1.9 Monte Carlo simulation of the development of an air shower from (a) a 250 GeV proton and (b) a 250 GeV γ-ray. From [52].

completed in 2002) in Namibia, the MAGIC telescope (one 17 m telescope, 2003, later accompanied by a second one) on the Canary island La Palma, VERITAS (four 12 m telescopes, 2003) in Arizona, and CANGAROO-III (four 10 m telescopes, 2001) in Australia. Pioneering work in the use of several telescopes at once ("stereoscopic system") was done by HEGRA that was operated with five telescopes on La Palma until 2002 [55, 57].

Interesting results from IACT experiments include the TeV detection of the Crab Nebula, a supernova remnant, that was first achieved by the Whipple experiment in 1989. Since then, the Crab Nebula has become the standard candle of TeV γ-ray astronomy and is used for calibration purposes because of its high and steady flux [58]. Other highlights are detections of supernova remnants [58, 55], extra-galactic objects like AGNs [59], unidentified sources in the Galactic plane [56] and measurement of various source spectra [58]. Similar to Milagro's observations in the northern sky, H.E.S.S. performed a survey of the Galactic plane visible in the southern sky from Namibia, see fig. 1.10 for a map. At the time of writing, the H.E.S.S. source catalog that is available online contained 58 sources of which 10 were not identified with known objects and some identifications were not yet certain [60].

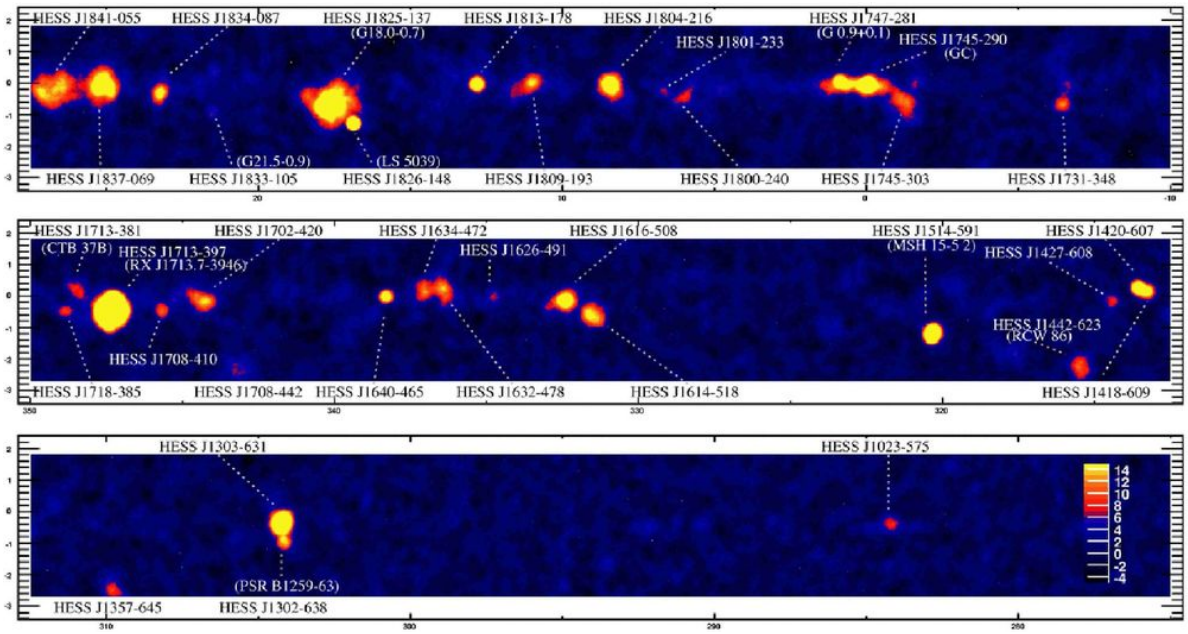

Figure 1.10 H.E.S.S. pre-trial significance map of the Galactic plane with data from 2004 to 2008. This is only an excerpt. From [56].

1.3 Neutrino Astronomy

Neutrinos are extremely light and elusive particles that stream through our bodies and even the entire Earth in vast numbers at every moment. Only a tiny fraction of those ever interacts during such a passage. Because neutrinos are only interacting via the weak interaction, their cross-sections are many orders of magnitude smaller than those of an electromagnetic particle: depending on energy $< 10^{-30}$ cm^2 or even $< 10^{-40}$ cm^2 (cf. fig. 1.12), compared to the typical electromagnetic cross-section $\sigma_T = 6.65 \times 10^{-25}$ cm^2 (the *Thomson cross-section*) [6]. This means neutrinos are hardly absorbed on their passage to us, but also that it is much more difficult to detect them.

Neutrino astronomy is, compared to γ-ray astronomy, still in its infancy. It experimentally began in the 1960s when Ray Davis Jr. carried out the Homestake experiment as first experiment to detect solar neutrinos [61]. Neutrino astronomy beyond the Sun was already imagined in the late 1950s, by the 1970s it became clear that kilometer-scale neutrino detectors would be required [24]. These enormous sizes of target material are only accessible via naturally existing reservoirs of, for instance, water and ice.

1.3.1 Motivation

The interest in neutrinos as cosmic "messenger" particles is founded on their unique properties:

- Neutrinos are neutral: Unlike CRs, they are not deflected by magnetic fields and travel in straight lines through the cosmos. This enables us to see point sources and do astronomy with neutrinos.
- Neutrinos are weakly interacting: A TeV neutrino has a cross-section around 10 orders of magnitude lower than a photon (cf. fig. 1.12). This prevents absorption of

neutrinos and allows to look into unaccessible regions, e.g. very dense environments where high-energy photons are absorbed in interactions with matter or thermal photons [6]. A related example is the interior of the Sun where MeV neutrinos are produced that are the only information carriers able to escape directly. Those are already studied by various detectors, e.g. Super-Kamiokande or SNO.

- Neutrinos do not interact with photons: For γ-rays of sufficiently high energies, the Universe is no longer transparent. Similar to the GZK cut-off (s. page 3), there is an energy threshold ($\sim 10^{13}$ eV [62]) above which propagating γ-rays interact with the CMB photons to produce e.g. e^+e^--pairs:

$$\gamma + \gamma_{\mathrm{CMB}} \longrightarrow e^+e^-$$

  If other photon fields are present (e.g. infrared or optical star light), these processes can even happen at lower γ-ray energies. For this reason, photons have only a finite mean free path that depends on their energy, see fig. 1.11. Neutrinos don't have any such restrictions and are thus the only cosmic messengers for ultra-high energies and very large distances.

- Neutrinos are the smoking gun for hadronic processes: γ-rays can point to sites of particle acceleration. However, they are produced both by accelerated electrons in leptonic processes as well as by accelerated protons/nuclei in hadronic processes (see section 1.2). From the observed γ-ray spectra, one cannot tell if their origin is leptonic or hadronic or a mixture of both. Because high-energy neutrinos can only be produced in weak interaction involving meson decay, a detection of astrophysical neutrinos would be an unambiguous proof of highly relativistic hadrons. A point source of neutrinos would thus be a very likely source of hadronic CRs and neutrinos would solve the long standing mystery about CR origin.

Neutrino astronomy at MeV up to few GeV energies already exists and succeeded to detect solar neutrinos and some 20 neutrinos from a supernova in the Large Magellanic Cloud (SN1987A) [6, 24]. Extra-terrestrial neutrinos from other sources have so far not been detected. The successful extension of neutrino astronomy to higher energies, exceeding few GeV, is highly anticipated and underway with the construction of kilometer-scale detectors like IceCube.

1.3.2 Neutrino flux predictions

Astrophysical neutrinos should arise in hadronic interactions such as pp, pn or $p\gamma$ collisions, producing charged and neutral pions that decay into neutrinos and γ-rays. It is thus natural to relate neutrinos to sources of either cosmic rays or γ-rays or both. Upper bounds on the neutrino flux can be obtained from both observations of cosmic rays and γ-rays.

Waxman and Bahcall derive an upper bound on the neutrino flux from cosmic ray sources, in particular AGN and GRBs [64]: Assuming that the cosmic rays can also escape from their production sites, contributing to the observed flux, the hadronic interaction must be optically thin. This sets an upper bound on the produced neutrino flux, using the observed flux of cosmic rays. The **Waxman-Bahcall bound** is $E^2\, d\Phi/dE = 2 \cdot 10^{-11}\ \mathrm{TeV\,cm^{-2}\,s^{-1}\,sr^{-1}}$ [64].

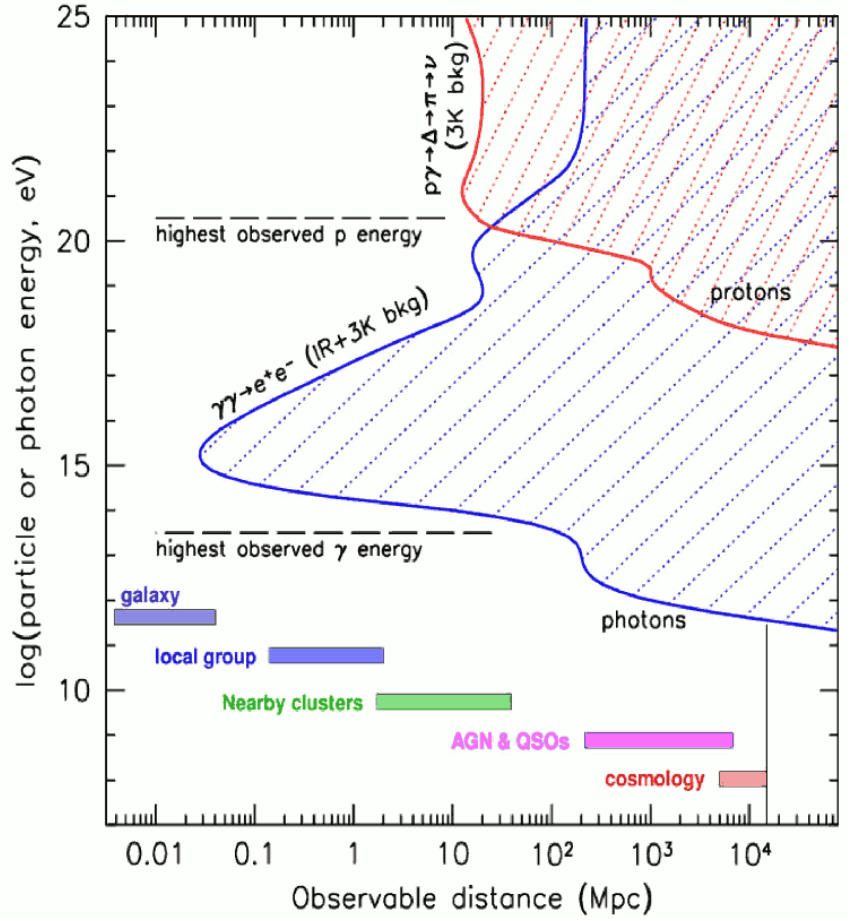

Figure 1.11 Observable distance ($\sim$ mean free path) in the Universe as function of particle energy for γ-rays and protons. The hatched regions are not accessible. From [63].

The generation process of the observed astrophysical γ-rays is currently unknown. From the spectra, it is in general not possible to tell if they are produced in hadronic or leptonic reactions. Assuming exclusively hadronic processes to be responsible for the γ-ray flux of a specific source, the upper bound on the associated neutrino flux can be estimated [65, 66]. E.g. in [65], between 4 and 10 muon neutrino events from the Crab nebula supernova remnant (SNR) are calculated for a km^2 detector within 1 yr.

1.3.3 Concepts of neutrino observatories

The main goal of high-energy neutrino astronomy is the detection of cosmic neutrinos, hopefully from a source associated with cosmic rays. Because the fluxes predicted from e.g. γ-ray observations are considerably low and because of the small neutrino cross-sections, very **large detector mass** (at least a Gigaton) is needed in order to obtain a signal [24, 63]. This necessity gave rise to the idea to use naturally available media as detector volume. In 1960 Markov proposed to detect neutrinos via the Cherenkov emission (see section 1.3.5) of charged particles produced in neutrino interactions and thus suggested to equip large optically transparent media like water or ice with optical modules [24]. This is the concept that is actually used today. Using water or ice as medium, the mass requirement translates into an instrumented volume of a cubic km (km^3). A km-

scale neutrino observatory will naturally be optimized for **high energies** (> 100 GeV). One reason being that a dense instrumentation for accurate measurement of low energy processes would be too expensive, another reason being that the emission spectra of the sources are expected to be flatter (harder) than that of the atmospheric background neutrinos so that a separation is easier at highest energies [24]. Other advantages of going to higher energies are the increased neutrino cross-section (see section 1.3.4) and the increased range of neutrino-induced muons that gives rise to an increased effective volume of the detector [67].

The biggest problem of neutrino astronomy is the incredibly high background. For a neutrino detector being essentially a muon detector, the largest background is by far (even deep in the ice or sea) the passage of muons produced in CR interactions in the atmosphere (see also section 2.1.4). In order to get rid of the atmospheric muon background, neutrino telescopes can use the **Earth as a shield**: Muons produced at the other side of the Earth are either absorbed or decay before reaching the detector. For neutrinos however, the Earth is transparent up to certain energies. Thus, a muon travelling upwards in the detector can only be the product of a neutrino interaction. But even after subtraction of the atmospheric muons, there is still a huge background of atmospheric neutrinos compared to the tiny fluxes of possible astrophysical neutrino sources. Neutrino astronomy at the moment faces a similar situation like γ-ray astronomy in the pre-1980s era: The small signal drowns in an overwhelming background and the only chance is to search for a significant clustering of events.

1.3.4 Interaction of neutrinos

For neutrinos passing through matter at high energies ($\gtrsim 10$ GeV) only deep inelastic scattering (DIS) of neutrinos on nucleons is important [6]. There are two different modes: charged current (CC) and neutral current (NC) reactions. CC interaction happens via exchange of a charged W boson and NC via the neutral Z boson:

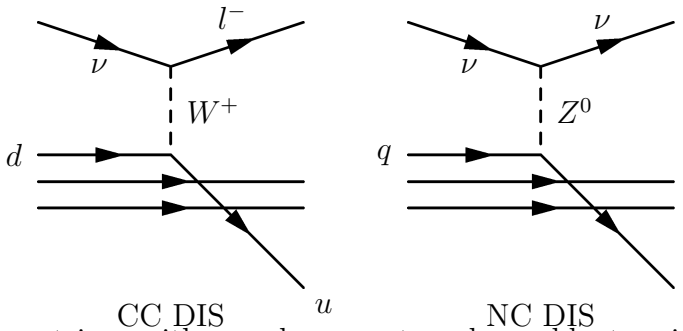

CC interactions of neutrinos with a nucleon create a charged lepton, i.e. an electron, muon or tauon. The hadronic rest from the nucleon starts a **hadronic cascade**. The electron initiates an **electromagnetic cascade**. A low energy τ also produces a cascade, but a high energy τ can travel up to ~ 100 m before decaying in another cascade. The muon usually travels across a long (up to several km [63]) **straight track**, losing some of its energy in ionization, Cherenkov emission and other processes. NC interactions produce only a hadronic cascade [24].

The cross-sections for both DIS processes are proportional to the neutrino energy up to ≈ 10 TeV and become $\propto \ln E_\nu$ at high energies, see fig. 1.12. For anti-electron-neutrinos $\bar{\nu}_e$, a special reaction is possible: the resonant production of a W^- boson in reaction with an electron: $\bar{\nu}_e + e^- \longrightarrow W^-$, called "Glashow resonance" [23, 68].

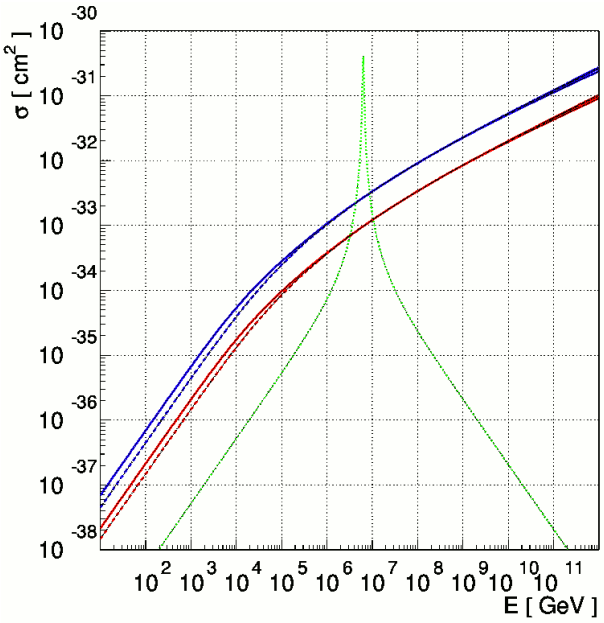

Figure 1.12 Simulated neutrino-nucleon cross-sections: Higher blue curves are CC, lower red are NC; solid are ν, dashed are $\bar{\nu}$. Green dotted is Glashow resonance $\bar{\nu}_e e^- \longrightarrow W^-$. From [68].

To illustrate how low the neutrino cross-sections are, let's consider as example a beam of neutrinos with a few TeVs energy, having a neutrino-nucleon CC DIS cross-section $\sigma = 10^{-35}\,\mathrm{cm}^2$, passing through a medium with nucleon number density n. During the passage through an infinitesimal slice of thickness dl, cross-sectional area A, the number of particles N_ν is reduced via interaction by an amount

$$dN_\nu = -N_\nu\, dP_{\mathrm{int}} = -N_\nu \frac{dN_{\mathrm{target}}\,\sigma}{A} = -N_\nu \frac{n\, dV \sigma}{A} = -N_\nu\, n\sigma dl$$

From which follows that the probability for a particle to pass through length l without interaction is $P = \exp(-n\sigma l) = \exp\left(-l/\lambda\right)$ with the mean free path λ defined as:

$$\lambda \equiv \frac{1}{n\sigma} = \frac{1}{\frac{N_{\mathrm{nucl}} N_A}{V_{\mathrm{mol}}}\sigma} = \frac{M_{\mathrm{mol}}}{N_{\mathrm{nucl}} N_A \rho\sigma} = \frac{1\,\mathrm{g}}{N_A \rho \sigma} \tag{1.5}$$

N_A is Avogadro's number, ρ is the medium's mass density, N_{nucl} the number of nucleons per molecule, and $M_{\mathrm{mol}} \approx N_{\mathrm{nucl}}$ grams the medium's atomic weight. In case of water as medium, $\rho = 1\,\mathrm{g/cm^3}$. So, for mean free path we have: $\lambda = \frac{1\,\mathrm{g}}{6\times 10^{23}\cdot 1\,\mathrm{g/cm^3}\cdot 10^{-35}\,\mathrm{cm}^2} = 1.7 \cdot 10^{11}\,\mathrm{cm}$, so 1.7 million km, or more than 4 times the distance from Earth to Moon. The interaction probability of a neutrino on a path of length l is accordingly:

$$P(l) = 1 - e^{-l/\lambda} \approx \frac{l}{\lambda}, \tag{1.6}$$

so for a TeV neutrino travelling 1 km in water: $\approx 6 \cdot 10^{-7}$. Table 1.1 gives an overview of neutrino mean free paths and interaction probabilities for different energies and media.

Medium	ρ	M_{mol}	n		Energy			
					1 MeV	1 GeV	1 TeV	1 PeV
	[g/cm^3]	[g]	[cm^{-3}]	σ [cm^2] =	$10^{-41.15}$	$10^{-38.15}$	$10^{-35.15}$	10^{-33}
Water	1	18	6×10^{23}		2.35×10^{12}	2.35×10^{9}	2.35×10^{6}	1.67×10^{4}
Rock (SiO_2)	2.6	60	1.56×10^{24}	λ [km] =	9.05×10^{11}	9.05×10^{8}	9.05×10^{5}	6.41×10^{3}
Lead	11.3	207	6.78×10^{24}		2.08×10^{11}	2.08×10^{8}	2.08×10^{5}	1.47×10^{3}
Water	1	18	6×10^{23}		4.25×10^{-13}	4.25×10^{-10}	4.25×10^{-7}	6×10^{-5}
Rock (SiO_2)	2.6	60	1.56×10^{24}	$P(1\,\text{km})$ =	1.10×10^{-12}	1.10×10^{-9}	1.10×10^{-6}	1.56×10^{-4}
Lead	11.3	207	6.78×10^{24}		4.8×10^{-12}	4.8×10^{-9}	4.8×10^{-6}	6.78×10^{-4}

Table 1.1 Neutrino mean free path (λ) and interaction probability for passage through 1 km ($P(1\,\text{km})$) of different media (considering only CC DIS). At PeV energies, the mean free path becomes comparable to the Earth radius and the Earth becomes opaque for neutrinos.

1.3.5 Detection of neutrinos

As indicated in section 1.3.4, there are basically two event topologies in a large neutrino detector: cascades (electrom. or hadronic) and tracks. These are also the two detection channels that are available in a Cherenkov based neutrino telescope. **Tracks** are mainly produced by muons (with a tiny contribution of extremely energetic τ leptons that can travel some 100 m). In a search for a cosmic neutrino point source, mainly muons are used as detection channel. The long tracks provide a long lever arm and allow best possible reconstruction of the muon direction which is close to the neutrino direction at high energies: $0.7^\circ \times (E_\nu/\text{TeV})^{-0.7}$ [69]. The overall resolution for reconstruction of muon neutrino direction is smaller than 1° in a km-scale neutrino detector and for long tracks [24]. A good angular resolution is important for detection of a point-like neutrino source as a clustering of events. Another advantage of the long tracks of muons is that many muons that were created kilometers below the detector will still pass through it and be detectable, so that the effective volume for muon detection is larger than the instrumented one [24]. **Cascades** will look almost point-like in the huge sparsely instrumented detector volume. Their direction can only be estimated very roughly ($\sim 30^\circ$ [24]), however their energy estimation is better than that of muons because they are fully contained in contrast to muons mostly leaving the detector [24]. This allows a better discrimination of a hypothetically harder signal spectrum from the atmospheric neutrino spectrum. Additionally, the atmospheric background is considerably smaller in the electron and tau channels than in the muon channel, which also motivates the use of cascades [24].

The detection mechanism is the detection of the optical and UV Cherenkov photons that are emitted by the charged particles from the neutrino interaction.

The Cherenkov effect

A charged particle moving through a dielectric medium with refractive index n with a velocity $v = \beta c$ higher than the phase speed of light c/n in the medium will cause the emission of Cherenkov radiation [6]. This is caused by polarization of the medium's atoms or molecules and can be compared to the phenomenon of a sonic boom produced by a super-sonic body. A charge moving below the speed of light also polarizes, but the photons emitted during relaxation of the polarized molecules cancel each other and no light is observed. Only if the polarizing particle moves above the speed of light, the radiation forms a shock front in form of a cone and is intensified similar to a super-sonic

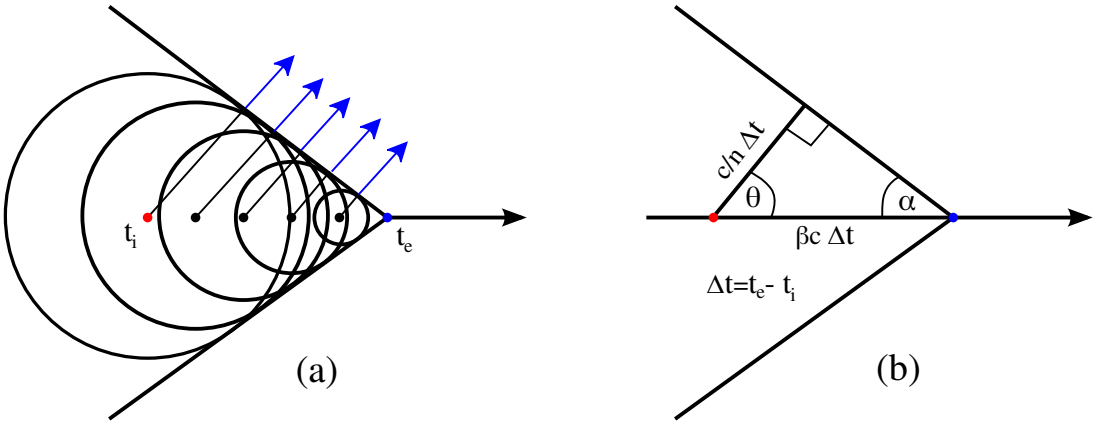

Figure 1.13 (a) A particle from which Cherenkov radiation originates travels in direction of the black arrow, from the left-most red point at time t_i to the right-most blue point at time t_e. The circles indicate wave fronts of radiation at time t_e that form a shock front in form of a cone that propagates in the direction of the blue arrows. (b) Geometry of the Cherenkov cone.

boom. This can be illustrated in a simple drawing, shown as fig. 1.13.

From the geometry of super-luminal emission of radiation (cf. fig. 1.13), the opening angle α of the Cherenkov light cone and the angle θ between particle direction and Cherenkov photon direction can be calculated:

$$\sin\alpha = \frac{1}{\beta n} \qquad \cos\theta = \frac{1}{\beta n}. \tag{1.7}$$

The condition for Cherenkov emission is $v > c/n$. It follows that at the threshold: $p = \gamma m v = \gamma m \frac{c}{n} = \frac{E}{mc^2} m \frac{c}{n} = \frac{E}{cn}$, from which with the energy-momentum relation $E^2 = p^2c^2 + m^2c^4$ follows the threshold energy:

$$E > E_{thr} = \frac{mc^2}{\sqrt{1 - \frac{1}{n^2}}}. \tag{1.8}$$

See table 1.2 for a list of Cherenkov angles and energy thresholds of different optical media.

Medium	refractive index n	$\alpha \geq$	$\theta \leq$	E_{thr} for e	E_{thr} for μ
water (20° C)	1.333 [6]	48.6°	41.4°	0.77 MeV	160 MeV
normal ice	1.31 [70]	49.8°	40.2°	0.79 MeV	164 MeV
air (sea level)	1.0003 [6]	88.6°	1.4°	20.9 MeV	4.3 GeV

Table 1.2 Cherenkov cone half-opening angle α, particle-photon angle θ (cf. fig. 1.13) and energy threshold for electron and muon for different optical propagation media. For the angles, the ultra-relativistic case of $\beta \approx 1$ is assumed (for lower velocities, α is larger and θ is smaller).

The spectrum of Cherenkov radiation is continuous and lies in the UV and visible range. Because it is proportional to λ^{-2} [6], smaller wavelengths dominate and this gives Cherenkov light its typical "blue glow" color when observed with the naked eye. However, "seeing" Cherenkov radiation is only possible if a very high persistent flux of relativistic particles is present, e.g. in a nuclear reactor. CR induced interaction events are not

visible with human eyes, because single passing particles produce photons only within a few nanoseconds.[7]

In neutrino observatories, the Cherenkov photons produced by the leptons from neutrino interaction are collected and recorded with optical modules (OMs) that usually contain a photomultiplier tube (PMT), that is capable of detecting individual photons with a ns time resolution. From the data supplied by the OMs, the time, direction and energy of the lepton can be reconstructed. The use of Cherenkov light of course requires the interaction and detection medium to be optically transparent.

1.3.6 Experiments

Experimental efforts in high-energy neutrino astronomy started in the 1970s with the DUMAND (Deep Underwater Muon And Neutrino Detection) project [71]. In 1987, a string of seven optical detectors was put in the deep sea off the island of Hawaii and demonstrated the feasibility of measuring CR muons with the Cherenkov technique and reconstructing their trajectories [72]. However, the planned km-scale DUMAND detector was never built and the project failed after a two-decade long effort due to technical problems. But DUMAND developed many detector technologies in use today and inspired installment of later **water detectors** [24]. A smaller instrument was installed in Lake Baikal in Siberia, which is the deepest lake in the world and at maximum 1.2 km deep [73]. It was operated since 1998 and was in 2005 upgraded to a 10 Mton detector. Preparation towards a km^3-scale detector with Gton volume is currently ongoing [74]. The Lake Baikal collaboration already published upper limits on the flux from WIMP annihilation in the Earth and the Sun and on diffuse extra-terrestrial neutrino flux [74].

Other water-based detectors were developed, tested and installed in the Mediterranean Sea by the ANTARES, NEMO and NESTOR collaborations. While the other two have basically performed R&D activities, ANTARES has deployed a 0.1 km^3 prototype detector consisting of 12 lines (cables) holding in total 900 optical modules (OMs), deployed near the French mediterranean coast. ANTARES has successfully proved the concept of a sea-based neutrino telescope [24]. In 2000, the three collaborations merged into the KM3NeT Consortium which aims at the construction and deployment of a Mediterranean km^3 neutrino telescope with 2015 as deadline, complementary to IceCube [62]. One motivation for KM3NeT is the ability to observe the Galactic Center and many Galactic sources (e.g. SNRs) that lie in the southern hemisphere through the Earth's muon shield which is not possible for IceCube [62]. Using water as medium has advantages over ice, with very long scattering lengths that can lead to a very good angular resolution [24] (up to $\sim 0.1^\circ$ [62]). Disadvantages of water are the decay of ^{40}K and bioluminescence of fish and other organisms which lead to a steady as well as time-variable background. Water currents have to be considered as well and the positions of the modules have to be monitored.

As a complement to the research activities in water, **Antarctic ice** has been considered as detector medium as well. The first prototype detector, AMANDA, has been deployed into the almost 3 km deep ice near the U.S. maintained Amundsen-Scott station at the geographic South Pole. It has been in operation from 2000 to 2009 and has, like ANTARES, been a proof of concept for a larger km^3-scale detector [24]. The successor of AMANDA, IceCube, has started to be deployed around AMANDA in 2005 and is to be completed

[7] They are relativistic, indeed, so a particle with $\beta \approx 1$ needs ~ 3 ns to travel 1 m.

in early 2011. It will be the largest neutrino detector ever built and the first with an instrumented volume of $\sim$1 km^3. First results from IceCube are presented in section 2.1.5. Compared to water, Antarctic ice has a shorter scattering length, but the attenuation length is longer [24]. Antarctic ice is surprisingly transparent, the absorption length of Antarctic ice is of the order of 100 m or more [24]. The radioactive and bioluminescent backgrounds of water are not present in sterile Antarctic ice, the only noise comes from the detector itself [24].

1.4 Possible Sources of Cosmic Rays

Like already mentioned, it is not yet clear from experiment how high-energy cosmic rays are produced. However, a number of theoretical ideas exists of where and how this might happen. First of all, it must be mentioned that there are two opposing principle ideas of the origin of CRs: These are subscribed as "top-down" and "bottom-up" scenarios. **Top-down** models of the origin of high-energy CRs propose the existence of very massive, yet unknown particles or topological defects (e.g. monopoles) that *decay or annihilate* into the particles observed as highly energetic cosmic rays [6, 7]. Such models of exotic particle decay or annihilation are capable of explaining production of CRs at ultra-high energies (above 10^{20} eV) where acceleration seems unlikely [6]. An observed flux beyond the GZK cut-off can also be explained by top-down scenarios [7]. **Bottom-up** approaches propose known astrophysical objects as candidates for *acceleration* of low energy particles (nuclei and electrons) to high energies [7]. Neutrinos can be expected in both top-down and bottom-up approaches and might provide very valuable information. A diffuse neutrino flux and the absence of point sources would speak for top-down generation of CRs. However, a diffuse neutrino flux could also be caused by many weak point sources. The detection of a point source of astrophysical neutrinos would strongly support bottom-up scenarios.

Several possible sources from bottom-up scenarios will be presented in this section after the introduction of the predominant theoretical models for cosmic particle acceleration. A general consideration of CR acceleration sites is the argument raised by Hillas [75, 8]: A particle can only gain energy in an accelerator as long as it is bound by its magnetic field B (like in a ring accelerator on Earth). As soon as the particle's Larmor radius $r_L = \frac{E}{ZeB}$ exceeds the size R of the accelerator, it escapes from the acceleration site, so the maximal achievable energy can be estimated to be $E_{\max} \propto BRZ$, where Z is the charge number of the particle. A **Hillas diagram** is a plot of B versus R in which classes of astrophysical sources are plotted according to their magnetic field strength and size. Following the Hillas argument, diagonal lines in the Hillas plot indicate possible combinations of B and R for a given maximum energy and for a given particle species.[8] Possible sources of those particles are those that lie on or above the respective line. A Hillas diagram is shown in fig. 1.14.

[8]The Hillas plot is double-logarithmic and from $B(R) = k \cdot \frac{1}{Z}\frac{E_{\max}}{R}$ follows

$$\log(B) = k - \log(Z) + \log(E_{\max}) - \log(R),$$

so that in the Hillas plot, points of constant $E_{\max}$ and Z lie on a line with slope -1.

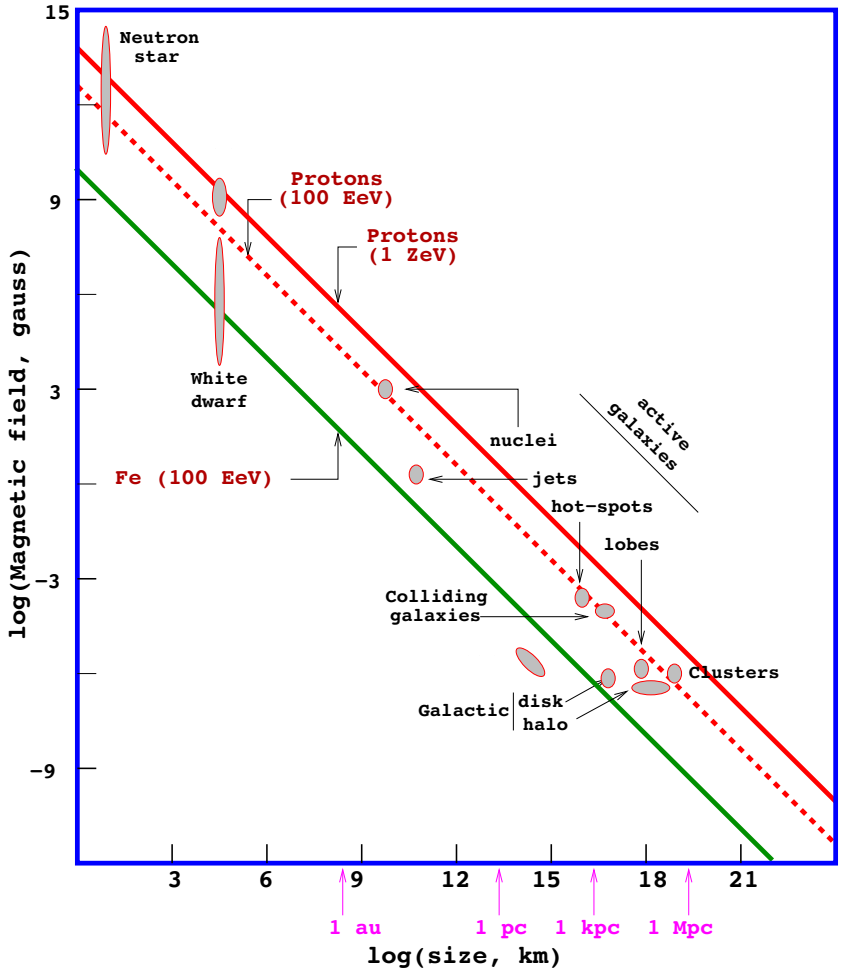

Figure 1.14 A Hillas diagram of some astrophysical objects, plotted with their magnetic field strength vs. size. Diagonal lines are drawn for some energy and particle charge and show which sources are capable of producing those particles. Sources below the line are not (max. energy is smaller), sources above are (max. energy is larger). From [76].

1.4.1 Acceleration Mechanisms

The most popular model for acceleration of CRs in astrophysical environments is the first order **Fermi acceleration** or "shock acceleration" [8]. It happens at a shock front, which is a density perturbation propagating through a medium (magnetic plasma) with a speed higher than the speed of sound. Particles scattering randomly on magnetic turbulences of the medium are gaining energy when crossing the shock front, moving from one side of the shock to the other. This is a stochastic process and on average, an energy gain is achieved that is proportional to the relative velocity of the magnetic plasmas on both sides of the shock [6, 8, 17, 77]. A shock front is assumed to develop e.g. in supernova remnants (SNRs) or jets where matter expands rapidly with velocities higher than the speed of sound in the environmental medium in which it expands. During a supernova explosion, several solar masses of material are ejected at a speed of $\sim 10^4$ km/s which is much faster than the speed of sound in the interstellar medium (ISM) which is ~ 10 km/s [77, 6]. Shocks probably also form in jets of AGNs and GRBs and are thought to be relativistic, i.e. with a speed $> 0.1c$ [77]. The (differential) energy spectrum of

the accelerated particles from a strong shock[9] is predicted by Fermi acceleration models to be a power-law $\propto E^{-2}$.[10] That is why this is a common assumed spectrum also for astrophysical neutrino signals, because the neutrinos produced at a CR acceleration site inherit the CR spectrum. But the spectrum could also be steepened by various effects [8, 77].

Another idea is the **direct acceleration** of particles, e.g. in strong electric fields generated by rotating neutron stars with high magnetic fields on the surface or in rotating accretion disks [7, 75]. Direct acceleration mechanisms do not lead to a power-law spectrum as naturally as Fermi acceleration, so they are usually disfavoured over stochastic acceleration processes [7].

1.4.2 Galactic Sources

Supernova Remnants

Very promising candidates as CR sources are supernova remnants that are the outer shell of a star after a supernova. Supernovae are among the most energetic events in the Universe, the total energy output can be in the range of 10^{53} erg [6].[11] A core-collapse supernova explosion occurs at the end of stellar evolution for stars with masses exceeding $\sim 8\ M_\odot$. With the supernova, stellar material is ejected into the interstellar medium and forms a supernova remnant (SNR). The SNR continues to expand and cool and this is believed to create a shock front leading to acceleration of particles. SNRs are sources of electromagentic emission in many wavelengths, the most prominent one being the Crab Nebula. SNRs have also been detected as sources of γ-rays up to TeV energies [54, 56]. Like mentioned before, the Crab Nebula is even used for calibration purposes in γ-ray astronomy [58].

[9] Strong shock means that the Mach number $\mathscr{M} = v/c_s$, which is the ratio between velocity and speed of sound, is $\gg 1$ [8].

[10] If the relative energy gain per shock crossing is ξ, then the particle's energy after n crossings is $E = E_0\,(1+\xi)^n$ from which follows

$$n = \frac{\ln(E/E_0)}{\ln(1+\xi)}.$$

However, n crossings are only possible if the particle didn't escape from the shock front region, so with escape probability p_{esc} per crossing, the number of particles with an energy $> E$ is $N(>E) \propto (1-p_{\text{esc}})^n$.

$$\Rightarrow \ln N(>E) = k + \frac{\ln(E/E_0)}{\ln(1+\xi)} \ln(1-p_{\text{esc}})$$

$$\Rightarrow N(>E) \propto E^{-\gamma+1} \quad \text{with} \quad \gamma \equiv -\frac{\ln(1-p_{\text{esc}})}{\ln(1+\xi)} + 1 \approx \frac{p_{\text{esc}}}{\xi} + 1 \approx \frac{R+2}{R-1}$$

where R is the compression ratio, and is 4 in the strong shock limit. It follows that the differential spectrum is $\frac{dN}{dE} \propto E^{-\gamma}$ with $\gamma = 2$ for strong shocks. [77, 8, 17]

[11] For comparison, this is an energy that corresponds to $8.2 \cdot 10^{11}$ years of energy output from the Sun in its current stage of evolution (having a luminosity of $3.846 \cdot 10^{33}$ erg s^{-1} [78]). Even though 99% of this energy is radiated in form of neutrinos, the bolometric electromagnetic luminosity of a supernova explosion can still exceed 10^{42} erg s^{-1} [6], which is comparable to the luminosity of a whole galaxy [78].

Pulsars

Another product of supernovae are neutron stars. Those are very compact objects (with nuclear density) that are produced in the core of a star during a supernova. If a neutron star has a magnetic field, it is called a pulsar, because it emits radiation only along an axis that spins with its very fast rotation which leads to "pulsed" detection. An example is again the Crab Nebula, because within the SNR shell resides a pulsar, the Crab pulsar. Pulsars have been first seen with radio telescopes and their very regular pulsed emission has astonished researchers. Pulsars can also be detected in γ-rays, e.g. the Fermi space telescope has detected at least 46 gamma-ray pulsars [79] and also Cherenkov telescopes like H.E.S.S. have seen very high energy photons from the direction of pulsars [80]. In the context of VHE pulsar emission, it is often spoken of pulsar wind nebulae (PWNe) in which the interaction of the pulsar wind and its surroundings seems to lead to VHE processes [80].

X-ray Binaries

X-ray binaries (XRBs) are systems consisting of a compact object (CO) and a companion star (CS). The CS loses matter which is accreted onto the CO and forms an accretion disk that is very hot and radiates thermally in X-rays. XRBs can also have jets which makes them potential sources for relativistic particles. They will be treated in depth in chapter 3 because the main part of this work is an analysis of the XRB Cygnus X-3.

1.4.3 Extra-galactic Sources

Active Galactic Nuclei

It is assumed that most galaxies have a supermassive black hole (SBH) in their center [78]. The SBH in our own Galaxy has been indirectly observed as very massive object whose density can only be explained by a black hole. It is itself not radiating even though its vicinity is a region of increased stellar density and thus more thermal radiation. However, there seem to be galaxies where the SBH is surrounded by an accretion disk that spirals towards the black hole and heats via inner friction. Vast amounts of gravitational energy are converted into radiation in a very efficient process (up to more than ten times more efficient than nuclear fusion, see p. 309 in [78]). The galactic core is "active", so the objects are called active galactic nuclei (AGNs). Matter from the accretion disk can be ejected in gigantic collimated jets of relativistic particles. There are several classes of objects, depending on their spectral properties, e.g. quasars (radio-loud AGNs, short for "quasi-stellar radio source"), quasi-stellar objects (radio-quiet AGNs, QSOs), blazars (quasars whose jet lies in the line-of-sight) and Seyfert galaxies. The different phenomenology is thought to be primarily due to different viewing angles and luminosities, but the underlying processes of accretion etc. could be very similar [78]. AGNs are also candidates for CR production, especially for the extra-galactic component. Gamma-ray experiments have detected signals from the position of several AGNs [81] and the Auger observatory has observed a correlation of highest energy CR events with the positions of nearby AGNs [28].

Gamma Ray Bursts

Gamma ray bursts (GRBs) are transient (short-lived), but extremely bright events of γ-ray emission that last between a fraction of a second up to several thousand seconds [82]. GRBs happen frequently: The GRB rate is estimated to be around 1000 per year for the full sky [83]. Occurring at this high rate and isotropically instead of clustered on the Galactic plane, it is most likely that they are of extra-galactic origin. What gamma ray bursts are is not completely clear. They are usually regarded to be special cases of supernovae (SNe) that are accompanied with a collimated jet of particles. If this jet, containing γ-rays and perhaps neutrinos, points towards the observer, it is recognized as a gamma ray burst. Because of the collimation of the jet in a small solid angle, the observed flux does not decrease much with distance. This explains why so many GRBs can be detected whereas SNe with isotropic emission cannot, since their intensity falls with the inverse square of the distance.

CHAPTER II

The IceCube Neutrino Observatory

The IceCube Neutrino Observatory is located at the geographic South Pole of Earth[1], buried in the $\sim$3 km deep ice on top of the Antarctic bedrock. It is currently the largest neutrino detector ever built. After its scheduled completion in 2011, it will encompass an instrumented volume of about 1 km^3 and consist of more than 5000 optical modules that are arranged in 80 normal strings and 6 special, denser instrumented strings that form the DeepCore array. At the time of writing, 79 of the 86 strings have been deployed and are currently taking data, among them 6 DeepCore strings that comprise IceCube's low energy extension, similar to the denser AMANDA array [84, 85].

The IceCube hardware, data acquisition system and data processing will be introduced in section 2.1. IceCube was preceded by the smaller AMANDA detector array, now surrounded by IceCube, that served mainly as a proof of principle for the km-scale IceCube detector. It was taking data until the end of the IceCube 40-strings season and the last year of its data taking was included into the sample used in this analysis to improve sensitivity for spectra softer than E^{-3}. That is why the AMANDA detector is introduced as well in section 2.2.

2.1 IceCube

The IceCube detector was planned to be completed in steps, since construction work at the South Pole is only possible during austral summer. First construction began in the 2004$-$2005 season, with deployment of the first string. Since January 2010, 79 of the total planned 86 strings are in ice and the array is scheduled to be completed in January 2011 [24]. The uncompleted arrays have already been taking data until they were superseded after one year by the next larger array. For this reason, a natural detector operation time of about one year has been established, labeled with the number of strings currently in the ice. Analyses of the taken data also follow this scheme and analyze IceCube data taken during one construction stage that has unchanged detector properties. In this work, data from the IceCube 40 strings season from 2008 to 2009 was used, combined with simultaneous data from AMANDA. The geometry of the IceCube 40 detector was rather asymmetrical and is illustrated in fig. 2.1. The data sample and its properties are discussed in section 4.2.1.

[1] At the US-operated Amundsen-Scott South Pole Station [24].

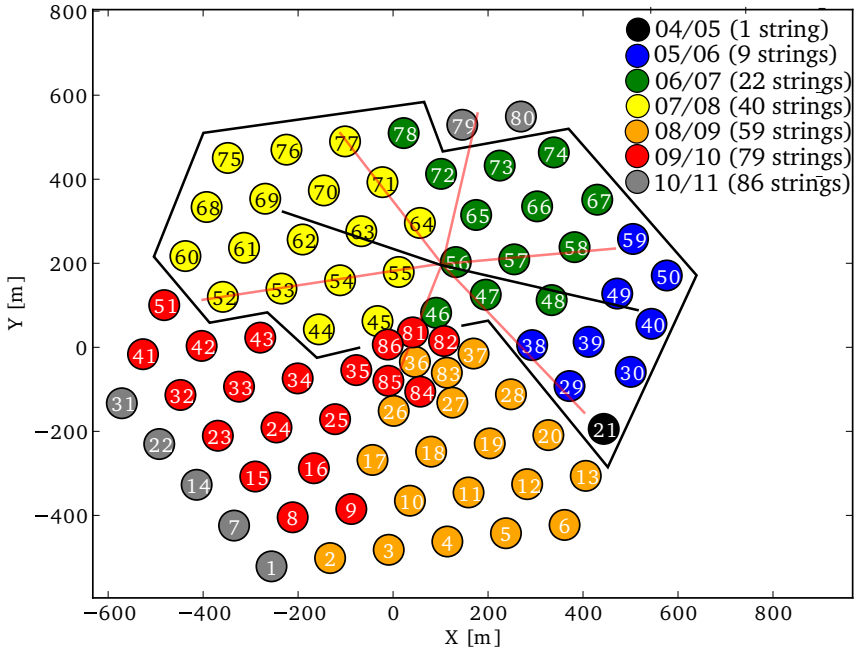

Figure 2.1 Map of the string positions, looking at the IceCube detector from above. The string number is printed on each string (DeepCore strings have numbers 81 to 86) whose measured or scheduled position is indicated with a circle. The colour of the circle refers to the time of string deployment and is given in the legend, where the first two numbers stand for the calendar years of the deployment season and the number in brackets for the total number of IceCube strings that were in ice after the deployment season. The IceCube 40-strings detector is highlighted by the black contour line. Its major symmetry axis lies along the black line, minor symmetry axes follow the red lines. These are visible in the azimuth distribution of the recorded data, see fig. 4.25a.

2.1.1 Detector components

The basic components of IceCube are the **strings** that are vertical arrays of digital optical modules (DOMs). Each string consists of 60 DOMs that are about 17 m apart and the strings are aligned in a hexagonal array with a spacing of ∼125 m between strings. The strings are put vertically into the ice between 1450 and 2450 m below the ice surface [24]. This is achieved by drilling holes with hot water, placing the string into the hole and letting the hole water refreeze. After completion in 2011, there will be 80 regular IceCube strings in total. Specialized strings are the six extra strings belonging to the **DeepCore** array. They have 60 special DOMs with higher quantum efficiency. The DOMs have a smaller vertical spacing of about 7 m and are located only in ice layers in the middle and bottom of the detector that are exceptionally clean [24]. Another two regular IceCube strings will be used as "in-fill" strings for DeepCore and will also have the closer vertical spacing [84, 85]. At the ice surface above each regular string, there is station belonging to the **IceTop** array, which is a separate detector for cosmic ray air showers, built with the intention to measure the primary cosmic ray flux and composition. Each IceTop station consists of two tanks filled with frozen water and two DOMs, used as Cherenkov detector similar to the Auger surface array [24]. Combination of IceTop and IceCube provides information about CR composition and allows calibration of the detector [24]. A schematic drawing of the IceCube detector is shown in fig. 2.2.

The main components of a **DOM** are a commercial photomultiplier tube (PMT) and mainboard electronics, housed by a pressure-resistant spherical glass shell, see fig. 2.3.

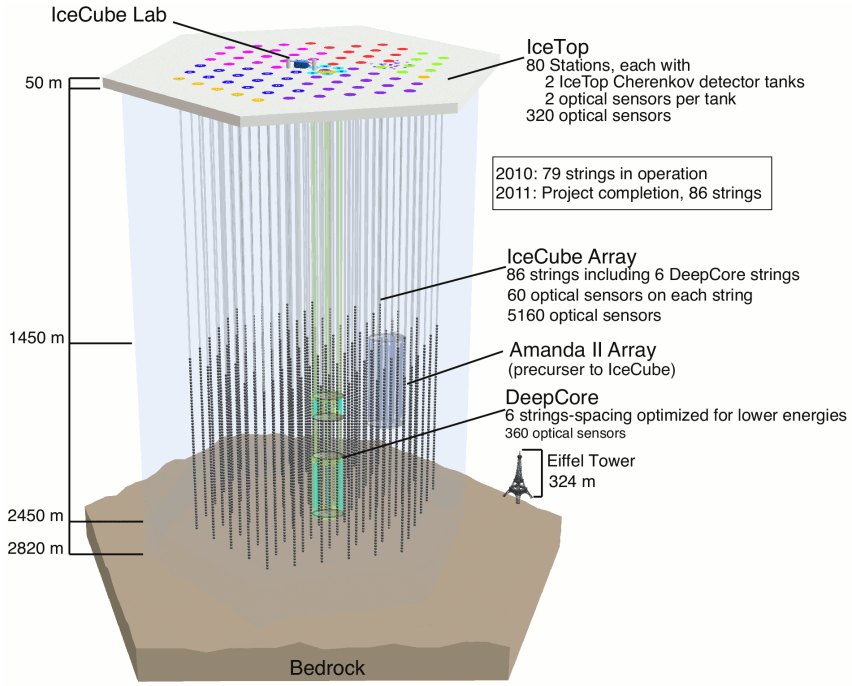

Figure 2.2 Sketch of the IceCube detector with the size of the Eiffel tower for comparison.

The IceCube DOMs have an R7081-02 PMT produced by Hamamatsu Photonics that has a diameter of 10 inches and a quantum efficiency[2] of $\sim 25\%$ at a wavelength of 390 nm (DeepCore DOMs have a higher quantum efficiency) [86].The PMTs have a gain of 10^7 [86] which means that one electron being knocked out of the negatively charged photocathode results in 10^7 electrons received at the anode.[3] The photocathode of the PMT is looking downward in order to optimally detect photons from upward moving muons. If only one photon knocks an electron out of the photocathode, then the PMT pulse is called a single photo electron (SPE) pulse, otherwise, one speaks of a multiple photo electron (MPE) pulse. The time series of the PMT pulse is called waveform and is processed by two different digitizers called ATWD (*Analog Transient Waveform Digitizer*) and FADC (*Fast Analog to Digital Converter*). ATWD has a higher time resolution, but covers a shorter time interval (128 bins of 3.3 ns covering 422 ns) whereas FADC records a longer time interval, but is coarser (256 bins of 25 ns covering 6400 ns). An example of a digitized waveform in the FADC and ATWD channels is given in fig. 2.4. Because the waveform is digitized before it is submitted to the surface, there is no data loss during the submission.

The waveforms are sent up via cable and received by a DOMHub, which is a computer responsible for the communication with all DOMs on one string. From the DOMHubs, the data are sent to other processing computers at the IceCube Lab (ICL) that sort the hits in time and check if the trigger conditions are met. If they are, the waveforms from

[2]The quantum efficiency (QE) is the ratio of released photo electrons per photon hitting the photocathode. It is a measure of the sensitivity of the PMT.

[3]In a photomultiplier tube, a photon releases a photo electron from a cathode via the photoelectric effect. The photo electron is accelerated onto a dynode where it hits off other electrons that are in turn accelerated onto the next dynode. After a cascade of several dynodes, a single electron has been multiplied to an enormous number of electrons. The ratio of electrons before and after the multiplication is called gain.

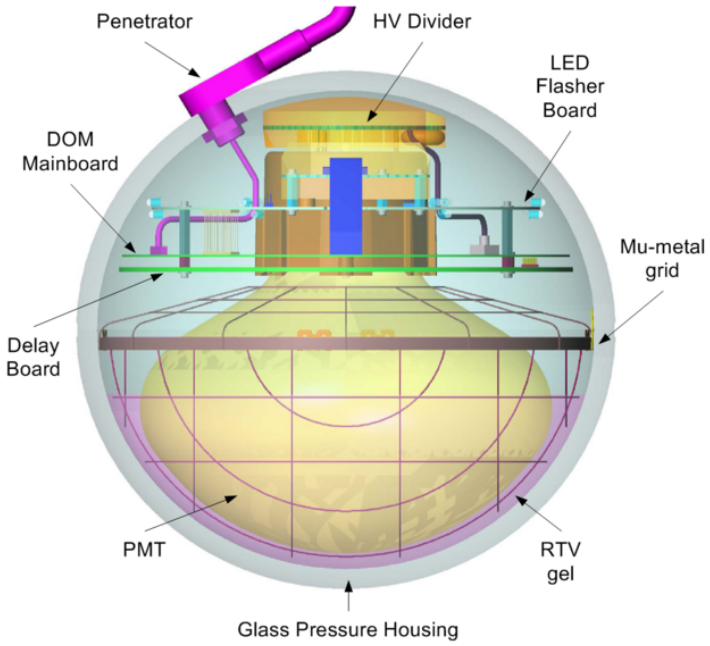

Figure 2.3 Schematic picture of an IceCube DOM. The DOM is connected with the surface via the pink cable. The mainboard contains the main electronics, e.g. the ATWD and FADC waveform digitizers. A special flasher board is equipped with 12 LEDs that allow calibration of the detector using a light source emitting at known wavelength, intensity and time. The central component is the 10 inch Hamamatsu PMT, surrounded by a mu metal grid to shield the PMT from the Earth's magnetic field and optically coupled with the glass housing by an RTV gel.

the hits are stored and processed further.

2.1.2 Data acquisition system

If the PMT pulse is rising above a fixed discriminator threshold, set at the pulse corresponding to 0.25 photo electrons (PE), then one speaks of the DOM being hit. The average hit rate of an IceCube DOM is more than $\sim$300 Hz which results in around 1.5 million DOM hits per second for the complete IceCube detector with more than 5000 DOMs [86]. Recording all these DOM waveforms would result in a much too high data rate and is not necessary since most of the DOM hits are caused by dark noise, e.g. radioactive decays (from ^{40}K in the glass sphere) or thermal noise. For the data to be recorded by the data acquisition (DAQ), certain **trigger** conditions must be met that reduce the amount of data significantly. The central part of the IceCube trigger is local concidence of DOM hits. If at least one of the nearest or next-to-nearest neighbours of a DOM (on the same string) is also hit within a time window of ± 1 μs, then the DOM is said to fulfill the local coincidence (LC) condition [87]. Only LC hits are considered for the triggers that are used. One of the most important triggers is called simple multiplicity trigger (SMT) and requires at least eight LC hits within a time window of 5 μs to initiate a read-out. Hits not fulfilling the LC condition are called isolated hits. If IceCube is operating in "hard local coincidence" (HLC) mode, then only LC hits are read out. In "soft local coincidence" (SLC) mode, isolated hits are read out as well, but reduced to only the highest amplitude bin and the two neighbouring bins of the FADC. Also in SLC mode, LC hits are required to fulfill the trigger conditions. Since May 2009 (the beginning

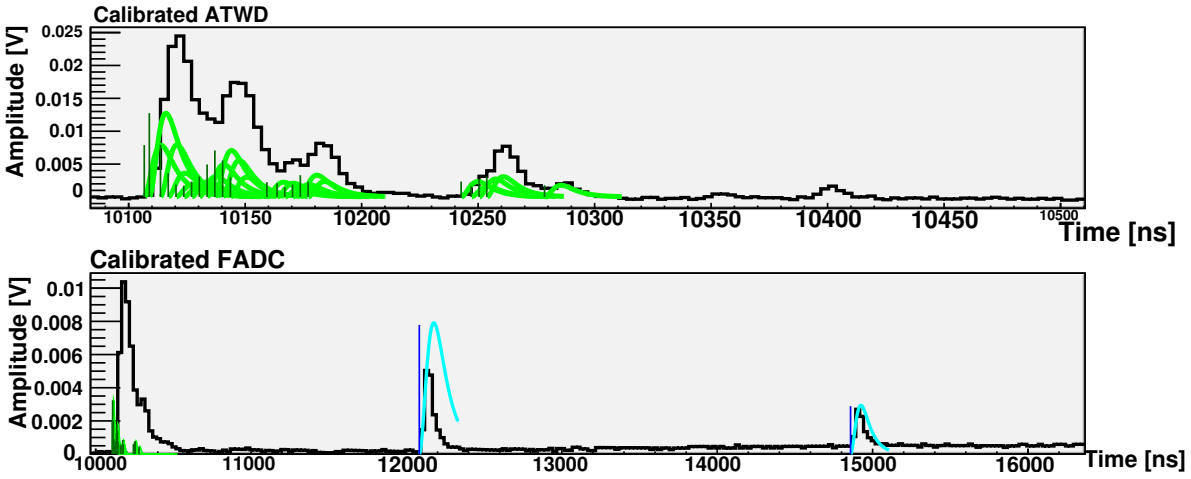

Figure 2.4 Example of a waveform recorded during IceCube 59-strings on String 50, DOM 7. While the FADC has only one channel, there are three ATWD channels with different amplification levels (16×, 2×, 0.25×) of which the unsaturated channel with highest amplification is used to store the data. In this case it is the one with 16× amplification. Via feature extraction code, the waveform is split into separate pulses (see curves on top of the histogram), whose charge and time are determined, indicated with a line. Pulses that come after the end of ATWD are marked with cyan color, the others are green. This plot was created by the author for a low level check of IceCube 59-strings data.

of the IceCube 59-strings season), IceCube is operating in SLC mode. In a global trigger mechanism, nearly simultaneous triggers from different detector components (IceCube, IceTop, AMANDA) are merged. If only AMANDA has experienced a trigger, then IceCube is read out anyway and the data are combined. This is why in principle IceCube is expected to be always up and ready when AMANDA is. This is not really the case, see footnote 16 in chapter 4.

Each trigger leads to a selection of data called **event** that can be maximally 40 μs long and tagged with a time-stamp to provide very accurate information of when the event happened, i.e. when the individual DOMs were hit. The time resolution of the IceCube DOMs is very good (∼few ns [87]) and the timing information is needed both for exact reconstruction of muon tracks and for distinction between events induced by neutrinos (signal) and events caused by atmospheric muons (background). All the events emerging from the trigger are stored on magnetic tape and transported to the North by plane during austral summer. In order to get the data already before, they are processed "online" by dedicated filters that aim to select only those events that are most interesting for common analyses. E.g. the "muon filter" selects track-like events interesting for point source analyses and the "cascade filter" aims at cascade-like (in IceCube almost point-like) events from electron or tau neutrinos. The online filters involve first-guess reconstructions and cut on the zenith angle (see section 2.1.4). The data reduction by the online filtering allows to send selected events via a satellite that has a bandwidth of 30 GB/day which is not enough to transfer all the triggered data.

2.1.3 Antarctic ice

A very important part of the detector calibration is a firm understanding of the ice properties. The antarctic ice is target medium, but also detection medium that allows the

propagation of Cherenkov photons and their detection with the DOMs. The scattering and absorption coefficients are defined as the inverse of the effective scattering and absorption length. They need to be known with sufficient accuracy in and near the detector because they allow to predict the propagation of Cherenkov photons in the ice. If the assumed values are too high or too low, then the expected number of photons hitting the DOMs is under- or overestimated. This has large impact on the reconstruction of the event energy and direction, since also the spatial photon distribution and the hit time distribution are influenced by scattering and absorption. Moreover, the response of the detector to a certain signal neutrino flux depends on the ice properties. Therefore, an accurate measurement of the ice properties is essential. The ice at the site of the IceCube detector is described in detail in [88].

With measurements made with pulsed and continuous light sources embedded in the AMANDA detector, it was possible to measure the **optical ice properties** and distinguish scattering and absorption of light in the wavelength range between 313 and 560 nm and depths between 1100 and 2350 m below surface [88]. **Scattering** is caused by trapped air bubbles and dust, **absorption** also by dust and by the ice itself. It was found that in shallower depths, the scattering coefficient is very high due to the air bubbles in the ice [88]. At $\sim$1350 m depth all bubbles have been converted to air-hydrate crystals under the high pressure and scattering on air bubbles vanishes because the refractive index of the crystals is very close to that of the surrounding ice [88]. Below 1300 m, both scattering and absorption coefficient follow the vertical variation of dust concentration which tracks climatological changes and is also seen in ice cores taken at other Antarctic sites. In particular, four dust peaks are identified between 1300 and 2300 m that are associated with colder climate during a non-glacial period and a broad peak due to the Last Glacial Maximum is found around 1300 m [88]. The scattering and absorption coefficient as function of wavelength and depth are shown in fig. 2.5. The scattering length is typically around 20 m and the absorption length around 100 m. The absorption length is up to 10 times larger than for cleanest laboratory ice [89] and is comparable to purified water in detectors for proton decay measurement like IMB and Kamiokande [90].

From comparison of the optical measurements with ice core measurements in Antarctica, the deep South Pole ice could be estimated to be between 23,000 years (at 1300 m depth) and 165,000 years old (at bedrock, 2800 m below surface) [91]. Its temperature profile varies from $-45°$C at 1300 m depth to $-9°$C at bedrock [92]. Furthermore, there exists an ice flow with velocity of 9 m/yr at the surface, but the ice is assumed to be at rest at the bedrock bottom, which leads to a small shear force on the deep ice below 2000 m depth. The shear force is not strong enough to cause damage to the IceCube strings within at least the next 20 years [92].

The optical properties of the ice are incorporated into the **simulation** of the IceCube detector and into the **reconstruction** of events. More recent measurements taken with the IceCube array extend to higher depths and allow more accurate results. They show a generally much clearer ice at greatest depths of IceCube ($2300 - 2500$ m) that motivated the construction of the DeepCore array. However, these are beyond the scope of this thesis. In section 5.3, the uncertainties on the ice properties and their impact on the calculated flux limits are discussed together with other systematic uncertainties.

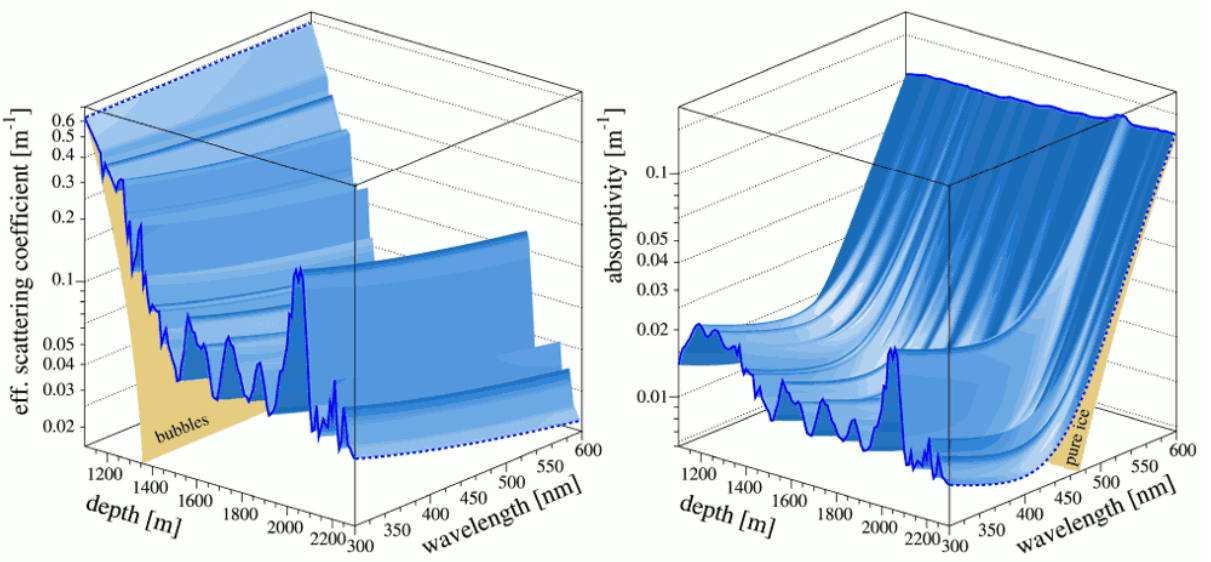

Figure 2.5 Optical scattering (left) and absorption coefficient (right) for deep South Pole ice as function of wavelength and depth. The contribution of air bubbles to the scattering and of pure ice to the absorption is shown in the background. Dashed lines emphasize general wavelength dependences. From [88].

2.1.4 Reconstruction and data selection

The reconstruction is done in several steps: First, a fast and rough estimation of the event direction is calculated. The result is used to already filter the events and select the most interesting ones. The filters are run online at the Pole and selected events are transferred via satellite. Then, more elaborate and time consuming reconstructions can be performed on the selected events, usually done offline. The advanced reconstructions involve the maximization of a likelihood function and use the simple estimates as initial guess for the minimizer [69]. For point source searches, only muon track reconstruction is important, since cascade reconstruction offers a much too bad directional resolution. This is why only muon reconstructions are described here.

An important first guess algorithm is the line-fit algorithm [69]. It ignores the light emission geometry in form of a Cherenkov cone and the scattering and assumes light propagation along a linear track with the velocity $\mathbf{v}$. Then, light would be expected at DOM positions $\mathbf{r_i} \approx \mathbf{r} + \mathbf{v} \cdot t_i$ at time t_i. The unknown vectors $\mathbf{r}$ and $\mathbf{v}$ can be obtained in a least squares method from the minimization of:

$$\chi^2 = \sum_i (\mathbf{r_i} - \mathbf{r} - \mathbf{v} \cdot t_i)^2$$

The χ^2 can be minimized analytically via differentiation with respect to the free parameters to obtain a vertex point $\mathbf{r}$ and a direction $\mathbf{v}$. Another first guess algorithm, the direct walk, selects possible track candidates by connecting two hit DOMs fulfilling various conditions. The track candidates are grouped into clusters and the cluster with most track candidates is selected as track [69].

More advanced muon track reconstruction is done via a maximum likelihood technique, i.e. by minimizing $-\log(\mathscr{L})$ for a likelihood function $\mathscr{L}$. In principle, a muon track can be assumed to go linearly through the detector so that it has five parameters: an arbitrary

anchoring point (x, y, z) and two angles (θ, ϕ) giving the track direction. The likelihood can be modeled in several ways. Using only the individual hit times t_i at DOM positions x_i, y_i, z_i, the likelihood is the product of the probabilities $p(\mathbf{r_i}|\mathbf{a})$ with hit information $\mathbf{r_i} = (x_i, y_i, z_i, t_i)$ and track hypothesis $\mathbf{a} = (x, y, z, \theta, \phi)$:

$$\mathscr{L} = \prod_{i=1}^{N_{\text{hit}}} p(\mathbf{r_i}|\mathbf{a})$$

with the number of PMT hits N_{hit}.[4] However, the likelihood may also contain other information, e.g. that the photo-electron is one of a number of photo-electrons on the module (MPE), or which modules have been hit and which have not been hit, or the recorded waveform amplitudes (the peak charge) [69]. The probability density function (p.d.f.) for arrival times of single photons $p(\mathbf{r_i}|\mathbf{a})$ can be calculated from Monte Carlo simulation of the Cherenkov photon propagation, accounting for the ice properties described in section 2.1.3. Alternatively, the Monte Carlo results can be parameterized with an analytical function called *Pandel function*, similar to a gamma distribution [69, 93]. The negative logarithm of the likelihood is minimized with respect to the track parameters $\mathbf{a}$ to find the most likely track hypothesis which yields the global minimum.

The likelihood space in (θ, ϕ) dimensions around the minimum of $-\log \mathscr{L}$ has an approximately parabolic shape. This is exploited to fit a paraboloid to the likelihood [94]:

$$-2 \cdot \log\left(\frac{\mathscr{L}(\theta, \phi)}{\mathscr{L}_{\max}}\right) = \frac{x^2}{\sigma_x^2} + \frac{y^2}{\sigma_y^2}$$

σ_x and σ_y are the major and minor axes of an error ellipse.[5] The error ellipse axes are usually circularized to a single error $\sigma = \sqrt{(\sigma_x^2 + \sigma_y^2)/2}$, called **paraboloid sigma**, and this can be used as an angular error estimate on an event-by-event basis [96, 23, 97].

The vast majority of events recorded with IceCube are down-going muon events from cosmic ray air showers. Only 1 in 10^6 events is an up-going muon produced by an atmospheric neutrino. By using the Earth as muon shield and applying filtering based on the first guess zenith angle, $\sim$1% of triggered events remain. However, only a small fraction of $< 10^{-3}$ of those filtered events are induced by atmospheric neutrinos, so that this sample is still dominated by down-going muons that were mis-reconstructed as up-going (cf. fig. 2.6). Examples for down-going muons appearing as up-going are uncorrelated coincident muons from several showers that pass first through the bottom, then through the top of the detector, multiple muons from one shower (a muon bundle) passing the detector or extensive scattering [69]. In these cases, reconstruction fails, often because

[4] Note that one DOM can be hit several times in one event.

[5] For a likelihood $\mathscr{L}(\theta)$ with maximum $\mathscr{L}_{\max}$ at $\hat{\theta}$, it is [95]:

$$\log \mathscr{L}(\hat{\theta} \pm \sigma_\theta) = \log \mathscr{L}_{\max} - \frac{1}{2}$$

Putting this relation into the paraboloid definition from above, we get:

$$-2\left(\log \mathscr{L}_{\max} - \frac{1}{2} - \log \mathscr{L}_{\max}\right) = 1 = \frac{x^2}{\sigma_x^2} + \frac{y^2}{\sigma_y^2}$$

I.e., an ellipse equation is satisfied and σ_x and σ_y are the axes of an error ellipse.

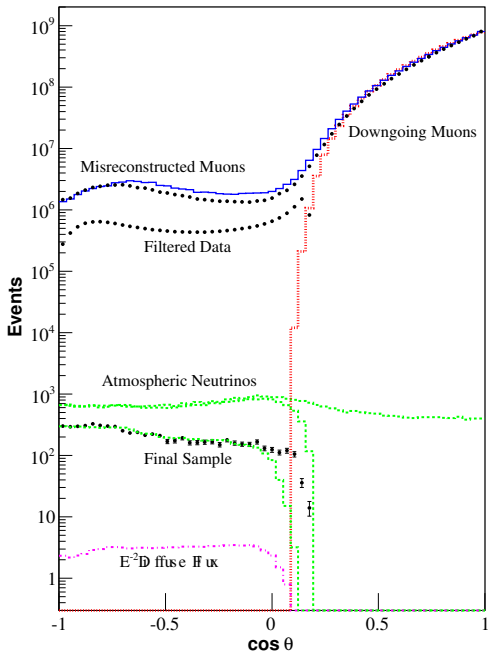

Figure 2.6 Zenith angle θ distribution of events at different selection levels for AMANDA-II detector. Green dashes (simulated atmospheric neutrinos) and black points (data) are from top to bottom: trigger level, filter level, and final selection level. Blue solid: simulated cosmic ray muons as reconstructed, red fine dotted: simulated cosmic ray muons as simulated (both at trigger level). Pink dash-dotted: reconstructed zenith distribution at final level for an E^{-2} spectrum diffuse flux. From [94].

the assumption of a single muon track is wrong, and may deliver an erroneous up-going track. For this reason, the quality of the track reconstruction must be estimated and cuts must be applied to arrive at a nearly pure final neutrino level. The final neutrino level of $O(10^3) - O(10^4)$ atmospheric neutrino events for the northern sky constitutes the irreducible background in a search for cosmic neutrinos.

Several quality parameters are calculated that help to select well-reconstructed events and reject background. One of the most important is so-called *reduced likelihood parameter* L:

$$L = \frac{-\log(\mathscr{L}_{\max})}{N_{\mathrm{Ch}} - 5} \tag{2.1}$$

which is the ratio of the found minimum to the number of degrees of freedom in the fit (number of data points minus the number of fit parameters).[6] Smaller values of L indicate higher track quality [69]. It is useful to compare the L of different reconstructions. E.g. if a forced down-going fit gives much better L than a forced up-going fit, then the event is likely to be down-going. Another quality parameter is the *smoothness* of the track which is a number close to 0 if the hits are distributed smoothly along the track and +1 or -1 if the hits cluster at the beginning or end, typical for background events. Other selection parameters are derived from the *time residual* of the hits: The recorded hit time t_{hit} is compared to the geometrically expected hit time t_{geo} if the photon would travel on

[6] For Gaussian probability distributions, it corresponds to the reduced chi-square.

a straight line without scattering:

$$t_{\text{res}} \equiv t_i - t_{\text{geo}} \tag{2.2}$$

The number of *direct hits* N_{dir} is defined as the number of hits that have a small time residual, e.g. $-15\,\text{ns} < t_{\text{res}} < 75\,\text{ns}$.[7] A large number of direct hits speaks for many unscattered photons and thus an event with high quality information [69]. A related parameter is the *direct track length* L_{dir} which is the distance between the first and last direct hit, if projected with the Chernekov angle onto the track [69].

2.1.5 IceCube performance

Because of its South Pole location, IceCube can observe sources at a constant zenith angle in the sky [98]. This means that the northern hemisphere is accessible all the time through up-going neutrinos. With common event selection and cut strategies, a simulation of the full IceCube detector (80 strings, without DeepCore array) produces a median angular separation of 0.8° between true event direction and reconstructed event direction (called *median angular resolution*) for a simulated differential neutrino flux $\frac{d\Phi}{dE} \propto E^{-2}$ [83]. The effective detector area[8] for muons is close to the geometric detector area of ~ 1 km^2 and varies between 0.3 km^2 for tens of GeV and 1.5 km^2 for tens of PeV muon energy at final selection level, for muons arriving from the northern sky [83]. The effective area for neutrinos is of course much smaller because of the small neutrino-nucleon cross-sections (see section 1.3.4) and ranges between 10^{-4} m^2 for 100 GeV and 10^3 m^2 for 1000 PeV [24]. Fig. 2.7 shows the neutrino effective area for 22 IceCube strings.

In the simulation from [83], completed IceCube is expected to set an average upper limit (sensitivity) of $E^2 \cdot d\Phi/dE = 8.1 \cdot 10^{-12}$ TeV cm^{-2} s^{-1} sr^{-1} on the diffuse muon neutrino flux after one year operation, which is well below the Waxman-Bahcall bound (s. page 15) [83]. The sensitivity or average upper limit for a point source signal after one year of data taking is expected to be $E^2 \cdot d\Phi/dE = 5.5 \cdot 10^{-12}$ TeV cm^{-2} s^{-1} sr^{-1} [83]. The energy threshold of the analyses is around 1 TeV due to energy selection cuts that

[7] A negative time residual appears to violate causality, but can happen due to PMT jitter and other effects without being physically unplausible. It might of course also indicate a coincident noise hit or the reconstructed track being wrong.

[8] Effective area A_{eff} is the cross-sectional area of a hypothetical detector in which every particle penetrating that area is recorded as event. In reality, not every particle going through the geometric area A_{geo} is detected or particles outside of the geometric area are detected as well. So, the effective area may be smaller or larger than the geometric area. Effective area A_{eff}, flux Φ and recorded *event rate* R are related via [23]:

$$R = \Phi \cdot A_{\text{eff}}$$

on the other hand, for *flux rate* F (particles per time passing through our detector) we have:

$$F = \Phi \cdot A_{\text{geo}},$$

so it follows $A_{\text{eff}} = \frac{R}{F} A_{\text{geo}}$. If in a simulation context F is seen as simulated events per time, R as detected events per time and A_{geo} as area in which events were generated, then [83]:

$$A_{\text{eff}} = \frac{N_{\text{detected}}}{N_{\text{generated}}} A_{\text{gen}}$$

Thus, the effective area can be obtained easily from detector simulation.

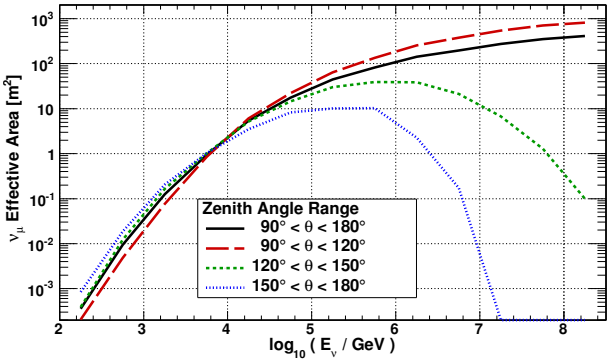

Figure 2.7 Solid-angle-averaged effective areas at final cut level of the IceCube 22-strings point source analysis for astrophysical muon neutrino fluxes ($\nu_\mu + \bar{\nu}_\mu$) at different declinations. The turnover at high energy for up-going events is due to absorption by Earth. From [99].

optimize sensitivity for an E^{-2} spectrum [83].

So far, IceCube has not detected any signal from astrophysical neutrino sources. Most recent results were obtained with IceCube in the 40 strings configuration. Several searches for point sources of astrophysical neutrinos showed no evidence for a signal [100, 24]. The IceCube 40-strings sample covers the northern (14,121 events) and the southern sky (22,779 events) with the northern sky dominated by atmospheric neutrino events and the southern sky, where a much higher energy cut was applied to reduce background, dominated by very high energetic atmospheric muon events. Among the searches is a scan over the whole sky for a significant spatial excess of events. On a grid with 0.1° spacing in right ascension and declination, an unbinned maximum likelihood search for a signal was performed (see section 4.2.3 for a description of a similar search), assuming a source to sit at each point of the grid. The results are shown in a significance map in fig. 2.8. The most significant deviation from background is located at 113.75° r.a. and 15.15° dec. with 11 signal events and a spectral index of 2.1 as best-fit parameters. The pre-trial probability for this to occur in a background only sample (called the p-value) is $5.2 \cdot 10^{-6}$, but the number of trials is large because of the large number of grid points. Repeating the experiment with Monte Carlo, 1817 out of 10000 random background only data sets have an equal or higher significance at any point in the sky, resulting in a post-trial probability of 18%. Upper limits on an E^{-2} flux of $\nu_\mu + \bar{\nu}_\mu$ lie around $E^2 d\Phi/dE = 2 \ldots 700 \cdot 10^{-12}$ TeV cm^{-2} s^{-1} depending on declination angle.

A search at the positions from a pre-defined list of 39 candidate sources has also been done to avoid the large number of trials. The most significant source on the list was PKS 1622-297 with a pre-trial p-value of 5% resulting in a MC calculated post-trial p-value of 62% [100]. Several stacking searches, summing up the events from various assumed source positions, were performed. A stacking of 16 Milagro TeV γ ray sources resulted in a post-trial p-value of 32%, a stacking of 127 local starburst galaxies revealed an under-fluctuation, so a p-value of 1, and stacking of five nearby clusters of galaxies yielded a post-trial p-value of 78% [100].

Other interesting research topics in IceCube are the study of atmospheric neutrinos, the search for GRB neutrinos, the search for a WIMP neutrino signal, e.g. from annihilating dark matter particles that accumulate in the Sun, the search for other exotic particles like slow monopoles and the search for supernova neutrinos that leave a trace in the overall increased noise rate, but are below the energy threshold of IceCube and not

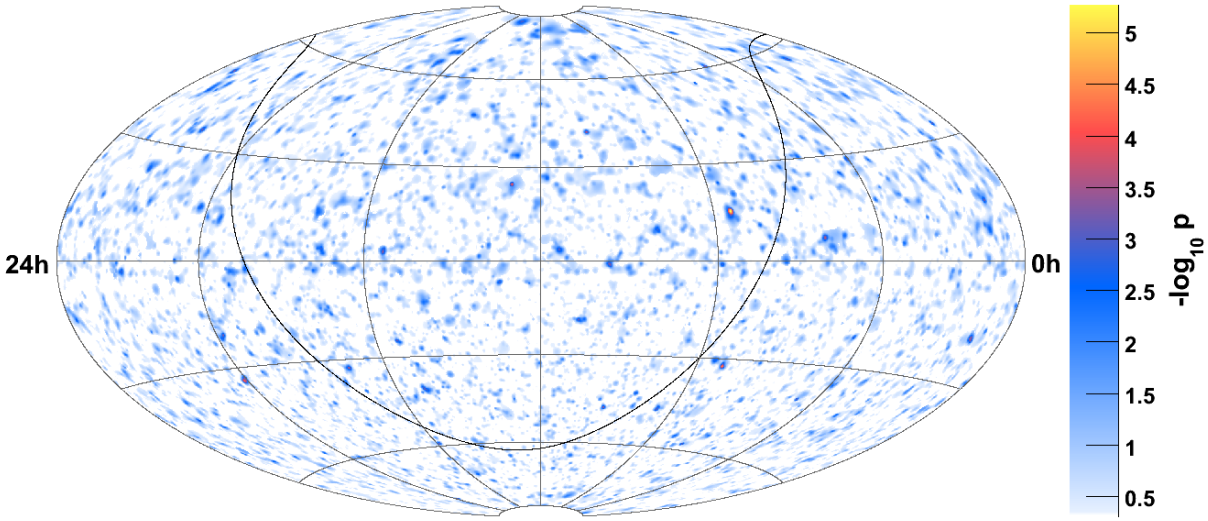

Figure 2.8 Equatorial sky map (epoch J2000) of pre-trial significances (given as probability in background only case, called p-value) of the all-sky point source scan on IceCube 40 strings data. From [100].

reconstructable. These and other subjects are beyond the scope of this thesis and can be found in other references, e.g. [24, 101, 102, 103]. Just one other interesting result is mentioned here which is a small anisotropy observed in the arrival direction of cosmic rays in the Southern sky using the 22 string IceCube detector. The huge background of cosmic ray muons allows high-statistics studies of cosmic rays with 4.3 billion muon events collected in the 22 strings IceCube season. They are reconstructed with median angular resolution of 3° and median energy of $\sim$20 TeV. The arrival direction distribution shows a small anisotropy with first-harmonic amplitude of 6.4×10^{-4} [104]. The cosmic ray muon anisotropy had already been observed in the Northern Hemisphere up to a few hundred GeV and up to the TeV range, e.g. by the Tibet array, Super-Kamiokande and Milagro [104]. However, IceCube measured for the first time an anisotropy in the Southern Hemisphere in the multi-TeV energy range. The relative intensity in declination belts is shown in a sky map in fig. 2.9. The relative motion of the solar system around the Galactic center (Compton-Getting effect) does not seem to fit to the data, since it predicts a deficit between right ascension 110° and 160° where the data reveal an excess. The effect might be caused by large scale structures in the Galactic magnetic field or by diffusive particle flux from a nearby cosmic ray source such as the Vela pulsar, the brightest γ-ray source in the sky [104, 24].

2.2 AMANDA

AMANDA (Antarctic Muon and Neutrino Detector Array) was a conglomerate of detector components to find out the best technology and geometry for the large scale detector IceCube. First construction of AMANDA dates back to 1992, when a prototype string of optical modules was deployed at the South Pole [98]. In 1993/1994, 4 strings with 80 optical modules were deployed at a depth of $800-1000$ meters [90]. Soon after the deployment it was realized that the ice at these depths is not ideal for muon tracking because

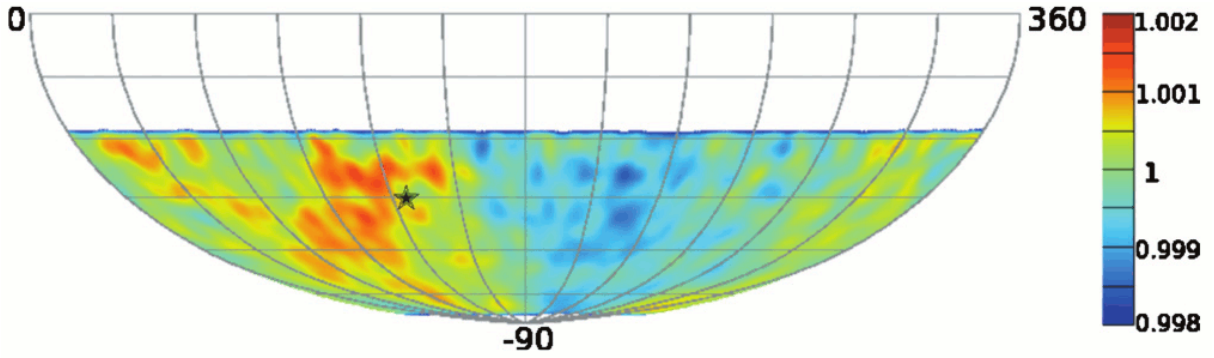

Figure 2.9 The relative intensity of arrival direction of cosmic ray muons in the Southern sky detected with 22 IceCube strings. The color scale represents the number of reconstructed events with respect to the average number of events in a declination belt of 3°. Thus, the natural zenith dependence of the distribution is hidden and the anisotropy in right ascension is visible. The star indicates the location of Vela. From [24].

the scattering due to air bubbles is too strong to allow accurate timing of Cherenkov photons needed for track reconstruction [89, 24]. In the 1995/1996 season, another 4 strings were deployed at depths between 1500 and 2000 m and AMANDA was finally completed in 2000 to consist of 19 strings holding 677 optical modules (OM), most of them between 1500 and 2000 m [69, 24]. The array operating since January 2000, often called AMANDA-II, has a roughly cylindrical shape and contains an inner core of 302 OMs on 10 strings referred to as AMANDA-B10. AMANDA-II recorded around 1000 neutrino events per year and for the past years of operation, until 2009, in a combined mode together with the growing IceCube detector [24]. AMANDA, in spite of being a successful proof-of-concept, had many technological problems, most of them coupled to the OMs submitting analogue signals to the surface [24]. The waveforms were digitized at the surface and only the time of threshold crossing and the maximum amplitude could be extracted, so basically only the first hit time could be used in the reconstruction, not the full information about the pulse shape like in IceCube [83, 24]. The unamplified analogue transmission required the OMs to be run at a very high gain of 10^9 which caused them to occasionally "spark" and produce light [24]. In later strings, the analogue electrical submission via coaxial or twisted pair cables was replaced by analogue optical submission via fibers, but this was sensitive to vibration and required regular manpower-intensive calibration [24]. On AMANDA string 18, first waveform digitizing OMs were deployed and performed well. This technology, as many others emerging from AMANDA, was adopted by IceCube [24].

2.2.1 Using a combined detector

Between 2007 and 2009, AMANDA and IceCube operated in a combined data taking mode. Analyses using the combined data sample can profit from the additional information provided by AMANDA. Because of the denser instrumentation of the AMANDA array, it is more optimized for lower energies. While IceCube's 125 m inter-string spacing is suitable for muon energies above a few TeV, AMANDA's energy threshold lies below 50 GeV [105]. Thus, AMANDA represents an important low energy extension of the incomplete IceCube detector, e.g. for WIMP searches. In the combined data taking mode, an AMANDA trigger also initiates an IceCube read-out and because IceCube is completely

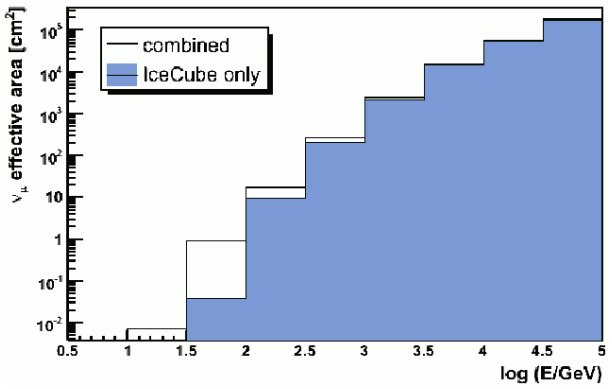

Figure 2.10 Effective detector area for muon neutrinos for a combined IceCube and AMANDA detector and for IceCube only in comparison. From [105].

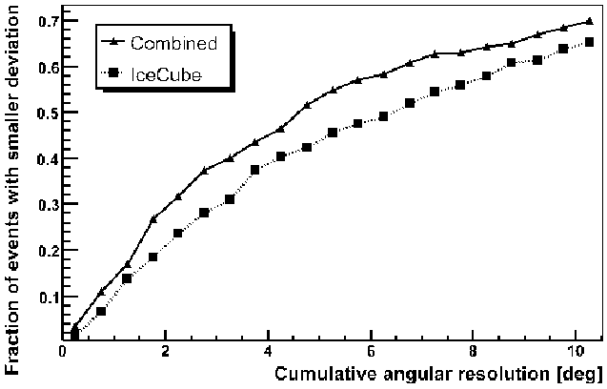

Figure 2.11 Angular resolution for a combined IceCube and AMANDA detector and for IceCube only in comparison. From [105].

surrounding AMANDA since the 2007 configuration of 22 strings, IceCube hits on strings adjacent to AMANDA expand the effective AMANDA volume and improve the angular resolution of the reconstruction due to the longer lever arm [105]. The surrounding IceCube DOMs can also be used as a veto. Events without hits in the veto region can be identified as starting or contained tracks. This allows to discriminate down-going muon events and select events from down-going neutrinos that start in the detector to become sensitive to sources in the Southern Hemisphere, e.g. the Galactic Center [105]. Selecting contained tracks imrpoves the energy resolution significantly. These ideas inspired the construction of the denser DeepCore array that substitutes AMANDA since 2010.

Enhancing the detector performance for lower energies of 10 GeV up to a few TeV is specifically interesting for investigation of sources with a spectrum steeper than the assumed E^{-2} spectrum originating from Fermi acceleration [105]. It is also possible that sources have an energy cut-off that prevents detection with IceCube. Gamma-ray observations indicate softer and cut-off spectra for several high-energy sources in our Galaxy, e.g. the Crab nebula [54]. Especially the observation of time-variable point sources profits from an extended energy range, since it increases the probability to detect events from the source. The also added background events are not hurting because the restriction to certain times and directions reduces background efficiently. This is why it was decided to use a combined IceCube and AMANDA data sample for the analysis outlined in section 4.2. In [105], Monte Carlo studies on the combined detector operation are presented. The effective detector area for muon neutrinos with and without integration of AMANDA is shown in fig. 2.10, the comparison of the angular resolution in fig. 2.11.

CHAPTER III

Cygnus X-3

Cygnus X-3 is a binary system in our Galaxy, consisting of a compact object (a black hole or neutron star) and a companion star, that are orbiting each other. Some years after its discovery in 1966, Cygnus X-3 (Cyg X-3) drew the attention of the high-energy astrophysics community because excesses of γ-rays and muons were reported from its direction in the 1970s and 1980s [106]. Even though the claimed detections could not be confirmed, it motivated quite a bit the advancement of high-energy astrophysics. Only very recently, at the end of 2009, the Fermi and AGILE gamma-ray space telescopes finally succeeded independently from each other to unambiguously detect GeV γ-ray emission from Cyg X-3 [107, 108, 109].

In section 3.1 and 3.2, X-ray binaries and the sub-class of microquasars are introduced in general. Afterwards, section 3.3 goes into details of the system of Cygnus X-3. It starts with a historical overview of its (partially unconfirmed) detections. Then general properties, multi-wavelength observations and correlations between different wavelengths are discussed. The chapter ends with a presentation of the γ-ray observation of Cyg X-3 and a summary that gives the motivation for performing a neutrino search on the Cyg X-3.

3.1 X-ray Binaries

An X-ray binary is a binary system, consisting of a non-degenerate star and a compact object—thought to be either a black hole or a neutron star—that orbit around each other [110]. A schematic picture of a typical X-ray binary is shown in fig. 3.1. The star is usually called 'stellar companion' or 'mass donor' because it loses matter (e.g. through stellar winds) that is gravitated towards the compact object (CO) where it spirals around the CO in an accretion disk [111, 112]. The accretion disk heats and emits huge amounts of energy in X-rays, hence the name "X-ray binary" [110, 111]. XRBs were first discovered in rocket flights starting in 1962 [113, 114, 115] and later studied with X-ray space telescopes like RXTE, Chandra X-ray observatory and XMM-Newton, just to name a few [115]. XRBs are very interesting objects because they allow the study of final stages of stellar evolution (neutron stars and black holes) [115], the study of matter in extreme conditions (e.g. they provide tests of general relativity in very strong gravitational fields) [115, 116, 111] and the study of the physics of accretion as well as the formation of jets, which might be analoguous to quasars or AGN in general [111, 110].

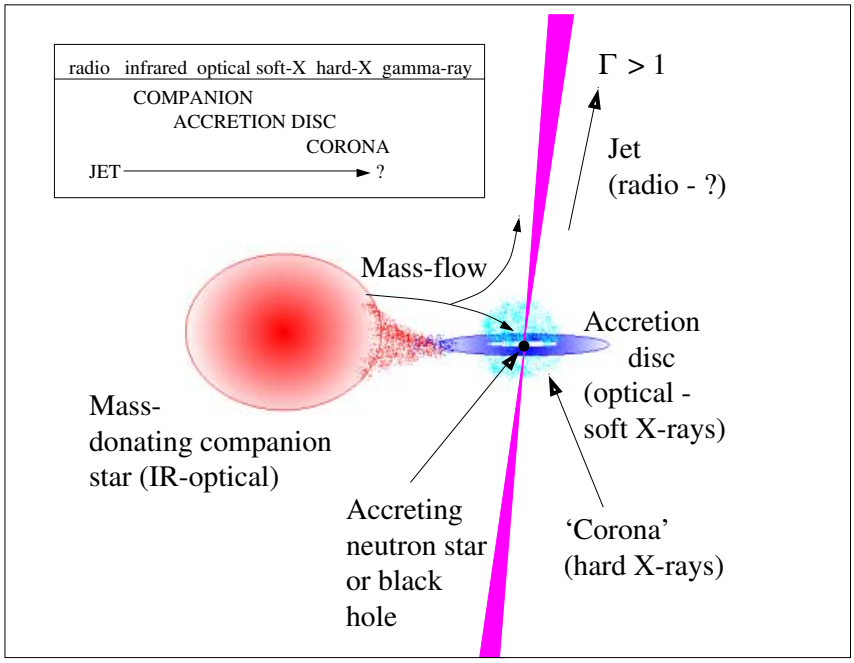

Figure 3.1 Sketch of the generally accepted structure of a typical X-ray binary system with the locations of the sites assumed to correspond to observed emission at different wavelengths. From [110].

The accretion-powered energy release is a process far more energetically efficient than nuclear fusion and the power output can exceed in some cases 10^{38} erg/s, which is $\approx 10^4 L_\odot$ and corresponds to the Eddington luminosity[1] of an object with one solar mass [110]. XRBs are characterized by a broad emission spectrum that spans from ≤ 1 GHz (~ 4 μeV) in the radio band to ≥ 1 MeV in γ-rays [110].

The most commonly used classification of XRBs is the division into high-mass XRBs (HMXBs) and low-mass XRBs (LMXBs) [115]. **HMXBs** comprise a compact object orbiting a massive ($M \geq 10\, M_\odot$) [115] OB class star and can be further divided into those with a Be star companion and those with a supergiant companion [118]. The majority (about 60%) of the 242 HMXBs in the catalogue of X-ray binaries in the Galaxy by Liu et al. (2006) [118] are known or suspected to be of the Be type and all Be systems found so far have probably a neutron star compact object [118]. **LMXBs** consist of a low-mass star

[1] The Eddington luminosity or Eddington limit is the natural limit on an object's luminosity under the assumption of mechanical stability. It is derived from the equilibrium of gravitational pressure and radiative pressure. The hydrostatic equilibrium for a spherical object yields for the gravitational pressure [78]:

$$\frac{dP}{dr} = -\frac{GM(r)\rho(r)}{r^2} = -g(r)\rho(r)$$

and continuum radiation pressure, if only Thomson scattering with electrons is considered, is: $dP/dr = -\frac{\sigma_T \rho L}{m_p c 4\pi r^2}$, so that for luminosity L follows:

$$L_{\mathrm{Edd}} = \frac{4\pi G M m_p c}{\sigma_T} \cong 1.3 \cdot 10^{38} \left(\frac{M}{M_\odot}\right) \mathrm{erg/s}$$

where σ_T is the Thomson scattering cross-section, M the mass of the central object and m_p the proton mass [6]. The Eddington limit has originally been derived for stars, but it can also be applied to accretion disks to estimate with the disk's luminosity its accretion rate [117].

(in general $M \leq 1\,M_\odot$) which transfers matter onto a NS or BH [119]. The companion can be e.g. a white dwarf or a late-type main-sequence star [119]. It is possible that its low mass is the result of matter transfer and that the star was originally of intermediate mass ($\sim 1.5 - 4\,M_\odot$). The catalogue by Liu et al. (2007) lists 187 LMXBs in the Galaxy and the Magellanic Clouds [119].

Because of the big difference in the masses of HMXB and LMXB companion stars, there are many differences between these systems. E.g. in HMXBs, the optical emission is dominated by the strong emission of the star, whereas in LMXBs, the star is so faint that it is often not detectable and optical emission is mainly due to reprocessed X-ray photons from the accretion disk [115]. The stellar winds of the companions in HMXBs are usually strong enough to power the accretion, however in LMXBs the accretion has to be realized by mass transfer through a Lagrangian point of the system (via the stars' Roche lobes) [115, 119]. The lifetime of HMXBs is limited by the high-mass companion star and is of the order of $\sim 10^5 - 10^7$ yr. The low-mass companion in LMXBs lives orders of magnitude longer, so that the lifetime of LMXBs is determined by the mass-transfer process and is $\sim 10^7$ – 10^9 yr [115]. This, in turn, leads to different spatial distribution of the XRBs: the short-lived HMXBs are, as younger systems, more often found in star forming regions along the Galactic plane, e.g. the Cygnus region. LMXBs tend to be older and are more often found towards the Galactic center and in globular clusters, where no new stars are born and stars are old [115].

Considering the search for high-energy neutrinos, HMXBs are more interesting, because they provide large densities due to the strong stellar wind [109]. They are thus a very good site for *pp* interactions producing neutrinos. XRBs with radio emission usually produce jets, as we will see later (see section 3.2) and are thus very promising candidates for high-energy particle acceleration. The Cygnus X-3 system, which is described later, is a HMXB with jets and thus fulfills both conditions.

XRBs containing a neutron star have different properties depending on the strength of its magnetic field: If the field is strong enough ($\geq 10^{11}$ G), then the accretion flow is linked to the rotation of the NS and channeled onto the magnetic poles, so that X-ray emission is intensified at the poles. The spinning of the NS leads to a modulation of the X-ray flux. This is called an accretion-powered X-ray pulsar, similar to an isolated radio pulsar, however it is generally radio-quiet [115, 110]. An XRB housing a NS with relatively low ($\leq 10^9$ G) magnetic field is called a Z source or Atoll source [110]. Z sources are the brightest persistent X-ray sources in the sky (the very brightest being Sco X-1) and are variable, but reliable radio sources [110]. XRBs with a NS can, as well as XRBs with a BH, be a transient source, i.e. be on a very low flux level for most of the time and then emit a largely increased flux during an outburst [115, 110]. XRBs that are not transient, but persistent[2], are still highly variable (factor 2 or more) in an aperiodic fashion that reflects the variable nature of the accretion process [115]. Finally, weakly-magnetic neutron stars with accretion disks can also undergo a special phenomenon: a thermonclear burst in which accreted material falls on the surface of the star and is compressed to densities and temperatures at which thermonuclear burning of helium (via nuclear fusion) can take place. This leads to a rapid increase in X-ray luminosity followed by a decay when the ignited layers expand and cool. This is called a Type I X-ray burst [115].

For **XRBs containing a black hole**, there are no different classes, each BH system is

[2]Persistent only means that the sources are clearly detectable at almost all times.

thought to be (in principle) able to enter all observed source states [110]. These "canonical" states of BH binaries are: the quiescent state, the high/soft (HS) state, the low/hard (LH) state and the very high (VH) state [116, 110].

- The **quiescent** state is the one that a typical BH binary spends most of its time in. It can be described as extraordinarily faint (in some cases only 10^{-8} of the outburst luminosity in the case of transients), with a non-thermal (power-law) and hard spectrum [116]. The faintness of the quiescent state (factor 100 lower compared to non-active states in NS binaries) might be explained by the existence of the event horizon which leads to a truncation of the (thermally radiating) inner accretion disk [116].

- The **high/soft** (HS) state refers to a generally higher luminosity and a spectrum dominated by thermal emission in the soft X-ray band (2 to 10 keV). The HS state is commonly modeled as $\sim$1 keV thermal emission from a multi-temperature accretion disk, with suppressed radio emission [116, 110].

- The **low/hard** (LH) state in turn has a generally lower luminosity and is dominated by non-thermal power-law emission in the hard X-ray band with a peak at $\geq$ 50 keV. The inner accretion disk might be truncated, like in the quiescent state, which leads to a decrease in temperature of the accretion disk [116]. In the LH state, a radio flux correlated with the X-ray flux exists that is often (maybe always) connected to a radio jet. Very large baseline interferometry (VLBI) images in the radio band show a spatially resolved radio jet during the LH state, e.g. for GRS 1915+105 and Cyg X-1. The radio emission in the LH state usually has a flat spectrum. It is quenched (suppressed) when the source enters the HS state [116].

- The **very high** (VH) state is characterised by a mixture of a thermal and non-thermal radiation [110], however with a steeper power-law than in the LH state [116]. It was first seen during maximum fluxes, e.g. a bright outburst of transient sources, thus the term "very high", but can also appear at lower flux levels [116]. In fact, it marks a transition between the low/hard and high/soft state and thus the name **intermediate** (IM) state was introduced [120].

The BH binary states and transitions between them can be presented in a **hardness-intensity diagram** (HID) [120]. It is a plot of an object's intensity (usually in X-rays) vs. the object's spectral hardness, which is defined as the ratio of the intensity in two energy bands [120] (usually the ratio of hard X-ray to soft X-ray intensity). The light curves of BH binaries are quite varied and can look very complicated. The hardness, however, shows considerable regularity and reveals a much more clarified picture in the HID [120]. A typical HID for a BH binary, in this case GX 339-4, is shown in fig. 3.2. The states in the HID mark the typical "Q-shape" (also referred to as "turtle head" [120]). There are four distinct branches that correspond to the canonical BHB states [120]:

- The vertical hard branch on the right is linked to the LH state.

- The vertical soft branch on the left is linked to the HS state.

- The two horizontal branches mark transitions between the LH and HS state and can be identified as very high (VH) or intermediate (IM) state.

The quiescent state is lying at the foot of the Q in the lower right of the diagram, since the source flux is very low with a hard spectrum [121]. The general movement of the source in the HID is that of a hysteresis, following the Q-shape in counter-clockwise direction. However, there can be more complicated behaviour [120]. For BH binaries producing jets, an interesting observation is made: A strong relativistic jet, associated with a strong radio flare, is ejected when the source crosses the so-called *jet line*, that is a vertical line in the HID, separating the VH/IM state and the HS state [121]. A schematic representation of an HID and the assumed disk-jet state of the binary is in fig. 3.3.

The strongest evidence for a neutron star in the system is the observation of periodic pulsations of the X-ray flux or of a thermonuclear burst. Both effects cannot be caused by a BH because it can have no magnetic field that is anchored within its event horizon and, having no material surface, but only the event horizon, the compression needed for a thermonuclear burst is not possible [115, 116]. However, the absence of pulsations and bursts is no evidence for the existence of the event horizon. Thus, evidence for existence of a black hole in an XRB most commonly stems from the estimation of the compact object's mass. There is a theoretical upper limit on the mass of a NS ($\simeq 3.2\,M_\odot$), so a CO exceeding this value is assumed to be either a black hole or something more exotic [115, 116]. However, this NS mass upper limit is not very certain [115] and the missing of a clear "smoking gun" evidence for the COs being black holes is reflected in the term "black hole candidate" that is often used.

Compared to the vast number of stars in the Galaxy, only a rather small number (few hundred) of XRBs have been detected so far. This indicates that they are rare among stellar systems [115], which makes sense, because the steps that lead to the formation of a binary system with a compact object (that is the end product of a supernova explosion) and a still living star appear to be rather unlikely [115]. In fact, it is still very poorly understood by which mechanisms XRBs are formed and evolve [115]. See table 3.1 for an overview of prominent XRBs and their properties.

3.2 Microquasars

XRBs can produce jets, i.e. relativistic outflows of matter that spread far beyond the dimensions of the binary system along the rotational axis of the accretion disk [110]. An XRB that produces relativistic jets is sometimes called a 'microquasar' because of the similarity to 'quasars' ('quasi-stellar radio sources') that are however around a million times bigger in size [111]. See fig. 3.4 for an artistic illustration of a microquasar. Quasars, like XRBs, consist of an accretion disk around a massive compact object that is, in case of quasars, always thought to be a black hole. The source of accretion matter is not a single massive star, but a huge number of stars in the center of a galaxy. However, the phenomenology of the accretion and of the generally two-sided jet look very similar in quasars and microquasars [111]. The presence of a jet is evidence for the acceleration of particles to high energies. These particles cool as the jet expands and produce radio synchrotron radiation. Thus, radio emission from XRBs is thought to be an indication for jets [110, 129].

The first discovery of an XRB producing a jet happened in 1979, when Margon et al. found jets in the system SS 433 [111, 131]. However, the phenomenon was regarded as very rare and the connection to quasars was not apparent, since the jets move only at 26%

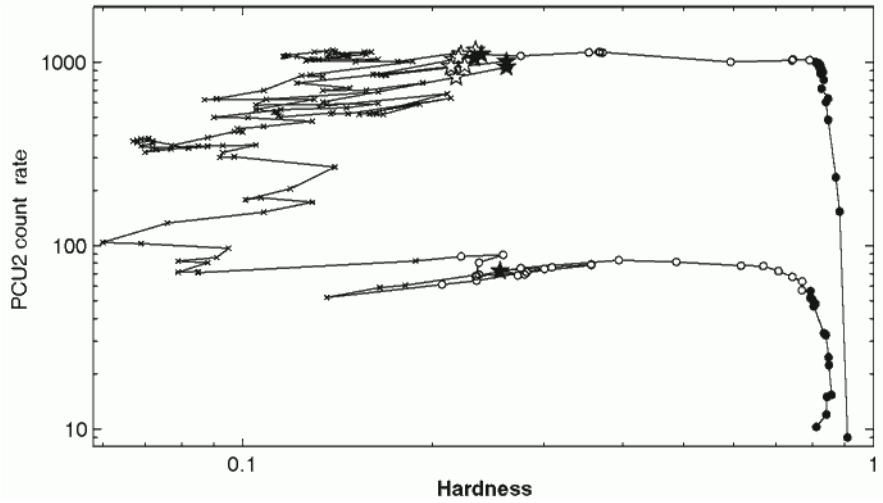

Figure 3.2 Hardness-intensity diagram (HID) for an outburst of black-hole binary GX 339-4. From [120].

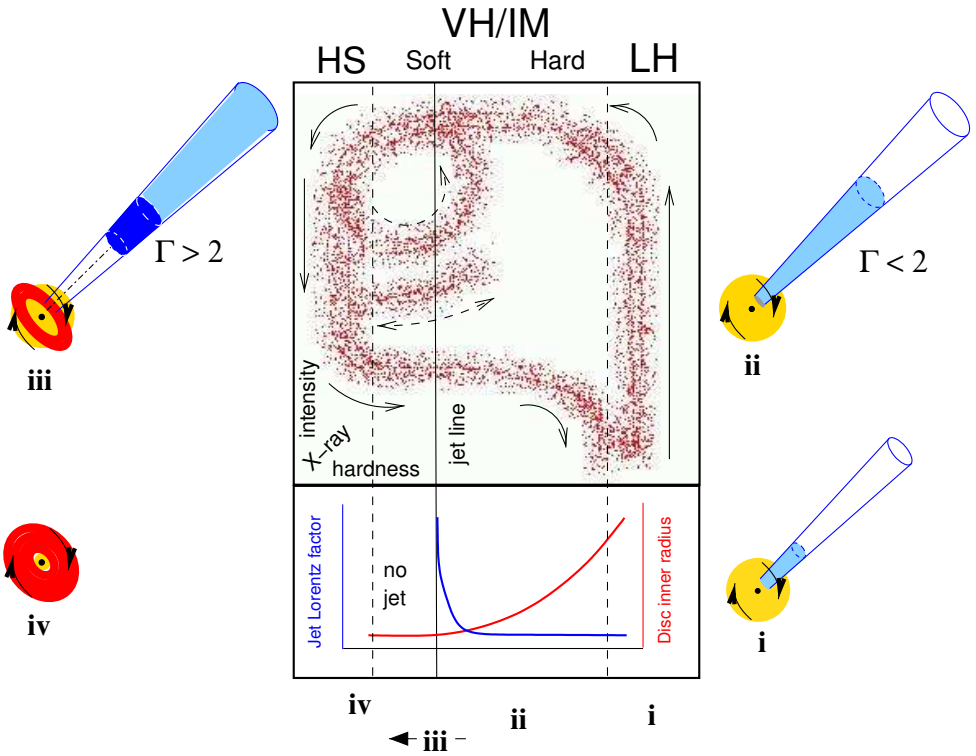

Figure 3.3 Schematic hardness-intensity diagram (HID) for a general black hole X-ray binary. HS = high/soft state, VH/IM = very high/intermediate state, LH = low/hard state. The source's general movement follows the Q-shape in anti-clockwise direction, but there can be other movements (e.g. dashed arrows). A crossing of the jet line results in production of a highly relativistic jet. The sketches with numbers i to iv show assumed flux contributions of various components: light blue = weakly relativistic jet, dark blue = highly relativistic jet, yellow = corona, red = accretion disk. In (i) and (ii), there is a steady jet during quiescent and low/hard state. In (iii), a relativistic shock travels through the jet which leads to cessation of jet production and disk-dominated HS state (iv). From [122].

Name	Type	RA [°]	Dec [°]	Dist. [kpc]	Orb. per.	CO (Mass)	Comments
Cyg X-1	HMXB	299.6	+35.2	2.0 ± 0.1 [116]	5.6 d [116]	BH ($6.9 - 13.2\ M_\odot$) [116]	One of few persistent BH binaries [120, 110], the classical black hole candidate [110].
Cyg X-3	HMXB	308.1	+41.0	9^{+4}_{-2} [121]	4.8 h [121]	BH? ($4.2 - 14.4\ M_\odot$) [123]	Has relativistic jet ejection and giant radio outbursts [121].
GRS 1915+105	LMXB	288.8	+10.9	$11 - 12$ [116]	33.5 d [116]	BH ($10 - 18\ M_\odot$) [116]	First XRB discovered with apparent superluminal motion of ejecta [111].
LS I +61 303	HMXB	40.1	+61.2	2.0 ± 0.1 [124]	26.5 d [124]	NS? ($1.5\ M_\odot$) [124]	Was discovered to emit VHE γ-rays by the MAGIC collaboration [125].
Sco X-1	LMXB	245.0	-15.6	2.8 ± 0.3 [126]	18.9 h [126]	NS ($1.4\ M_\odot$) [127]	Brightest persistent (non-solar) X-ray source in the sky [127, 110].
SS 433	HMXB	288.0	+5.0	5.0 ± 0.5 [128]	13.1 d [128]	BH? ($4.3 \pm 0.8\ M_\odot$) [128]	First XRB discovered to produce jets [110, 111].

Table 3.1 An overview of important X-ray binary systems in the Galaxy with one of the commonly used names, the equatorial sky coordinates (right ascension and declination), the distance from Earth to the object, the orbital period, the nature and mass (if known) of the compact object and some comments. If no references are given, then taken from [118] or [119].

of the speed of light, but in quasars, jets move at speeds very close to the speed of light [111]. In the 1990s, it was possible to resolve XRB jets with the technique of radio interferometry. The morphology of the two-sided jets found in e.g. 1E1740.7-2942 resembled that observed in quasars, thus, the term 'microquasar' was coined [132]. In 1994, Mirabel et al. observed **superluminal motion** of the jet ejecta from the microquasar GRS 1915+105. Superluminal motion is the movement of objects across the sky at apparent velocity higher than the speed of light [133]. GRS 1915+105 was producing an eruption in X and γ-rays, followed by a bipolar ejection of bright plasma, whose displacement in the sky could be followed in time (cf. fig. 3.5). The observed movement, with knowledge of the distance, corresponds to apparent velocities higher than the speed of light. The results can be explained as a geometric effect[3] and with two plasma clouds ejected anti-symmetrically at 98% of the speed of light [129]. Superluminal motion is a phenomenon observed since

[3]Relativity dictates that no particle can move faster than the speed of light. But apparent superluminal motion is possible if the source of radiation is moving towards the observer at velocity close to the speed of light along a path with a small angle θ to the line of sight. Then, the source almost "overtakes" the light that it emits. The result is that light emitted at two distinct points in the sky is detected in a much shorter time interval than it was emitted. A radiating cloud will look as if it moves faster than light across the sky [134].

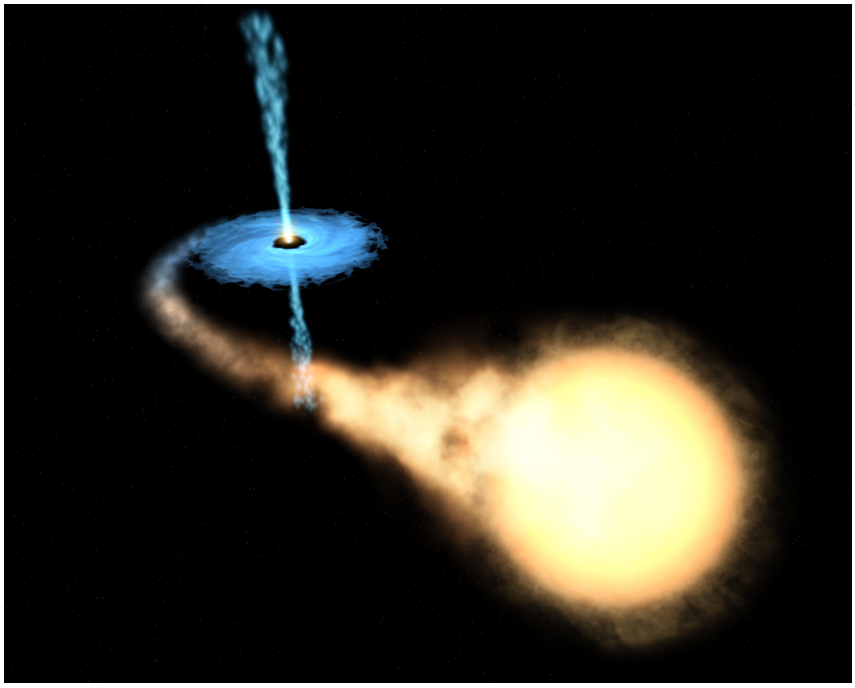

Figure 3.4 An artist's conception of the microquasar GRO J1655-40, taken from [130].

more than 30 years for quasars [134]. The observation of ultra-relativistic jets in XRBs strengthens the idea of physical analogy between microquasars and quasars.

Within the **microquasar analogy**, it is assumed that the basic physical processes behind accretion and jet ejection are the same in all systems [134]. The sizes and time scales of the system are proportional to the mass of the black hole, so that between an XRB with a black hole of stellar mass[4] and a supermassive black hole with a mass of several million solar masses or more, the differences can be 6 orders of magnitude or more [134]. See tab. 3.2 and fig. 3.6 for a comparison of properties of a typical microquasar and a typical quasar. Because of the much smaller time scales, microquasars may allow the study of processes which would take thousands of years in a quasar. They are very interesting for the study of the connection between accretion of matter and ejection of jets [134].

The gas in the accretion disk is probably magnetized [134]. This gives rise to current theories of disk-jet coupling that try to explain the formation of relativistic jets through magneto-hydrodynamic processes in which rotational energy of the compact object and/or the accretion disk is used for acceleration and released as a jet, while some matter falls towards the gravitational attraction center [129]. In GRS 1915+105, an abrupt fall of the X-ray luminosity can be observed at the beginning of the ejection of a relativistic jet that is first seen in infrared, then in radio wavelengths [134, 129]. The fall of X-ray luminosity could be interpreted as disappearance of the hot inner part of the accretion disk beyond the horizon of the black hole. As the accretion disk is reconstructed, energy is released from the accretion disk as a jet of relativistic plasma that expands and cools, becoming transparent to its own synchrotron radiation, first in infrared, then in radio frequency [129] (cf. fig. 3.7). A similar process has later been observed in a quasar, but on the time scale of years, instead of several minutes [129, 111].

[4] up to a few tens times that of the Sun

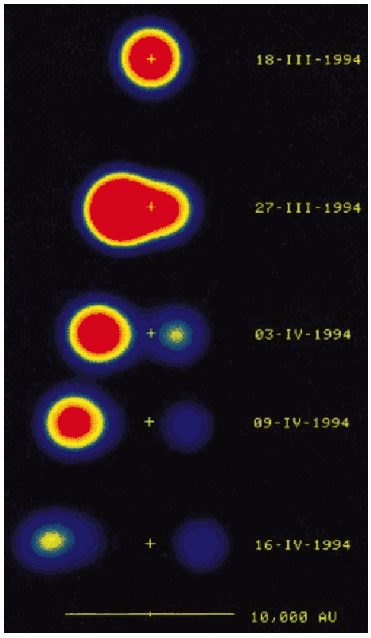

Figure 3.5 Time sequence of the observation of superluminal motion in GRS 1915+105 in 1994. From [133].

First considered to be something very exotic, there is more and more evidence that the presence of jets is characteristic for many, maybe even the majority of XRBs [110]. This would mean that microquasars are rather the rule than the exception. In [110], it is suggested that radio emission might correspond to evidence for jet production, whereas X-ray emission is taken as evidence for accretion processes.

3.3 The System of Cygnus X-3

3.3.1 A history of detection

Cygnus X-3 was among the first X-ray sources discovered [123], namely during a rocket flight in 1966 [106, 135]. In 1972, a giant radio outburst (flare) was seen from Cyg X-3 that drew much attention, since it turned Cyg X-3 into the brightest radio source in the sky [106]. Within the next 15 years afterwards, Cyg X-3 continued to cause excitement in the astrophysics community, as numerous experiments in space, on ground and below ground detected excesses at high energies that were attributed to Cyg X-3 [106]:

- In the MeV range: Data from a balloon flight in 1975 indicated $\approx 3.5\sigma$ directional excess of photons at the Cyg X-3 position and the satellite SAS-2 saw a directional excess too, as well as a time modulation approximately matching the orbital period of Cyg X-3 [106].

- More than 10 γ-ray detections of Cyg X-3 have been reported in the 1970s and 80s by atmospheric Cherenkov experiments (sensitive in the TeV range), e.g. by the Crimean group (USSR), the Dugway experiment, the Fly's Eye experiment and others [106]. Most of them have not seen a time-integrated spatial excess at Cyg X-3 and rely on excesses at the $(2.5 - 4)\sigma$ level in the phase of recorded events

	Quasar	Microquasar
Mass of CO	$\geq 10^6\ M_\odot$	$1 \ldots 20\ M_\odot$
Accretion disk size	10^9 km	10^3 km
Jet size	10^6 ly	1 ly
Accretion disk temp.	10^3 K	10^6 K
Time scales	$100 - 10000$ yr	h or d

Table 3.2 Dimensions of some properties of quasars and microquasars in comparison [134].

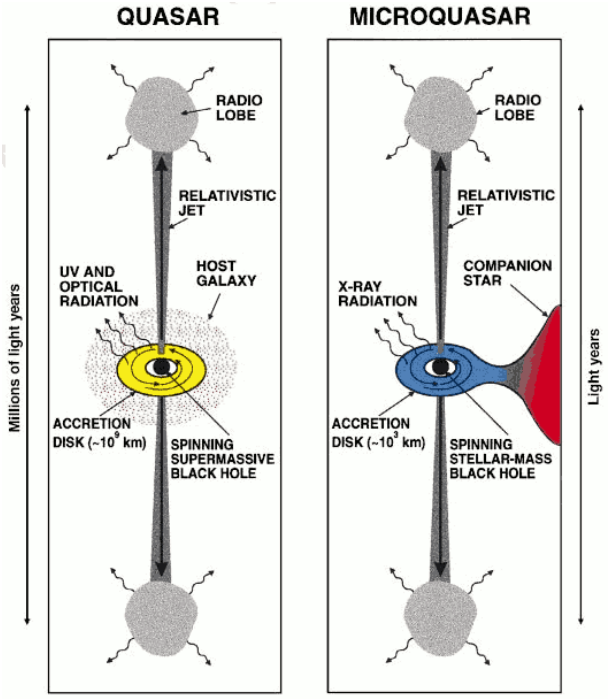

Figure 3.6 Illustration of the unified picture of quasars and microquasars, from [134].

w.r.t. Cyg X-3's orbital period, which was criticized. Moreover, the background in these γ-ray experiment samples was still very large (see section 1.2) and maybe even included some unknown components [106].

- Extensive air shower experiments (sensitive in the PeV range) saw similar excesses in the phase distribution of the events, e.g. the Kiel group and the Haverah Park experiment, and criticism was raised as well [106]. E.g. the event selection was inconsistent and it is unclear if photon-induced showers were selected.

- In 1985, several underground muon detectors (Soudan-1, NUSEX, IMB, and others) reported muon events in direction of Cyg X-3 modulated with its orbital period of 4.79 hours. However, a muon signal observed at the reported levels would imply non-Standard Model particle physics, e.g. the existence of a new neutral particle producing those muons [106]. Other detectors operated at the same time didn't observe an excess.

The observation of high-energy photons from Cyg X-3 in the MeV, TeV and PeV range was so encouraging to some that they considered the puzzle of cosmic ray acceleration in our Galaxy as almost solved and it was assumed that Cygnus X-3 "may be one of the major (or possibly the only) source(s) of cosmic rays active in our Galaxy at the present time" ([136]). Cyg X-3 motivated considerably the development of high-energy gamma-ray astronomy [109]. However, all the claimed detections at high to ultra-high energies were not confirmed by later more sensitive experiments in the late 1980s and 1990s and were for themselves not statistically significant enough for an undisputable detection [109, 106]. Maybe, the detections were the result of unknown or uncontrolled background (systematic error) combined with improper statistical analysis. It is still today not completely clarified

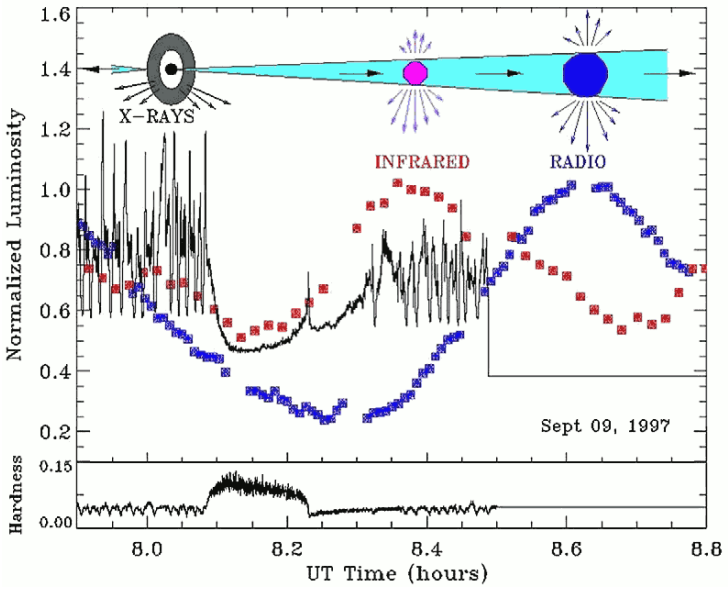

Figure 3.7 Temporal sequence of the formation of a jet in microquasar GRS 1915+105. The X-ray emission from the hot inner disk drops suddenly as matter disappears beyond the event horizon. Then, a relativistic jet expands and becomes transparent first to infrared, then to radio photons. From [111].

if Cyg X-3 was in an unusually active state at the time of the less sensitive experiments or (like most experts believe) if everything was a statistical fluke [6]. However, in 2009, γ-ray emission from Cyg X-3 up to the GeV range was definitely established by the Fermi and AGILE satellite experiments, see section 3.3.4.

3.3.2 General Properties of Cygnus X-3

Cyg X-3 is in many ways an unusual XRB system. After the discovery of Cyg X-3 in 1966, it took almost 30 years to unveil the nature of the stellar companion [107]: Infrared observations indicate that it is a star of the **Wolf-Rayet** (WR) class [137, 138]: a massive OB star in a later evolutionary stage with helium burning and a strong and dense stellar wind. The WR donor star might be the cause for many of Cyg X-3's unique attributes [123]. In [138], the stellar wind velocity is estimated to be $\sim$1500 km s^{-1} and the mass-loss rate of the WR star $\gtrsim 10^{-5}\ M_\odot\ \mathrm{yr}^{-1}$ leading to a density of up to 10^{13} cm^{-3} at the CO location, which is orders of magnitude more than in all other systems [109]. The wind is also one of the reasons why it is so difficult to understand this system, as it is likely to be enshrouded in the dense wind environment that causes absorption and scattering [123, 139]. Additionally, Cyg X-3 is heavily obscured in optical wavelengths by the interstellar medium (ISM) in the line-of-sight which prevents optical spectroscopy and further complicates its study [106, 137]. Because of these difficult observational conditions, it was not possible to determine the dynamical parameters if the binary and it is still not evident if the **compact object** is a NS or a BH [123]. Recent publications show increased evidence for a BH, but it is not unambiguous yet [123, 140].

The system shows a periodic modulation of X-ray and infrared emission with period $P = 4.79$ h (~ 0.2 d) that is usually interpreted as the **orbital period** [121, 106]. This is a rather short orbital period, typical for LMXBs, but the Wolf-Rayet donor star

should be massive with a mass of perhaps 30 $M_\odot$ [123] demonstrating that it is a HMXB. Following Kepler's third law ($a^3 \propto P^2(M_1 + M_2)$) [78], the orbit is much tighter than in other HMXB systems. The **distance** to Cyg X-3 is uncertain. It depends heavily on the method used for its estimation and varies between 3.4 and 13 kpc [141, 121]. Most authors in literature cite either a distance of 7 kpc (e.g. [141], [109]) or 9 kpc (e.g. [123], [121], [140]). Cyg X-3 is located in the Galactic plane, probably at the edge of the Galaxy [106]. For observers on Earth, it appears in the complex Cygnus region that hosts star forming regions and thus many bright sources [108, 109]. Its **position** in the sky is at right ascension 308.107° ($20^\mathrm{h}32^\mathrm{m}25\overset{\mathrm{s}}{.}78$) and declination +40.958° ($+40°57'27\overset{''}{.}9$) in equatorial coordinates or Galactic longitude $l = 79.8455$ and Galactic latitude $b = +0.7001$ in Galactic coordinates (both for epoch J2000). These coordinates were retrieved from the HEASARC [142] and SIMBAD [143] databases and originate from the 2MASS catalogue of point sources observed in infrared wavelengths [144].

Cyg X-3 is a **persistent** X-ray and radio source [140], one of the brightest X-ray sources in the Galaxy (with a flux of $10^{37} - 10^{38}\,\mathrm{erg\,s^{-1}}$ [145]) and the brightest radio source among X-ray binaries [140, 145], with a quiescent flux density up to 100 mJy[5] and a flaring flux density up to 20 Jy [121]. The radio flux can change rapidly (within few days or hours) by more than three orders of magnitude [140] and the total energy output of Cyg X-3 can reach $\approx 10^5$ times the emitted power of our Sun [106]. Cyg X-3 produces collimated **relativistic jets** in connection with the radio flares that qualify it as a microquasar [141, 109]. Radio observations in the 1980s and 90s with the Very Large Array, MERLIN and Very Long Baseline Interferometry during or shortly after a large radio flare suggested two-sided ejection of radio-emitting plasma. The apparent transverse speed was estimated to be $0.3c$ for a distance of 10 kpc [145]. High-resolution images taken with the Very Long Baseline Array (VLBA) in 1997 following a few days after a large radio flare above 10 Jy show a curved[6] one-sided jet [145]. The jet speed is estimated to be $\gtrsim 0.81c$ [145] and it is speculated that the jet might be pointed almost directly towards us with an inclination angle $\lesssim 14°$ to the line-of-sight [145]. Another observation with VLBA in 2001, indicating a curved two-sided jet consisting of of discrete knots, is shown in fig. 3.8.

3.3.3 Phenomenology of spectral states

This section introduces the spectral behaviour of the Cyg X-3 and is very important for the analyses described later in this work (see chapter 4). After discussion of a few details, the hardness-intensity diagram and the jet line are introduced that are essential for the analysis in section 4.2.

The X-ray spectral states of Cyg X-3 show similarity to the canonical spectral states of BH binaries, e.g. there are two main states, hard and soft. But there are some significant differences and their physical interpretation remains rather uncertain [140]. Because of strong X-ray absorption (most likely due to the Wolf-Rayet wind), it is difficult to determine the instrinsic spectral shapes and luminosities [140, 141]. For Cyg X-3 being a very strong radio source, there also exists a state classification based on radio observations (see e.g. [147]). However, the behaviour in radio and X-rays is highly correlated and this led to a more unified picture. In Szostek et al. (2008) [140], both the X-ray states and the

[5] Jansky (Jy) is a unit for flux density used in radio astronomy. $1\,\mathrm{Jy} = 10^{-23}\,\mathrm{erg\,cm^{-2}\,s^{-1}\,Hz^{-1}} = 10^{-26}\,\mathrm{W\,m^{-2}\,Hz^{-1}}$ [106, 78].

[6] The curvature is interpreted as precession of the jet.

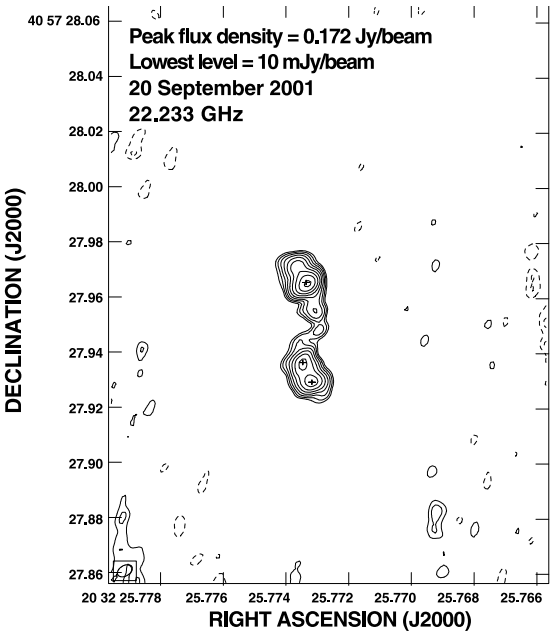

Figure 3.8 Image taken with the VLBA on 2001 September 20 at 22 GHz, a few days after the beginning of a major radio flare on September 14. The jet is visible as series of discrete knots (whose positions were fitted and are shown as crosses). It is more likely two-sided and lies almost in the north-south direction. The best fit jet speed is $\beta \sim 0.63$. From [146].

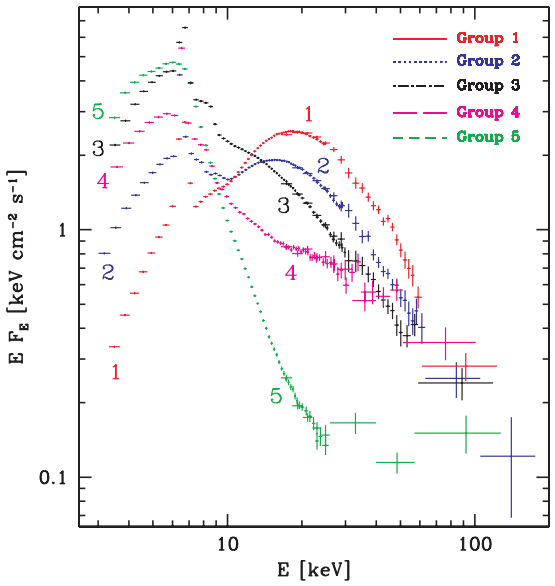

Figure 3.9 X-ray spectral classes of Cyg X-3, derived from 42 X-ray spectra recorded with the RXTE/PCA (3-25 keV) and RXTE/HEXTE (15-110 keV) instruments. Shown are the averaged spectra of five spectral groups that are defined by decreasing X-ray flux at 20 keV. From [140].

radio states of Cyg X-3 are revisited and the connections between them are studied. The following presentation is based on the work of Szostek et al.

The averaged **X-ray spectra** of Cyg X-3 are presented in fig. 3.9. They are classified into 5 groups that are characterized by the spectral hardness: Group 1 has the hardest spectrum (low soft X-ray flux, high hard X-ray flux) and group 5 has the softest spectrum (high soft X-ray flux, low hard X-ray flux), the other groups lie in between. Groups $1-2$ are classified as *hard* state, groups $3-4$ as *intermediate/soft* state and group 5 as *ultrasoft* state. Thus, we see roughly the canonical low/hard state (group $1-2$) with weak thermal and strong non-thermal power-law emission peaking at hard X-rays, the high/soft state (group $4-5$) dominated by thermal disk emission in soft X-rays (but with a hard tail), and an intermediate state as transition.[7]

The four **radio states** defined by Waltman et al. [147] (*quiescent*, *minor-flaring*, *quenched*, *major-flaring*) are revisited and complemented with two new state classifications in Szostek et al. (2008) [140]. The new classification also considers soft X-ray behaviour and is based on the 8.3 GHz radio light curve from GBI (Green Bank Interferometer) and the 3-5 keV soft X-ray light curve from RXTE/ASM (All Sky Monitor on board Rossi X-ray Timing Explorer), covering a period of 1414 days. The states are

[7]Note that due to absorption, the bolometric X-ray flux in the soft state is lower by a factor of $\sim 3-4$, whereas in the hard state, absorption only reduces the bolometric flux only by factor ~ 1.3. Considering this when looking at fig. 3.9, the intrinsic bolometric X-ray flux is really significantly "higher" in the high/soft state.

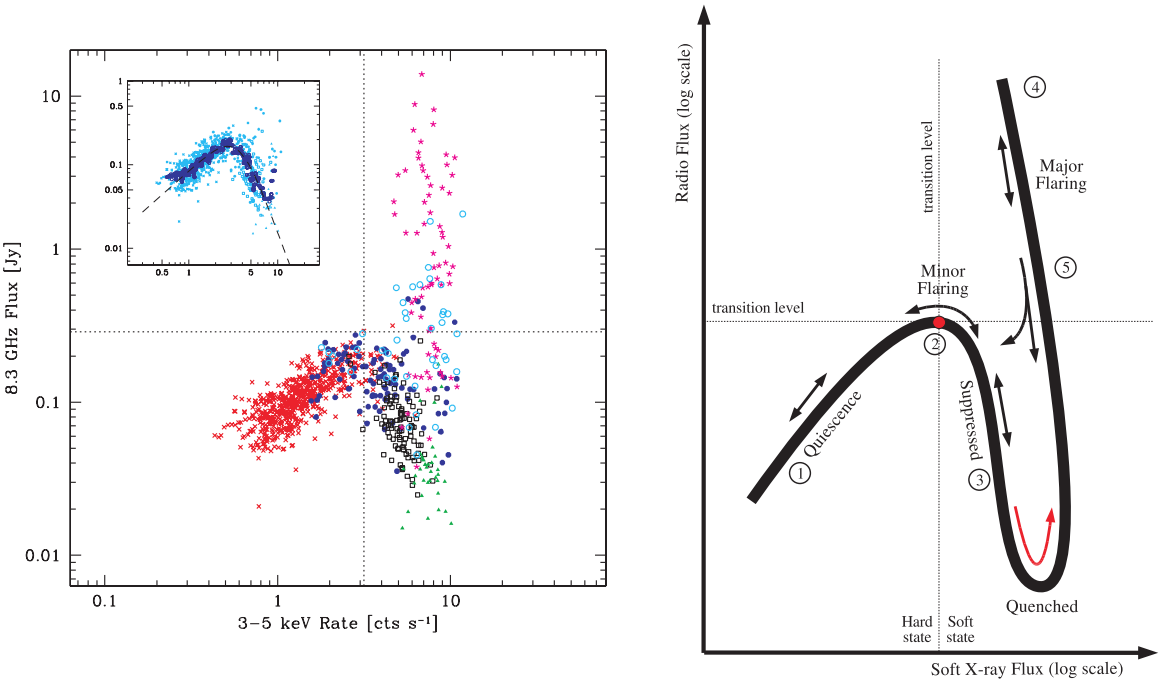

Figure 3.10 Flux-flux diagram of the radio vs. soft X-ray flux in Cyg X-3. *Left:* A plot made from data (GBI and RXTE/ASM). The symbols indicate the type of radio state (red cross: quiescent, blue filled circle: minor-flaring, black open square: suppressed, green triangle: quenched, magenta star: major-flaring, cyan open circle: post-flare). *Right:* A schematic version. The different radio/X-ray states and the transitions between them are visible. Radio states are labeled with their name, the encircled numbers stand for the X-ray spectral group (ranging from group 1, hardest, to group 5, softest state). The transition flux levels are indicated as dotted lines. Arrows indicate possible transitions and the red arrow in the quenched state emphasizes that evolution only in one direction is observed, forming a hysteresis. From [140].

defined as follows:

1. *Quiescent*[8] state: Radio and soft X-ray are correlated and below a certain level, the "transition level", which is $\simeq 0.3$ Jy for radio and a count rate of $\simeq 3$ s^{-1} for ASM soft X-ray. Radio flux is $\sim 50 - 200$ mJy.

2. *Minor-flare* state: Soft X-ray flux is at its transition level, radio flux varies from low flux up to its transition level ($\lesssim 0.3$ Jy).

3. *Suppressed* state: Radio flux is below its transition level, soft X-ray flux is above it and anti-correlated with radio. No radio flare follows.

4. *Quenched* state: Radio flux is at its minimum ($\lesssim 30$ mJy), soft X-ray flux is at its maximum (anti-correlation with radio). A major radio flare (> 1 Jy) follows.

5. *Major-flare* state: Soft X-ray flux is above transition level and almost constant, radio flux moves up and down by a large factor ($1 - 20$ Jy).

6. *Post-flare* state: Return after major flare to either minor-flaring or suppressed state, but *not* to the quenched state.

[8] Note: This definition of quiescent does not refer to the quiescent state defined as X-ray state in LMXBs, that are much fainter than the quiescent state of Cyg X-3 [140].

The X-ray/radio states and transitions between them are neatly visualized in a radio vs. soft X-ray **flux-flux diagram**, that also reveals the correlations and anti-correlations. The "saxophone" shaped flux-flux diagram is shown in fig. 3.10. The transition level marks the transition from hard (quiescent) state to the other soft states (suppressed, quenched, major-flare, post-flare). At the transition level itself lies the minor-flare state. Above the soft X-ray transition level, the positive correlation between radio and soft X-ray turns into a negative one (an anti-correlation). Important to note here is that the movement in the flux-flux diagram follows a certain track, which can be travelled mostly in both directions. Only after the quenched state (the dip in the flux-flux diagram), there seems to always follow a major flaring state and after the major flaring state, the quenched state is avoided, so that a **hysteresis** is visible. Also note that the radio flux usually stays below a certain level, but during strong flares, it moves rapidly up and down and rises above **1 Jy**, which is used to classify a "major" radio flare.

The hard X-ray flux and the soft X-ray flux are anti-correlated in all states, so that a flux-flux diagram with radio flux vs. hard X-ray flux (in [140] the hard X-ray is represented by the 20-100 keV flux measured with BATSE) looks just like the "saxophone" in fig. 3.10, but mirrored vertically. In particular, during the quenched state and the major flaring state, the radio and hard X-ray flux are correlated, whereas during the quiescent state, they are anti-correlated. The fact that during a major flare, the soft X-ray flux is almost constant, while the hard X-ray flux is correlated with radio speaks for a stable accretion disk (delivering the soft X-ray blackbody radiation) and variable active regions above the disk (delivering the high-energy tail of hard X-rays), so a jet [140].

Cyg X-3 can also be studied in the **hardness-intensity diagram (HID)**, a tool usually applied to transient BH binaries. The concept of the HID was already introduced in section 3.1. Cyg X-3's HID was intensively studied in Koljonen et al. (2010) [121], which is used as reference for the following presentation. Koljonen et al. linked radio observations to the HID and recognized six distinct states dependent on the position in the HID and the simultaneous radio flux. An HID of Cyg X-3 is presented in fig. 3.11. It was constructed from RXTE/PCA data with the hardness defined as the count ratio of the 10-15 keV range and the 3-6 keV range. The HID appears similar to a classical BH binary HID because it also has the typical Q-shape (see e.g. fig. 3.3). But the main differences are: The LH state is not a vertical branch on the right side, but is confined to the bottom of the diagram, together with the quiescent state (the vertical branch on the right is from a flaring state and is more of the intermediate type than of the LH type). The center of the Q is filled as well, with data points from flaring periods. The source doesn't move in circles on the edge of the Q, but also crosses the body of the Q without displaying a hysteresis like in classical HIDs. For each value of hardness, there is a considerable scatter in intensity and this scatter is much wider in the HS/flaring states on the left than it is in the LH/quiescent states on the right. Part of the intensity scatter is due to the strong orbital modulation, X-ray flaring also increases intensity variability.

When the (nearly) simultaneous radio flux is taken into account as well, three main regions appear in the HID: the *quiescent*, *flaring* and *hypersoft* region, with a medium, high and very low radio flux level, respectively. Depending on the hardness and the X-ray spectra, these can be further subdivided to form six states, as labeled in fig. 3.11. These are: Quiescent, Transition, Flaring/Hard X-ray (FHXR), Flaring/Intermediate (FIM), Flaring/Soft X-ray (FSXR) and Hypersoft. They correspond vaguely to the radio/X-ray states described above: The quiescent state from S08 (Szostek et al. 2008) lies in the

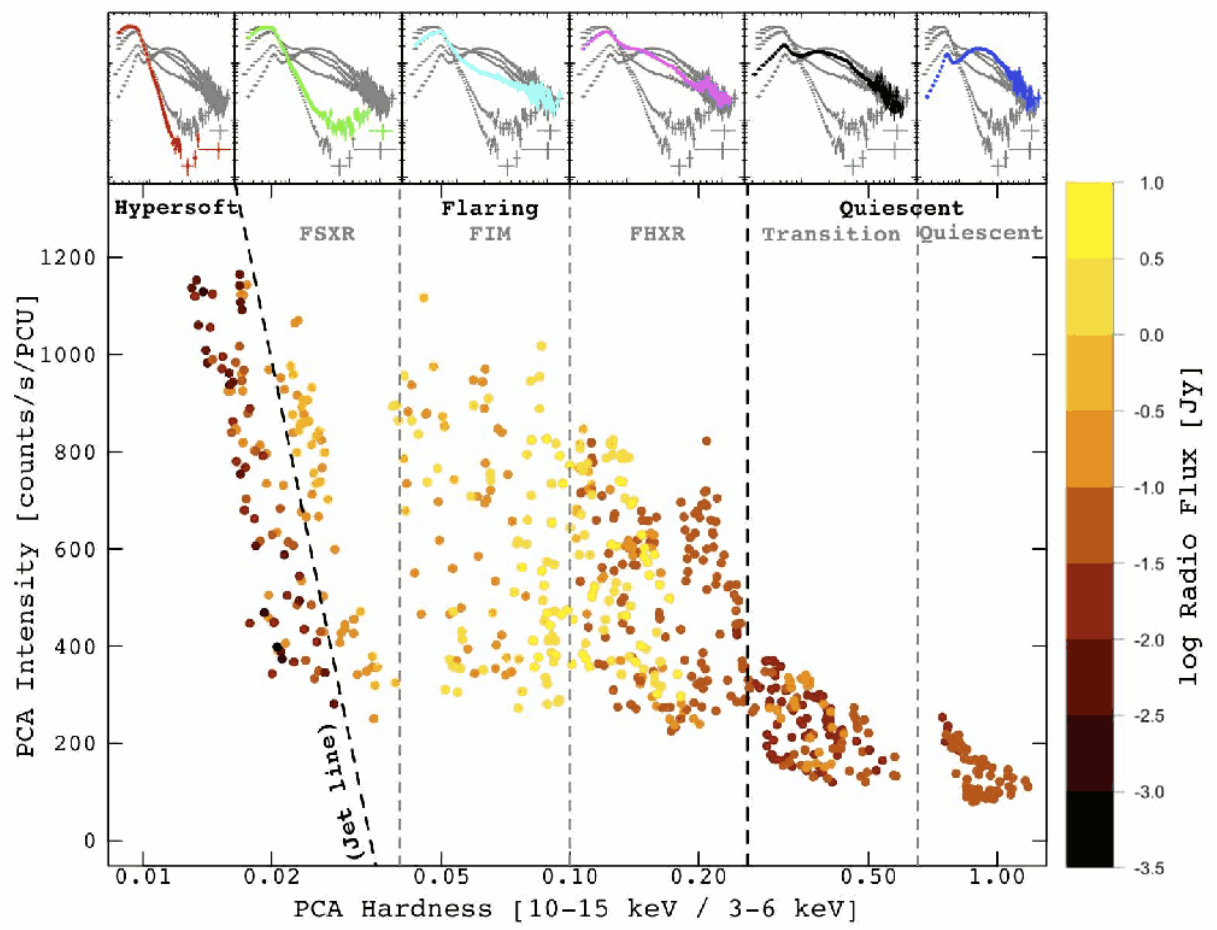

Figure 3.11 Hardness-intensity diagram (HID) for Cyg X-3 using 135 pointed RXTE/PCA observations (X-ray). The quasi-simultaneous radio flux from GBI, RATAN-600 and Ryle telescopes is visible as colour of the data points. This shows clearly the different X-ray/radio states in the HID. Six distinct states are separated by dashed lines and the characterising X-ray spectrum (between 3 and 100 keV) is printed on the top of each division. These averaged spectra (from right to left) correspond to spectral groups 1, 2, 3, 4, 5 and 5 as defined in Szostek et al. (2008) [140]. From [121].

Quiescent and Transition state from K10 (Koljonen et al. 2010), the minor-flare state in S08 spreads over the Transition and FHXR state from K10, the suppressed and post-flare state lie in the FHXR as well, the major-flare state of S08 is spread across the FHXR, FIM and FSXR states (the whole flaring region) and the quenched state from S08 lies in the Hypersoft state of K10. The six states of K10 also correspond to the X-ray spectral groups from S08, except that the ultrasoft (group 5) is split into two groups: FSXR and hypersoft (see also the caption of fig. 3.11).

A very interesting feature in the HID is the line separating the FSXR and the Hypersoft state regions: This line is the so-called **jet line** (cf. fig. 3.3) and unlike other transient black hole XRBs, Cyg X-3 crosses the jet line from right to left (from FSXR to Hypersoft) without producing a major radio flare. **Only when it crosses from left to right (when hardness increases after the hypersoft state), a major flare occurs** [121]. This is a remarkable behaviour and it will be exploited later in this work to identify when major radio flares are occurring (see chapter 4). Moreover, in [121], it is emphasized that production of high-energy particles in the GeV/TeV range might occur during the hypersoft state that is linked to the quenched radio state. This is indicated by a high-

energy tail in the hard X-ray spectrum and by observation of GeV γ-rays by AGILE [108] and Fermi [109] (see section 3.3.4) before the onset of a major radio flare, when Cyg X-3 was in a state similar to the hypersoft state [121].

For a search of high-energy emission of photons and in particular neutrinos correlated with radio flares, information about the timing of the quenched state relative to the radio flare is interesting. Even though each radio flare is different and maybe in a sense unique [121], most observations indicate that Cyg X-3 enters the quenched state about $10 - 20$ days before the onset of a major radio flare. E.g. Trushkin et al. have reported observations of a $10 - 12$ [148] and 18 days [149, 150] separation of the beginning of the quenched state and the flare. However, the quenched state can last shorter or longer, even 50 days or more (e.g. compare to fig. 3 in [140]). It is also unknown when during the quenched state high energy particles can be produced, perhaps only during the last few days, which is supported by the γ-ray observations in the GeV domain (see section 3.3.4).

3.3.4 Gamma-ray observation of Cygnus X-3

In late 2009, two groups working with gamma-ray satellite telescopes published detection of a transient γ-ray source above 100 MeV consistent with being the Cyg X-3 position. These observations were made independently from each other and with high enough significance that we now finally have, after the long history of doubtful detections (see section 3.3.1), incontrovertible evidence for the γ-ray emission of Cyg X-3 [107]. One of the reasons why it took so long to unveil this is that γ-ray emission occurs only during special episodes, namely (as it appears) during the quenched radio state, when hard X-ray flux is strongly suppressed [107] (see also section 3.3.3). Other reasons are the complexity of the Cygnus region that hosts the Cyg X-3 and the strong absorption [108, 109]. Important results are that the γ-ray spectrum appears to be steep, maybe indicating absorption, and that the γ-ray emission is followed by a radio flare a few days later [107].

The two gamma-ray telescopes that did the job are AGILE and Fermi and their observations ([108], [109]) are presented in the following.

The **AGILE satellite** was launched into space in 2007 by ASI (Italian Space Agency) [107]. It can monitor sources in 100 MeV $-$ 10 GeV γ-ray band, has a large field of view (2.5 sr) and a good angular resolution that allows to resolve the field around Cyg X-3, hosting star formation sites, OB associations and several prominent X-ray sources, as well as a dominant gamma-ray pulsar at 0.4° from Cyg X-3 [108]. AGILE has observed Cyg X-3 at γ-ray energies between mid-2007 and mid-2009. By integrating all AGILE data (taking into account diffuse γ-ray flux), a weak gamma-ray source consistent with the Cyg X-3 position is found at 4.6σ level with a flux of $(10 \pm 2) \cdot 10^{-8}$ photons cm^{-2} s^{-1} above 100 MeV [108]. Additionally, transient γ-ray emission from a flaring source also consistent with the Cyg X-3 position is detected in four distinct episodes. The significance of all flaring data together is at the 5.5σ level with an average flaring flux of $(190 \pm 40) \cdot 10^{-8}$ photons cm^{-2} s^{-1} above 100 MeV. The average spectrum between 100 MeV and 3 GeV is described by a power law with spectral index 1.8 ± 0.2 [108]. All four γ-ray flares occur during distinct minima of the hard X-ray flux ($15-50$ keV), 3 of 4 γ-ray flares are followed by a major radio flare and 2 of 4 are associated with a radio quenched state (one of those is the one not followed by a major radio flare) [108]. This gives evidence that the emergence of high-energy particles occurs at or near the quenched/hypersoft state (cf. section 3.3.3)

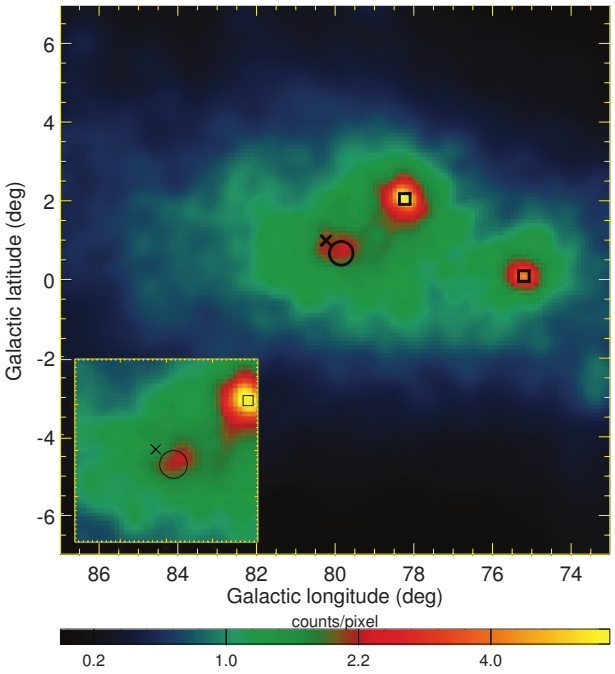

Figure 3.12 Fermi/LAT map (200 MeV−100 GeV) of a 14° × 14° region centered on Cyg X-3 during a γ-ray active period (without background subtraction). The Cyg X-3 source is shown by the circle. There are two bright gamma-ray pulsars (boxes) and the nearby PSR J2032+4127 (cross). The strong Galactic diffuse emission of the Cygnus region is visible as overall "glow". The inset shows the 4° × 4° center of the image, but using only data from off-pulse intervals of PSR J2032+4127. From [109].

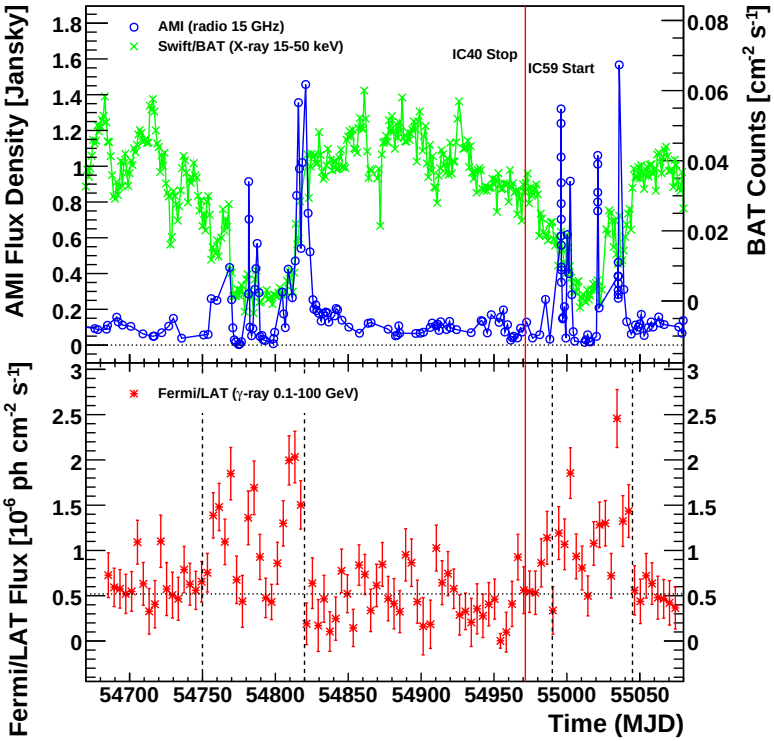

Figure 3.13 Light curves of Cyg X-3 from August 2008 until September 2009. At the top are the 15 GHz radio light curve from the AMI radio telescope (blue circles) and the 15 − 50 keV hard X-ray light curve from the BAT instrument on Swift (green crosses). Below is the Fermi/LAT 100 MeV − 100 GeV light curve. The two active periods are marked with vertical dashed lines; dotted horizontal lines indicate the 0 Jy level (top) and the average γ-ray flux in non-active periods (bottom). BAT data from [151], AMI data from Guy Pooley (private communication), LAT data from Stéphane Corbel (private communication) and published in [109].

in which the source spends only few percent of its time [108]. The AGILE detection of Cyg X-3 is the first direct evidence for time-variable extreme particle acceleration and non-thermal emission from a microquasar [108]. It is unknown, whether the emission is of leptonic or hadronic origin.

NASA's **Fermi Gamma-ray Space Telescope** (formerly known as GLAST [152]) was launched into space in 2008 [107]. Its Large Area Telescope (LAT) works in the range 100 MeV − 100 GeV [109] and is more sensitive than AGILE [107]. In [109], the Fermi LAT collaboration reports results from observavtions of Cyg X-3 between 4 August 2008 and 2 September 2009. A variable high-energy γ-ray source is detected that is identified with Cyg X-3 [109]. The gamma-ray pulsar PSR J2032+4127 is located very close to Cyg X-3 ($\sim$30 arcmin according to the Fermi LAT positioning) and constitutes a large background to the Cyg X-3 observation, but was removed in the analysis by selecting only LAT data during off-pulse phase intervals of PSR J2032+4127 (this preserves $\sim$80% of LAT live time). A γ-ray source consistent with the location of Cyg X-3[9] is found with a

[9]The source position is fitted to be (epoch J2000) right ascension = 308.5° and declination = 40.96°

significance of more than **29 standard deviations** ($> 29\sigma$). Fig. 3.12 shows a map of the region around Cyg X-3, as observed with the Fermi/LAT.

The variability of the source in γ-rays is visible from its LAT light curve shown in fig. 3.13. In order to investigate the data and Cyg X-3's behaviour, this plot was created by the author, comparing the Fermi/LAT light curve with the observations in radio and soft X-rays. There are two active periods from modified Julian date[10] (MJD) 54750 to 54820 (11 Oct to 20 Dec 2008) and from MJD 54990 to 55045 (8 Jun to 2 Aug 2009). The spectrum in the two active periods is fitted with a power law of spectral index $2.70 \pm 0.05(\text{stat}) \pm 0.20(\text{syst})$, where the systematic error comes from the uncertainty on the diffuse emission. The average photon flux in the active periods is $1.19 \pm 0.06(\text{stat}) \pm 0.37(\text{syst}) \cdot 10^{-6}$ photons cm^{-2} s^{-1} above 100 MeV, corresponding to an isotropic γ-ray luminosity of $L_\gamma \approx 3 \cdot 10^{36}$ erg s^{-1}. This luminosity was also found by AGILE [108] and is similar to what was originally reported by the SAS-2 satellite in the early 1970s [109].

To secure the detection even more, the Fermi LAT analyzers searched for the 4.8-hour orbital modulation in the data from the Cyg X-3 position. No modulation is apparent when using the whole data set, but in the data from the two active periods only, two peaks stand out in the power spectrum, that correspond to the orbital period of Cyg X-3 and its second harmonic. The probability of finding a modulation that strong at the known period of Cyg X-3 by chance is calculated to be $\sim 2.4 \cdot 10^{-9}$ [109]. Moreover, the γ-ray flux is correlated with the radio flux monitored by the AMI and OVRO radio telescopes with a significance of more than $\sim 3\sigma$. The γ-ray flares seem to occur a few days before the radio flares (consistent with the picture from the previous sections), but the lag between γ-rays and radio is not well constrained and is calculated as 5 ± 7 days.

The orbital modulation of the radiation implies that the production occurs within the binary system. However, if the γ-rays were produced too close to the accretion disk, they would be asorbed by pair production on the soft X-ray photons. A leptonic origin of the γ-radiation is discussed in [109]: The modulated flux might be due to anisotropic inverse Compton-scattering. However, the densities of up to 10^{13} cm^{-3}—unique among microquasars—could provide a target for substantial hadronic interactions with nuclei of the stellar wind, given accelerated protons or nuclei are present. This would also cause neutrinos to be produced so that a neutrino detection from Cyg X-3 would confirm the presence of relativistic hadrons and allow the study of Cyg X-3's possible contribution to cosmic ray particles [109, 107].

Interestingly, Cyg X-3 has not been detected by TeV gamma-ray telescopes yet, even though it shows emission features in the GeV γ-rays similar to other XRBs which were also observed in the TeV range (e.g. LSI +61 303) [153]. There exist **upper limits on the TeV flux** from Cyg X-3: The MAGIC collaboration reports observations of Cyg X-3 for about 70 hours between March 2006 and August 2009 during different radio/X-ray states and also during enhanced γ-ray emission detected by Fermi and AGILE, but found no evidence for a very high energy (VHE) signal [141]. An upper limit to the integral flux for energies above 250 GeV was set to $2.2 \cdot 10^{-12}$ photons cm^{-2} s^{-1} at 95% confidence level, which is the best limit so far for VHE emission from Cyg X-3. The MAGIC upper limits are still consistent with an extrapolation of the Fermi spectrum (photon index 2.7), but would be far below an extrapolation of the AGILE spectrum (photon index 1.8) [141]. The non-detection indicates that the location of the VHE photon emitter could be at

with uncertainty of 0.04° at 95% confidence level.

[10] See footnote 9 in chapter 4.

the innermost part of the jet where **absorption is strong** [141]. However, MAGIC's observations were mainly carried out a few days before or after a major radio flare, which might be the wrong time for TeV emission. In [141], it is concluded that future generations of Cherenkov telescopes might be able to detect a signal from Cyg X-3 if the observation takes place at the time of peak emission during a jet ejection. Bednarek (2010) [153] has calculated the theoretical γ-ray flux above few 100 GeV to be a factor 10 below current sensitivities for an emitter inside the Cyg X-3 binary system, even though it can deliver a GeV flux consistent with the Fermi flux. Due to $e^{\pm}$ pair production on the radiation field of the WR star, escape of γ-rays above few tens of GeV is not very likely. So, absorption makes observation of VHE photons very difficult. In case of a hadronic scenario, the co-produced neutrinos would not have these restrictions.

3.4 Neutrinos from Cygnus X-3

In Bednarek (2005) [154], predictions on the neutrino flux from Cyg X-3 are made based on a model of accelerated nuclei that photo-disintegrate upon collision with thermal photons from the accretion disk and/or the Wolf-Rayet star. Released neutrons move toward the accretion disk and/or star and produce neutrinos and γ-rays in hadronic interactions with matter, e.g.

$$n + p \longrightarrow p + p + \pi^- \quad \text{or} \quad n + p \longrightarrow n + n + \pi^+ \quad \text{or} \quad n + p \longrightarrow n + p + \pi^0.$$

The γ-ray photons are absorbed inside the star or disk, but neutrino absorption is negligible. The model has various parameters and considers different emission regions that lead to different neutrino spectra and direction of the emission (cf. fig. 3.14). Detectable fluxes are predicted with event rates of $\sim 2 \ldots 16$ events per year per km^3 in a neutrino telescope like IceCube if the spectrum of accelerated nuclei is steeper than a spectral index of 2.5. If no signal is detected, then the results from the full IceCube detector would strongly constrain these models.

In previous point source searches with neutrino data from the IceCube and AMANDA detectors, no hint for a signal from Cyg X-3 was found. The most recent point source search dedicated to Cyg X-3 was using the final data from the AMANDA-II detector [94]. There, Cyg X-3 was included in a predefined list of 26 interesting Galactic and extra-galactic objects. For each object on the list, a time-independent unbinned maximum likelihood search was carried out (see the time-integrated part in section 4.2.3). The result for Cyg X-3 was a probability of 29% to observe the test statistic by chance, before correction for trials. An upper limit on the flux of $\nu_\mu + \nu_\tau$ neutrinos with E^{-2} spectrum from Cyg X-3 was set at $E^2 d\Phi/dE \leq 6.59 \cdot 10^{-11}$ TeV cm^{-2} s^{-1} with 90% confidence. The time-independent point source searches in 22 strings IceCube data [99] and 40 strings IceCube data [100] did not include Cyg X-3 in the predefined source list. However, a sky scan was performed, in which the unbinned maximum likelihood method was performed on a grid finer than the angular resolution. The 90% confidence level upper limit resulting from the IceCube 40-strings sky scan at the Cyg X-3 position lies at $E^2 d\Phi/dE \lesssim\leq 2 \cdot 10^{-11}$ TeV cm^{-2} s^{-1} for an E^{-2} flux of $\nu\mu + \bar{\nu}_\mu$ [100].

The aforementioned neutrino searches were all time-integrated and did not include time information of the events. On the IceCube 22-strings and 40-strings data, a time-

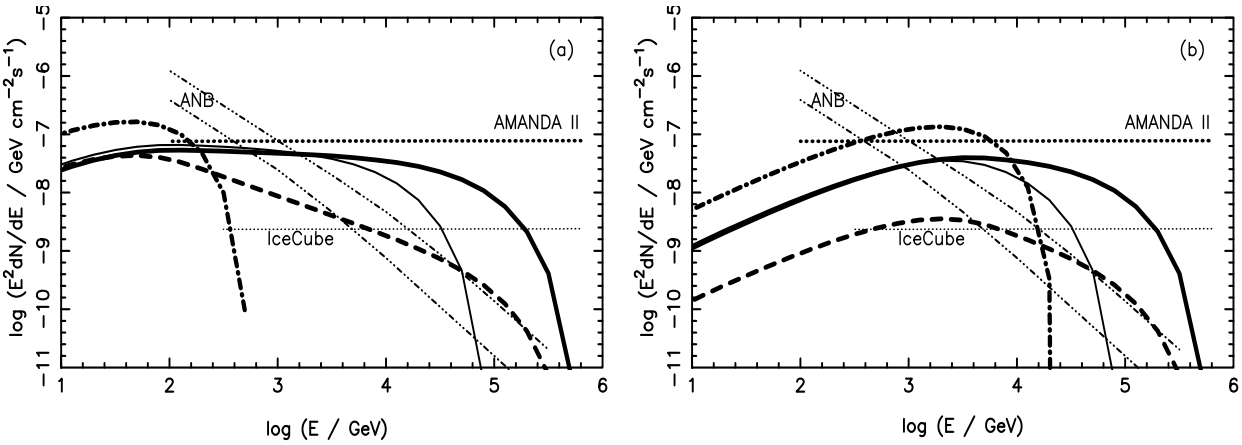

Figure 3.14 Model predictions for neutrino emission from Cyg X-3. Shown are the differential energy spectra of muon neutrinos, multiplied by E^2, as predicted in [154]. Calculations for interaction of neutrons with the accretion disk (*a*) and with the Wolf-Rayet star (*b*). The curves are for a nuclei power-law spectrum $\gamma^{-\kappa}$, with $\kappa = 2$ and cut-off at Lorentz factor $\gamma_{\max} = 10^6$ (*thin solid curves*) and 10^7 (*thick solid curves*) and for $\kappa = 2.5$ and $\gamma_{\max} = 10^7$ (*thick dashed curves*). *Thick dot-dashed curves* are for mono-energetic nuclei with Lorentz factor $2 \cdot 10^3$ in case of (*a*) and $2 \cdot 10^5$ in case of (*b*). The triple-dot–dashed curves indicate the atmospheric neutrino background within 1° of the source. The upper limit from first 3 yr of AMANDA-II operation [155] and the expected sensitivity (average upper limit) for 3 yr of full IceCube [156] are shown as horizontal dotted lines. From [154].

dependent analysis was performed as well on Cyg X-3, namely a search for an excess of events that arrived at a certain phase of the orbital period [157, 158, 159]. Thus, it not the event times were used, but the phase of the event times with respect to the orbital period of the binary system. Cyg X-3 was among a list of seven Galactic microquasars with well known orbital period. The results are interesting: The pre-trial chance probability (p-value) was 9% in case of IceCube 22 [158] and 0.186% in case of IceCube 40 [159]. The latter value was corrected for trials to a p-value of 1.8%. This is still compatible with background, but it is a faint hint for a signal. In the IceCube 40-strings search, Cyg X-3 was the most significant source and in the 22-strings search, it ranked second. These results contribute to the motivation of the search performed for this thesis. However, we are not biased by it, since the analysis developed here (see chapter 4) is not using the phase information of the events, but is searching for a neutrino excess during certain time periods.

3.5 Summary and Motivation for Neutrino Search

Cyg X-3 has a long history of claimed and later revised detections in high-energy astrophysics and because of this has become both famous and infamous (see section 3.3.1). The source has motivated the development of the field considerably and yet the early hints for high-energy emission remained unconfirmed for a long time. Only since late 2009, we know securely that Cyg X-3 *is indeed* a γ-ray emitter thanks to the detections by AGILE and Fermi (see section 3.3.4).

We have seen that Cyg X-3 is in many ways a very special XRB. It remains enigmatic even more than 40 years after its discovery (see sections 3.3.2, 3.3.3). Despite the strong absorption, Cyg X-3 is one of the strongest X-ray sources in our sky and among the

strongest radio sources during its giant outbursts. Cyg X-3's jets are the strongest ones of all microquasars and provide a very good site for particle acceleration. In order to establish Cyg X-3 as a source of cosmic rays, evidence for hadronic processes is needed. A detection of neutrinos from Cyg X-3 would provide such an evidence [109].

The detection of GeV photons from Cyg X-3 and the hints of γ-ray absorption (see section 3.3.4) make it an even more interesting candidate for a search of neutrino emission. Neutrinos might be copiously produced together with γ-rays and escape from the production site, while γ-rays are absorbed. This is why analyses of data from the neutrino detectors AMANDA and IceCube were performed in this work to search for a neutrino signal from Cyg X-3. The highly time-variable behaviour, detected in radio and X-rays as well as in the recent γ-ray observations, implies that the production of high energy particles happens only during special intervals that probably precede a major radio flare. For this reason, a time-dependent search was carried out, using multi-wavelength data in order to search for neutrino events that are correlated in time with the major radio flares of Cyg X-3. However, a time lag between neutrinos and radio flares is allowed and is searched for. This results in better chances of detection compared to time-integrated searches that were already performed (see above and section 4.2.5) and has the advantage that it tests physics assumptions without being too model-specific.

CHAPTER IV

Data Analyses

After the general physics introduction in chapter 1 and the presentation of the detectors belonging to the IceCube Neutrino Observatory in chapter 2, the astrophysical object known as Cygnus X-3 was discussed in chapter 3, together with motivation for a search for neutrino emission from Cyg X-3. We established a time-dependent neutrino point source search with IceCube and AMANDA data, based on physical assumptions and adjusted to the specific phenomenology of Cyg X-3. In contrast to time-integrated neutrino searches already performed [94], the analysis can take advantage of the multi-wavelength information about active phases of Cyg X-3, which enhances sensitivity.

From the phenomenology of the source, such as the observation of relativistic jet ejection connected with major radio flares, it appears reasonable to search for high energy neutrinos in time correlation with the major flares (see chapter 3). This chapter is going to present the performed data analyses on Cyg X-3, searching for neutrino events correlated in space and time with Cyg X-3 flares.

Many unsolved questions remain about the γ-ray emitting binary system. A neutrino detection would provide valuable new information and increase physical understanding of the system, e.g. accretion and jet physics and the connection to particle acceleration. It would also reveal Cyg X-3 as a source of Galactic cosmic rays.

Particle physics experiments with low statistics, such as a neutrino detector expected to detect only a handful signal events from a point source, are employing "blind" data analysis techniques. This means that the data sample is not looked at until the analysis plans and the hypothesis that is to be tested are finalized.[1] This is done in order to avoid that the analyzer is affected by the data in his or her assumptions and analysis optimizations.[2] Before the main analysis was performed on blind data, simpler studies on already unblinded data were carried out. This was meant to provide a hypothesis that the blind analysis can test. Therefore, this chapter is split in two parts: A non-blind study of AMANDA-II data taken between 2000 and 2006 and an analysis on blind data taken with IceCube in the 40-strings stage (2008 – 2009 data taking season) combined with AMANDA.

[1] E.g. for IceCube data, this means that the arrival times and directions of individual events are not allowed to be looked at. The sample is kept "blind".

[2] For more information on the topic of blind analysis and prevention of "experimenter's bias", the reader is referred to [160] and [161].

4.1 Analysis of AMANDA data

In spite of the detailed knowledge on Cyg X-3 presented in section 3.3, there is still very little known about high-energy processes in the system. E.g. it is generally unknown when hadronic acceleration might take place and when neutrino emission might be expected. Naturally, one would assume a connection with the most violent features of Cyg X-3 which are the giant radio outbursts. There is at least some observational evidence that high-energy emission precedes the major radio flares, but the exact time-scale in unclear.

Because the data sample taken with AMANDA is already unblinded and even publicly available, it was ready to be explored, searching for a possible hint of a signal from Cyg X-3. This was meant to be used for a later hypothesis test on IceCube 40-strings and AMANDA data (see section 4.2). Many different tests have been tried, mostly searches for a significant correlation of neutrino events with radio flaring. General analysis techniques were developed that could be used in the later, more sophisticated analysis on blind data.

The investigations presented here are the following:

- Use of a radio flare threshold to define search windows (see 4.1.3)
- Stretching the search windows from a flare threshold (see 4.1.4)
- Shifting and stretching the search windows from a flare threshold (see 4.1.5)
- Varying the spatial bin size (see 4.1.6)
- Using a spatial weight term in the test statistic (see 4.1.7)

4.1.1 Data used

This study was performed using an event sample from the AMANDA-II detector taken within seven years ($2000 - 2006$) [94]. The sample consists of 6595 neutrino candidate events, originating in the Northern Sky, and is publicly available in the world-wide web under `http://www.icecube.wisc.edu/science/data/amanda7year/`. The data selection techniques applied to the raw AMANDA data in order to arrive at the final sample[3] are beyond the scope of this work and are described in detail in [94].

The public and unblind status of the data allowed a non-blind study concerning a possible correlation of neutrino events with Cygnus X-3 radio flares/jets. A first look at the AMANDA events, drawn on X-ray and radio light curves from Cyg X-3, is presented in fig. 4.1. The sample was compared mostly to radio data taken with the Ryle radio telescope between Jan 2000 and Jun 2006 at 15 GHz that was received via private communication from Guy Pooley. Pooley is observer at the Arcminute Microkelvin Imager (AMI) telescope, formerly the Ryle telescope, and has been monitoring variable radio sources like XRBs for many years. See [162] for more information on the Cyg X-3 radio monitoring data.

[3] The original sample contained $1.29 \cdot 10^{10}$ events recorded in 1387 days (3.8 years) of detector livetime, mainly downward propagating muons produced by cosmic ray air showers. The final sample (6595 events) is restricted to the northern hemisphere of the sky and contains mainly upgoing atmospheric neutrino events (of which $\sim 30\%$ of the original number are kept), with a contamination from misreconstructed downgoing muons estimated to be $< 5\%$ for declination $\delta > 5^\circ$ [94].

It was decided to use radio data because the radio flaring activity, that is connected with relativistic jet emission, is most clearly visible in the radio light curve: the radio flux changes by orders of magnitude, a flux density above 1 Jy clearly marks a major flare (see section 3.3.3). Drawbacks of using radio data as tracer for flares are the irregular coverage (sometimes, there are gaps of several days or longer in the data), the less accurate time resolution compared to X-rays, and the fact that radio photon production is not directly connected to high energetic photon production. Synchrotron radio emission happens farther outside of the system after the ejecta have cooled and become transparent to radio wavelengths, so that the radio flare probably lags behind the high-energy flare (see chapter 3).

4.1.2 Simulation

In order to estimate the statistical significance of an observation, it has to be compared to a large number of observations of data samples that correspond to the null hypothesis, in this case: observations of background only samples. The background only observation has to be simulated, e.g. by Monte Carlo techniques, i.e. by drawing random numbers for the event properties and thus generating a random event sample. In this specific (and very simple) case, only the number of events falling in a certain spatial bin and a certain time bin (time "window") is used as test statistic. This means that instead of simulating all properties of the events, only the total number of events falling in the spatial bin (assumed to be a Poissonian random variable) and the time of each event (assumed to be uniformly distributed) needs to be simulated. The exact simulation procedure is as follows: First, the total number of AMANDA events near Cyg X-3 is counted (using a certain bin size (see section 4.1.6) for selection of close events). Then, a Poissonian random number is drawn, using the real event number as mean, to get a random number of close events falling into the search bin.[4] Afterwards, for each random event, a uniformly distributed time is drawn.

In the event time simulation, the AMANDA uptime has to be taken into account. The detector was not taking high-quality data during 100% of the time and in particular, there have been prolonged periods of detector instability or maintenance (including the austral summers November 1 through February 15) that have to be excluded from the sample. In consequence, there exist many intervals in which an event detection is not possible and simulated events must not be generated. A uniform event time was drawn from an interval between 0 and the total uptime of 1387.93 d and then redistributed into the

[4] This is a simplification. The regular way to generate random events in IceCube is the technique of "azimuth scrambling". In this technique, real data events in a zenith band around the source are taken from the sample, each event is assigned a new random (in general uniformly distributed) azimuth angle, but all other properties of the event are kept, e.g. its zenith angle. Thus, the scrambled events keep their correct zenith dependent properties, but nevertheless a random sample is produced in which all traces of point sources are removed. Doing azimuth scrambling also puts a Poisson distributed number of events into the spatial bin around the source. Since for this study only the number of events was needed, the azimuth scrambling was replaced by drawing a random number from a Poisson distribution, for sake of simplicity. Redoing the study with azimuth scrambling showed only a little ($\lesssim 10\%$) down-scaling of all calculated significances, so the earlier results were not discarded. This is because there was a slight under-fluctuation in the total number of events in the source bin (which was used as Poissonian mean), so that with azimuth scrambling, the total number of events in the bin is on average higher. In section 4.1.7, azimuth scrambling was used and also in the later IceCube+AMANDA study in section 4.2.

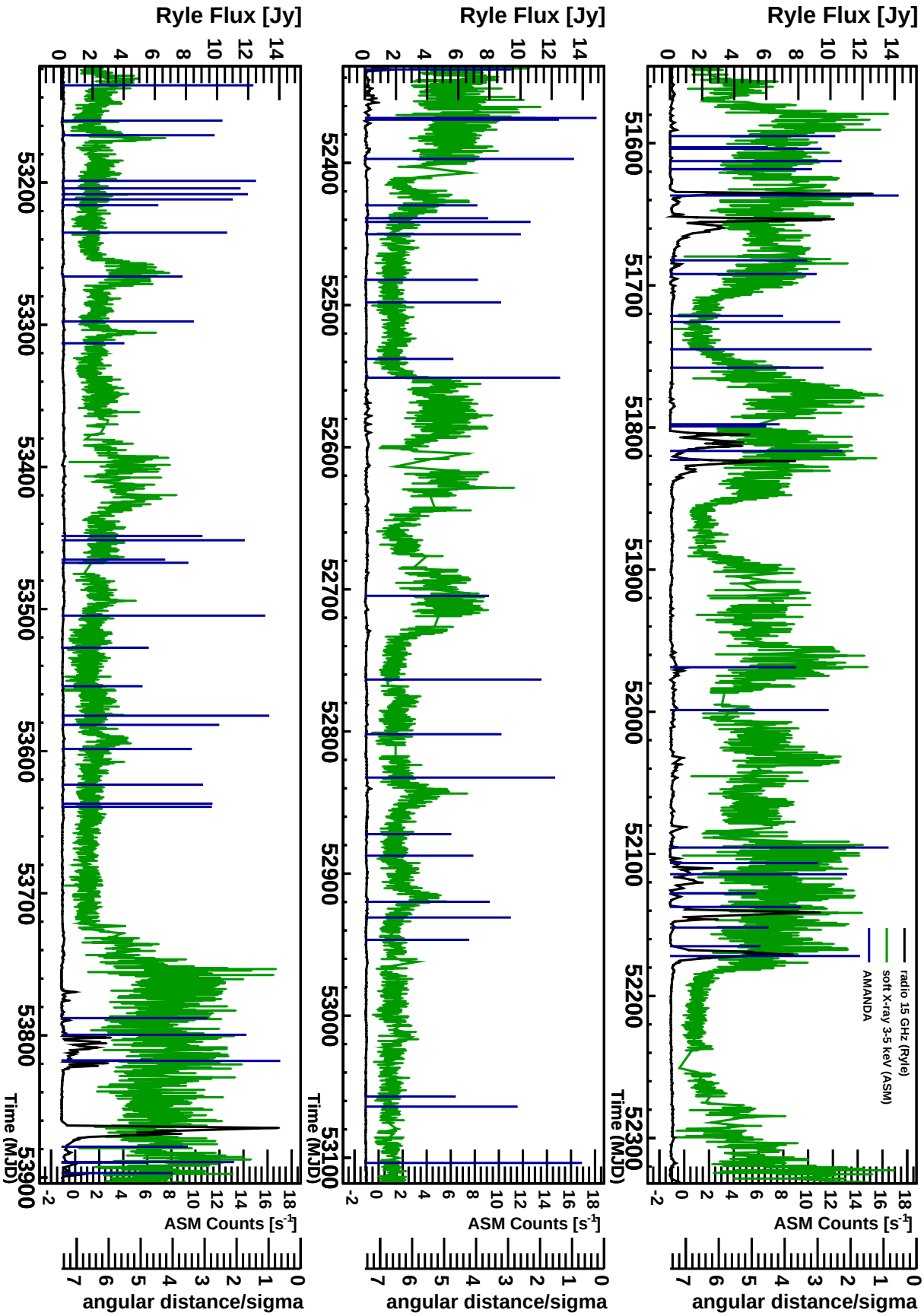

Figure 4.1 Ryle 15 GHz radio light curve (black), RXTE/ASM $3-5$ keV soft X-ray light curve (green) and AMANDA events (blue lines) between Feb 2000 and June 2006. The height of the line corresponds to the event's angular distance to Cyg X-3 in units of the angular resolution (error) estimate, so-called paraboloid sigma. The smaller the dist./sigma ratio, the higher the line. ASM data is from [163], Ryle data from G. Pooley (private communication) [164].

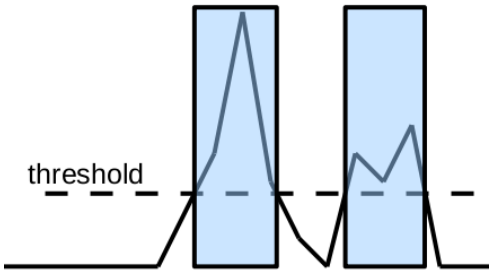

Figure 4.2 Illustration of the definition of flare intervals (used as time window in the search) with the use of a radio light curve and a radio flare threshold. The flare interval begins as soon as the flux rises above the threshold and ends when it drops below.

Year	My uptime [d]	Braun's uptime [d]
2000	141.25	197
2001	190.15	193
2002	204.83	204
2003	219.48	213
2004	212.98	194
2005	220.69	199.26
2006	198.55	186.95
Total	1387.93	1387.21

Table 4.1 Comparison of the self-calculated detector uptime and the uptime calculated by Braun [165].

corresponding uptime interval. To estimate the uptime of AMANDA and obtain intervals of uptime and downtime, the final sample was scanned for gaps between events.[5] It was found that defining all gaps greater than 19.7 h as detector downtime reproduces quite well the original sample uptime calculated by J. Braun et al. for the sample [165, 94]. See table 4.1 for the year-wise uptime in comparison to Braun's results. The most important point is to exclude the large gaps when AMANDA was off for $2-3$ months during South Pole summer.

4.1.3 Varying the radio flare threshold

The Cyg X-3 light curve from the Ryle radio telescope was used to define the intervals in which Cyg X-3 underwent radio flaring. As long as the radio flux density is above a certain threshold value, we define Cyg X-3 as being in a flaring state. The time interval that emerges from that definition (cf. fig. 4.2) was used as time window for the neutrino search. AMANDA events whose direction is separated 10° or less from Cyg X-3 were selected to look for a correlation. The decision on the spatial bin radius of 10° was rather ad hoc and taken because of the rather bad angular resolution of AMANDA. As test statistic, the number of events that fall in both the spatial bin and the time window was used.

The flare threshold has been varied and each time the test statistic was evaluated. Afterwards, the significance of the result has been calculated from a background only (null hypothesis) distribution of the test statistic, obtained from 10^5 toy MC experiments like described in section 4.1.2. In fig. 4.3, the test statistic distributions are shown for different choices of the flare threshold. From these distributions, the probability of the observation under the assumption of the null hypothesis—also called p-value—can be calculated via integration. The p-value was converted to significance in Gaussian standard deviations

[5] Because the event rate of the final sample is very low (only ∼4.8 events per day), this is not an accurate estimate of the up- and downtime intervals. The gap scan should be done on a much lower data level where the event rate is still 1 Hz or more. However, this would have needed a lot of more effort and computational time, so it was neglected for this simple study. It is however done in the analysis in section 4.2.

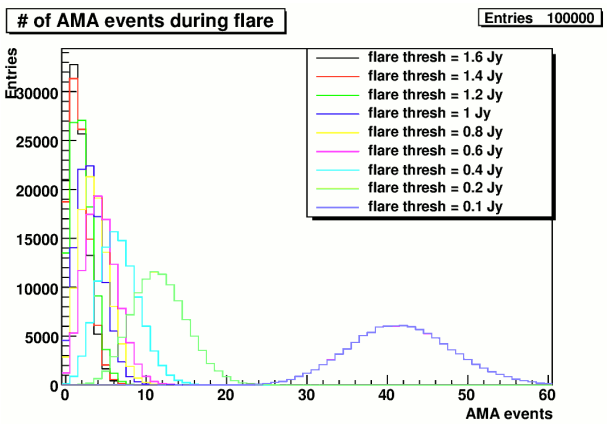

Figure 4.3 Distributions of number of events (used as test statistic) falling inside spatial bin (10° radius) and time windows for different radio flare thresholds. Each distribution has 10^5 entries. The lower the flare threshold, the wider and more numerous the flare intervals become, so that on average more events fall into the time windows defined by the flare intervals. The distributions are basically Poisson distributions, so with higher mean μ, the standard deviation $\sqrt{\mu}$ also gets bigger.

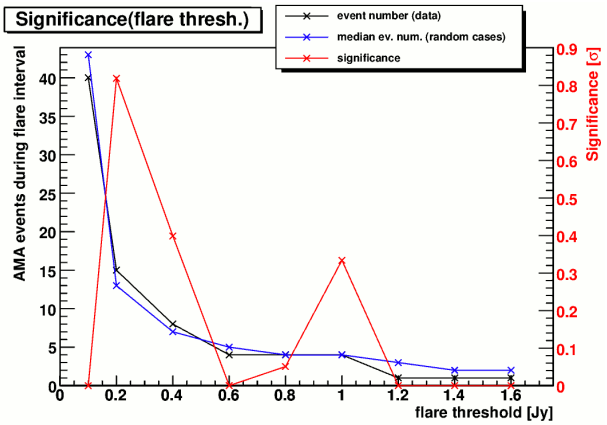

Figure 4.4 Results of the significance study as function of the flare threshold: Number of AMANDA events in time windows (black), median number of events from random experiments (blue) and significance in units of Gaussian standard deviations σ (red). The significance was calculated taking the obtained probability of a random occurrence, the p-value, as one-sided p-value of a Gaussian distribution. For underfluctuations (p-value > 50%), significance was set to zero.

using the one-sided tail of the Gaussian distribution function. Fig. 4.4 shows the results of the significance study: Highest significance is obtained for a flare threshold of 0.2 Jy, with a smaller peak at 1 Jy, but overall significance is very small (well below 1σ). Because the highest significance occurs not for major flares (>1 Jy), but smaller flares (>0.2 Jy), this might be a hint that neutrino emission is shifted in time so that the excess comes from smaller flares before or after major flares. But considering the very low significance, this is not very meaningful. This is of course to be expected of the AMANDA-II sample, because also other analyzers found no hint for any neutrino point source, also at the position of Cyg X-3 [94].

For the next parts, the flare threshold was set to 1 Jy which is the threshold flux density for major radio flares as defined in [140] (see section 3.3.3). The work concentrated on a possible time lag of neutrino emission with respect to the major radio flares.

4.1.4 Stretching the time windows

In order to integrate also over events coming before or after a flare, the time windows, found by setting the flare threshold to 1 Jy, were stretched (extended) to earlier or later times by various values. A positive stretch parameter stands for an extension of the time window to times after the flare by that amount, a negative one means extension to times before the flare (cf. fig. 4.5). Like before, the number of AMANDA events caught inside the windows was used as test statistic and events inside a circular search bin with 10° radius around Cyg X-3 were considered. The stretched windows can be overlapping, which was not possible before the stretching. However, events are not double-counted in the test statistic if they fall in two windows or more.

The results are displayed in fig. 4.6. Compared with the unstretched windows, much

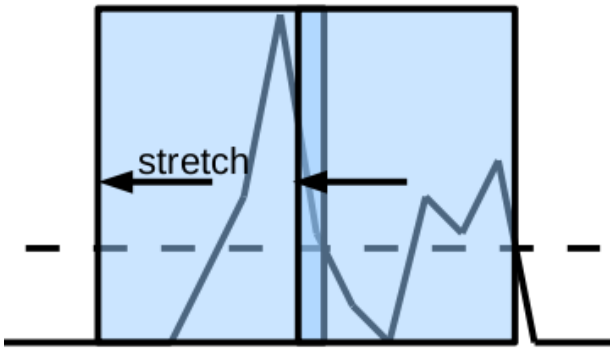

Figure 4.5 Illustration of the stretched time windows: The windows are defined as explained above and extended to earlier or later times. This can cause windows to overlap.

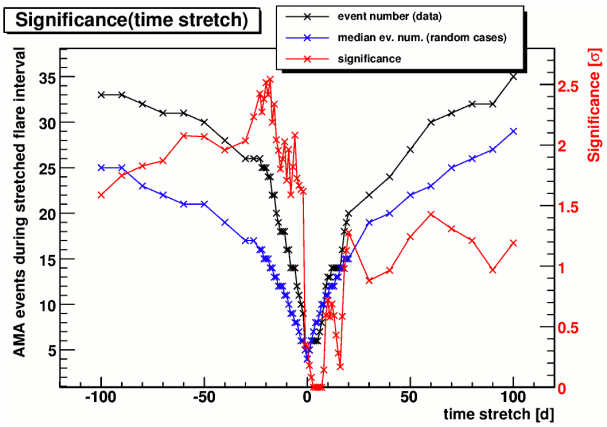

Figure 4.6 Results of the window stretching as function of the stretch parameter. See fig. 4.4 for comments. Each significance was calculated with 10^5 MC experiments.

higher significances were obtained (up to $\sim 2.5\sigma$). The significance as function of the stretch parameter shows a clear asymmetry: Stretches to earlier times lead to higher significances than stretches to later times. The significance peaks at -18 days and declines afterwards. This could be an indication of a neutrino-radio flare correlation with the neutrino events coming earlier than the radio flare. Up to a time scale of ~ 20 days before the flares, the significance increases if events are added to the search window. Interestingly, this is a natural time scale for the quenched radio state or hypersoft state to begin before a major radio flare. There have been observations of the quenched state being entered $10 - 20$ days before the onset of a flare. And there are speculations that during the quenched/hypersoft state, high energy emission could take place (see section 3.3.3).

Significance peaks at -6 and -18 days with p-values of 1.9% and 0.55% that correspond to 2.08σ and 2.54σ, respectively. Because this result was obtained with a scan of the stretch parameter, many trials were carried out and the chance of getting a high significance by chance is bigger. This is why for the highest significance of 2.54σ at -18 days, a post-trial p-value has been calculated by performing the same significance study on 10^6 random background only samples and counting the fraction of cases that have a maximum significance equal to or higher than 2.54σ. The post-trial p-value becomes **4.01%** (1.75σ), so the trial factor is ~ 7.3, even though the number of trials was 61. The trial factor is much smaller than the number of trials because the trials were highly correlated: When the windows are stretched, a large fraction of the windows overlaps with the windows before the stretch, so that most parts of the windows were already used before.

4.1.5 Shifting the time windows

In this study, the search windows obtained with the 1 Jy flare threshold were shifted by various values to the earlier times (negative shift parameter) and to later times (positive shift parameter) to account for a possible time lag between neutrino signal and radio flare. Fig. 4.7 shows an illustration of this. Again, events within 10° from Cyg X-3 were selected. The resulting significance as function of the shift parameter (cf. fig. 4.8) is very spiky, but

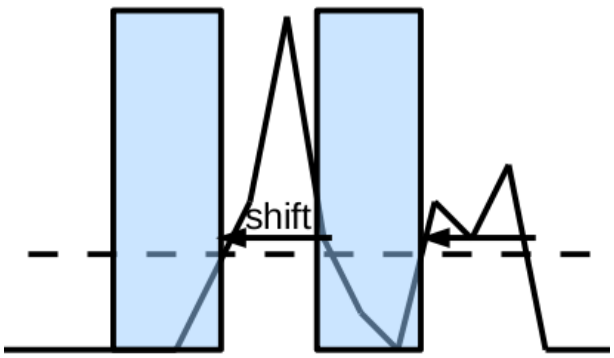

Figure 4.7 Illustration of the shifted time windows: The windows are defined as explained above and shifted synchronously to earlier or later times.

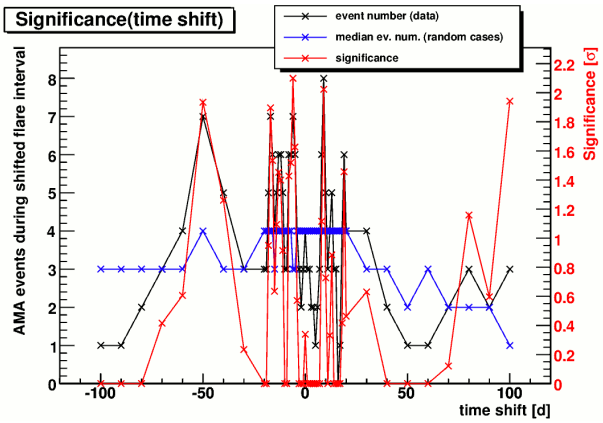

Figure 4.8 Results of the window shifting as function of the shift parameter. See fig. 4.4 for comments. Each significance was calculated with 10^5 MC experiments.

also shows a slight preference of times before the flare. On the other hand, at +100 days shift, the significance is also high which probably cannot be physically connected to the radio flares and underlines that these are random fluctuations.

The unstretched windows are rather short: 6 of the 19 windows have a length of 0 days (this happens if only one radio data point was above the 1 Jy threshold), the average duration is 3.2 days. A neutrino signal that is more extended than the radio light curve indicated could be missed. That is why it was tried to not only shift the windows, but stretch them as well to increase their length. A scan over different possible shift and stretch parameter combinations was done. This time, the stretch was always performed to both sides symmetrically, so that a stretch of 1 day stands for an expansion of the interval to minus 1 day on the left and plus 1 day on the right. See fig. 4.9 for the resulting significance map.

Fig. 4.9 shows a clear favoring of a shift to earlier times, with the highest significance occurring for shifts around −10 days and stretches of 4−8 days. This is again in accordance with the phenomenology of the source, since high energy particles are expected to be emitted a few days before major radio flares (see section 3.3.3). However, this does not have to mean anything because the number of trials is large and the significances that are seen have to be expected in a background only sample. After correction for trials, this significance would be at the 1σ level, so we must assume that we see only random fluctuations in a background only sample.

4.1.6 Variation of the bin size

So far, a circular bin with a radius of 10° was used for studying the significance of neutrino event excesses with respect to radio flares. This means, all final sample events that were reconstructed within 10° from the Cyg X-3 position were selected for the correlation study. This is of course a very large area in the sky, covering almost the entire Cygnus region which is very complex and contains many sources. The bin size was chosen so large in order to securely include all possible events from Cyg X-3, also possible low energy events that were reconstructed with a large deviation from their intrinsic direction. However, even the AMANDA-II detector, that had a point spread function (PSF) inferior to IceCube's

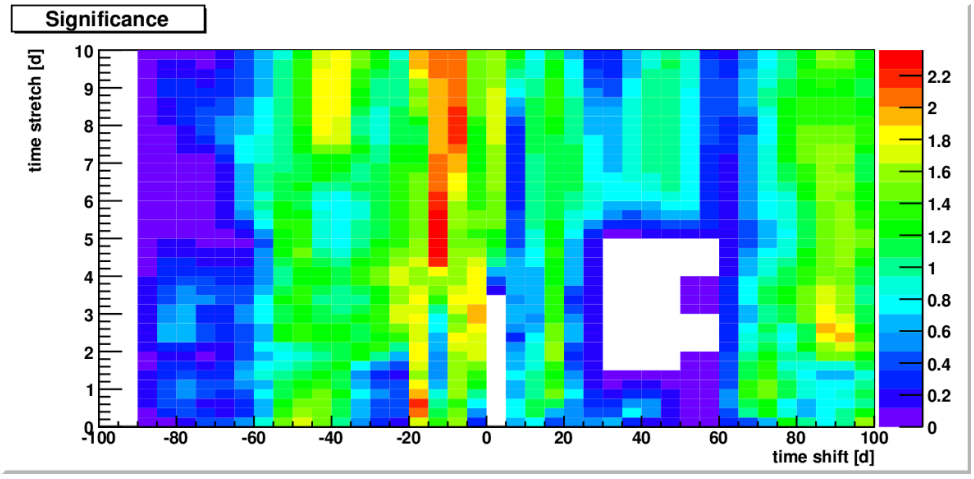

Figure 4.9 Results of the shift-stretch combination. The color code indicates the significance in Gaussian standard deviations (σ). Negative shift means shifting the search windows to earlier times, positive shift means shift to later times. The stretch parameters refer to stretching the interval both on left and right side by the indicated value (expanding it by twice the indicated value). Each significance was calculated with 10^5 MC experiments.

(mainly because of the smaller size of the detector array), achieves a median angular resolution of $\approx 2°$ [94, 166]. The optimal bin size for binned analyses with AMANDA was about $2.25° - 3.75°$, depending on declination [167, 168]. For these reasons, the impact of a different bin size on the analysis was studied.

Fig. 4.10 shows a map of the AMANDA events around Cyg X-3 that contribute most to the study. The red events in fig. 4.10 are those that contribute to the highest significance found in the scan of the stretch parameter. The highest pre-trial significance was 2.54σ and was obtained for a stretch parameter of -18 days (see section 4.1.4). In total, 24 events fell into the search windows, so there are 24 red events in total. Half of those events are lying in the outer ring between 8° and 10° distance to Cyg X-3, while 3 of the 24 are within 2°. So, most of the significance of the result is delivered by events that are constructed at around 4 times the median angular resolution of the detector or more. For comparison, the cumulative PSF of the AMANDA final sample is shown in fig. 4.11.

Reducing the spatial bin size and redoing the studies, e.g. the time stretch parameter scan, provides an entirely different picture. Since the significance of a shift or stretch to earlier times is caused to a large extent by events between 8° and 10° from Cyg X-3, a reduction of the bin size removes the preference of times before flares. Fig. 4.12 presents stretch scan results for bin sizes of 2°, 4°, 6° and 8°. At 8° bin size, the structure seen in the significance for 10° (cf. fig. 4.6) is visible for the first time, even though the asymmetry of the left and right branch is not there and the significance is dominated by a peak at -2 days (1.92σ). Increasing the bin size further beyond 10° results in significance curves similar to the 10° result: The right and left branch have a rather similar significance (unlike fig. 4.6, where the left branch lies at a higher significance), but the domination by the peaks around -20 remains there. The significance curves are very sensitive to a change of the bin size up to $\sim 8 - 10°$ (see fig. 4.12 and 4.6), but rather stable at larger bin sizes. This is due to the cumulative nature: If the absolute bin size is small, an increase by 2° adds relatively much more events to the bin than a 2° increase at large bin size—simply because the relative solid angle that is added becomes smaller for larger bin

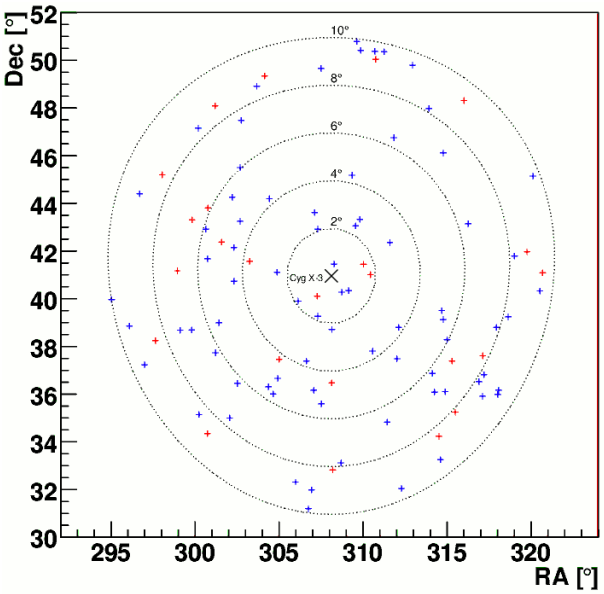

Figure 4.10 Map of the reconstructed positions of the recorded AMANDA events 'close' to Cyg X-3. The cross in the middle is the position of Cyg X-3. The contours show the indicated angular distance from it. The pluses mark the AMANDA events: Blue pluses are events that occurred outside of search windows, red pluses are those that occurred during search windows. This is for a stretch of the windows to 18 days before flaring (−18 d).

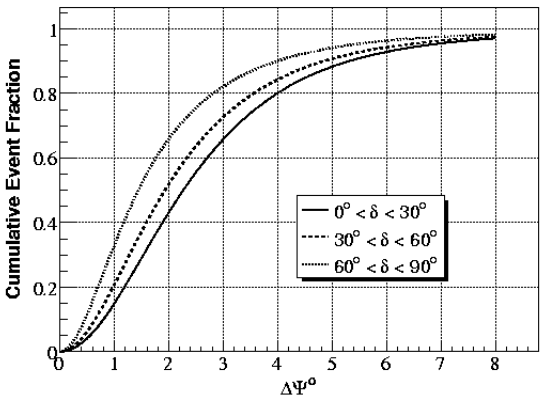

Figure 4.11 AMANDA 7-yr final sample Point Spread Function (PSF) for E^{-2} muon neutrino events from [94]. The x-axis shows the angular distance ($\Delta\Psi$) between the true (from MC simulation) and the reconstructed direction and the y-axis shows the cumulative number of events that have a $\Delta\Psi$ smaller or equal. Cyg X-3 is at declination 40°, so its PSF is similar to the thick dashed curve in the middle.

radii.[6]

The overall significance decays while going to bin sizes larger than 10°. This reveals a small relative over-fluctuation of the number of events correlated with radio flares within 10° from the Cyg X-3 position and a small relative under-fluctuation of correlated events at larger distances.

Concluding the bin size investigation, it was seen that the highest significances are mainly caused by outliers that are unlikely to originate from the source position. It must be mentioned that in the AMANDA 7-yr final sample prepared by J. Braun et al. [94], a cut on the reconstruction error sigma was applied (there are no events with a sigma higher than $\sim 3.2°$ in the final sample). Assuming that the event-specific reconstruction error is reliable, there should only be a small fraction of events reconstructed far away from the true direction. Considering the PSF of the final neutrino sample in fig. 4.11, one would expect less than 5% (maybe $\sim 3\%$) of E^{-2} spectrum events to be reconstructed

[6] If the number of events in the bin is assumed to be proportional to the bin's solid angle and the solid angle of the bin is approximated by a circle on a plane surface (πr^2), then the number of added events relative to the number of events before the increase of the bin size is

$$F \approx \frac{\pi(r_2^2 - r_1^2)}{\pi r_1^2} = \left(\frac{r2}{r1}\right)^2 - 1 = \left(1 + (r_1/2)^{-1}\right)^2 - 1 \propto \frac{1}{r_1} + \frac{1}{r_1^2}$$

for an increase from r_1 to $r_2 = r_1 + 2°$. E.g. if $r_1 = 2°$ and $r_2 = 4°$, then $F \approx 3$, but for $r_1 = 10°$ and $r_2 = 12°$, $F \approx 0.44$.

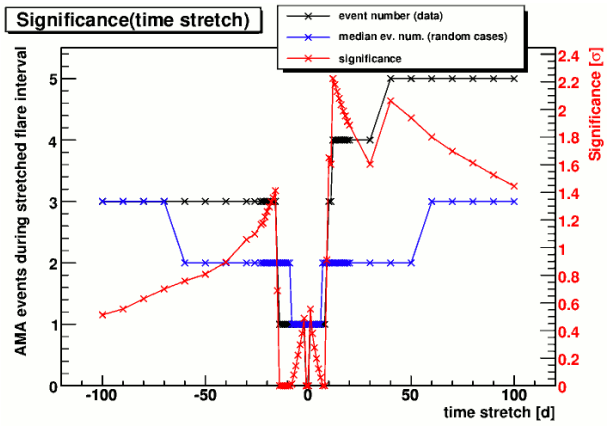

(a) 2° bin radius

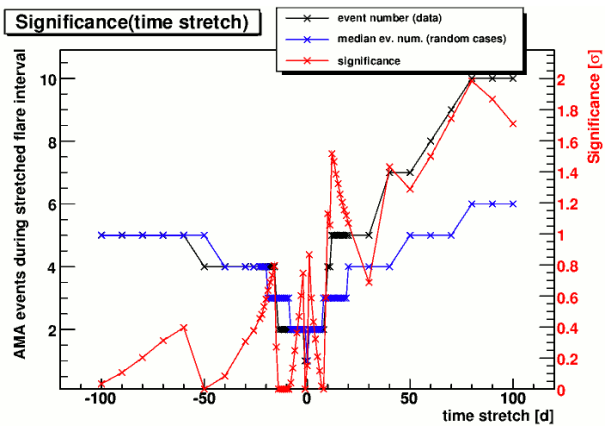

(b) 4° bin radius

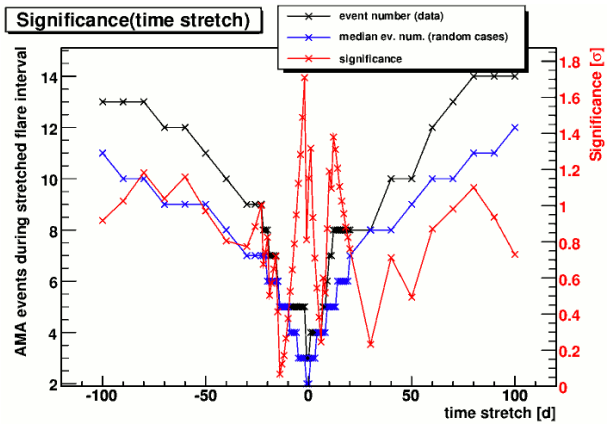

(c) 6° bin radius

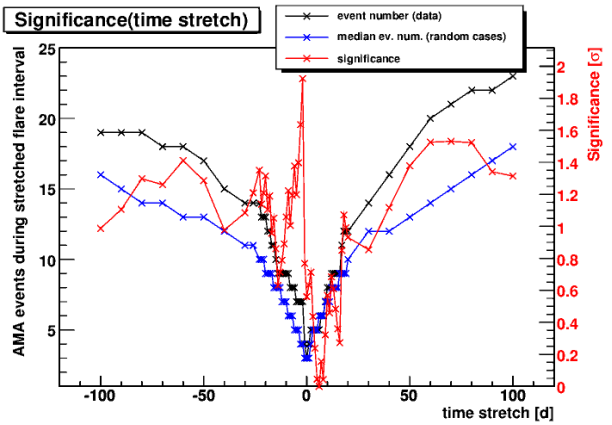

(d) 8° bin radius

Figure 4.12 Results of stretch parameter scans with bin sizes lower than 10°. See fig. 4.4 for comments. Each significance was calculated with 10^5 MC experiments.

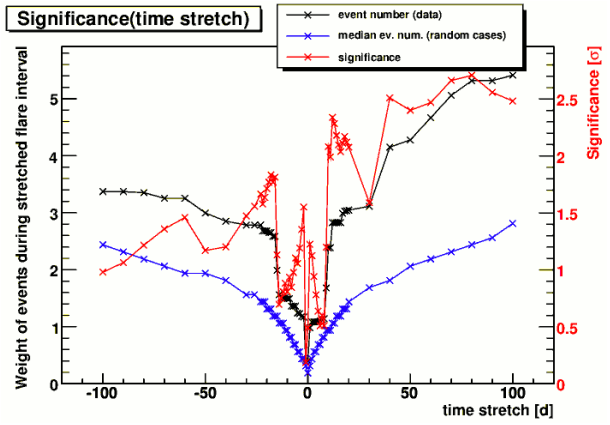

(a) Spatial weight $\exp(-\Delta\Psi/\sigma)$

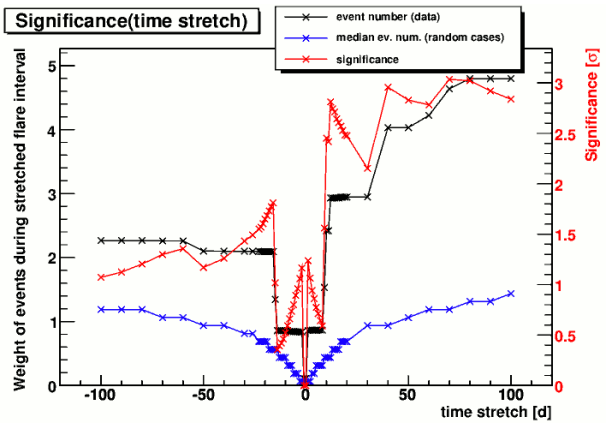

(b) Spatial weight $\exp(-\Delta\Psi^2/\sigma^2)$

Figure 4.13 Results of stretch parameter scans, introducing of a spatial weight into the test statistic. Each event falling into the bin and time window is given a weight according to the term in the subcaption. See fig. 4.4 and text for comments. Each significance was calculated with 10^5 MC experiments.

$\geq 8°$ off their true direction.[7]

This shows that the bin size was chosen *too large* to obtain a meaningful result and motivated to introduce a *weight term* in the test statistic to account for the spatial distance of the events from the source as well as the assumed error of the reconstruction.

4.1.7 Using a spatial weight term

So far, the test statistic had simply been the number of events that fell into the search bin around Cyg X-3 and the search time windows correlated with radio flares. Because it appeared necessary to include a space information stricter than the 10° bin (see section 4.1.6), the searches were redone with a spatial weight factor, for instance $e^{-\frac{\Delta\Psi}{\sigma}}$, where $\Delta\Psi$ is the angular distance between the reconstructed event and the assumed source position (see eq. 4.7) and σ is the angular error estimate from the reconstruction (the paraboloid sigma) that was assigned to each event. So, instead of counting each event inside the windows as equivalent, a much smaller weight was given to events that were farther off the Cyg X-3 position. The test statistic was no longer the plain number of events, but the sum of the weight terms of those events inside the time windows and search bin. Because the spatial information from the events is needed, the simple drawing of a random time had to be complemented by azimuth scrambling[8], so that each simulated event had a random direction as well as a random time.

The results of the space weighted searches with weight terms of $e^{-\frac{\Delta\Psi}{\sigma}}$ and $e^{-\frac{\Delta\Psi^2}{\sigma^2}}$ can be found in fig. 4.13 and fig. 4.14. They appear quite similar to an unweighted search with a bin radius of 4° (compared with plots in fig. 4.12). Taking the space weight into account, the preference of search windows *before* the flare disappears. Instead, we have an even higher significance **after** the flares, with the highest values at $70-100$ days after, which seems unphysical. This is not in agreement with the phenomenology of the source anymore, from which one would expect neutrino events up to 20 days before the radio flares. However, it must be stressed again that this doesn't have much meaning since the significance is not high enough. Everything is compatible with a background only hypothesis.

4.1.8 Interpretation and conclusion

During investigation of the AMANDA 7-yr sample **no significant deviation from a background only hypothesis** was discoverd. There is no clear fluctuation that points to a certain time window or a certain time shift between the radio flaring activity and neutrino arrival times. Thus, no hint of a signal could be extracted from the AMANDA data sample and no specific hypothesis was constructed from this. Following this conclusion, the later analysis on data from IceCube 40-strings and AMANDA did not test a hypothesis based on AMANDA data, but a hypothesis based on the phenomenology of the source from other observations. Time windows defined from flaring activity were used and shifted up to 20 days, which is the reported time scale between quenched state and major flaring state, see section 3.3.3.

[7] The PSF is a little bit worse for a softer spectrum, but at 8° or more, the changes are negligible, as visible in a figure on [166].

[8] Actually, not the azimuth was scrambled, but the right ascension was randomly drawn, while the declination was kept.

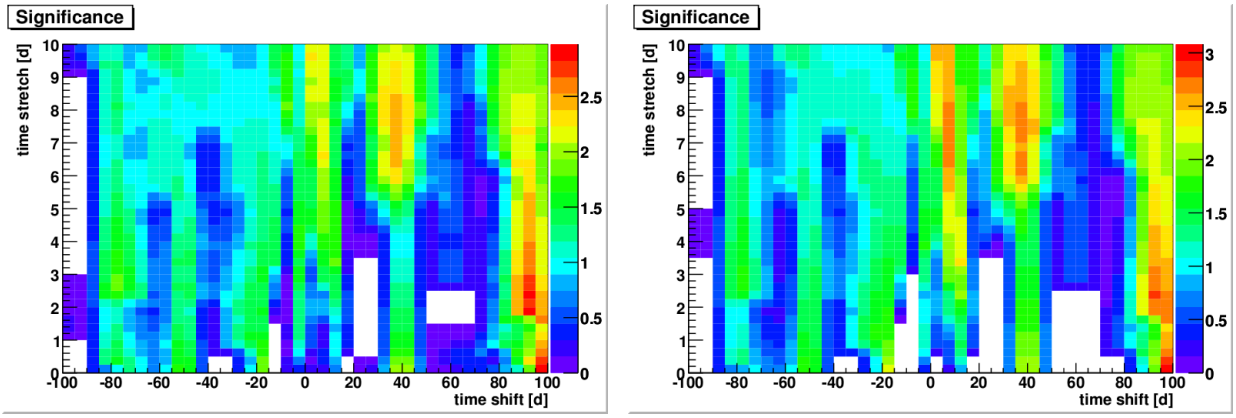

(a) Spatial weight $\exp(-\Delta\Psi/\sigma)$ **(b)** Spatial weight $\exp(-\Delta\Psi^2/\sigma^2)$

Figure 4.14 Results of the shift-stretch combination. The color code indicates the significance in Gaussian standard deviations (σ). See fig. 4.9 for comments. Each significance was calculated with 10^5 MC experiments.

4.2 Analysis of IceCube 40-strings and AMANDA data

The studies described above were only pre-studies for the analysis performed on data from the combined IceCube 40-strings and AMANDA detector (in the following referred to as IC40+AMANDA). The combined IC40+AMANDA neutrino sample was prepared at the Max-Planck Institute for Nuclear Physics in Heidelberg by S. Odrowski, A. Gross, E. Resconi, C. Roucelle, Y. Sestayo and M. Voge. It is described in section 4.2.1. For the simulation of a point source signal from Cyg X-3, MC datasets produced by the IceCube collaboration with Neutrino Generator (based on ANIS [169]) were used that were processed with the same cuts as the data sample. For the hypothesis that was tested, time intervals of flaring activity were extracted from radio data taken with the AMI telescope and X-ray data taken with RXTE/ASM and Swift/BAT, see section 4.2.2.

An unbinned maximum likelihood method was chosen as analysis method. Like before, search windows were used to search for flare-correlated neutrino events from Cyg X-3. However, the test statistic is defined in a more elaborate way: it is a likelihood ratio and includes the fitted maximum likelihood, see section 4.2.3 for details. Because a likelihood fit was used to find the most signal-like set of parameters that maximizes the likelihood, a scanning over the parameter space like it was done in previous sections was not necessary (except for the estimation of initial values for the maximization). There were, however, a few other important differences in methodology with respect to the AMANDA 7-yr studies:

- The search windows were defined by both radio and X-ray data (as opposed to radio data alone), which causes the windows to be broader because of less strict selection criteria. See section 4.2.2.
- The windows were not stretched and/or shifted relative to the flaring activity, but only shifted, because they are already reasonably long or even quite long (e.g. $\sim$20 days)
- The windows were not shifted synchronously, but each window was treated sep-

arately and shifted individually. This change was introduced to account for the possible uniqueness of each flare (see e.g. [121]). Additionally, all windows were shifted synchronously too, to search for several weak neutrino flares that are only detectable if taken together.

4.2.1 Neutrino sample

The generation of the final neutrino sample that was used in the analysis was not a focus of this work. It was prepared mainly by S. Odrowski and is not described in full detail. The data were taken during the combined IceCube 40-strings and AMANDA season that started on 6 April 2008 (MJD[9] 54562) and ended on 20 May 2009 (MJD 54971). Because the data were taken with two separate detectors, there are different classes of events depending on how the detectors reacted:

- **IceCube only events** are events that triggered only IceCube. AMANDA may as well have hits, but because it was not triggered, they were not read out.
- **Combined events** are events that triggered AMANDA. IceCube may have been triggered or not. The event is read out from IceCube either way, since an AMANDA trigger initiates IceCube read-out.
- **IceCube events** are events that triggered IceCube, no matter what happened to AMANDA.
- **AMANDA events** are events that triggered AMANDA, no matter what happened to IceCube. A synonym for combined events.
- **MPE events** are events for which an MPE reconstruction is used in the analysis (see below for explanation). This is an IceCube only reconstruction, as the MPE fit uses only IceCube's hit information. All IceCube only events are MPE events.
- **SPE events** are events for which an SPE reconstruction, including data from both detectors, is used in the analysis. This could also be called combined reconstruction. Combined events are either SPE or MPE events (see below).

Some of the event classes are illustrated in fig. 4.15 in a set diagram. During the time of data taking, there have been various intervals when one or both detectors have not been in operation or have been unstable and producing unreliable data, not useful for the analysis. By scanning the reliable data for gaps at analysis level 3, the up- and downtime intervals have been estimated (see section 4.2.4). From these, the **detector live times** follow as sum of all uptime intervals: The IceCube live time in the combined IC40 and AMANDA era is 375.8 days and the AMANDA live time is 306.2 days. The time when AMANDA was down, but IceCube taking data, amounts to 70.5 days, which implies 0.9 days of AMANDA live time without IceCube being in operation, which is however neglected (see footnote 16). So, the overall live time of the combined detector is 376.7 days during a period of 408.78 days from start to end of the data taking, total live time is accordingly $\sim$92.2%.

[9] MJD stands for Modified Julian Date. It goes back to the Julian Date (JD) used by astronomers to measure time that is defined as number of days since noon on January 1, 4713 B.C., which corresponds to JD 0. Modified Julian Date (MJD) starts at midnight rather than noon (+0.5) and subtracts 2.4 million days for more convenient present dates: MJD = JD − 2400000.5 [170].

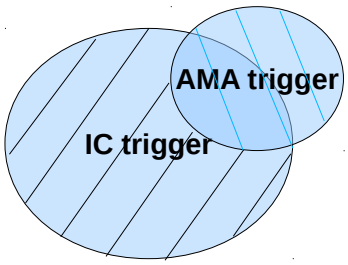

Figure 4.15 Set diagram of different classes of events in the combined IceCube and AMANDA sample. The ellipses represent IceCube events (have an IceCube trigger) and AMANDA events (have an AMANDA trigger). The black hatching marks the IceCube only events, the blue hatching indicates the combined events.

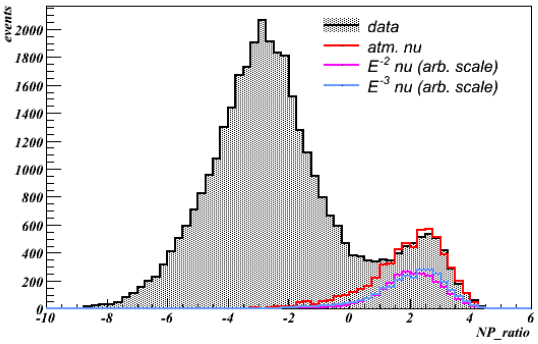

Figure 4.16 Distribution of the Neyman-Pearson likelihood ratio that is used as main cut parameter for IceCube events. The separation between the bulk of muon events (left peak) and the neutrino events (right peak) is clearly visible. The distributions for neutrinos of different spectra come from MC simulation. The N-P cut requires the ratio to be ≥ 1. Plot made by S. Odrowski, MPIK Heidelberg.

In a regular IceCube analysis, it is decided on *one* event reconstruction that is suitable for the analysis. In this case, however, we have a combined detector that has special requirements. In the final neutrino sample, *two* reconstructions are present: One is based on a likelihood using multi-photo-electron (**MPE**) p.d.f. and employs only hit information from the IceCube DOMs. The other is using single-photo-electron (**SPE**) p.d.f., but takes the hits from all modules, both AMANDA OMs and IceCube DOMs. The first one, MPE, is more correct because it takes into account that the hit is one of several hits on the module, whereas in the SPE reconstruction[10] the hit is treated as a single independent hit [69]. Therefore, MPE reconstruction should always be used if possible. However, it turned out that the SPE reconstruction performs better for low energy combined events and yields a better angular resolution. In contrast, for IceCube only events and for high energy combined events that have dominantly IceCube hits, the MPE reconstruction is the better choice. The conclusion is that the best performance comes from an event-by-event selection of one or the other reconstruction: IceCube only events always use the MPE reconstruction. For combined events, the optimal criterion, derived from MC simulation, is to use SPE if the reconstructed muon energy is below $10^{4.5}$ GeV ($\approx$32 TeV) and otherwise MPE.

For each reconstruction, a paraboloid fit to the likelihood space has been performed to obtain an estimate of the reconstruction's angular error, so-called paraboloid sigma (see section 2.1.4). It is just an event-by-event estimator on the error of the reconstruction. The real angular reconstruction error of the sample, the angular resolution or **point spread function** (PSF), depends on energy and zenith angle and can be determined via Monte Carlo simulation. It is shown in fig. 4.17 for an E^{-3} and E^{-2} spectrum. There is no reliable energy estimator for the combined events, since the calculation can use only IceCube hits. Because no consistent energy estimator is available for the whole sample, the

[10] Historically, this is sometimes called Jams SPE reconstruction, because the first-guess algorithm Jams was used.

energy estimator was abandoned altogether and the likelihood in the maximum likelihood search has no energy term. This is no big restriction, since the sample was aimed at searching for soft spectra, e.g. $\propto E^{-3}$, which is close to the $E^{-3.7}$ of atmospheric neutrinos, so that the energy information has very limited power to discriminate between atmospheric and signal neutrinos. The combined IC40 and AMANDA sample was designed so that it is optimized for soft spectra or spectra with a cut-off significantly below 1 PeV, which is achieved by using the low energy extension from AMANDA. Without energy estimator, it is however less sensitive to harder spectra like E^{-2} in comparison with a regular IceCube only analysis.

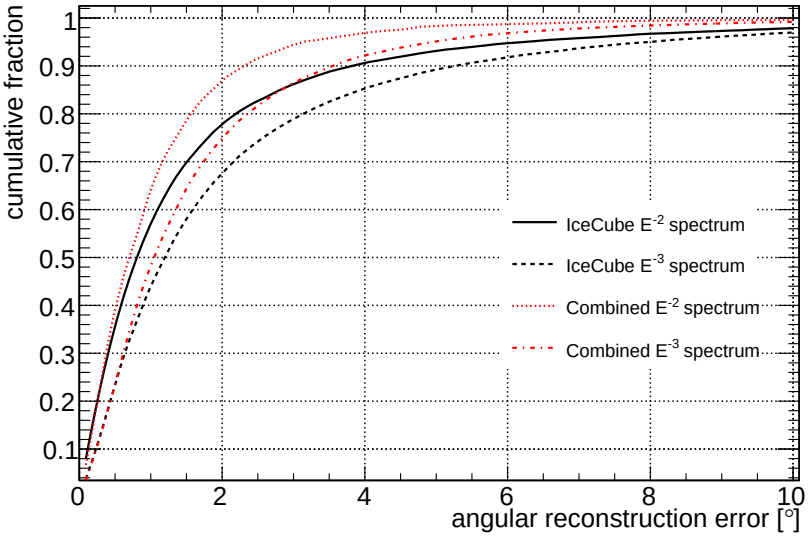

Figure 4.17 Point spread function (PSF) averaged over the Northern sky for IceCube only events (black solid and black dashed) and for combined events (red dotted and red dash-dotted). The curve indicates the fraction of events being reconstructed with an error smaller than the abscissa value. The overall angular resolution is very close to the IceCube only one, with a median value of $\sim$0.83° for E^{-2} and $\sim$1.17° for E^{-3}.

In order to arrive at a clean neutrino level (level 4 in this case), one has to apply **cuts** on various parameters that help to select signal events and dismiss background events. The main part of the cut strategy is based on the Neyman-Pearson lemma [171] and uses a ratio of signal and background likelihood as cut parameter to cut on IceCube only events. P.d.f.s of various quality parameters (see section 2.1.4) enter the Neyman-Pearson likelihood, e.g. reduced likelihood parameter L, paraboloid sigma, N_{dir} and L_{dir}. The p.d.f.s to construct the likelihood are obtained from Monte Carlo for signal and from a 10.4 days live time data sample for background. See fig. 4.16 for a distribution of the Neyman-Pearson ratio. Additional cuts for high energy events and for combined events are used that maximize the signal efficiency.[11] The final sample is a clean atmospheric neutrino sample that has a signal efficiency of 40% with respect to level 3 and contains only a small muon contamination of $\sim$2.4% that are mainly coincident muon events. The total number of events in the sample is 19554, thereof 16482 events during AMANDA uptime and 3072 events during AMANDA downtime. 4292 events are combined events

[11] Signal efficiency is the fraction of signal events that is kept by the cuts. One tries to maximize signal efficiency while minimizing contamination of background events.

that triggered AMANDA (so 15262 events are IceCube only) of which 3224 are events that only triggered AMANDA and would not be there without the AMANDA integration.

4.2.2 Definition of the search windows

The definition of the search windows from radio and X-ray monitoring data is a central part of the analysis since it provides the hypothesis that is to test: the intervals of flaring (or potential flaring) that are assumed to be connected to a neutrino signal from the source, allowing for a certain time lag between radio and neutrino flare (see section 3.3.3).

The outcome of the window determination are **four flaring periods** during the live time of the 40 strings IceCube detector, resulting in a 11.1 days long window, a 22.9 days long window, a 11.9 days long window and a window of 13.1 days length. So, the search windows are in total covering a period of **59 days**, which is more than would be expected from previous radio and X-ray data. It appears that Cyg X-3 was particularly active, especially in the beginning of the IceCube 40 era, when it was crossing the jet line several times during a short period.

The motivation for the use of radio data as a tracer of radio flares is the same as in section 4.1: The radio light curve shows the giant radio outbursts most clearly and the selection criterion is easy. Radio data taken with the AMI radio telescope[12] taken at 15 GHz was used, obtained via private communication from Guy Pooley [173]. See [162] for more information on the Cyg X-3 radio monitoring data. The search windows delivered by the radio light curve are presented below.

One of the main motivations to extend the window selection data to X-ray data was the unavailability of public radio data for the first ~ 1.5 months of IC40+AMANDA operation. The interest in the first 1.5 months was increased by the report of a strong radio flare during this period: An Astronomer's Telegram (ATel) was issued, stating that Cyg X-3 was flaring with peak flux densities of more than 16 Jy (11.2 GHz)[13] on 18 April 2008 [174]. X-ray data from NASA missions has advantages since it is publicly available, the monitoring of Cyg X-3 is more regular in X-ray (at least once per day) and the time resolution is better than for radio.[14] Drawbacks are that the light curves are more complicated and it is less straight-forward to identify the radio flaring in the X-ray light curves.

Gamma-ray data (e.g. from Fermi) was deliberately not used to trace the flares because the analysis is meant primarily as correlation search with *radio flares*. Cyg X-3's phenomenology is not well studied in γ-rays yet and the connection of γ-rays with radio is not clear. Furthermore, the γ-ray telescopes are not as stable as the X-ray telescopes and other sources might bias the Cyg X-3 light curve due to the worse angular resolution.[15]

Therefore, a method to see major radio flares in X-ray data was developed. The X-ray light curves used come from the All Sky Monitor on the Rossi X-ray Timing Explorer (short RXTE/ASM or ASM), available at [163], and from the Burst Analyzer of Transients on board the Swift satellite (short Swift/BAT or BAT), available at [151]. The details of

[12] The Arcminute Microkelvin Imager (AMI) telescope is the successor of the Ryle telescope [172].

[13] The 15 GHz spectrum was interpolated with the radio spectrum from [174] and the 15 GHz flux of the flare was put in fig. 4.23.

[14] Valeriu Tudose, private communication, 14 April 2010.

[15] E.g. in the Fermi/LAT detection of Cyg X-3, a gamma-ray pulsar needed to be removed by cutting on its active phase intervals, see section 3.3.4.

the window selection are given below.

Search windows defined by radio light curve

This study on Cyg X-3 was started with the idea to use radio light curve as trigger of flaring activity and to search for a correlation between radio flares and neutrinos. Also, the radio light curve has most dramatic changes with respect to the quiescent flux during flares and we believe it to be a more stable tracer of flaring activity than other wavelengths.

Following the state classification in literature (see section 3.3.3), major radio flares are highly variable and show flux density peaks of at least 1 Jy. This was used as threshold to define the search windows, like already in the AMANDA studies. A search window starts with the time of the first data point that has a flux density above flare threshold and ends with the time of the last data point above flare threshold. The radio light curve during the IC40+AMANDA era is shown in fig. 4.22 and fig. 4.23. Note that the first weeks of the radio light curve are missing because the Ryle telescope was still upgraded to the AMI during this time. The radio search windows (rounded to 0.1 days) for IC40+AMANDA obtained from the definition are listed in table 4.2 and also plotted in fig. 4.22. Note that the first window is defined by only one single data point above 1 Jy, so that is has zero length. This is not a problem because this window will be included in one of the X-ray windows defined below.

Window	**Start [MJD]**	**Stop [MJD]**	**Duration [d]**
Window 1	54815.8	54815.8	0
Window 2	54818.4	54820.8	2.4

Table 4.2 The search windows defined by the radio light curve.

Search windows defined by X-ray data

From the soft and hard X-ray light curves (shown in fig. 4.18 and fig. 4.1 for the AMANDA era and in fig. 4.23 for the IC40 era), it is not obvious what flux levels indicate major radio flaring. In general, there is an anti-correlation of hard and soft X-rays and the flaring occurs during the soft state (periods of higher soft X-ray and lower hard X-ray flux). But there is no particular threshold on the soft and/or hard X-ray flux that can be used to identify major radio flares in analogy to the radio light curve. The soft state persists for months and it is not clear when during this soft state major radio flares occur. A helpful tool for the study of the X-ray states is the hardness-intensity diagram (HID) (see sections 3.1 and 3.3.3). However, as you can see in fig. 3.11, it is also not easy to isolate the flaring state via cuts in the parameter space of the HID, since the points that correspond to flaring scatter broadly across the diagram and are always accompanied by non-flaring points with much lower radio intensity.

The solution to the problem of radio flare selection is to consider the time-sequence of the states. As the reader might already have noticed in fig. 4.18 or fig. 4.23, major radio flaring seems to correlate with a certain state transition. The hard X-ray flux starts to rise to “normal” levels while the soft X-ray flux stays roughly constant or decays to its hard state level. The single parameter that indicates this transition is the spectral

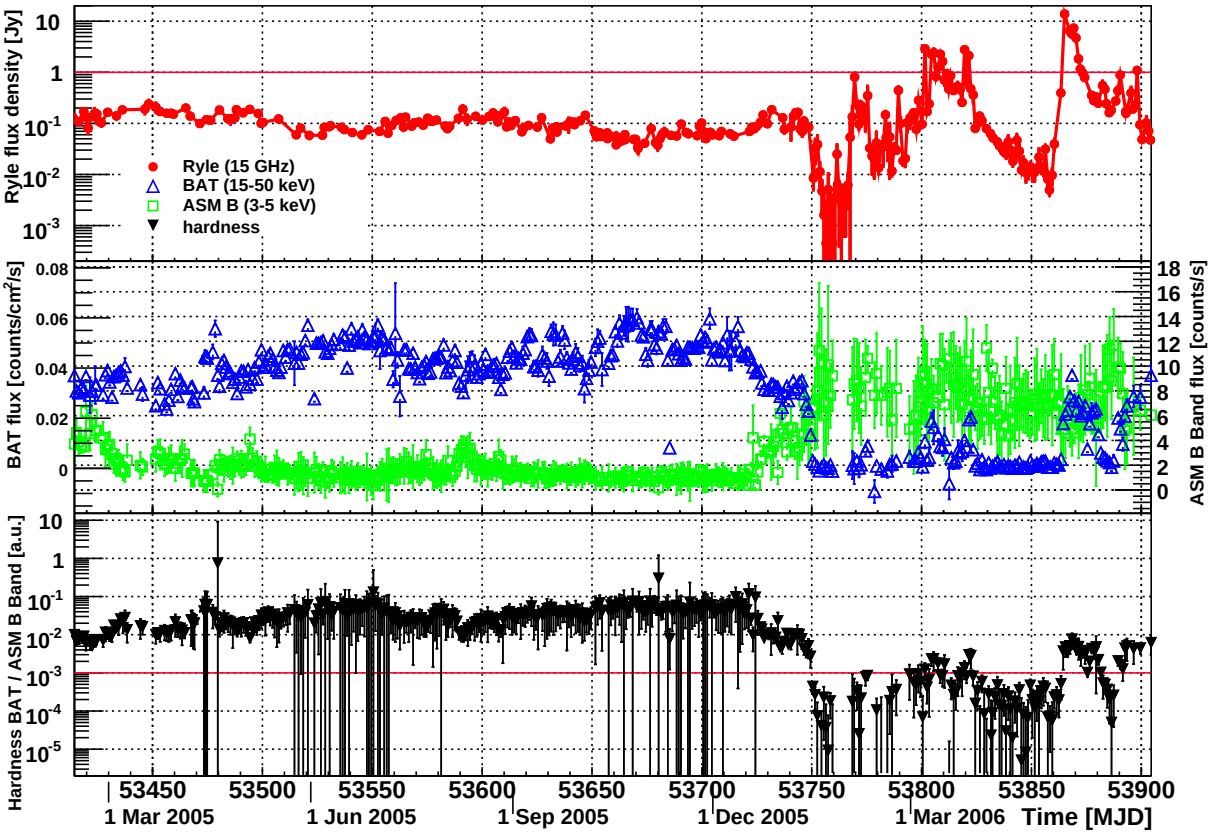

Figure 4.18 Collection of multi-wavelength light curves for a period of 492 days at the end of the AMANDA-II era, where data in hard X-rays (Swift/BAT [151]) as well as soft X-rays (RXTE/ASM [163]) and radio (Ryle 15 GHz [164]) is available. The hardness, defined as ratio of BAT counts to ASM B counts, is plotted in the lowest panel.

hardness that was below a certain level and then increases. This is very clear in the HID, where the source moves from the hypersoft state (the leftmost part of the diagram) to a harder state at the beginning of flaring. A vertical jet line can be drawn that indicates the onset of major radio flaring if it is crossed from left to right.

The jet line, which is in fact simply a threshold on the spectral hardness, was chosen empirically so that it allows major radio flare predictions that are compatible with the simultaneous radio data. Also, different hardness definitions using different energy bands were tried (ASM B Band $3-5$ keV, ASM C Band $5-12$ keV, ASM Sum Band $1.5-12$ keV, BAT $15-50$ keV). The best results were obtained with a hardness defined as ratio between the Swift/BAT counts and the RXTE/ASM B Band counts. The jet line was found to be best put at a hardness of $\frac{\text{BAT}}{\text{ASM B}} = 0.001$. An HID using the BAT/ASM B Band hardness and the ASM Sum Band intensity is shown in fig. 4.19.

A remaining problem was that the jet line crossing only tells about the time when a major radio flare begins, not about its evolution and the time when it stops. Therefore, the algorithm was written such that it reports all X-ray observation times of states that lie *on the right* side of the jet line and occur within a certain time window after a state *on the left side* of the jet line. Thus, it reports the times of harder states *after* a jet line crossing, up to a certain maximal time after the last state *before* jet line crossing. This maximal time was chosen such that the resulting state reports coincide well with the radio flaring seen in the radio light curve. It was chosen to be 10 days, which is longer than the

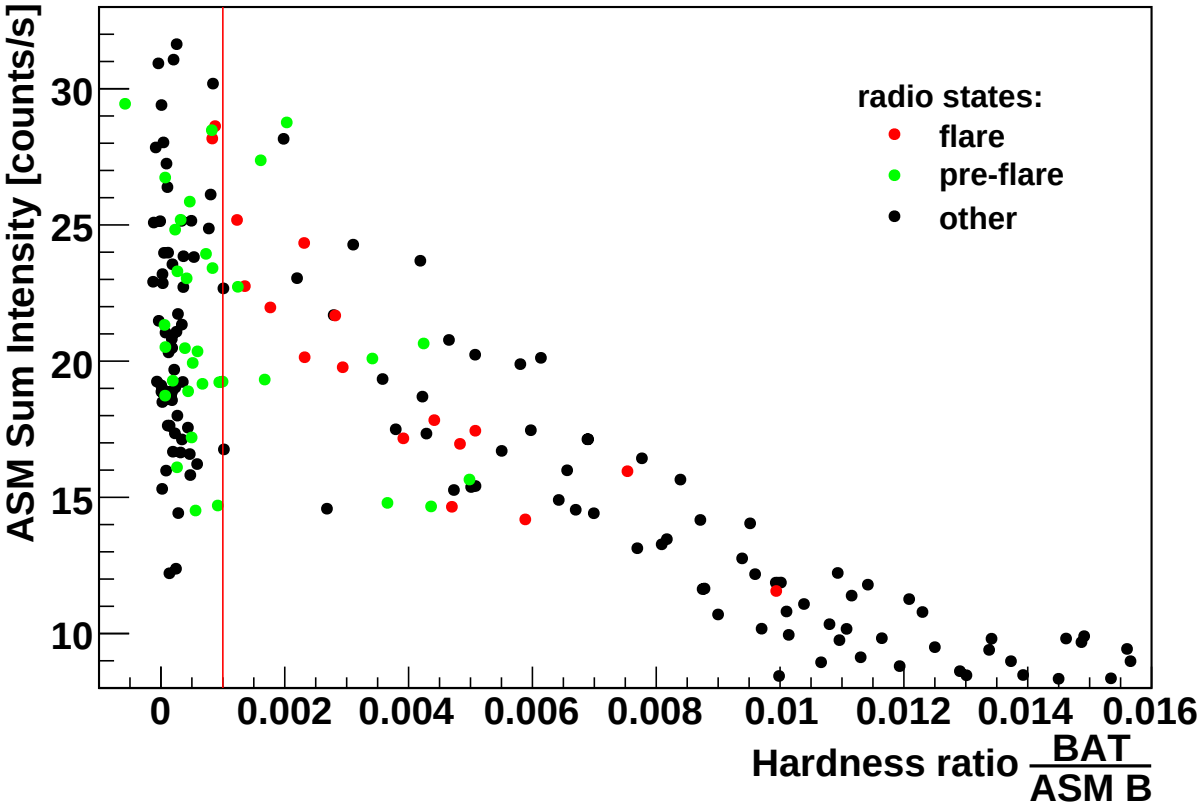

Figure 4.19 Hardness-intensity diagram (HID) using RXTE/ASM and Swift/BAT data. The jet line is defined to be at a spectral hardness of 0.001 and is visualized by a red line. Red points are X-ray observations with a nearly simultaneous radio flaring (>1 Jy) observation. Green points are X-ray observations that are followed by a radio flaring observation within the next 10 days, all other points are painted black. The jet line separates most green and red points. Jet line crossings result exclusively in a flaring state or a pre-flare state. No crossings with a black end point occur (with the application of the 10 days time limit).

typical flare length of $\sim 1-4$ days, because there are usually multiple flares one after the other that all need to be covered. For unusually short flaring periods, this might be too long, however, for others it might even be too short. This is the reason why the X-ray window selection is less strict than the radio one and gives broader windows. The maximal time sets the typical time-scale for an X-ray defined window. The optimization of the parameters was done using simultaneous BAT, ASM and Ryle radio data (15 GHz) for 492 days at the end of the AMANDA era (from MJD 53414 to MJD 53905). Before that, the Swift/BAT was not yet operational, afterwards, Ryle was not in operation anymore because it was upgraded to AMI.

To get from a set of times to time windows, each major radio flare (>1 Jy) in all Ryle data during the 7-yr AMANDA era ($2000-2006$) was fitted with a Gaussian function of the form $\kappa\, e^{-(t-t_0)^2/2\sigma^2}$ (cf. fig. 4.20). The resulting parameters σ (width) and a κ (normalization constant) were averaged to provide the average width and amplitude of a major radio flare in 15 GHz:

$$\bar{\sigma} = 1.16 \text{ d} \quad \text{and} \quad \bar{\kappa} = 4.81 \text{ Jy}. \tag{4.1}$$

Because each of the times from the algorithm (see above) can in principle be the time

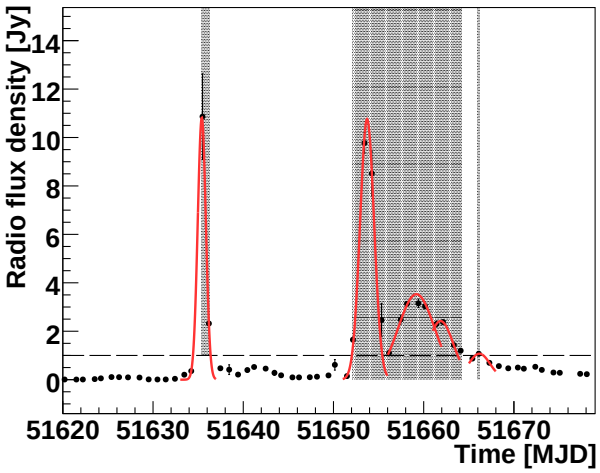

Figure 4.20 Excerpt from the Ryle radio light curve during the AMANDA era (∼6.5 years in total) with some major radio flares and fitted Gaussian functions plotted on top. All flares rising above 1 Jy were used for fitting.

of a major radio flare, a Gaussian with the average parameters—representing an average flare—was centered on each of the times. Then, the intervals of "pseudo" radio flux above 1 Jy constituted the time windows. Most adjacent potential flaring times blend into a single window. The resulting windows for the end of the AMANDA era are depicted in fig. 4.21. Applying the exactly same method to the X-ray data from the IC40 era results in the windows presented in fig. 4.22 and listed in table 4.3 (rounded to one digit after the decimal sign).

Window	Start [MJD]	Stop [MJD]	Duration [d]
Window 1	54571.4	54582.5	11.1
Window 2	54584.5	54607.4	22.9
Window 3	54637.6	54649.5	11.9
Window 4	54811.5	54819.6	8.1
Window 5	54820.4	54824.6	4.2

Table 4.3 The search windows defined by the X-ray data.

Combined windows

The radio-obtained and X-ray-obtained time windows were merged with a logical OR-operation to get combined search windows which were used in the analysis. They are largely identical with the X-ray time windows (see above). The numerical values of the combined search windows are listed in table 4.4. A plot with all the light curves, the hardness vs. time and the final combined windows for the IceCube 40-strings era is found in fig. 4.23. Some interesting notes:

- Window 2 is rather long because Cyg X-3 underwent three jet line crossings within ∼10 days (cf. fig. 4.23), which results in a window longer than 20 days.
- Combined window 4 was originally X-ray window 4 and 5, "glued together" by the extended radio window 2.

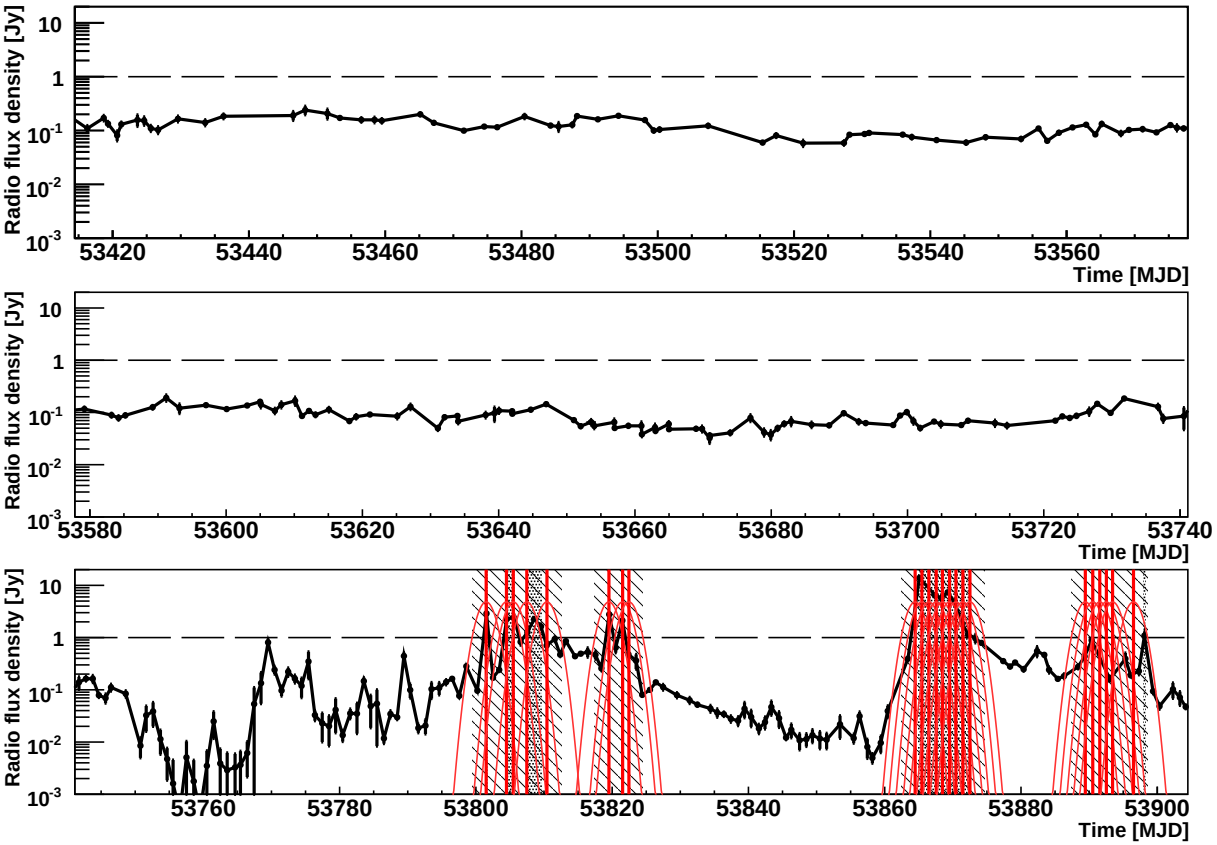

Figure 4.21 The Ryle radio light curve at the end of the AMANDA-II era with possible times of flaring as red lines and with average flare Gaussians on top. These give rise to the search windows, shown as hatched areas. The radio-induced search windows are plotted as dotted areas.

- Radio window 1 had a length of zero, but it is completely contained in combined window 4.
- A minor radio flare around MJD 54780 remained just below the flare threshold of 1 Jy in the radio monitoring. The hardness also stays just under the jet line, so the jet is not selected, which is a confirmation that the method selects *major* radio flares correctly.

Window	Start [MJD]	Stop [MJD]	Duration [d]
Window 1	54571.4	54582.5	11.1
Window 2	54584.5	54607.4	22.9
Window 3	54637.6	54649.5	11.9
Window 4	54811.5	54824.6	13.1

Table 4.4 The search windows from radio and X-ray data merged into a single set of windows.

4.2.3 Analysis method

The analysis works similar to the significance studies that were done on AMANDA 7-yr data. However, the calculation of the test statistic is considerably more elaborate and

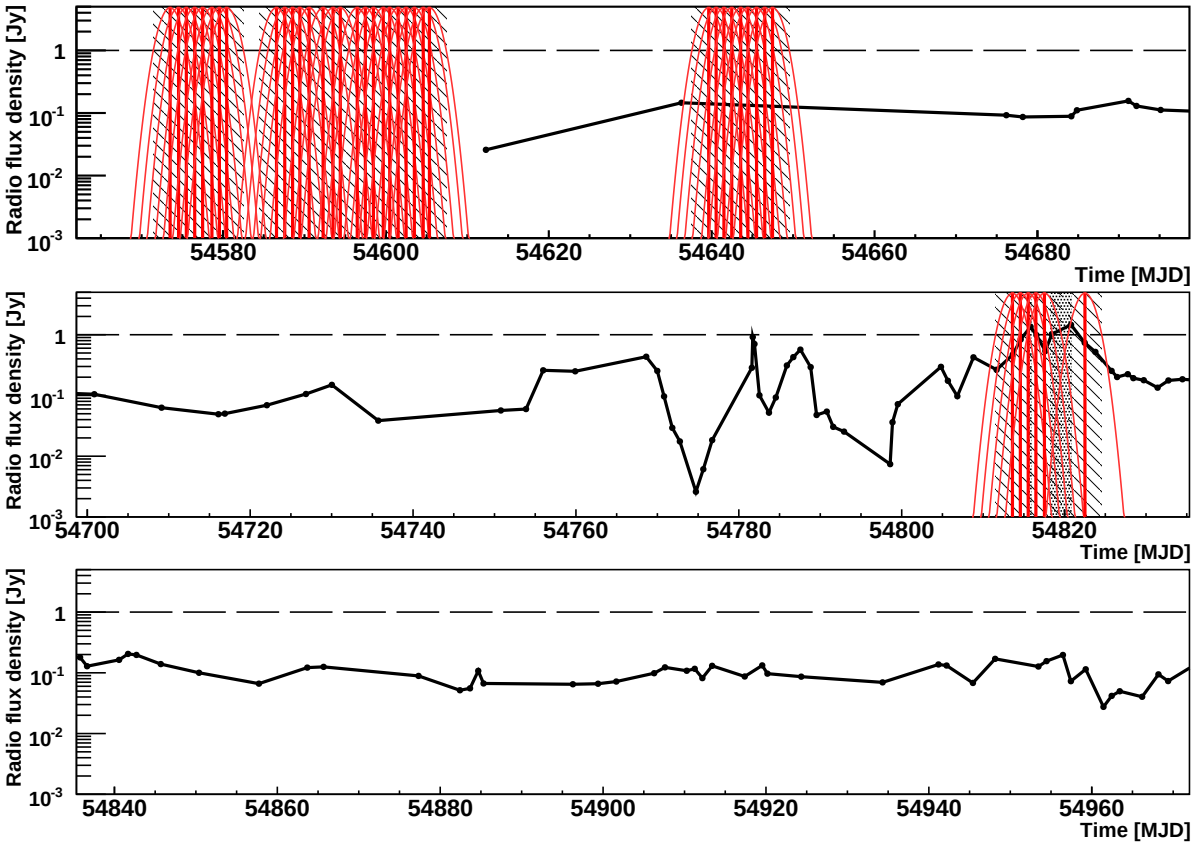

Figure 4.22 The radio light curve during the IC40+AMANDA era with possible times of flaring as red lines and with average flare Gaussians on top. These give rise to the search windows, shown as hatched areas. The radio-induced search windows are plotted as dotted areas.

is there is no need to define (spatial or temporal) bins anymore. Instead, every event in a declination band around the assumed source is used, assigning a certain weight to each event, that is actually a "likelihood" that this event is a signal event or not. As before, time windows are used in which a signal flux is assumed to originate. These were derived in section 4.2.2 and are incorporated in the likelihood calculation. Since the exact hypothetical neutrino light curve is unknown, the time windows are allowed to be shifted away from their original position. The shifting is included in a fitting process, in which the total likelihood of the sample is maximized. Thus, no scanning of the parameter space is needed anymore. The applied method is called **unbinned maximum likelihood** and is at the moment the standard search method for point sources in IceCube, since it is suited for samples with a weak signal and a high level of background. For references on the maximum likelihood method in neutrino astronomy, see e.g. [175] and [157].

The unbinned maximum likelihood method works roughly as follows:

1. For each event, two numbers are calculated from the signal and the background probability density function (p.d.f.). These numbers correspond to the probability that this event is a signal or a background event.

2. These signal and background probabilities are scaled with the expected mean number of signal events and mean number of background events, respectively. The result might be called the probability of each event to occur in the experiment.

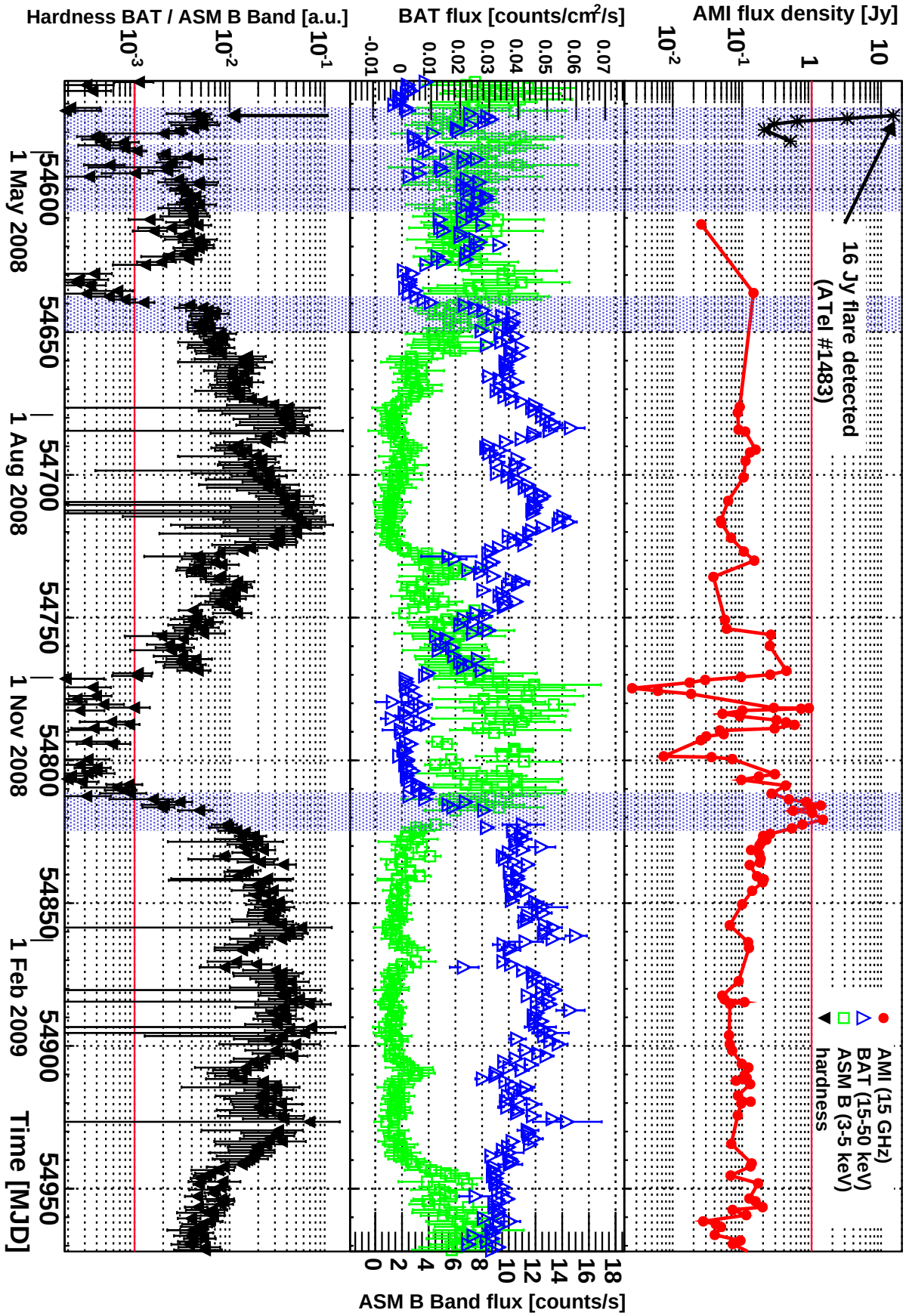

Figure 4.23 Collection of multi-wavelength data for the IC40 era (410 days) with light curves in hard X-rays (Swift/BAT [151]) as well as soft X-rays (RXTE/ASM [163]) and radio (AMI 15 GHz [173]). The hardness, defined as ratio of BAT counts to ASM B counts, is plotted in the lowest panel. The dotted areas indicate the combined search windows for the IC40+AMANDA analysis. A major radio flare reported in ATel #1483 [174] was interpolated to 15 GHz and plotted on the radio panel. The time of peak flux is indicated with an arrow in the hardness panel.

3. All the numbers from all events in the sample (typically a declination band around the source) are multiplied to form the likelihood of the sample.

The **likelihood** can be written down as:

$$\mathscr{L}(n_s) = \prod_{i=1}^{N} \left(\frac{n_s}{N} S_i + \left(1 - \frac{n_s}{N} \right) B_i \right), \tag{4.2}$$

where n_s is the expected mean number of signal events in the sample (events coming from a point source in our case), N is the total number of events in the sample and S_i and B_i are the signal and background p.d.f.s evaluated for event number i. The likelihood can be *maximized* with respect to n_s to find the number of signal events that describe the sample best. In practice, $-\log(\mathscr{L})$ is *minimized*. The logarithm reduces the risk of reaching the boundaries of numerical precision (e.g. for very small likelihood values) and the minus sign is because for minimization, there exist stable numerical libraries like Minuit [176].

Once the likelihood has been maximized, it can also serve to provide a **test statistic**. A common test statistic used for point source searches is the likelihood ratio λ. It consists of the ratio between the likelihood for the background only case and the maximum likelihood:

$$\lambda = -2 \cdot \operatorname{sign}(\hat{n}_s) \cdot \log \left[\frac{\mathscr{L}(0)}{\mathscr{L}(\hat{n}_s)} \right] \tag{4.3}$$

In the above formula, $\hat{n}_s$ denotes the *best fit* number of signal events, which maximizes the likelihood. So it should be: $\mathscr{L}(\hat{n}_s) \geq \mathscr{L}(0)$, since $\mathscr{L}(\hat{n}_s)$ is the maximum of $\mathscr{L}$. Thus, the ratio of the two likelihoods should always be ≤ 1 and its logarithm ≤ 0. The minus sign in front produces a positive λ, unless the sign of the number of signal events is negative, in which case λ is negative as well. Therefore, under-fluctuations of background, producing a negative number of signal events (a "sink") are visible as well in the test statistic. The greater λ, the more source events are likely to be in the studied sample. A λ close to zero is likely for a background only sample and negative λ indicates a sink of events.

Time-Integrated

The time-integrated, i.e. time-independent, version of the method is used for comparison purposes to see the improvement gained from the time-dependent search (see section 4.2.5). The p.d.f.s for the time-integrated method are the standard p.d.f.s used high-energy neutrino point source searches [175]. They have no time-dependent term, the actual detection times of the events are irrelevant. The sample is only studied in its spatial properties and perhaps its energy distribution. In our case, also the energy of events is neglected, because using AMANDA, no reliable energy estimator is available (see section 4.2.1).

The time-integrated **background p.d.f.** is very simple: The background is simply assumed to be uniform, so it is a constant. It has no time term and is normalized in space (integration over whole declination band gives 1):

$$B = \frac{1}{\Omega_{\text{band}}} \tag{4.4}$$

Ω_{band} is the solid angle of the declination band. A declination band of $\pm 5°$ around

the position of Cygnus X-3, which is at declination $\delta = 40.96°$, is used, so (declination $\delta \in \left[-\frac{\pi}{2}, +\frac{\pi}{2}\right]$ and right ascension $\alpha \in [0, 2\pi]$):

$$\Omega_{\text{band}} = \iint_{\alpha\,\delta} \cos\delta \; d\alpha \, d\delta = 2\pi \int_{\delta-5°}^{\delta+5°} \cos\delta \; d\delta = 2\pi \left(\sin(\delta + 5°) - \sin(\delta - 5°)\right) \approx 0.827 \text{ sr.} \tag{4.5}$$

A correction of B for detector asymmetry or changing rate of the detector is not needed. This is because we are not interested in the times of our events. We just look at the spatial pattern and that is not changed by these effects. Even if there are spatial defects at work (like the detector asymmetry that causes a non-flat azimuth distribution), then these are averaged out by the rotation of the earth. Each point in the sky moves at constant speed through all the azimuth angles, so there is no direction in the sky that would be preferred—given integration time is large enough.

The **signal p.d.f.** also has no time-term, only a space term that is a normalized 2D-Gaussian:

$$S(\Delta\Psi, \sigma) = \frac{1}{2\pi\sigma^2} \, e^{-\frac{\Delta\Psi^2}{2\sigma^2}} \tag{4.6}$$

$\Delta\Psi$ is the angular distance between the event direction $\mathbf{x}$ and the assumed source location $\mathbf{x_0}$ and can be thought of as the metric of the curved celestial sphere. Its functional form for declination δ and right ascension α is:

$$\Delta\Psi = \|\mathbf{x} - \mathbf{x_0}\| = 2 \arcsin \sqrt{\sin^2\left(\frac{\delta_1 - \delta_2}{2}\right) + \cos\delta_1 \cos\delta_2 \sin^2\left(\frac{\alpha_1 - \alpha_2}{2}\right)} \tag{4.7}$$

σ is the event's angular error estimate, that is obtained, e.g. by the paraboloid reconstruction. The Gaussian causes the signal p.d.f. to be $\ll 1$ everywhere except close to the source. The definition of what exactly 'close to the source' is comes from the angular resolution estimate σ. If the reconstruction algorithm assumes a bad resolution (large σ), then the event is allowed to be farther away from the source without having a negligible signal p.d.f.

Time-Dependent

The time-dependent version of the unbinned maximum likelihood method is not so straightforward. The reason is that the data sample comes from a combined detector with different rates and different reconstructions used depending on if AMANDA was on or off and the quality of the respective reconstruction. The p.d.f.s used here have no energy term, because with the use of AMANDA, no reliable energy estimator is available (see section 4.2.1).

The **background p.d.f.** should account for the detector asymmetry, so the probability to get an event with a preferred azimuth angle should be higher. Also, it should account for the different detector operation modes[16] (AMANDA on and AMANDA off), so the

[16] For simplicity, IceCube is assumed always on when AMANDA is on. This is to be expected from the DAQ design (see section 2.1.2), but is not strictly true. It allows to divide all events in only two classes: AMANDA on and AMANDA off, which implies an operating IceCube detector. More realistic would be three classes: only IceCube on, only AMANDA on, both on. But the approximation is almost correct, as there is only a total time of 0.9 days where AMANDA was on, but IceCube not.

event probability should scale up and down with AMANDA on and off. The background p.d.f. was chosen to be:

$$B(c, a(t), \phi) = \frac{2\pi}{\Omega_{\text{band}}} \left(\delta_{c0} P_{\text{MPE}}(\phi_{\text{MPE}}) + \delta_{c1} P_{\text{Jams}}(\phi_{\text{Jams}})\right) \cdot \frac{\delta_{a0}\, R_{\text{AMAoff}} + \delta_{a1}\, R_{\text{AMAon}}}{R_{\text{AMAoff}}\, T_{\text{AMAoff}} + R_{\text{AMAon}}\, T_{\text{AMAon}}} \tag{4.8}$$

The Kronecker deltas above are defined as: $\delta_{ij} = \begin{cases} 1, & \text{if } i = j \\ 0, & \text{if } i \neq j \end{cases}$. The boolean c is 0 if for this event it was decided to use the MPE reconstruction and 1 if it is a combined event so that it has the Jams SPE reconstruction[17] (only one or the other is true). Similarly, boolean a is 0 if the event happened during AMANDA downtime and 1 if the event happened during AMANDA uptime. So, for each event, only one of the terms in the first and second factor is chosen. $P_{\text{Jams}}(\phi_{\text{Jams}})$ and $P_{\text{MPE}}(\phi_{\text{MPE}})$ are the normalized azimuth angle distributions of the Jams SPE and the MPE reconstruction azimuth (shown in fig. 4.25b), so $\int P_{\text{reco}}(\phi_{\text{reco}})\, d\phi_{\text{reco}} = 1$. They don't depend on the zenith angle, since they are computed for the whole sample (northern sky). $R_{\text{AMAon}} \approx 0.62$ mHz and $R_{\text{AMAoff}} \approx 0.50$ mHz are the rates during the time when AMANDA was on and off (shown in fig. 4.26b) and $T_{\text{AMAon}} \approx 306.15$ days and $T_{\text{AMAoff}} \approx 70.54$ days are the livetimes during the AMANDA on and AMANDA off time.

The background p.d.f. is normalized with respect to integration over the whole zenith band from $\theta_0 - 5^\circ$ to $\theta_0 + 5^\circ$ ($\theta_0 \approx 130.96^\circ$ is the constant zenith of Cyg X-3 at the South Pole) and over time of detector operation:[18]

$$\begin{aligned} \iiint_{\theta\,\phi\,t} B \sin\theta\, d\theta\, d\phi\, dt &= \frac{2\pi}{\Omega_{\text{band}}} \cdot \int_\theta \sin\theta\, d\theta \cdot \int_\phi P(\phi)\, d\phi \cdot \\ &\quad \cdot \int_t \frac{\delta_{a0}\, R_{\text{AMAoff}} + \delta_{a1}\, R_{\text{AMAon}}}{R_{\text{AMAoff}}\, T_{\text{AMAoff}} + R_{\text{AMAon}}\, T_{\text{AMAon}}}\, dt = \\ &= \frac{2\pi}{\Omega_{\text{band}}} \cdot \frac{\Omega_{\text{band}}}{2\pi} \cdot 1 \cdot \frac{R_{\text{AMAoff}}\, T_{\text{AMAoff}} + R_{\text{AMAon}}\, T_{\text{AMAon}}}{R_{\text{AMAoff}}\, T_{\text{AMAoff}} + R_{\text{AMAon}}\, T_{\text{AMAon}}} = 1 \end{aligned}$$

The **signal p.d.f.** does not account for detector asymmetry and changing event rates like the background p.d.f. It is following standard time-dependent point source methods

This happens mainly at the beginning or end of runs for up to 2 minutes (on average 38 seconds).

[17] See footnote 10.

[18] Note the different formulae for Ω_{band} depending on the coordinates: For declination $\delta \in \left[-\frac{\pi}{2}, +\frac{\pi}{2}\right]$:

$$\Omega_{\text{band}} = \iint_{\alpha\,\delta} \cos\delta\, d\alpha\, d\delta = 2\pi \int_\delta \cos\delta\, d\delta,$$

but for zenith angle $\theta \in [0, \pi]$:

$$\Omega_{\text{band}} = \iint_{\phi\,\theta} \sin\theta\, d\phi\, d\theta = 2\pi \int_\theta \sin\theta\, d\theta.$$

[157] and has a Gaussian space term and a Gaussian time term:

$$S(t, t_{\text{shift}}, \Delta\Psi, \sigma) = \frac{1}{2\pi\sigma^2}\, e^{-\frac{\Delta\Psi^2}{2\sigma^2}} \cdot \frac{1}{k}\sum_{j=1}^{k} \frac{1}{\sqrt{2\pi}\sigma_j} e^{-\frac{(t-t_{0,j}-t_{\text{shift}})^2}{2\sigma_j^2}}, \tag{4.9}$$

where we have k search windows and each search window is represented by a Gaussian function with index j that is centered at $t_{0,j}$, the center of the window. The Gaussian width is $\sigma_j = \Delta T_j/(2\sqrt{2\ln 2})$ if ΔT_j is the length of the search window and with this definition, the Gaussian corresponding to that window has a FWHM that is equal to ΔT_j. The **search windows are allowed to be shifted** back or forth by a value t_{shift} (negative t_{shift} means shift to earlier time, positive means shift to later time). That means that the original window center $t_{0,j}$ is changed to $t_{0,j} + t_{\text{shift}}$. $\Delta\Psi$, the angular distance between the reconstructed event direction and the source position in the sky, and σ, the angular uncertainty of the event's reconstruction, are the same as discussed above for the time-intergated search.

The signal p.d.f. is normalized in time because each Gaussian time term is normalized and the sum of those Gaussians is divided by the number of Gaussians. It is also normalized in space since the 2D-Gaussian is normalized.[19]

The complete **likelihood** and its dependencies in the time-dependent case, using the p.d.f.s from above, is:

$$\mathscr{L}(n_s, t_{\text{shift}}) = \prod_{i=1}^{N} \left(\frac{n_s}{N}\, S_i\left(t_i, t_{\text{shift}}, \Delta\Psi_i, \sigma_i\right) + \left(1 - \frac{n_s}{N}\right) B_i\left(c_i, a(t_i), \phi_i\right) \right) \tag{4.10}$$

or more concise:

$$\mathscr{L}(n_s, t_{\text{shift}}) = \prod_{i=1}^{N} \left(\frac{n_s}{N}\, S_i\left(t_{\text{shift}}\right) + \left(1 - \frac{n_s}{N}\right) B_i \right) \tag{4.11}$$

All quantities with index i are taken from the individual events and are thus determined. N, the total number of events (in the zenith band), is determined as well. Other quantities (like rates, livetimes, the solid angle of the zenith band) are constant and are not listed as dependencies. There are only two free parameters and those are: n_s, the number of signal events in the sample, and t_{shift}, the time shift of the search windows.

The likelihood is maximized, i.e. $-\log(\mathscr{L})$ is minimized, with respect to the two parameters n_s and t_{shift}. Both of them are limited to certain ranges, for different reasons. t_{shift} is limited to a symmetric interval of a few days, in this case $t_{\text{shift}} \in [-20\,\text{d}, +20\,\text{d}]$. This is part of the hypothesis: We expect a neutrino signal in a physically reasonable time before or after a flare (see section 3.3.3). To remain unbiased, neutrino emission after flares (positive t_{shift}) is also tested, not only before flares, like expected from the phenomenology. n_s is required to be non-negative, so $n_s \in [0, N]$. This choice must not necessarily be made, as a negative number of signal events tells about an under-fluctuation of expected background events. However, there are numerical issues, because e.g. in the case of low statistics it can be $S_i/B_i < 1$ for all events (if there are no events near the source) which leads to a best fit n_s at $-\infty$. The main reason why n_s should not be nega-

[19] To be more precise, the normalization is only exact in a Euclidean space and for integration to infinity. But these subtleties don't affect the method.

tive is, however, that a global maximum of the likelihood at negative n_s can hide a local maximum at positive n_s. Since the analysis is not supposed to find the most significant deviation from the null hypothesis—including a significant *lack* of events—but the most significant *excess* of events, the minimizer is not allowed to find a negative n_s.

Following the general introduction from above, the **test statistic** λ can be defined as:

$$\lambda(\hat{n}_s, \hat{t}_{\text{shift}}) = -2 \cdot \log \left[\frac{\mathscr{L}(n_s = 0)}{\mathscr{L}(\hat{n}_s, \hat{t}_{\text{shift}})} \right] \tag{4.12}$$

In this definition, the sign of the best-fit number of signal events $\hat{n}_s$ has been dropped, since $\hat{n}_s \geq 0$. In the case of $n_s = 0$, only the background p.d.f. contributes to the likelihood, so the background only likelihood does not depend on t_{shift}.

4.2.4 Technical details

Uptime calculation

It is crucial for the time-dependent analysis to know the times when the detector was on (uptime) and when it was off (downtime). Because the data sample is a combined sample consisting of data from two independent detectors, the uptime determination needs to be done for each detector separately. This has been done by scanning all events from reliable detector operation at analysis level 3. The time difference between successive events was calculated for IceCube and for AMANDA, requiring that the event has proper reconstructions (SPE and MPE for IceCube, SPE for AMANDA) and the reconstructions are all upgoing, plus some quality cuts on the AMANDA events to exclude instability periods of the AMANDA detector. The rate using this event selection at level 3 is 5.6 Hz for IceCube and 0.6 Hz for AMANDA which is sufficient for a reliable uptime calculation. The resulting histograms (see fig. 4.24) of the time difference between events were used to decide on a threshold time difference above which a gap is considered to be downtime. The threshold time was estimated to be $\Delta T_{\text{cut}} \sim 4.8$ s for IceCube and $\Delta T_{\text{cut}} \sim 78$ s for AMANDA.

After the gap threshold was found, a histogram with ΔT_{cut} as bin width was created. If at least one event at level 3 occurred during the time corresponding to that bin, it was set to 1 (corresponding to uptime), otherwise it stayed 0 (corresponding to downtime). This produced the intervals of up- and downtime that were used for the analysis. It is slightly less strict than the cut on the time difference implies because it is possible that a gap slightly larger than the cut value causes no downtime if the "phase" of the histogram allows this. Only if the gap is $> 2\Delta T_{\text{cut}}$, a downtime will be guaranteed.

Background Simulation

The generation of random background only samples is necessary to construct a test statistic distribution, from which the significance of the observation is calculated. Background only samples were produced by taking the real data events from the IC40+AMANDA sample and randomizing them in time and space. The "scrambling" of real data is done in order to reduce possible systematic errors of a pure Monte Carlo simulation. As much properties as possible are tried to keep intact, e.g. the zenith and azimuth angle distribution, that depend on the detector geometry, the Earth shielding effect etc. The scrambling

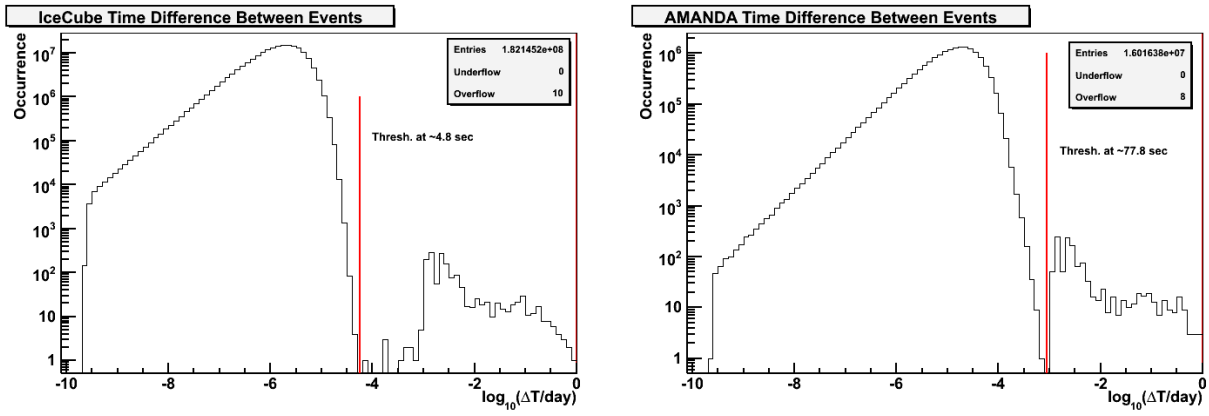

(a) IceCube **(b)** AMANDA

Figure 4.24 Histogram of time difference between successive events. There is an exponential fall of the time difference, until it drops to zero. Larger time differences are very unlikely to occur during detector uptime, so it can be interpreted as a gap due to detector downtime. The cut that decides between up- and downtime is indicated as red line.

was only done for events that have a declination angle within in the declination band of $\pm 5°$ around Cygnus X-3, since only those events are relevant for the search. Cygnus X-3 is at a declination of 40.95°, so the declination band spans from 35.95° to 45.95° declination. The exact simulation procedure was as follows.

- The zenith angle from the event is adopted to keep the original zenith distribution of the events.
- The azimuth angle is adopted as well to keep the original azimuth distribution and account for detector asymmetry: Along some axes of the detector, more modules are lined up than along others. This results in a higher acceptance for particles that travel along the preferred axes and the azimuth distribution reflects this. See fig. 4.25.
- The angular error of the reconstruction (paraboloid sigma) is taken from the event and kept. Because the azimuth is also kept, events going down the longer detector axes, that can be reconstructed better due to the longer lever arm, have a smaller sigma just like in real data.
- The time is drawn from a uniform distribution, since for background, no time dependence of the event rate is expected. The IC40+AMANDA data sample contains mostly upgoing neutrino events, so the seasonal variation of the event rate can be neglected. Fig. 4.26b shows the daily event rates at final level and it is clear that they can be assumed as flat compared with fig. 4.26a. However, there is a change in event rate depending on the status of the AMANDA detector. That is why each event retains its AMANDA status, i.e. an AMANDA on event will be given a uniform random time during the AMANDA on intervals, an AMANDA off event gets a uniform random AMANDA off time. By this procedure, the natural rate difference between AMANDA on and off is reproduced.[20]

[20] See footnote 16.

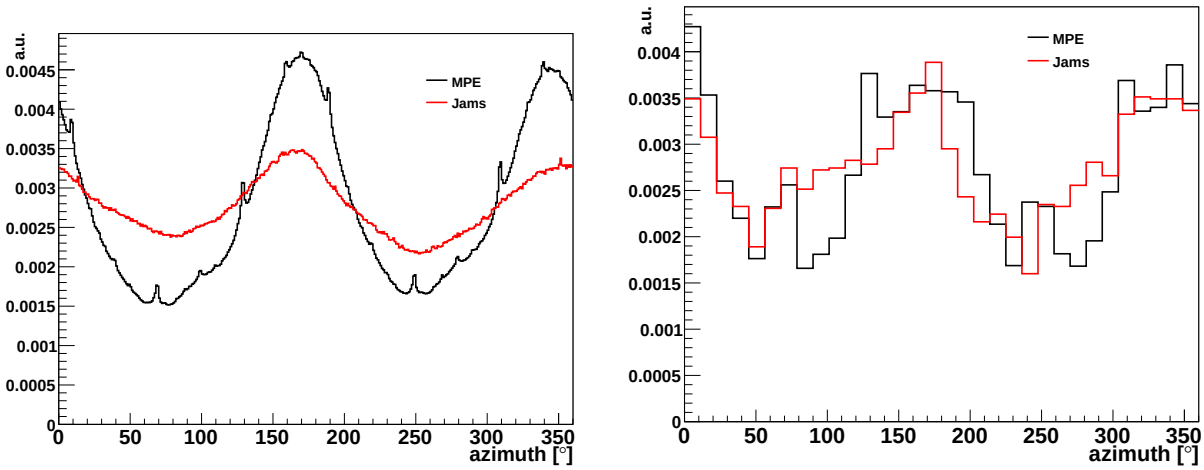

(a) Level 3 **(b)** Final Level

Figure 4.25 Normalized distribution of the reconstructed azimuth angle of the whole sample with MPE (using event information from IceCube only) and Jams SPE reco azimuth (using event information from both detectors). Fig. (a) shows the azimuth distributions at data level 3, fig. (b) is for final level (level 4). The overall sine like behaviour reflects the rectangular shape of the detector (the peaks correspond to the black lines in fig. 2.1). At level 3, six narrow peaks are visible on top of that, representing symmetry axes of the detector that run across many DOMs (the red lines in fig. 2.1). The distributions in (b) are used in the background p.d.f. of the likelihood (see eq. 4.8). The bin width is chosen larger to smooth out random fluctuations due to the small statistics.

- Right ascension and declination are computed from zenith, azimuth and time via coordinate transformation. Thus, even though only the time was randomized, the spatial position is randomized as well since the same azimuth angle will be transformed into a random uniform right ascension.

Signal Simulation

The simulation of signal events is needed in order to derive the test statistic distribution of a certain assumed point source signal. Random signal events were added to a background only sample, according to different flux strengths. The comparison of the background plus signal λ distributions with the background only λ distribution delivers the discovery potential and sensitivity of the analysis (see section 4.2.5).

For the simulation of a time-variable point source, a certain temporal behaviour must be assumed that results in a time p.d.f. that gives the probability to detect an event at a given time. In this analysis, a time p.d.f. was chosen that has the same shape as the time term used in the signal p.d.f. of the likelihood (see eq. 4.9): A normalized Gaussian function $\frac{1}{\sqrt{2\pi}\sigma} e^{-\frac{(t-t_0)^2}{2\sigma^2}}$ that has a FWHM that corresponds to the search window length ($\sim$12 days for a typical window). A real flare might be much narrower: The radio flares show an average FWHM of $2\sigma\sqrt{2\ln 2} = 2.73$ days with $\sigma = 1.16$ days (see eq. 4.1), so that in this case the discovery potential would be better. The signal was centered at minus 5 days relative to the search window center to test if the window is shifted correctly, see fig. 4.27.

Signal simulation is more complicated than background simulation and was performed as follows (see fig. 4.29 for an example of a simulated dataset):

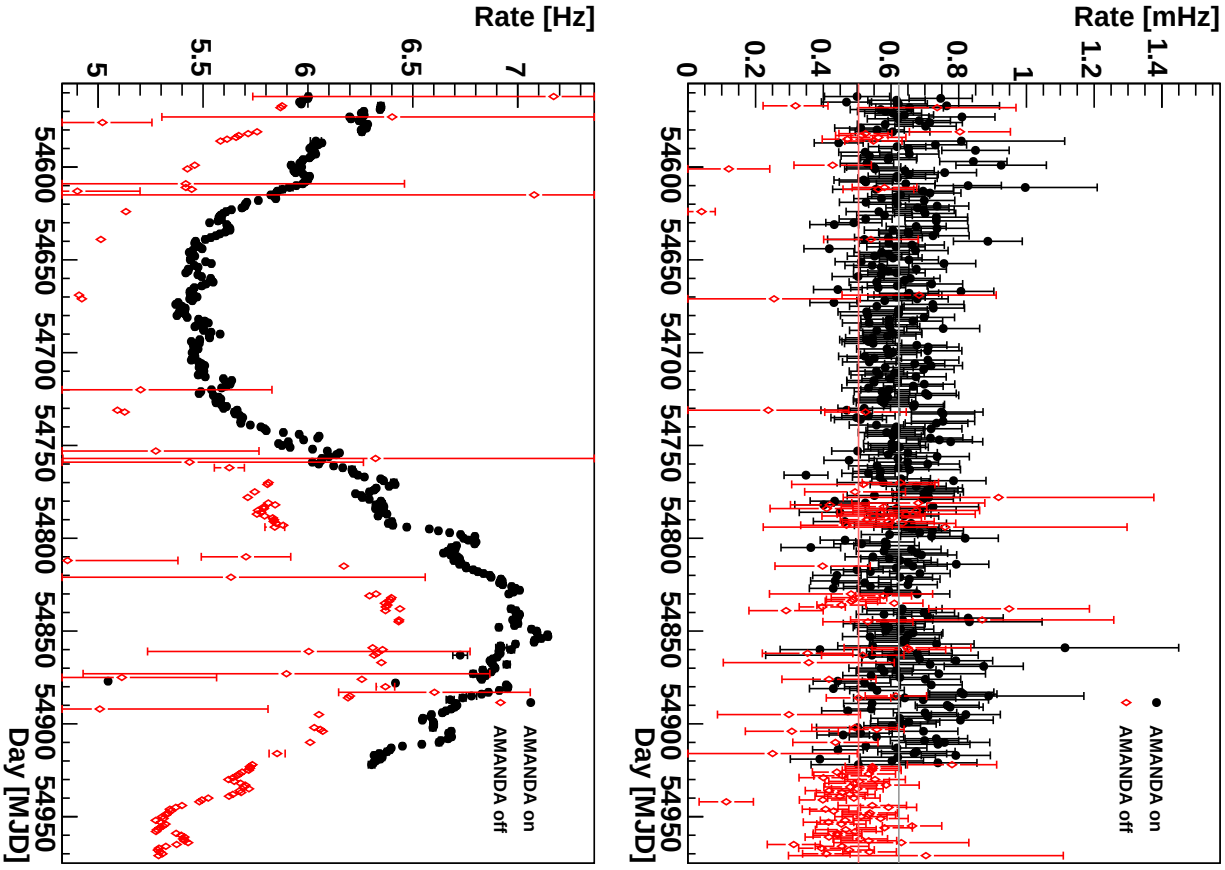

(a) Level 3 **(b)** Final Level

Figure 4.26 Daily event rates in the final sample for AMANDA on intervals (black) and AMANDA off intervals (red). The statistical fluctuation and error of AMANDA off intervals can be very large if the interval was very short, especially at level 3. The seasonal variation of the rate is very clear at level 3, but not visible at final level (level 4), also because only northern sky events were selected. At final level, the average rates for AMANDA on and AMANDA off (used in eq. 4.8) are shown as gray and pink line.

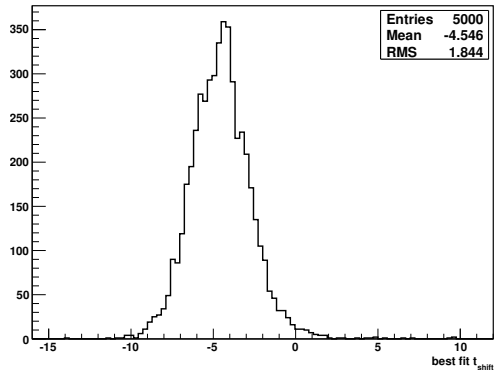

Figure 4.27 Distribution of the best fit value for parameter t_{shift} for window 1 and an allowed window shift of $-20 \ldots 20$ days, from the likelihood maximization on 5000 MC datasets that had a scrambled background and a Poissonian average of 10 signal events following an E^{-2} energy spectrum inserted at -5 days. The slight irregularity is probably owing to the low statistics.

- To account for **rate changes**, the time p.d.f. is multiplied with a time series of the event rate, that was scaled so that its average value is 1. A higher than average rate results in a scale factor >1, lower than average in a factor <1. At times when AMANDA was on, the time p.d.f. is up-scaled and when it was off, it is down-scaled. When the detector was off completely it is zero.

- To account for **detector asymmetry**, the time p.d.f. is multiplied with a time series of the source's azimuth weight. The azimuth distribution is not flat and with the rotation of the earth, the source's azimuth angle changes continuously. At certain azimuth angles, detection of neutrinos from the source will be more likely, at others less. The azimuth distribution used is obtained from MC simulation (processed to final level), SPE and MPE azimuths are merged into one distribution. The resulting time p.d.f. has a quite detailed structure and an example is shown in fig. 4.28.

- Via a loop over the MC events (that are reweighted to correspond to the desired energy spectrum and flux strength), a certain flux is converted into a number of signal events: Each event's probability is compared to a uniform random number between 0 and 1. If the number is smaller than the probability, then the event is selected. The number of signal events obtained is what would be expected from a constant flux during full operation time.

- The time p.d.f. is integrated numerically. If it were a pure Gaussian, its integral would be 1. The value of its integral may be larger or smaller than 1 (because the Gaussian is up- and downscaled at times) and is used to rescale the estimated number of signal events. This is needed to account e.g. for a possible large fraction of detector downtime near the time of the signal center or a higher than average fraction of AMANDA on livetime.

- According to the rescaled number of signal events, random event times are drawn from the time p.d.f. Each time it is checked if this is an event during AMANDA on or AMANDA off time.

- A set of MC events that might occur during AMANDA on and one of events that might occur during AMANDA off is constructed. The events are present in the correct ratios, i.e. more events with high probability will be present and fewer events with low probability. From this pool of AMANDA on and AMANDA off events, one MC event is chosen randomly for each random event time.

- The declination of each chosen MC event is the source declination plus the MC event's reconstructed zenith minus the MC event's true zenith. The right ascension is chosen analogously with the source r.a. and the MC azimuth angles. Thus, the detector PSF is applied to the point source signal. The angular resolution (paraboloid sigma) is taken from the MC event.

- Zenith and azimuth are computed from decl., r.a. and time via coordinate transformation.

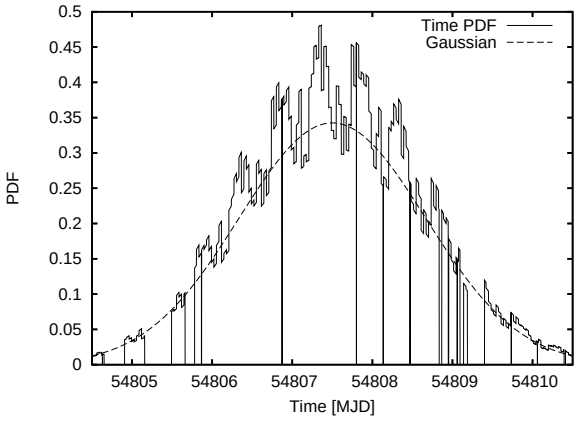

Figure 4.28 Example of how the time p.d.f. used for simulating signal event times can look like. The Gaussian distribution function that is used for construction is plotted for comparison. A drop to zero means that the detector was not operating at that time. General large up- or downscaling is due to AMANDA on or off. Smaller scale structure comes from the azimuth distribution that is mapped on the Gaussian as the source position moves across the sky and changes its azimuth angle.

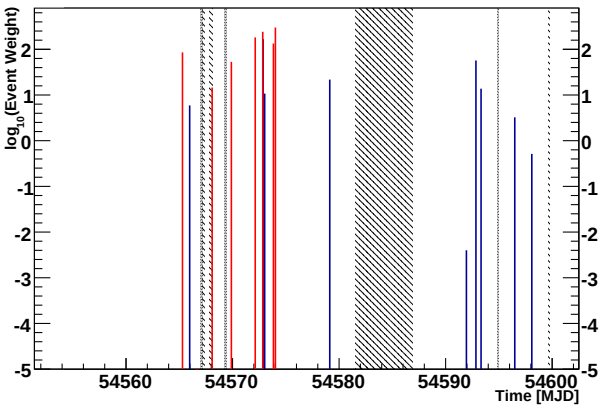

Figure 4.29 Arbitrarily selected simulation of events within 7° to the Cygnus X-3 position. The lines indicate the time of the event detection. Background events have blue lines, signal events red lines. The line height corresponds to the spatial term in the signal p.d.f. that is used in the likelihood (see eq. 4.9). Periods when AMANDA was off (but IceCube on) are shown as hatched areas. Periods when both detectors were off are shown as dotted areas.

Likelihood maximization

For practical reasons, not the likelihood $\mathscr{L}$ is maximized, but $-\log(\mathscr{L})$ is minimized (see section 4.2.3). The Minuit package [176] in the version that comes with ROOT is used as minimizer. The likelihood depends on the two parameters n_s and t_{shift} that are varied to find the function minimum and are restricted to some lower and upper limit. Fig. 4.30 shows an example of the $-\log(\mathscr{L})$ likelihood function as two-dimensional function. The minimizer needs initial guesses for the fit parameters. If these initial guesses are very far from the global minimum, the minimizer can get stuck in a local minimum. This is especially a problem when a box shaped[21] time term is used in the signal p.d.f. of the likelihood, because of the abrupt changes of the function that cause the minimizer to get stuck at a fast rising function "wall". The more stable numerical behaviour during minimization was one of the reasons why it was decided to use a Gaussian shaped time term, not a box. However, even with a smooth likelihood, the minimizer can return parameters that are slightly off the true minimum. This is why an algorithm was used that includes **scanning of the parameter space** to find initial values and verify the result of Minuit. A parameter scan at constant $n_s = 2$ with varying t_{shift} returns the initial guess for t_{shift} (called `seed1`) which yields the minimal likelihood during the scan. Then, a first Minuit minimization is done with $n_s = 2$ and $t_{\text{shift}} =$ `seed1` as initial values which returns a best fit n_s at which another scan is performed. Further minimizations with improved start values are initiated if the seed has changed or if there is a disrepancy between the seed and the best fit value. The full algorithm is outlined in fig. 4.31 and produced reliable minimization in $\sim$200 cases checked by eye.

[21] Box means in this case a function that is 0 outside of the search window and constant inside.

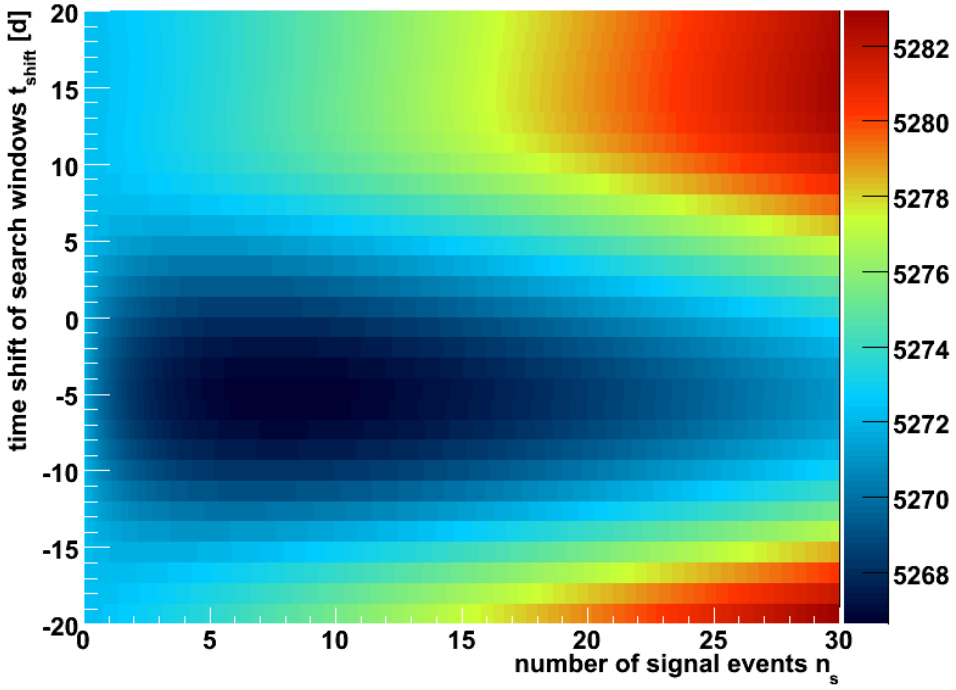

Figure 4.30 Example of the likelihood function, or more precisely $-\log(\mathscr{L})$, evaluated for a sample with scrambled background events and 8 inserted signal events following an E^{-3} spectrum. The signal events were placed according to a time distribution that is like the search time distribution, but shifted -5 days in time. The minimum of the function lies around the same parameter values: $n_s \approx 8$ and $t_{\text{shift}} \approx -5$.

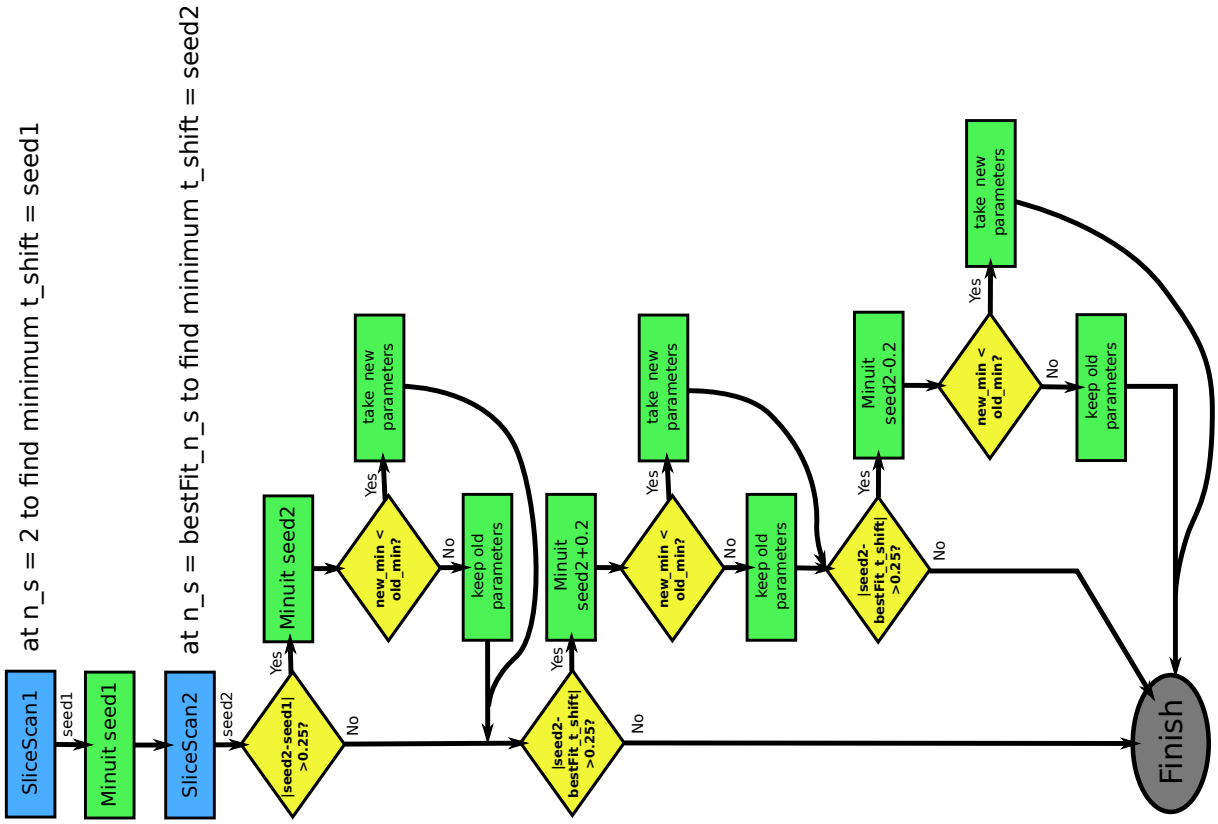

Figure 4.31 Algorithm used to find the minimum of $-\log(\mathscr{L})$ involving scanning of parameter space (`SliceScan1` and `SliceScan2`) and Minuit. Each scanning (step size 0.5 days of t_{shift} at constant n_s) returns the value of t_{shift} that yields a minimal likelihood (`seed1` and `seed2`). This is used as start value of the Minuit minimizations. In case of discrepancies, minimization is redone with different seed.

4.2.5 Discovery potentials and sensitivities

Applying the unbinned likelihood method (see section 4.2.3) to a large set of simulated or randomized data sets (see section 4.2.4), distributions for the test statistic λ can be calculated. From the comparison of the λ distribution for the background only case with those for simulated signal cases, the discovery potential is obtained. See fig. 4.32 and fig. 4.33 for plots of a background only test statistic distribution and a few background plus signal distributions.

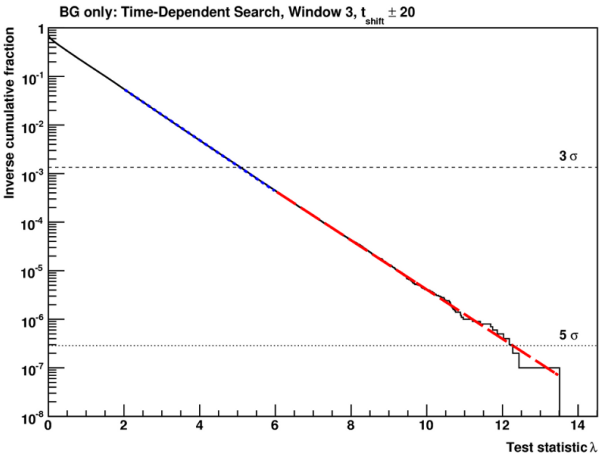

Figure 4.32 Background only test statistic distribution (with 10^7 entries) in "inverse" cumulative presentation, i.e. it shows the value of the integral over the normalized λ distribution, integrating from right to left. This is for search window 3 and t_{shift} between -20 d and 20 d. The threshold on lambda is found at the point where the shown histogram reaches the specific p-value threshold ($\approx 1.3{\cdot}10^{-3}$ for 3σ and $\approx 2.9{\cdot}10^{-7}$ for 5σ in this case), indicated as dashed/dotted horizontal line. Exponential fits to the histogram are performed to obtain the 3σ threshold (blue dashed line) and the 5σ (red dashed line).

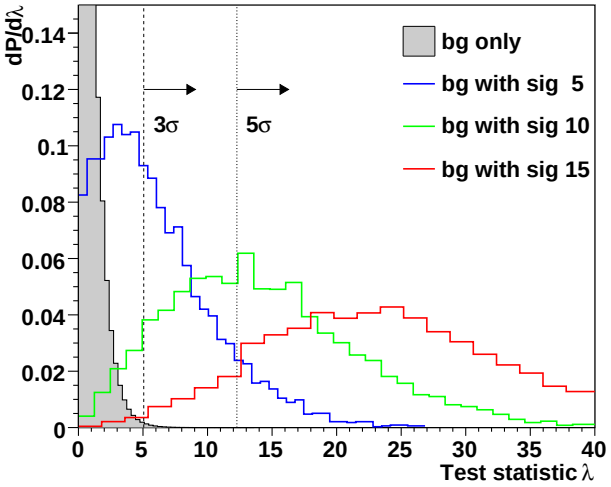

Figure 4.33 Test statistic distributions in comparison. These are for search window 3 and t_{shift} between -20 days and 20 days. Distributions for background only case (10^7 entries) and background plus injected signal (5000 entries) for different signal strengths are shown and the threshold for 3σ and 5σ is plotted. The signal is assumed to have an E^{-3} energy spectrum (without cut-off). Signal strength is given in the legend in units 10^{-11} TeV^2 cm^{-2} s^{-1} sr^{-1}.

The procedure to **calculate the discovery potential** is the following: From the background-only lambda distribution, a threshold on λ—corresponding to the desired significance—is calculated which is the starting point of an integral over the distribution whose value equals the desired p-value threshold.[22] Fig. 4.32 shows an example in which the significance threshold on λ is visible. For a detection, we require the p-value that we get from the data analysis to be smaller than the threshold p-value, i.e. λ is required to be larger than the threshold. This means that the integral of a signal lambda distribution from the λ threshold to the right is the probability that the experiment results in a detection. After the calculation of the detection probability for various signal flux strengths, *the discovery potential is easily obtained as the signal flux required for a detection prob-*

[22] The p-value for a given test statistic λ_{obs} is the probability that in background only case (the null hypothesis), a test statistic as incompatible or more incompatible as λ_{obs} occurs. In our case: the probability for $\lambda \geq \lambda_{\text{obs}}$. Significance and p-value can be converted into each other via the normal distribution. E.g. a 5σ significance corresponds to a one-sided p-value of $\approx 2.87 \cdot 10^{-7}$.

ability of 50%. In other words, the flux whose median λ lies at the λ threshold is the discovery potential. See fig. 4.33 and 4.34 for illustrations.

A similar, yet different, quantity is the **sensitivity**. In this work, sensitivity is defined as the flux required to obtain a test statistic value greater than the median background only value in 90% of experimental trials, also called *90% median sensitivity or Neyman sensitivity.* Fig. 4.35 shows an example of the probability to get a $\lambda > \lambda_{\text{median}}$ for different flux strengths where the sensitivity is the flux that gives a probability of 0.9.

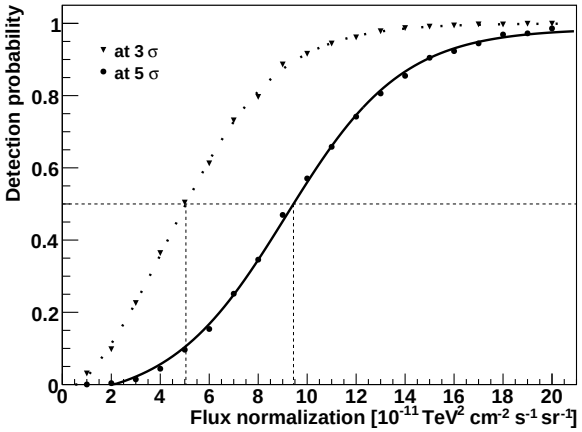

Figure 4.34 Detection probability as function of simulated signal flux for an E^{-3} spectrum. The signal was inserted 5 days before the center of window 3 and the window allowed to be shifted within −20 and 20 days. The points were fitted with a curve to interpolate to the flux that gives a probability of 0.5 (the discovery potential).

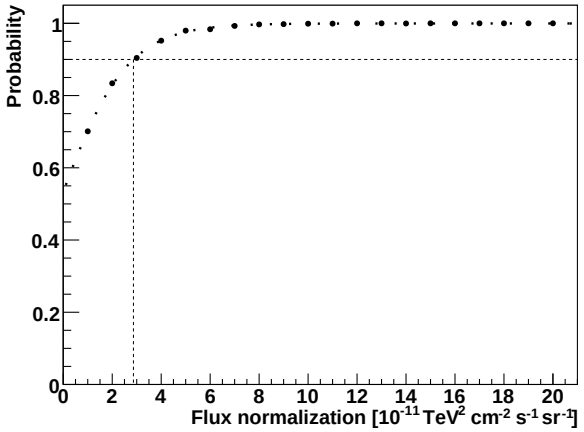

Figure 4.35 Probability for $\lambda > \lambda_{\text{median}}$ as function of simulated signal flux for an E^{-3} spectrum. Like in fig. 4.34, this is for window 3. The points were fitted with the same curve used in fig. 4.34 whose function was inverted to get the flux that yields a probability of 0.9 (the sensitivity).

For the calculation of the discovery potentials and sensitivities, the background only lambda distribution was calculated with 10^7 MC experiments. Such a high number is needed to get a good estimate of the 5σ threshold.[23] Background plus signal distributions were calculated for several flux strengths with 5000 trials each. The calculation was performed for each window separately as well as for all windows together. The signal was injected with a time distribution that equals the time term in the likelihood, only shifted 5 days to the left of the window center. For all windows together, one flare was put at each window, so four flares in total. Otherwise, one flare was injected at the window. All numbers were calculated for t_{shift} within $-20 \ldots 20$ days and for comparison also for the time shift within $-10 \ldots 10$ days to see if the improvement of the discovery potential legitimates a shorter time scale.

Discovery potential and sensitivity were calculated in terms of signal flux strength and in terms of Poissonian mean number of signal events. The calculated signal flux (units $\frac{\text{particles}}{\text{cm}^2\,\text{s}}$) is actually the equivalent flux of a steady point source producing the same number of events. So the fluence (flux integrated over time, units $\frac{\text{particles}}{\text{cm}^2}$) of a steady source emitting during the entire detector operation was put into the window. The actual flux is higher, since the same fluence occurs during a shorter time. But, for easier comparison

[23] The 5σ p-value is $p \approx 2.87 \cdot 10^{-7}$, so only in one out of $1/p \approx 3.5 \cdot 10^6$ trials, a test statistic value that large or larger occurs in the background only case.

with time-independent analyses, the discovery potential is not given in fluence, but in equivalent steady flux. Detector operation went from MJD 54562.37 to MJD 54971.15, so the given flux numbers can be multiplied with a factor of $35,318,369\,\mathrm{sec} \approx 408.78\,\mathrm{days}$ to be converted to fluence. The numbers presented as flux in tables 4.5 and 4.6 are the normalization constant $\Phi_0 = E^\gamma\, d\Phi/dE$ of the differential muon neutrino flux $d\Phi/dE = \Phi_0\, E^{-\gamma}$. The units of $d\Phi/dE$ are $\mathrm{TeV}^{-1}\,\mathrm{cm}^{-2}\,\mathrm{s}^{-1}\,\mathrm{sr}^{-1}$ and the energy E is given in TeV. So, Φ_0 has units $\mathrm{TeV}^{\gamma-1}\,\mathrm{cm}^{-2}\,\mathrm{s}^{-1}\,\mathrm{sr}^{-1}$, i.e. $\mathrm{TeV}^2\,\mathrm{cm}^{-2}\,\mathrm{s}^{-1}\,\mathrm{sr}^{-1}$ for an E^{-3} spectrum and $\mathrm{TeV}\,\mathrm{cm}^{-2}\,\mathrm{s}^{-1}\,\mathrm{sr}^{-1}$ for an E^{-2} spectrum.

Table 4.5 lists the discovery potentials and sensitivities calculated for a signal neutrino energy spectrum $\propto E^{-3}$. The tabulated numbers are also visualized in a plot in fig. 4.36. On average, 46.3% of the flux in the time-integrated search is needed for a 5σ discovery with the time-dependent search and a window shift up to ± 20 days. Shifting the window up to ± 10 days, 45% of time-integrated flux is needed on average. The flux for a 5σ discovery lies in the range of $10^{-10}\,\mathrm{TeV}^2\,\mathrm{cm}^{-2}\,\mathrm{s}^{-1}\,\mathrm{sr}^{-1}$ for E^{-3}. Table 4.6 lists the same things for a spectrum $\propto E^{-2}$. The tabulated numbers are also visualized in fig. 4.37. On average, 50.3% of the flux in the time-integrated search is needed for a 5σ discovery with the time-dependent search and a window shift up to ± 20 days. Shifting the window up to ± 10 days, 49% of time-integrated flux is needed on average. The flux for 5σ lies in the range of $10^{-11}\,\mathrm{TeV}\,\mathrm{cm}^{-2}\,\mathrm{s}^{-1}\,\mathrm{sr}^{-1}$ for E^{-2}.

The gain in discovery potential, narrowing the shift range from ± 20 to ± 10 days, is only $< 3\%$. This is not enough to justify a shift range smaller than ± 20 days, since this is the time scale that is motivated from phenomenology (see section 3.3.3). Furthermore, using the larger time scale reduces model-dependence. This is why it was decided to use the ± 20 days range for the window shift.

The paramaters of this analysis have not been optimized in order to get the best possible discovery potential or sensitivity. Nevertheless, the performance is still better than a time-independent search by a factor of ~ 2. Also compared to related analyses, e.g. the IceCube 40-strings microquasar periodicity analysis (see section 3.4), discovery potential and sensitivity look very acceptable. The periodicity analysis needs between ~ 6.6 and more than 12 events for a 5σ discovery from Cyg X-3, depending on the width of the neutrino signal with respect to the orbital period [177]. For an assumed E^{-2} signal spectrum, the analysis described here needs roughly 8 events for a discovery, which is a discovery potential that the periodiciy analysis would achieve for a signal width of 5% of the orbital period (~ 15 minutes).

An advantage of this analysis is that the hypothesis is defined by physics assumptions and the phenomenology of Cyg X-3, so that it can be used to test these assumptions. An additional information about the lag between a possible neutrino signal and the radio flaring will be obtained as well, constrained by a physically reasonable time scale.

This analysis consists of five searches: one search on each of the 4 windows separately and one using all windows simultaneously. For each search, it is shown (see above) that the discovery potential is better than in the time-integrated search, given the signal lies within the range of the search window shift and has the width of the window or narrower. The analysis was developed for blind data from the IceCube 40-strings configuration and the AMANDA detector. These data have been unblinded to apply the analysis to them. The results of the unblinding are presented in chapter 5.

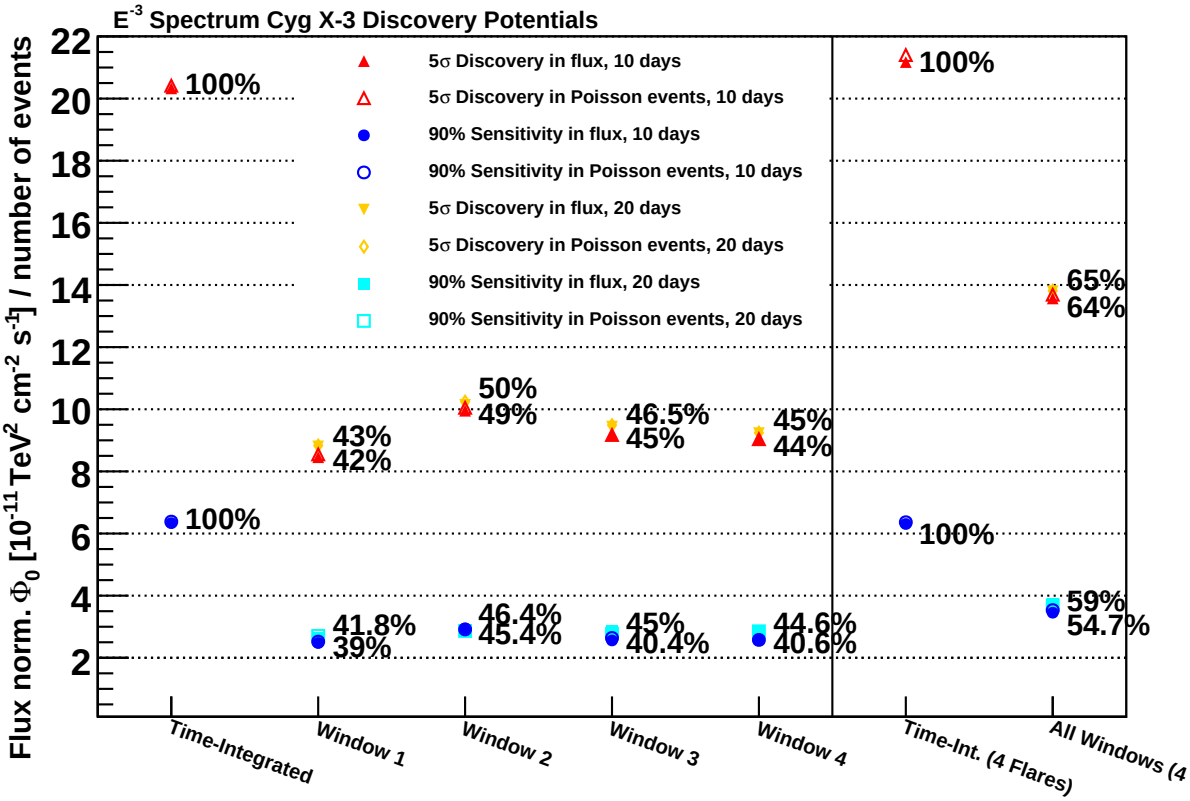

Figure 4.36 Visualization of the discovery potentials and sensitivities for an E^{-3} signal spectrum.

.

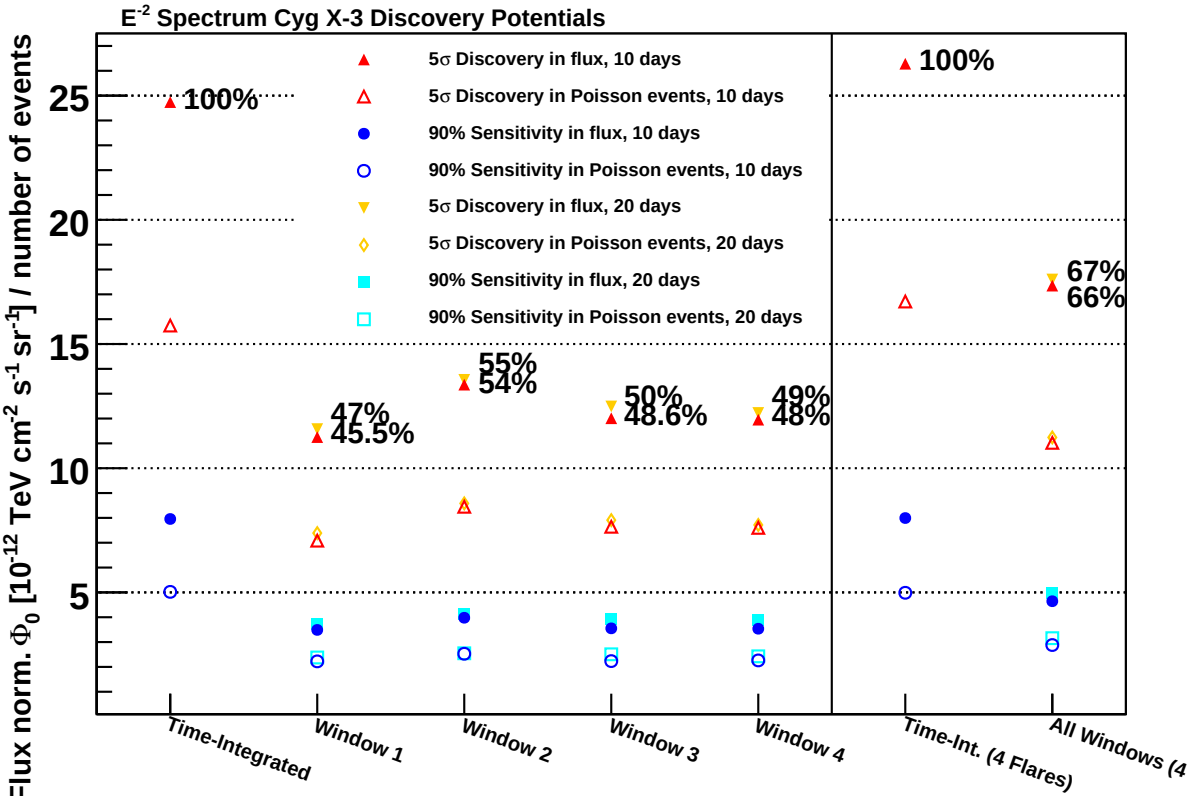

Figure 4.37 Visualization of the discovery potentials and sensitivities for an E^{-2} signal spectrum.

.

E^{-3} spectrum:

Flux normalization Φ_0:

Search	**3σ Disc. Pot.** $[\mathbf{TeV^2\,cm^{-2}\,s^{-1}\,sr^{-1}}]$	**R.**	**5σ Disc. Pot.** $[\mathbf{TeV^2\,cm^{-2}\,s^{-1}\,sr^{-1}}]$	**R.**	**Med. Sens.** $[\mathbf{TeV^2\,cm^{-2}\,s^{-1}\,sr^{-1}}]$	**R.**
Time-Integr. 1 Flare	$11.24 \cdot 10^{-11}$	1.000	$20.33 \cdot 10^{-11}$	1.000	$6.33 \cdot 10^{-11}$	1.000
Window 1 ±20 days	$4.67 \cdot 10^{-11}$	0.415	$8.80 \cdot 10^{-11}$	0.433	$2.65 \cdot 10^{-11}$	0.418
Window 2 ±20 days	$5.53 \cdot 10^{-11}$	0.492	$10.14 \cdot 10^{-11}$	0.499	$2.88 \cdot 10^{-11}$	0.454
Window 3 ±20 days	$5.05 \cdot 10^{-11}$	0.449	$9.44 \cdot 10^{-11}$	0.464	$2.86 \cdot 10^{-11}$	0.451
Window 4 ±20 days	$4.91 \cdot 10^{-11}$	0.437	$9.23 \cdot 10^{-11}$	0.454	$2.83 \cdot 10^{-11}$	0.446
Window 1 ±10 days	$4.39 \cdot 10^{-11}$	0.391	$8.46 \cdot 10^{-11}$	0.416	$2.48 \cdot 10^{-11}$	0.391
Window 2 ±10 days	$5.26 \cdot 10^{-11}$	0.468	$9.95 \cdot 10^{-11}$	0.490	$2.94 \cdot 10^{-11}$	0.464
Window 3 ±10 days	$4.67 \cdot 10^{-11}$	0.416	$9.18 \cdot 10^{-11}$	0.451	$2.56 \cdot 10^{-11}$	0.404
Window 4 ±10 days	$4.64 \cdot 10^{-11}$	0.413	$9.02 \cdot 10^{-11}$	0.444	$2.57 \cdot 10^{-11}$	0.406
Time-Integr. 4 Flares	$11.58 \cdot 10^{-11}$	1.000	$21.18 \cdot 10^{-11}$	1.000	$6.31 \cdot 10^{-11}$	1.000
All Windows ±20 days	$7.43 \cdot 10^{-11}$	0.641	$13.80 \cdot 10^{-11}$	0.652	$3.72 \cdot 10^{-11}$	0.589
All Windows ±10 days	$7.13 \cdot 10^{-11}$	0.616	$13.57 \cdot 10^{-11}$	0.641	$3.45 \cdot 10^{-11}$	0.547

Poisson mean number of events:

Search	**3σ Disc. Pot.** **[Poisson ev.]**	**R.**	**5σ Disc. Pot.** **[Poisson ev.]**	**R.**	**Med. Sens.** **[Poisson ev.]**	**R.**
Time-Integr. 1 Flare	11.37	1.000	20.41	1.000	6.38	1.000
Window 1 ±20 days	4.71	0.414	8.83	0.433	2.71	0.424
Window 2 ±20 days	5.58	0.491	10.25	0.502	2.86	0.449
Window 3 ±20 days	5.01	0.441	9.49	0.465	2.78	0.435
Window 4 ±20 days	4.98	0.438	9.24	0.453	2.85	0.447
Window 1 ±10 days	4.46	0.392	8.55	0.419	2.52	0.395
Window 2 ±10 days	5.32	0.468	10.05	0.492	2.91	0.457
Window 3 ±10 days	4.70	0.413	9.17	0.449	2.64	0.413
Window 4 ±10 days	4.66	0.410	9.04	0.443	2.58	0.404
Time-Integr. 4 Flares	11.73	1.000	21.40	1.000	6.36	1.000
All Windows ±20 days	7.51	0.640	13.82	0.646	3.69	0.580
All Windows ±10 days	7.14	0.609	13.69	0.640	3.53	0.556

Table 4.5 For an E^{-3} signal spectrum: 50% discovery potential for $3\sigma/5\sigma$ threshold and 90% median sensitivity. *Top:* Flux. *Bottom:* Poisson mean. "R." is the ratio to the time-integrated value for the preceding column. Note that the numbers for 4 injected flares ("Time-Integr. 4 Flares" and "All Windows...") represent the total injected flux, i.e. 4 times the flux injected at each flare.

E^{-2} spectrum:

Flux normalization Φ_0:

Search	**3σ Disc. Pot.** [**TeV cm^{-2} s^{-1} sr^{-1}**]	**R.**	**5σ Disc. Pot.** [**TeV cm^{-2} s^{-1} sr^{-1}**]	**R.**	**Med. Sens.** [**TeV cm^{-2} s^{-1} sr^{-1}**]	**R.**
Time-Integr. 1 Flare	$13.76 \cdot 10^{-12}$	1.000	$24.74 \cdot 10^{-12}$	1.000	$7.96 \cdot 10^{-12}$	1.000
Window 1 ±20 days	$6.08 \cdot 10^{-12}$	0.442	$11.57 \cdot 10^{-12}$	0.468	$3.73 \cdot 10^{-12}$	0.469
Window 2 ±20 days	$7.18 \cdot 10^{-12}$	0.522	$13.56 \cdot 10^{-12}$	0.548	$4.12 \cdot 10^{-12}$	0.518
Window 3 ±20 days	$6.54 \cdot 10^{-12}$	0.476	$12.49 \cdot 10^{-12}$	0.505	$3.93 \cdot 10^{-12}$	0.493
Window 4 ±20 days	$6.40 \cdot 10^{-12}$	0.465	$12.22 \cdot 10^{-12}$	0.494	$3.87 \cdot 10^{-12}$	0.486
Window 1 ±10 days	$5.79 \cdot 10^{-12}$	0.421	$11.25 \cdot 10^{-12}$	0.455	$3.49 \cdot 10^{-12}$	0.439
Window 2 ±10 days	$6.82 \cdot 10^{-12}$	0.495	$13.36 \cdot 10^{-12}$	0.540	$3.98 \cdot 10^{-12}$	0.500
Window 3 ±10 days	$6.05 \cdot 10^{-12}$	0.440	$12.01 \cdot 10^{-12}$	0.486	$3.55 \cdot 10^{-12}$	0.447
Window 4 ±10 days	$6.06 \cdot 10^{-12}$	0.441	$11.95 \cdot 10^{-12}$	0.483	$3.54 \cdot 10^{-12}$	0.445
Time-Integr. 4 Flares	$14.19 \cdot 10^{-12}$	1.000	$26.29 \cdot 10^{-12}$	1.000	$7.99 \cdot 10^{-12}$	1.000
All Windows ±20 days	$9.37 \cdot 10^{-12}$	0.661	$17.60 \cdot 10^{-12}$	0.669	$4.96 \cdot 10^{-12}$	0.620
All Windows ±10 days	$9.03 \cdot 10^{-12}$	0.636	$17.35 \cdot 10^{-12}$	0.660	$4.64 \cdot 10^{-12}$	0.581

Poisson mean number of events:

Search	**3σ Disc. Pot.** [**Poisson ev.**]	**R.**	**5σ Disc. Pot.** [**Poisson ev.**]	**R.**	**Med. Sens.** [**Poisson ev.**]	**R.**
Time-Integr. 1 Flare	8.72	1.000	15.74	1.000	5.02	1.000
Window 1 ±20 days	3.78	0.434	7.39	0.469	2.38	0.474
Window 2 ±20 days	4.48	0.514	8.58	0.545	2.55	0.508
Window 3 ±20 days	4.08	0.468	7.91	0.502	2.51	0.499
Window 4 ±20 days	3.98	0.457	7.71	0.490	2.43	0.483
Window 1 ±10 days	3.63	0.416	7.08	0.450	2.22	0.443
Window 2 ±10 days	4.30	0.493	8.45	0.537	2.53	0.504
Window 3 ±10 days	3.79	0.434	7.64	0.485	2.23	0.445
Window 4 ±10 days	3.82	0.438	7.60	0.483	2.26	0.450
Time-Integr. 4 Flares	8.86	1.000	16.71	1.000	4.98	1.000
All Windows ±20 days	5.87	0.663	11.24	0.673	3.16	0.633
All Windows ±10 days	5.64	0.637	11.02	0.660	2.88	0.578

Table 4.6 For an E^{-2} signal spectrum: 50% discovery potential for $3\sigma/5\sigma$ threshold and 90% median sensitivity. *Top:* Flux. *Bottom:* Poisson mean. "R." is the ratio to the time-integrated value for the preceding column. Note that the numbers for 4 injected flares ("Time-Integr. 4 Flares" and "All Windows...") represent the total injected flux, i.e. 4 times the flux injected at each flare.

CHAPTER V

Results

In chapter 4, the analyses that were performed on the microquasar Cyg X-3 (see chapter 3) have been explained in detail. The main analysis is the one applied to blind data from the IceCube 40-strings and AMANDA detectors. It is employing a time-dependent version of the unbinned method of maximum likelihood. The analysis consists of five separate searches: one search on each of the four interesting periods, called search time windows, that are connected with the state of radio flaring, plus one additional search using all four windows simultaneously.

Performing the search for each window separately has the advantage that different behaviour of the source, for instance different delay between a neutrino flare and a flare seen in radio/X-ray, can be accounted for (see sections 4.2.2 and 3.3.3. Because the searches are five individual hypothesis tests, each of them delivers a separate result that will be presented in this chapter. The final result of the analysis is the best one from the individual searches (see section 5.1).

5.1 Significances

The probability that the observation occurs by chance in case of the null hypothesis is called p-value. It may also be called significance, especially when converted to number of standard deviations using a one-sided tail of a normal distribution.

For each of the five searches that were performed, one p-value was obtained. The smallest one of the five was taken as **final p-value**. Because not only one search (one trial) was made, it was corrected considering the multiple trials via Monte Carlo simulation: Doing 2000 Monte Carlo (MC) experiments with background only sample, each time the smallest p-value was kept. The corrected final p-value is the fraction of MC experiments in which a p-value equal to or smaller than the p-value from the real experiment occurred. Thus, it is the probability of obtaining from a background only sample—just by chance—a result as incompatible or more incompatible with the null hypothesis. The distribution of p-values from MC experiments is shown in fig. 5.2 below.

The smallest p-value came from window 1 and is 22.3% without correction for trials. After correction for trials via the 2000 MC experiments (cf. fig. 5.2), the final p-value becomes $\sim$**57%**. The trial factor that corrects for trials is therefore $\sim$2.6 and significantly lower than the assumed factor of 5, because the trials are not independent from each other. *This is completely compatible with the null hypothesis* that the sample is pure background

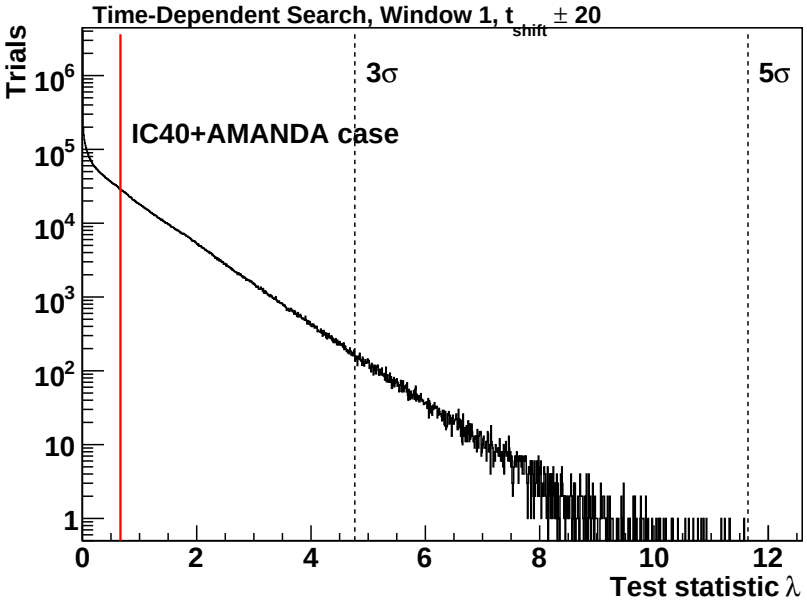

Figure 5.1 Background only test statistic distribution for window 1 with 10^7 entries. The p-value is calculated as value of the integral over the distribution, starting at the observed λ from the analysis (red line).

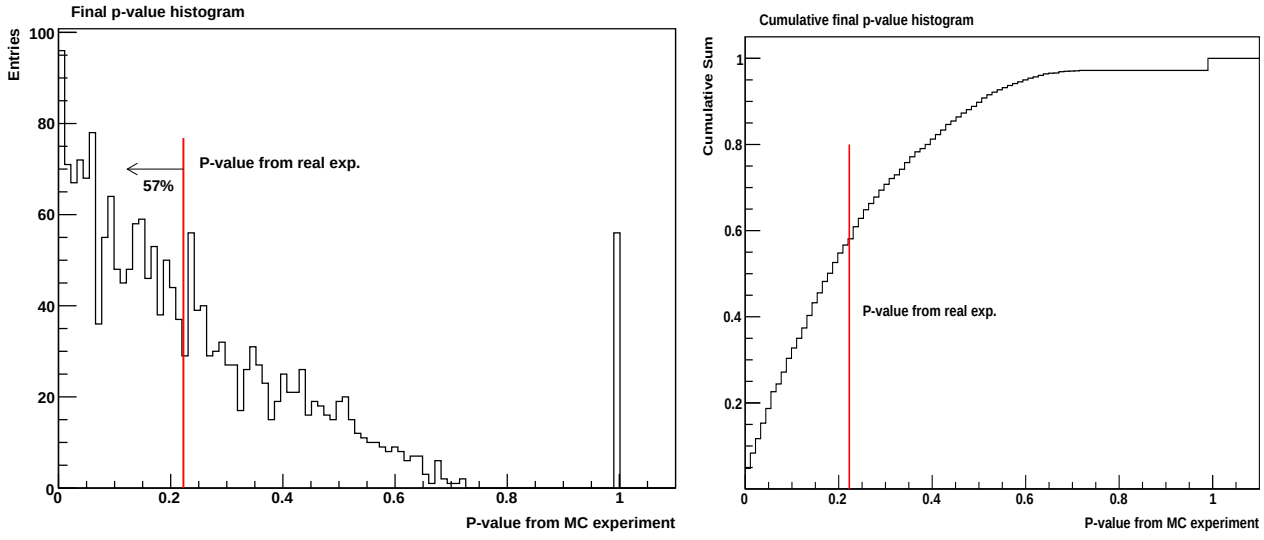

(a) Normal **(b)** Cumulative

Figure 5.2 Distribution of p-values obtained from 2000 MC experiments, each time performing the 5 searches and keeping the smallest p-value. The smallest p-value that occurred in the real experiment (analysis applied to IC40+AMANDA sample) was 22.3% and is shown as red line. *(a)* Integrating to the left starting at the red line gives the trial corrected final p-value. Note that the distribution is evacuated at higher p-values because of the selection of the smallest p-value. *(b)* The trial corrected final p-value can be read off the histogram directly.

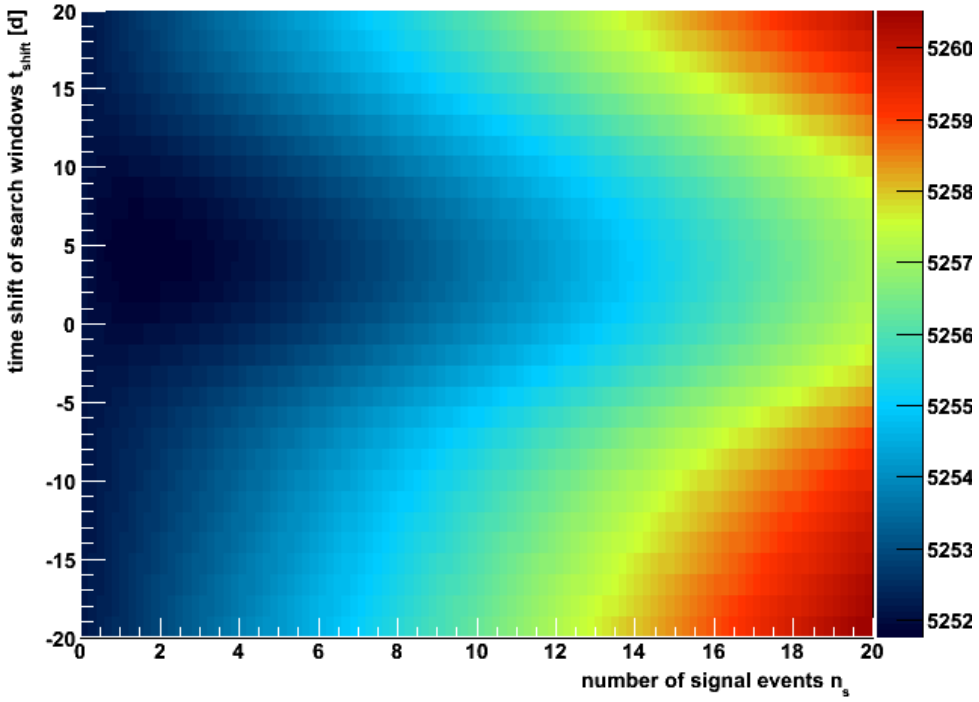

Figure 5.3 Likelihood "landscape" of $-\log(L)$ for window 1 and the unblinded data sample from IC40 and AMANDA. The minimum lies within the dark blue area.

and contains no signal from the Cygnus X-3 position during the time of the search.

The results for each search are summarized in detail in the following table. It shows the best fit values of the two parameters from the likelihood maximization (see section 4.2.3): the number of most likely signal events n_s and the time shift of the respective window(s) t_{shift}. For window 1, the likelihood function $-\log(L)$ is plotted in fig. 5.3 and the minimum is visible as dark blue area at the position of the found parameters. The next column gives the value of the test statistic λ that results from the maximized likelihood, followed by the number of events that lie inside the window boundaries after the shifting. However, also events outside of the boundaries can contribute to the likelihood, because the time p.d.f. corresponding to the window is a Gaussian, that does not drop to zero immediately at the edge of the window. The next column is the number of background events expected to fall into the window on average, obtained from the same 2000 MC experiments that were used to calculate the final p-value, with the standard deviation given behind the plus/minus sign. The last column lists the pre-trial p-value from each window. Fig. 5.1 shows the normalized lambda distribution for window 1 with the observed λ drawn as red line. The p-value follows as integral over the distribution to the right, starting at the red line.

5.2 Upper limits

For each of the five searches, flux upper limits were calculated. The calculation is done under the assumption that there was a neutrino flux with a time behavior like the time term in the signal p.d.f. (see eq. 4.9): a Gaussian shaped emission with FWHM that equals the window duration. The center of the signal p.d.f. was put at the best fit time

Search	$\hat{n}_s$	$\hat{t}_{\text{shift}}$ [d]	λ	Events	Exp. bg. ev.	p-value (pre-trial)
Window 1	1.60	+4.46	0.665	5	2.59 ± 1.34	0.223
Window 2	0.81	-15.05	0.108	5	4.55 ± 1.94	0.424
Window 3	0.94	-0.58	0.382	3	2.98 ± 1.46	0.389
Window 4	0.92	+20.00	0.658	0	3.01 ± 1.48	0.244
All Windows	1.04	+2.05	0.101	12	10.43 ± 3.02	0.507

Table 5.1 Results from the unblinding of the five searches. The columns are: best fit number of obs. signal events n_s, best fit window time shift t_{shift}, test statistic λ, number of events within window boundaries, number of expected background events within window boundaries and the p-value.

shift of the respective window, because the shifted window position catches the most signal-like deviation from a background only sample. So, the calculation puts an upper limit on the most signal-like episode. At the other episodes within the shift range, the signal flux can be excluded even further.

For the calculation of the upper limits, the same signal simulation was used that already served for the calculation of discovery potential and sensitivity. The simulation consists of only muon and anti-muon neutrino events, so the upper limit is set on a muon neutrino flux. The fluence corresponding to a steady point source of a certain flux strength was put into each simulated flare. In table 5.2, the upper limits are given in both the fluence and the equivalent steady flux of a source emitting the same fluence in the whole detector operation time of 408.78 days. What is presented is the normalization constant $\Phi_0 = E^\gamma \, d\Phi/dE$ of the differential flux $d\Phi/dE = \Phi_0 \, E^{-\gamma}$ (or the differential fluence $\int d\Phi/dE \, dt$). See section 4.2.5 for information about the equivalent steady flux, the conversion to fluence and the flux normalization constant Φ_0. The units of the fluence upper limits are the same as for flux, except that the s^{-1} is missing, since fluence is the time-integrated flux.

Upper limits labeled "NP" were calculated in a Neyman-Pearson fashion (similar to the median sensitivity): They correspond to the flux needed to get a λ greater than the observed λ in 90% of cases and represent a 90% confidence level upper limit. Fig. 5.4 demonstrates this upper limit calculation. In addition, upper limits using Feldman-Cousins statistics were calculated, labeled "FC", that were found to be more conservative. The calculation follows the definition in [178] and includes the construction of a confidence belt that represents the confidence interval as function of the test statistic λ. The confidence level (CL) was set to 90% as well and the upper limit is the upper edge of the confidence belt at the position of the observed λ, see fig. 5.5 for the confidence belt of window 1.

The lowest 90% confidence level Feldman-Cousins fluence limits are $2.1 \cdot 10^{-4}$ TeV cm^{-2} for an E^{-2} spectrum (window 3) and $1.43 \cdot 10^{-3}$ TeV cm^{-2} for an E^{-3} spectrum (window 2). The equivalent steady flux, also listed in table 5.2, is actually the average flux over the full detector operation time, given that it follows the Gaussian shape used in the simulation. In other words: The flux on which the limit is set, is close to zero almost all of the time, but much higher than the averaged value during a limited interval (the search window).

Following this reasoning, my upper limits are not capable of constraining the model of Bednarek (2005) (see section 3.4). The quoted flux limits would indeed exclude some of the scenarios presented in Bednarek (2005), but the flux limit during the assumed production of neutrinos is considerably higher. E.g. the peak flux of the Gaussian emission

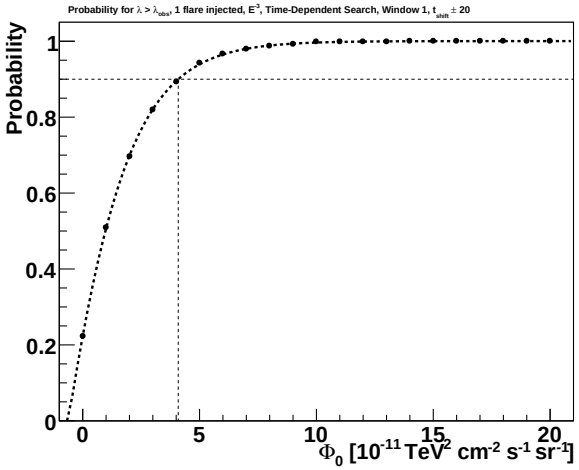

Figure 5.4 Probability to obtain a $\lambda > \lambda_{\text{obs}}$ as function of simulated flux for window 1 and E^{-3} spectrum. The 90% CL upper limit is defined as the flux needed for a probability of 0.9.

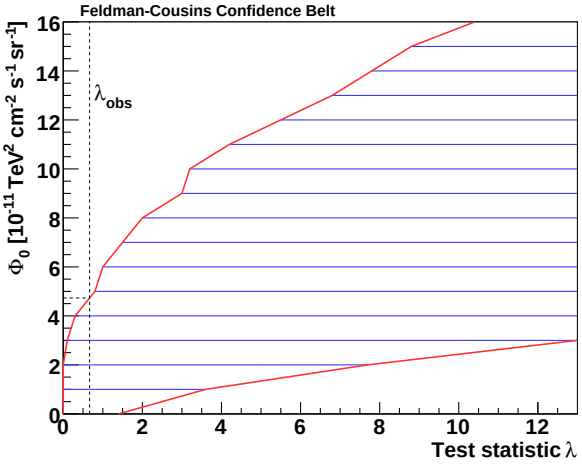

Figure 5.5 The Feldman-Cousins confidence belt (red lines show its boundaries), constructed from the horizontal confidence intervals (blue lines) that are determined via an ordering principle based on likelihood ratios, as defined in [178]. The upper limit is the upper bound of the confidence belt at the observed value of λ. This is for window 1 and an E^{-3} spectrum.

E^{-3} spectrum:

Search	NP Flux [TeV^2 cm^{-2} s^{-1} sr^{-1}]	NP Fluence [TeV^2 cm^{-2} sr^{-1}]	FC Flux [TeV^2 cm^{-2} s^{-1} sr^{-1}]	FC Fluence [TeV^2 cm^{-2} sr^{-1}]
Window 1	$4.09 \cdot 10^{-11}$	$1.44 \cdot 10^{-3}$	$4.73 \cdot 10^{-11}$	$1.67 \cdot 10^{-3}$
Window 2	$3.35 \cdot 10^{-11}$	$1.18 \cdot 10^{-3}$	$4.04 \cdot 10^{-11}$	$1.43 \cdot 10^{-3}$
Window 3	$3.38 \cdot 10^{-11}$	$1.19 \cdot 10^{-3}$	$4.47 \cdot 10^{-11}$	$1.58 \cdot 10^{-3}$
Window 4	$4.44 \cdot 10^{-11}$	$1.57 \cdot 10^{-3}$	$6.07 \cdot 10^{-11}$	$2.14 \cdot 10^{-3}$
All Windows	$3.66 \cdot 10^{-11}$	$1.29 \cdot 10^{-3}$	$5.00 \cdot 10^{-11}$	$1.77 \cdot 10^{-3}$

E^{-2} spectrum:

Search	NP Flux [TeV cm^{-2} s^{-1} sr^{-1}]	NP Fluence [TeV cm^{-2} sr^{-1}]	FC Flux [TeV cm^{-2} s^{-1} sr^{-1}]	FC Fluence [TeV cm^{-2} sr^{-1}]
Window 1	$5.56 \cdot 10^{-12}$	$1.97 \cdot 10^{-4}$	$7.33 \cdot 10^{-12}$	$2.59 \cdot 10^{-4}$
Window 2	$4.65 \cdot 10^{-12}$	$1.64 \cdot 10^{-4}$	$6.04 \cdot 10^{-12}$	$2.13 \cdot 10^{-4}$
Window 3	$4.65 \cdot 10^{-12}$	$1.64 \cdot 10^{-4}$	$5.94 \cdot 10^{-12}$	$2.10 \cdot 10^{-4}$
Window 4	$5.95 \cdot 10^{-12}$	$2.10 \cdot 10^{-4}$	$7.65 \cdot 10^{-12}$	$2.70 \cdot 10^{-4}$
All Windows	$4.82 \cdot 10^{-12}$	$1.70 \cdot 10^{-4}$	$7.00 \cdot 10^{-12}$	$2.47 \cdot 10^{-4}$

Table 5.2 Calculated upper limits for simulated $\nu_\mu + \bar{\nu}_\mu$ E^{-3} spectrum flux (*top*) and simulated ν_μ E^{-2} spectrum flux (*bottom*). "NP" upper limits were calculated with Neyman-Pearson statistics, "FC" upper limits were calculated with Feldman-Cousins statistics. The presented flux is an equivalent steady flux (see text) and was converted into fluence with a factor 35, 318, 369 s (see text and section 4.2.5).

is around 30 times higher than the quoted average flux, except for window 2, where it is only around 17 times higher.[1] This would produce a lowest upper limit of $E^2 d\Phi/dE = 1 \cdot 10^{-10}$ TeV cm^{-2} s^{-1} on peak flux for an E^{-2} spectrum, which is above the limit set by AMANDA-II. This is because the search is not optimized to produce the lowest limits. E.g. because the windows are allowed to be shifted to periods of event clusters, the upper limits naturally come out higher than in a time-integrated search with less degrees of freedom.

5.3 Systematic uncertainties

The upper limits quoted in table 5.2 were calculated without consideration of systematic uncertainties. Sources of systematic error can be grouped into the following categories:

- Uncertainties on the detector response, especially the DOM sensitivity.
- Uncertainties on the ice properties and Cherenkov light propagation.
- Uncertainties on the interaction and propagation of neutrinos and muons.

The effect of these uncertainties on calculated sensitivities or upper limits is not directly visible and can only be estimated with Monte Carlo simulation, varying parameters within their uncertainty intervals. The uncertainties generally depend on neutrino energy and thus on the assumed neutrino energy spectrum. The impact of the main sources of uncertainty on the expected event rate is summarized in table 5.3 for an E^{-2} and E^{-3} spectrum. In this analysis, the background is obtained from the data via scrambling. That is why an uncertainty on the background rate (e.g. an uncertainty of the atmospheric neutrino flux) does not affect the analysis. Only the uncertainty on a signal simulation, that involves simulation of the detector, must be considered. That is why the p-values from section 5.1 do not suffer from systematic uncertainties, only flux upper limits, sensitivities and discovery potentials.

The uncertainties in table 5.3 for an E^{-3} spectrum are presumably slightly smaller[2] for IceCube because of the larger detector size and improved technology [83]. Implementing the systematic error on the number of events in the flux upper limit calculation generally results in a smaller systematic error on the flux limit [83, 179]. So, the error on the upper limits can be estimated to be around $10 - 15\%$ and certainly below 20%.

[1] With a time-variable flux (peak flux f_0) $f(t) = f_0\, e^{-\frac{(t-t_0)^2}{2\sigma^2}}$, fluence F and equivalent steady flux f_{const}:

$$F = \int_{t_i}^{t_e} f(t)\, dt = \sqrt{2\pi}\sigma\, f_0 \stackrel{!}{=} f_{\text{const}} \cdot (t_e - t_i).$$

$\sigma = \Delta T/(2\sqrt{2\ln 2})$ (see eq. 4.9), ΔT is window length and $t_e - t_i$ is 408.78 days. It follows:

$$f_0 = \frac{2(t_e - t_i)}{\Delta T}\sqrt{\frac{\ln 2}{\pi}}$$

[2] Additionally, the estimated error due to the neglected ν-μ angle was for a binned point source search and should be smaller for an unbinned search.

Class	Error source	E^{-2}	E^{-3}
Detector response	Optical module sensitivity	±9%	$^{+5\%}_{-17\%}$
	Optical module time resolution	n/a	±2%
Ice properties	Scattering & absorption coefficient	±11%	±5%
μ and ν interaction	μ energy loss	±8%	±1%
	ν cross-section, rock density		±3%
	ν-μ angle	n/a	$^{+0\%}_{-8\%}$
	Sum	**±16%**	$\mathbf{^{+8\%}_{-20\%}}$

Table 5.3 The impact of main sources of systematic error on the expected event rate. The values are for muon neutrinos. E^{-2} spectrum values were estimated for IceCube 40-strings in [100]. E^{-3} spectrum values were estimated for AMANDA-II in [168]. The "n/a" means that the value is not important or negligible.

5.4 Search windows and event times

Fig. 5.6 shows the position of the shifted windows (dotted area) relative to the original window position (dashed lines) defined in section 4.2.2. The recorded IceCube 40-strings and AMANDA events within 5° from the Cyg X-3 position are plotted as blue lines. The position of the line stands for the time when the event occurred, the height corresponds to its spatial weight (the spatial term used in the signal p.d.f.). The windows are numbered from 1 to 4, chronologically. In the individual searches (fig. 5.6a, Window 1 and 2 were both shifted onto the same set of events that maximized the likelihood function. Window 4 was shifted away from a number of events, towards a single event that was given 100 times more weight and is the most signal-like event with respect to Cyg X-3 in the whole sample. In fig. 5.6b, the same information is given for the collectively shifted windows.

The plots in fig. 5.7 show the individually shifted windows in more detail. Again, blue lines depict the events. On top of the window, the Gaussian time term that corresponds to the window is plotted. The Gaussian is centered on the window and its FWHM equals the duration of the window. The signal p.d.f., used in the likelihood of the analysis, is the product of the spatial term (= line height) and the time term (= value of Gaussian function). During maximization of the likelihood, the algorithm attempts to shift the maximum of the Gaussian (the center of the window) close to high blue lines (events with high signal probability). The exact outcome of the likelihood maximization is a compromise, considering all contributions from all events, and results in the window position that maximizes the signal p.d.f. and thus the likelihood function.

Fig. 5.7d shows again the reason, why window 4 was shifted away from the events that fell inside: The single event that occurred 20 days after the original window ends has a weight that is 100 times bigger than the ones from the other events. Thus, the single event gives a higher signal p.d.f. than all the other events together. The window is shifted up to the allowed maximum of 20 days to come as close to the event as possible and doesn't even reach the event with its boundary. But still, the contribution from the single event is considerably high. That is why window 4 has no event in its boundaries, but still a p-value comparable with the one from window 1 that has 5 events inside. (Note: Some events in the plots are not visible because their weight was too small to fit into

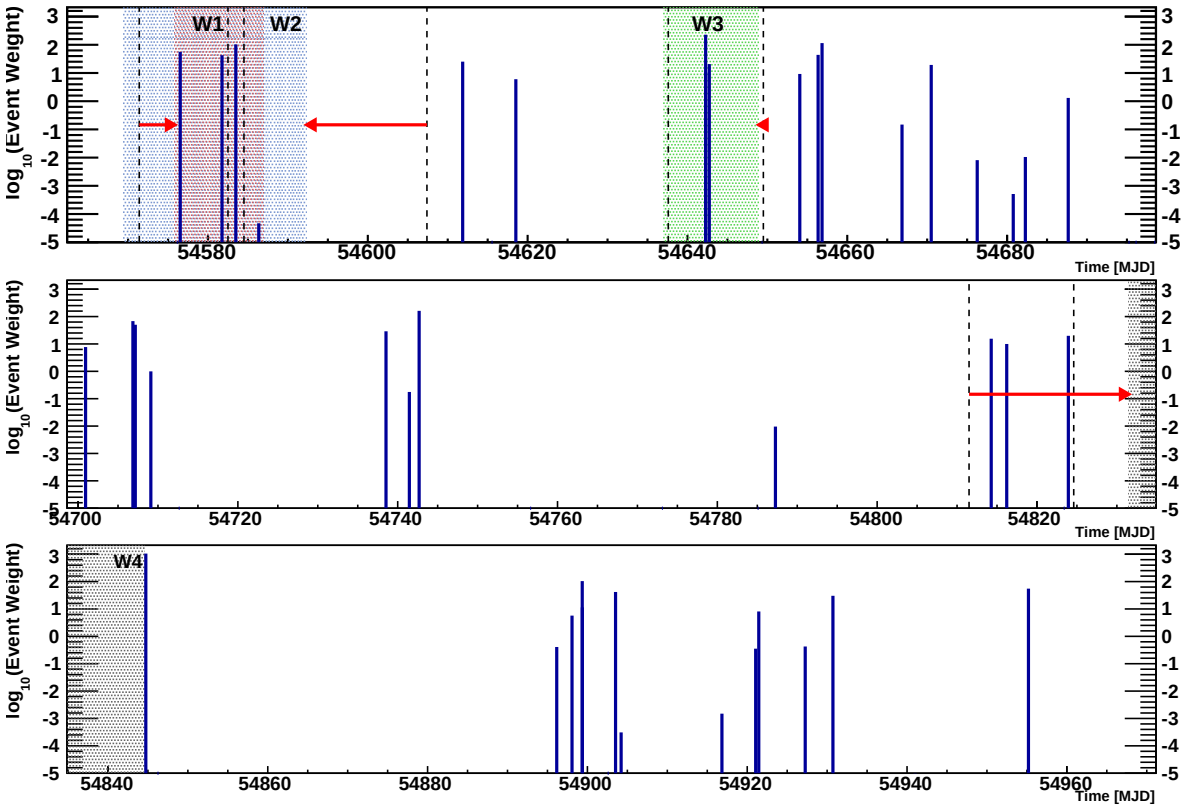

(a) Individual window shift

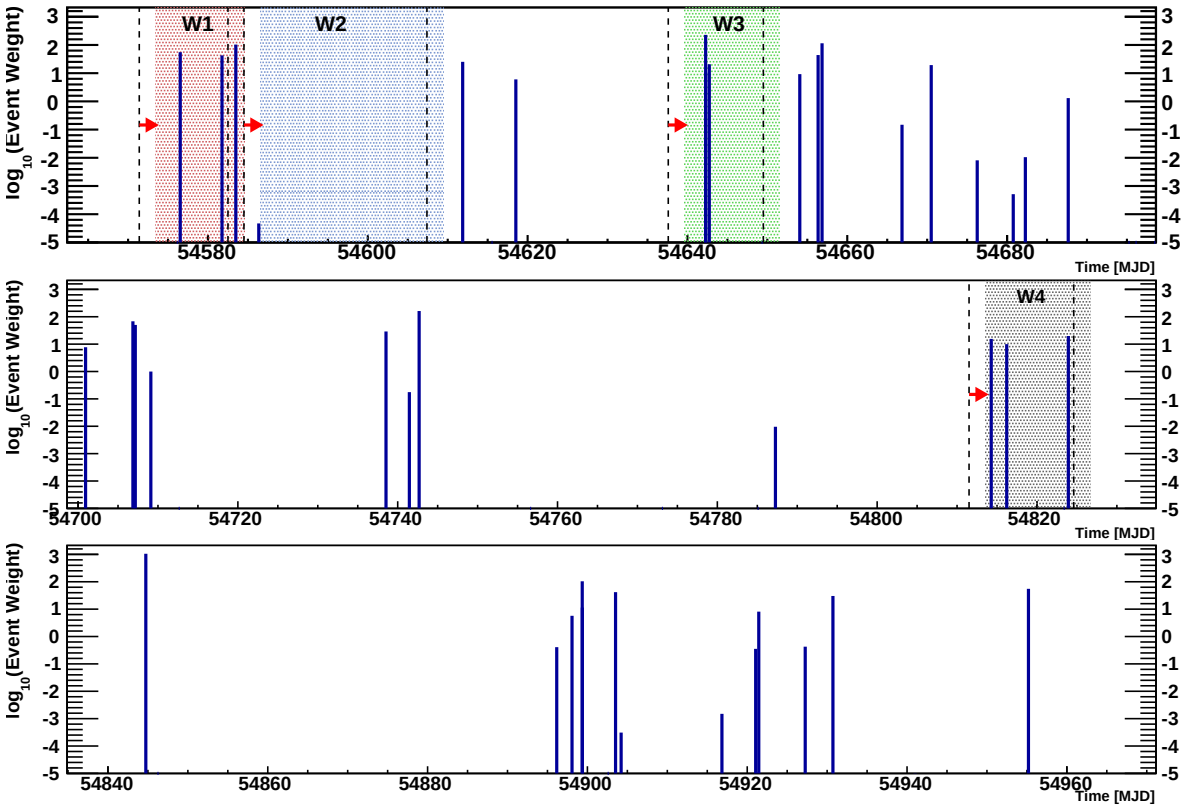

(b) Collective window shift

Figure 5.6 The shifted time windows with respect to the defined window position. Blue lines depict events with the line height corresponding to the $\log_{10}$ of their spatial weight. The original unshifted window position is indicated with dashed lines, the direction and amount of the shifting is indicated with a red arrow and the window after the shifting is the blue dotted area.

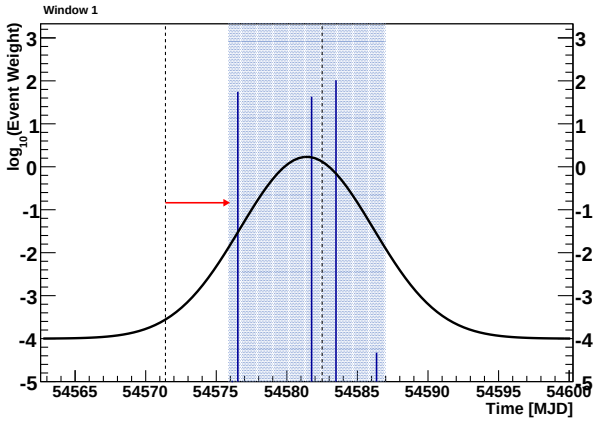

(a) Window 1

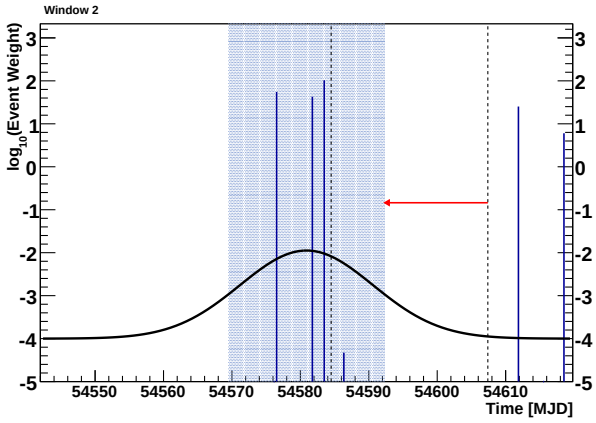

(b) Window 2

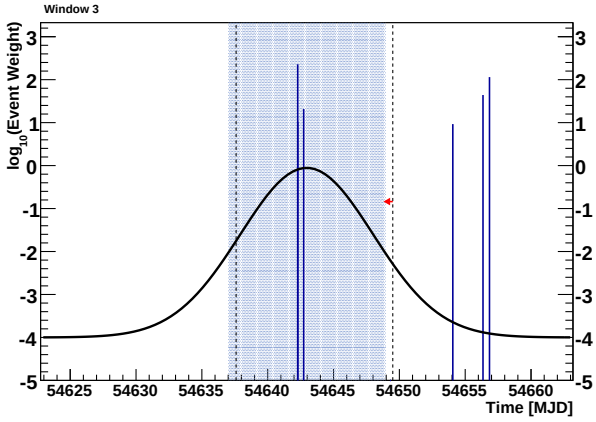

(c) Window 3

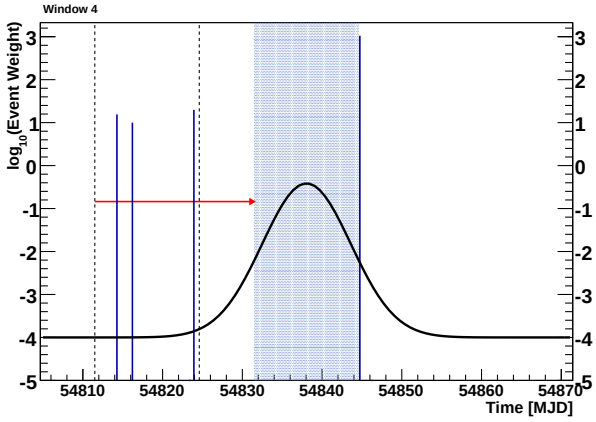

(d) Window 4

Figure 5.7 The individually shifted search windows in more detail. The Gaussian time term is plotted as well. See text for more information.

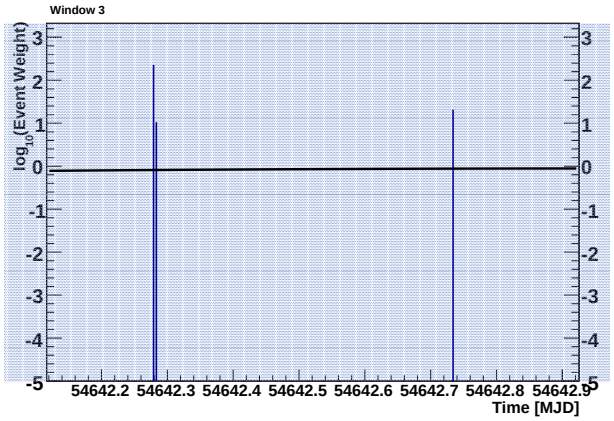

Figure 5.8 Zoomed version of fig. 5.7c (window 3), showing the pair of events close in time, revealing that the number of events in window 3 is three, not two.

the logarithmic scale, i.e. smaller than 10^{-5}. This is why only four events can be seen in window 1 and 2, but the total number is five.)

In window 3 (see fig. 5.7c) something interesting happened: It looks like only two events fall into the window, but it's actually three. Two events followed rather close in time ($\sim$6 minutes) with an angular separation of 1.8°. They blend into a single line in fig. 5.7c, but after zooming into the window, they are resolved as two separate events, shown in fig. 5.8.

5.5 Sky map and event directions

The sky map of the events close to Cyg X-3 is shown in fig. 5.9. There is no significant clustering of events visible at the position of Cyg X-3. There are some event clusterings in the map, but these are expected to occur by chance in a pure background sample. So, also from the spatial distribution of events, everything looks consistent with the background only case.

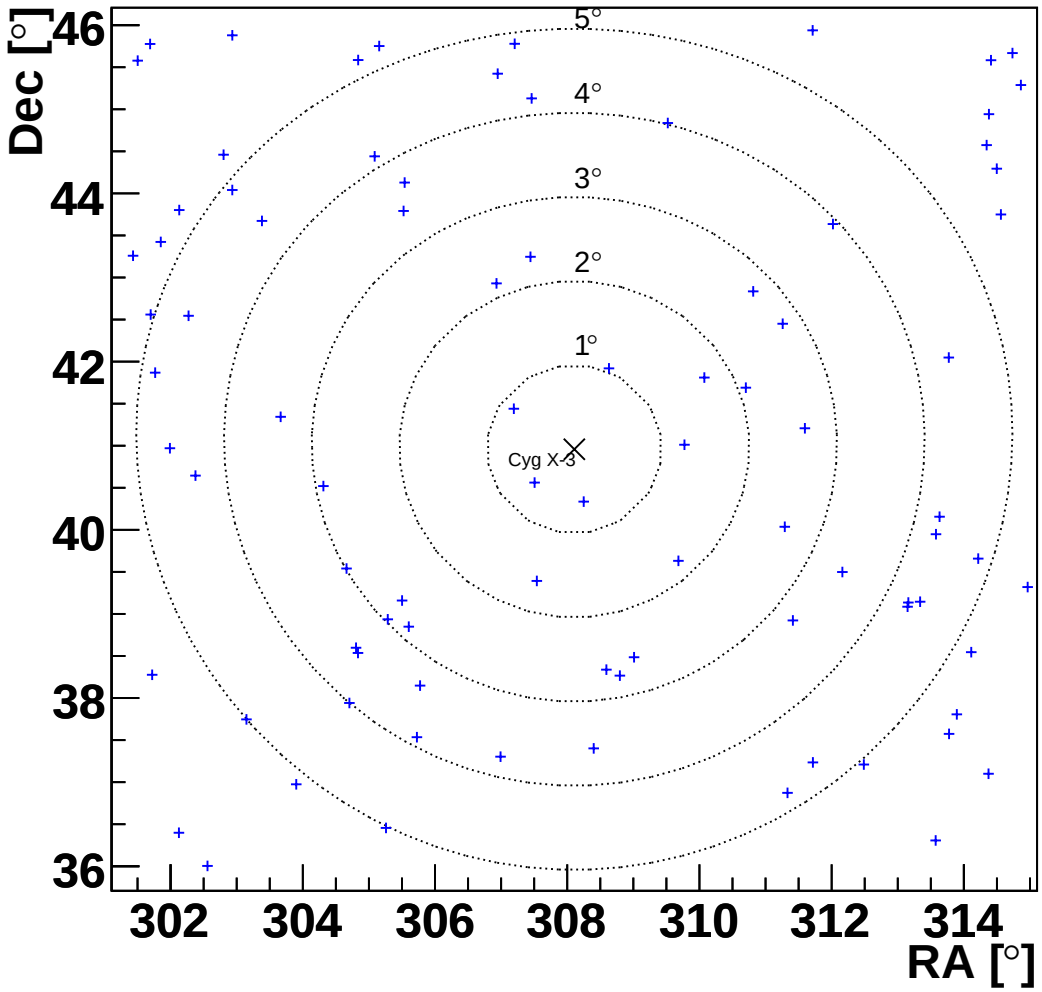

Figure 5.9 Map of the event directions within a 5° radius from Cyg X-3. The assumed position of Cyg X-3 is indicated with a black cross. The reconstructed event directions are plotted as blue plusses. Dotted contours show points of the same angular distance to Cyg X-3, which is printed at each contour.

CHAPTER VI

Summary

In this work, it has been demonstrated that a search for high-energetic astrophysical neutrinos from the microquasar Cygnus X-3 (Cyg X-3) is well motivated because of the evidence for strong particle acceleration and high densities, enabling efficient neutrino production and causing high γ-ray absorption. Previous analyses of neutrino telescope data have not been time-optimized and did not use information about variability of the source.

This is why the phenomenology of Cyg X-3 has been studied in detail. A time-dependent search for astrophysical neutrinos from Cyg X-3 was carried out analyzing data collected with the IceCube and AMANDA neutrino telescopes. It is based on physics assumptions and triggered by multi-wavelength observations of the source that indicate major radio flaring which is connected with particle ejection in form of jets and thus constitutes a period of possible neutrino production. The use of the time information enhances the sensitivity with respect to a time-independent analysis. It further enables to test if the hypothesis of a jet-neutrino connection is correct. Additionally, a time lag of up to 20 days between radio flare and neutrino signal was allowed which reduces the model-dependency and provides more information about the neutrino production processes.

The novel analysis method was applied to data collected between 2008 and 2009 with the 40 strings IceCube and the AMANDA detector in a combined operation mode. The results did not point to a possible neutrino signal from the Cyg X-3 within 20 days of the time of major radio flaring. The observation is completely compatible with the hypothesis of a background only sample.

6.1 Summary of multi-wavelength studies

Cyg X-3's phenomenology and spectral behaviour in many wavelengths was carefully studied in literature and in received data. It was found that the X-ray binary is similar to other binary systems, however shows many peculiarities, that can mostly be explained by strong stellar winds and a close orbit that lead to very high densities in the system. Cyg X-3 is highly time-variable and there is evidence for time-variable relativistic outflows, or jets, that indicate acceleration of particles to high energies. The jet ejections are associated with a giant radio outburst, or radio flare, that can reach up to 20 Jy. The high density provides a good environment for neutrino production via pp or $p\gamma$ reactions and it is likely that γ-rays at TeV energies are strongly absorbed in the dense fields. It is

thus not known at which intensity very high energy particles are produced and a neutrino search is highly motivated to gain insight.

In the context of a search for neutrinos correlated with the Cyg X-3 jet ejection, an algorithm was developed to identify major radio flaring periods from radio data and, more importantly, from X-ray data (see section 4.2.2). The flare can be seen directly in radio data. However, radio monitoring data is not always available. Therefore, a method was found to select periods of radio flaring from X-ray data, which has a higher time resolution and is easier available. It is based on spectral hardness and relies on the empirically observed increase of the hardness at the onset of a flare, after a spectral state of very low hardness, so-called hypersoft state.

6.2 Summary of the neutrino studies

Several studies on the Cyg X-3, motivated by the phenomenology, were performed using neutrino telescope data (see chapter 4). Because of the time-variability of Cyg X-3, the focus was put on time-dependent analyses.

In section 4.1, neutrino events recorded between 2000 and 2006 with the AMANDA-II detector were investigated in a non-blind fashion. The neutrino sample was compared to Cyg X-3 light curves, in particular the radio light curve at 15 GHz. The intention was to search for a hint of a signal in time correlation with radio flares. No signal hint strong enough to motivate a test on blind data was found, but several useful analysis techniques were developed.

With the experience from the AMANDA-II study, a more sophisticated study was performed on blind data from the combined IceCube 40-strings and AMANDA detector (see section 4.2). General techniques from the earlier studies, like the use of shifted time windows, could be re-used. However, a time-dependent unbinned maximum likelihood method was employed to enhance the sensitivity of the analysis. A central part was the construction of the search windows, defined from multi-wavelength data as mentioned in the previous section.

Because the exact neutrino light curve from Cyg X-3 cannot be determined and it is possible that there is a time lag between radio flares and neutrino flares, the time windows defined from radio flaring were allowed to be shifted by up to 20 days with respect to their original position. Since the analysis is based on physics assumptions, it is not optimized for best possible sensitivity or limit setting potential. However, the sensitivity is better than that of a time-independent search on the same data sample and comparable to other time-dependent analyses on IceCube 40-string data. Because the combined IceCube 40 plus AMANDA sample is improved for soft spectra, it has especially good sensitivity for sources with emission spectra softer than $\propto E^{-3}$.

In total, five blind searches were performed: one searching in each of the four windows and one searching in all windows together. The results were presented in chapter 5. The statistically most significant result came from window 1 with a pre-trial probability of 22.3%, given the null hypothesis (no signal) is correct. The trial-corrected probability is 57% which means that **the sample is perfectly consistent with the background only hypothesis**. Not even a hint for a signal from Cyg X-3 in correlation with the major flaring was found and because of the low significance, the fitted time lags have only very limited meaning.

Upper limits on the signal fluence (time-integrated flux) during all search windows lie at $1.8 \cdot 10^{-3} \, (E/\mathrm{TeV})^{-3} \, \mathrm{cm}^{-2} \, \mathrm{sr}^{-1} \, \mathrm{TeV}^{-1}$ and $2.5 \cdot 10^{-4} \, (E/\mathrm{TeV})^{-2} \, \mathrm{cm}^{-2} \, \mathrm{sr}^{-1} \, \mathrm{TeV}^{-1}$ for an E^{-2} and E^{-3} spectrum respectively. The upper limit on the fluence at the search windows can be converted to an average flux over the whole detector operation, assuming no flux outside of the search window periods. The flux upper limit during the search windows is however much higher than the average, so that no models are constrained.

6.3 Conclusion and Outlook

Cyg X-3 has caused much excitement in the history of high-energy astrophysics and continues to do so with the first convincing detection of γ-rays from Cyg X-3 with the AGILE and Fermi space telescopes. Hopefully, this story will be continued with a neutrino detection and the establishment of Cyg X-3 as hadronic acceleration site and source of cosmic rays. Cyg X-3 remains, after all the research work that has been done in the field, a quite enigmatic object and future studies could bring more surprises.

If γ-ray telescopes fail to detect Cyg X-3 because of the absorption, then the only chance is to see the source in neutrinos. Therefore, it is recommended to repeat an analysis of this kind with future neutrino telescope data. The IceCube 59-strings data have not yet been analyzed for point sources and the nearly complete IceCube 79-strings detector is taking data at the moment, including most of the DeepCore extension, enhancing the sensitivity for energies below 1 TeV. In 2011, the full km^3 IceCube detector will start its operation. With these more powerful instruments, a point source detection of Cyg X-3 might be possible, even with more pessimistic emission scenarios. In case of no signal detection, very stringent upper limits will be put on the emission models after few years of IceCube operation.

Additionally, more work on the low level side of the analysis should be invested, e.g. improvement of the track reconstruction and the detector simulation in order to more efficiently discriminate background events while keeping a higher fraction of signal events. No-one knows for sure how far the neutrino astronomy community is away from the detection of a point source. It definitely cannot hurt to get as much potential as possible out of the detectors.

Acknowledgements

Writing this thesis would have been impossible without the help of many kind souls that contributed to it in various ways:

First of all, I'd like to thank Elisa for not only supervising me, granting me a glimpse of her scientific perspective, but also for encouraging me and cheering me up with a joke, when I was taking things too seriously.

Then, I'd like to thank Caren Hagner for being my kind tutor and fair examiner in good old Hamburg (now for the second time!).

Great thanks go to my one-year-long colleagues: Sirin for producing this fine data sample and helping me whenever I got stuck. Claudine for being there when I needed someone to talk to (also when I got stuck...). Olaf for all his deep(Core) knowledge about IceCube and life in general. Yolanda for bringing in the right astronomer's perspective and for talking funny things. Martin for the feeling of being not the only diploma student and for the nice "nerdy" conversations. Also a big personal thank you for the nice time with you!

Furthermore, I thank Mike Baker for the advice and guidance on all the technical time-dependent details. Big thanks to Chad Finley, Jon Dumm, Jose and the other point source people for helpful comments and leading me to the goal. Thanks to Nick and Subir for being my referees and thank you to Jim Braun for his nice papers and work on the AMANDA-II sample. And to all the other great IceCube people that I forgot to mention here.

A big special thank you goes out to Guy Pooley for his super-cool attitude and the willingness to spread his data without hesitation—that's the right scientific spirit! And equal thanks to other people that I received data from, e.g. Stéphane Corbel.

Thanks for all other scientists that I had helpful contact with, like Valeriu Tudose and Anna Szostek. Thanks to Karri Koljonen, Hannikainen, McCollough et al. (again Guy Pooley!) for the paper about the "jet line" that was very important for my work.

Thanks to the other nice people at MPIK: Iwona, Olga, Ioanna, Eva, Ervin, Dave, Roland, Jörg, Julia, Florian, Bernd, Stefan, Anne...

And last, but not least, a huge thank you to my dearest friend Ann-Kathrin. Without you I wouldn't have made it!

Bibliography

[1] V. Hess. Observations in low level radiation during seven free balloon flights. *PHYSIKALISCHE ZEITSCHRIFT*, 13:1084–1091, 1912.

[2] V. Hess. Victor F. Hess - Nobel Lecture. In *Nobel Lectures, Physics 1922-1941*, Amsterdam, 1965. Elsevier Publishing Company. URL http://nobelprize.org/nobel_prizes/physics/laureates/1936/hess-lecture.html. 29 Aug 2010.

[3] C. Anderson. The positive electron. *Physical review*, 43(6):491–494, 1933. ISSN 0031-899X. doi: 10.1103/PhysRev.43.491.

[4] S. Neddermeyer and C. Anderson. Note on the nature of cosmic-ray particles. *Physical review*, 51(10):0884–0886, 1937. ISSN 0031-899X. doi: 10.1103/PhysRev.51.884.

[5] C. Lattes, H. Muirhead, and G. Occhialini et al. Processes Involving Charged Mesons. *Nature*, 159(4047):694–697, 1947. ISSN 0028-0836. doi: 10.1038/159694a0.

[6] Todor Stanev. *High energy cosmic rays; 2nd ed.* Springer-Praxis books in astrophysics and astronomy. Springer, Berlin, 2004.

[7] P. Bhattacharjee and G. Sigl. Origin and propagation of extremely high-energy cosmic rays. *Physics Reports*, 327(3-4):109–247, 2000. ISSN 0370-1573. doi: 10.1016/S0370-1573(99)00101-5. URL http://arXiv.org/abs/astro-ph/9811011v2.

[8] M. Kachelrieß. Lecture notes on high energy cosmic rays. *arXiv.org e-Print archive*, 2008. URL http://arxiv.org/abs/0801.4376v1. arXiv:0801.4376v1 [astro-ph].

[9] D. Asner et al. W. Yao, C. Amsler. Review of particle physics. *Journal of physics. G, Nuclear and particle physics*, 33(1):1, 2006. ISSN 0954-3899. doi: 10.1088/0954-3899/33/1/001.

[10] I. Usoskin. A History of Solar Activity over Millennia. *arXiv.org e-Print archive*, 2008. URL http://arxiv.org/abs/0810.3972v1. arXiv:0810.3972v1 [astro-ph].

[11] A. Penzias and R. Wilson. A Measurement of Excess Antenna Temperature at 4080mc/s. *The Astrophysical Journal*, 142(1):419, 1965. ISSN 0004-637X. doi: 10.1086/148307.

[12] K. Greisen. End to Cosmic-Ray Spectrum. *Physical review letters*, 16(17):748, 1966. ISSN 0031-9007. doi: 10.1103/PhysRevLett.16.748.

[13] G. Zatsepin and V. Kuzmin. Upper Limit of Spectrum of Cosmic Rays. *JETP LETTERS-USSR*, 4(3):78, 1966.

[14] M. Takeda, N. Hayashida, and K. et al. Honda. Extension of the Cosmic-Ray Energy Spectrum beyond the Predicted Greisen-Zatsepin-Kuz'min Cutoff. *Physical review letters*, 81(6):1163–1166, Aug 1998. ISSN 0031-9007. doi: 10.1103/PhysRevLett.81.1163.

[15] R. Abbasi, T. Abu-Zayyad, and M. Allen et al. First observation of the Greisen-Zatsepin-Kuzmin suppression. *Physical review letters*, 100(10), 2008. ISSN 0031-9007. doi: 10.1103/PhysRevLett.100.101101.

[16] J. Abraham, P. Abreu, and M. Aglietta et al. Measurement of the energy spectrum of cosmic rays above 10(18) eV using the Pierre Auger Observatory. *Physics letters. B*, 685(4-5):239–246, 2010. ISSN 0370-2693. doi: 10.1016/j.physletb.2010.02.013.

[17] Thomas K Gaisser. *Cosmic rays and particle physics*. Cambridge Univ. Press, Cambridge, 1990.

[18] J. Abraham, P. Abreu, and M. Aglietta et al. Upper limit on the cosmic-ray photon fraction at EeV energies from the Pierre Auger Observatory. *Astroparticle physics*, 31(6):399–406, 2009. ISSN 0927-6505. doi: 10.1016/j.astropartphys.2009.04.003.

[19] G. Sigl, S. Lee, and P. Bhattacharjee et al. Probing grand unified theories with cosmic-ray, gamma-ray, and neutrino astrophysics. *Physical review. D. Particles and fields*, 59(4), 1999. ISSN 0556-2821.

[20] P. Sreekumar, D. Bertsch, and B. Dingus et al. Egret observations of the extragalactic gamma-ray emission. *The Astrophysical Journal*, 494(2):523–534, 1998. ISSN 0004-637X. doi: 10.1086/305222.

[21] M. Israel, W. Binns, and A. Cummings et al. Isotopic composition of cosmic rays: results from the cosmic ray isotope spectrometer on the ACE spacecraft. *Nuclear physics. A*, vol.758:201–8, 2005. ISSN 0375-9474. doi: 10.1016/j.nuclphysa.2005.05.038.

[22] H. Kolanoski. IceTop Science, 11 Sep 2010. URL http://www.expeditions.udel.edu/antarctica08/blog-dec-12-2008.html.

[23] James Braun. *A Maximum-Likelihood Search for Neutrino Point Sources with the AMANDA-II Detector*. PhD thesis, University of Wisconsin – Madison, 2009.

[24] F. Halzen and S. Klein. Invited review article: IceCube: an instrument for neutrino astronomy. *Review of scientific instruments*, 81(8):081101, 2010. ISSN 0034-6748. doi: 10.1063/1.3480478. URL http://arxiv.org/abs/1007.1247v2.

[25] Walter Heitler. *The Quantum Theory of Radiation; 2nd ed.* International series of monographs on physics. Oxford Univ. Press, London, 1944.

[26] P. Auger. Extensive cosmic-ray showers. *Reviews of modern physics*, 11(3/4):0288–0291, 1939. ISSN 0034-6861. doi: 10.1103/RevModPhys.11.288.

[27] G. Matthiae. The AUGER experiment - status and results. *arXiv.org e-Print archive*, 2008. URL http://arxiv.org/abs/0802.2214v1. arXiv:0802.2214v1 [astro-ph].

[28] J. Abraham, P. Abreu, and M. Aglietta et al. Correlation of the highest-energy cosmic rays with nearby extragalactic objects. *Science*, 318(5852):938–943, 2007. ISSN 0036-8075. doi: 10.1126/science.1151124. URL http://arxiv.org/abs/0711.2256v1.

[29] N.N. Volodich, N. Grigorov, and V. Nesterov et al. Study of Chemical Composition of Primary Cosmic Rays in Moderate Energy Region with Earth Satellites PROTON 1 and PROTON 2. *IZVESTIYA AKADEMII NAUK SSSR SERIYA FIZICHESKAYA*, 31(8):1229, 1967. ISSN 0367-6765.

[30] N. Grigorov. Measurement of the Proton Spectrum at Energies Above 1-TeV by the SOKOL Detector on a Satellite. *JETP letters*, 49(2):83–88, 1989. ISSN 0021-3640.

[31] S. Borisov, M. Boezio, and S. Voronov et al. Measurement of the high-energy electron and positron spectrum in the PAMELA experiment. *Bulletin of the Lebedev Physics Institute*, 37(6):184–190, 2010. ISSN 1068-3356. doi: 10.3103/S1068335610060096.

[32] K. Asakimori, T. Burnett, and M. Cherry et al. Cosmic-ray proton and helium spectra: Results from the JACEE experiment. *The Astrophysical Journal*, 502(1):278–283, 1998. ISSN 0004-637X. doi: 10.1086/305882.

[33] P. Maestro, H. Ahn, and P. Allison et al. Measurements of cosmic-ray energy spectra with the 2(nd) CREAM flight. *Nuclear physics. B, Proceedings, supplements*, 196:239–242, 2009. ISSN 0920-5632. doi: 10.1016/j.nuclphysbps.2009.09.045.

[34] P. Gorham, P. Allison, and B. Baughman et al. Observational constraints on the ultrahigh energy cosmic neutrino flux from the second flight of the ANITA experiment. *Physical review. D, Particles, fields, gravitation, and cosmology*, 82(2), 2010. ISSN 1550-7998. doi: 10.1103/PhysRevD.82.022004.

[35] H. Klages, W. Apel, and K. Bekk et al. The KASCADE experiment. *Nuclear physics. B*, pages 92–102, 1997. ISSN 0550-3213.

[36] P. Sokolsky. The view from HiRes. *AIP conference proceedings*, 579(579):296–304, 2001. ISSN 0094-243X. doi: 10.1063/1.1398183.

[37] R. Shellard. First results from the Pierre Auger Observatory. *Brazilian journal of physics*, 36(4A):1184–1193, 2006. ISSN 0103-9733. doi: 10.1590/S0103-97332006000700012. URL http://arxiv.org/abs/astro-ph/0609060.

[38] Auger Collaboration. The Pierre Auger Project Design Report. Technical Report FERMILAB-PUB-96-024, FERMILAB, Batavia, IL, 1996.

[39] J. Abraham. Properties and performance of the prototype instrument for the Pierre Auger Observatory. *Nuclear instruments & methods in physics research. Section A, Accelerators, spectrometers, detectors and associated equipment*, 523(1-2):50–95, 2004. ISSN 0168-9002. doi: 10.1016/j.nima.2003.12.012.

[40] M. Settimo. Hybrid detection of Ultra High Energy Cosmic Rays with the Pierre Auger Observatory. *Journal of Physics - Conference Series*, 203, 2010. ISSN 1742-6588. doi: 10.1088/1742-6596/203/1/012127.

[41] J. Abraham, P. Abreu, and M. Aglietta et al. Correlation of the highest-energy cosmic rays with the positions of nearby active galactic nuclei. *Astroparticle physics*, 29(3):188–204, 2008. ISSN 0927-6505. doi: 10.1016/j.astropartphys.2008.01.002.

[42] A. Cuoco and S. Hannestad. Ultrahigh energy neutrinos from Centaurus A and the Auger hot spot. *Physical review. D. Particles and fields*, 78(2), 2008. ISSN 0556-2821. doi: 10.1103/PhysRevD.78.023007. URL http://tinyurl.sfx.mpg.de/rd3h&issn=0556-2821.

[43] F. Halzen and A. Ó Murchadha. Neutrinos from Auger Sources. *arXiv.org e-Print archive*, 2008. URL http://arxiv.org/abs/0802.0887v2. arXiv:0802.0887v2 [astro-ph].

[44] J. Goodman, HAWC Collaboration, and Milagro Collaboration. PHYSICS with HAWC. *AIP conference proceedings*, 1085:809–812, 2009. ISSN 0094-243X.

[45] T. Weekes. Gamma-ray astronomy at the highest energies. *Nuclear instruments & methods in physics research. Section A, Accelerators, spectrometers, detectors and associated equipment*, 280(2-3):349–357, 1989. ISSN 0168-9002. doi: 10.1016/0168-9002(89)90931-5.

[46] K. Pinkau. History of gamma-ray telescopes and astronomy. *Experimental astronomy*, 25(1-3):157–171, 2009. ISSN 0922-6435. doi: 10.1007/s10686-009-9143-z.

[47] W. Atwood, A. Abdo, and M. Ackermann et al. The Large Area Telescope on the Fermi Gamma-ray Space Telescope Mission. *The Astrophysical Journal*, 697(2):1071–1102, 2009. ISSN 0004-637X. doi: 10.1088/0004-637X/697/2/1071.

[48] NASA/DOE/International LAT Team, 23 Sep 2010. URL http://www.nasa.gov/images/content/267641main_allsky_labeled_HI.jpg.

[49] P. Michelson, W. Atwood, and S. Ritz. Fermi Gamma-ray Space Telescope: high-energy results from the first year. *Reports on Progress in Physics*, 73(7):074901–074901, 2010. ISSN 0034-4885. doi: 10.1088/0034-4885/73/7/074901.

[50] A. Hillas. Differences between gamma-ray and hadronic showers. *Space science reviews*, 75(1-2):17–30, 1996. ISSN 0038-6308. doi: 10.1007/BF00195021.

[51] R. Atkins, W. Benbow, and D. Berley et al. TeV gamma-ray survey of the northern hemisphere sky using the Milagro observatory. *The Astrophysical Journal*, 608(2):680–685, 2004. ISSN 0004-637X. doi: 10.1086/420880.

[52] T. Weekes. Very high energy gamma-ray astronomy. *Physics Reports*, 160(1-2):1–121, 1988. ISSN 0370-1573. doi: 10.1016/0370-1573(88)90177-9.

[53] P. Hüntemeyer. Milagro in high energy gamma-ray astrophysics. *Acta physica Polonica. B*, pages 601–4, 2008. ISSN 0587-4254.

[54] F Aharonian, A Akhperjanian, and A Bazer-Bachi et al. Observations of the Crab nebula with HESS. *Astronomy and astrophysics*, 457(3):899–915, 2006. ISSN 0004-6361. doi: 10.1051/0004-6361:20065351.

[55] H. Völk. High energy gamma-ray astronomy. *Nuclear physics. B, Proceedings, supplements*, 138:492–501, 2005. ISSN 0920-5632. doi: 10.1016/j.nuclphysbps.2004.11.108.

[56] R. Chaves, E. Wilhemi, S. Hoppe, and HESS Collaboration. The HESS Galactic Plane Survey. In *HIGH ENERGY GAMMA-RAY ASTRONOMY*, volume 1085 of *AIP CONFERENCE PROCEEDINGS*, pages 219–222. American Institute of Physics, New York, 2009. ISBN 978-0-73-540616-2.

[57] F. Aharonian, A. Akhperjanian, and M. Beilicke et al. TeV gamma-ray observations of SS-433 and a survey of the surrounding field with the HEGRA IACT-system. *Astronomy and astrophysics*, 439(2):635–643, 2005. ISSN 0004-6361. doi: 10.1051/0004-6361:20042248.

[58] M. Raue and HESS Collaboration. First results from the HESS Cherenkov telescope system in Namibia. *Neutrinos and Explosive Events in the Universe*, 209:269–273, 2005.

[59] M. Punch and HESS Collarobation. Results from observations of AGNs with the HESS telescope system and future plans. *Exploring the Cosmic Frontier*, pages 175–178, 2007.

[60] The H.E.S.S. Collaboration. The H.E.S.S. Source Catalog, 23 Sep 2010. URL http://www.mpi-hd.mpg.de/hfm/HESS/pages/home/sources/.

[61] K. Lande. The Life of Raymond Davis, Jr. and the Beginning of Neutrino Astronomy. *Annual review of nuclear and particle science*, 59:21–39, 2009. ISSN 0163-8998. doi: 10.1146/annurev.nucl.010909.083753.

[62] D. Lattuada. Neutrino astronomy with underwater km^3 telescopes. In *AIP Conference Proceedings*, volume 1213, pages 215–218. 2010. ISBN 978-0-73-540756-5. doi: 10.1063/1.3362586.

[63] P. Hulth. Ultra high energy neutrino telescopes. *International journal of modern physics. A, Particles and fields, gravitation, cosmology*, 21(8-9):1914–1924, 2006. ISSN 0217-751X. doi: 10.1142/S0217751X06032861.

[64] E. Waxman and J. Bahcall. High energy neutrinos from astrophysical sources: An upper bound. *Physical review. D. Particles and fields*, 59(2), 1999. ISSN 0556-2821.

[65] J. Alvarez-Muniz and F. Halzen. Possible high-energy neutrinos from the cosmic accelerator RX J1713.7-3946. *Astrophysical journal*, 576(1):L33–L36, 2002. ISSN 0004-637X. doi: 10.1086/342978.

[66] F. Villante and F. Vissani. How precisely can neutrino emission from supernova remnants be constrained by gamma ray observations? *Physical review. D. Particles and fields*, 78(10), 2008. ISSN 0556-2821. doi: 10.1103/PhysRevD.78.103007.

[67] P. Bosetti. DUMAND status report. *Nuclear physics. B*, pages 466–468, 1996. ISSN 0550-3213.

[68] Dmitry Chirkin and Wolfgang Rhode. Muon Monte Carlo: A high-precision tool for muon propagation through matter. 2004.

[69] J. Ahrens, X. Bai, and R. Bay et al. Muon track reconstruction and data selection techniques in AMANDA. *Nuclear instruments & methods in physics research. Section A, Accelerators, spectrometers, detectors and associated equipment*, 524(1-3): 169–194, 2004. ISSN 0168-9002. doi: 10.1016/j.nima.2004.01.065.

[70] H.S. Sandhu and G.B. Friedman. Refractive Index of Ice. *American journal of physics*, 33(1):62, 1965. ISSN 0002-9505. doi: 10.1119/1.1971238.

[71] V. Berezinskii and G. Zatsepin. Possible experiments with very high energy cosmic neutrinos: the Dumand project. *Soviet physics. Uspekhi*, 20(5):361, 1977. ISSN 0038-5670.

[72] J. Babson, B. Barish, and R. et al Becker-Szendy. Cosmic-ray muons in the deep ocean. *Phys. Rev. D*, 42(11):3613–3620, Dec 1990. doi: 10.1103/PhysRevD.42.3613.

[73] A. Roberts. The Birth of High-Energy Neutrino Astronomy - A Personal History of the DUMAND Project. *Reviews of modern physics*, 64(1):259–312, 1992. ISSN 0034-6861. doi: 10.1103/RevModPhys.64.259.

[74] A. Avrorin, V. Aynutdinov, and V. Balkanov et al. The baikal neutrino telescope–results and plans. *Nuclear Instruments and Methods in Physics Research Section A: Accelerators, Spectrometers, Detectors and Associated Equipment*, In Press, Corrected Proof, 2010. ISSN 0168-9002. doi: DOI:10.1016/j.nima.2010.06.041. URL http://www.sciencedirect.com/science/article/B6TJM-508X377-6/2/c1d04b4f20821a7596eb96a91aef1696.

[75] A. Hillas. The Origin of Ultra-High-Energy Cosmic-Rays. *Annual Review of Astronomy and Astrophysics*, 22:425–444, 1984. ISSN 0066-4146. doi: 10.1146/annurev.aa.22.090184.002233.

[76] L. Anchordoqui, T. Paul, and S. Reucroft et al. Ultrahigh energy cosmic rays: The state of the art before the Auger observatory. *International journal of modern physics. A, Particles and fields, gravitation, cosmology*, 18(13):2229–2366, 2003. ISSN 0217-751X. doi: 10.1142/S0217751X03013879.

[77] R. Protheroe. Acceleration and interaction of ultra high energy cosmic rays. *TOPICS IN COSMIC-RAY ASTROPHYSICS*, 230:247–285, 1999. URL http://arxiv.org/abs/astro-ph/9812055.

[78] A. Weigert, H.J. Wendker, and L. Wisotzki. *Astronomie und Astrophysik: ein Grundkurs*. Lehrbuch Physik. Wiley-VCH, 2005. ISBN 3-527-40358-2.

[79] A. Abdo, M. Ackermann, and M. Ajello et al. The First Fermi Large Area Telescope Catalog of Gamma-ray Pulsars. *The Astrophysical journal. Supplement series*, 187 (2):460–494, 2010. ISSN 0067-0049. doi: 10.1088/0067-0049/187/2/460.

[80] M. Renaud, S. Hoppe, and N. Komin et al. Pulsar Wind Nebula candidates recently discovered by H.E.S.S. *AIP conference proceedings*, pages 285–8, 2008. ISSN 1931-3039. doi: 10.1063/1.3076661. URL http://arxiv.org/abs/0811.1559v1.

[81] A. Lemiere. AGN observations with H.E.S.S. *AIP conference proceedings*, no.745: 443–8, 2005. ISSN 0094-243X. doi: 10.1063/1.1878443.

[82] B. Morsony, D. Lazzati, and M. Begelman. The origin and propagation of variability in the outflows of long-duration gamma-ray bursts. *Astrophysical journal*, pages 267–76, 2010. ISSN 0004-637X. doi: 10.1088/0004-637X/723/1/267.

[83] J. Ahrens, J. Bahcall, and X. Bai et al. Sensitivity of the IceCube detector to astrophysical sources of high energy muon neutrinos. *Astroparticle physics*, 20(5): 507–532, 2004. ISSN 0927-6505. doi: 10.1016/j.astropartphys.2003.09.003.

[84] D. J. Koskinen and D. Cowen. Status of DeepCore at the IceCube Neutrino Observatory. *Nuclear Physics B Proceedings Supplement*, 2010. URL https://docushare.icecube.wisc.edu/dsweb/Get/Document-56300/koskinenDeepCoreStatus_new.pdf. paper in preparation.

[85] D. Cowen et al. for the IceCube Collaboration. The Design and Performance of IceCube DeepCore. IceCube Internal Document, paper in preparation, 19 Oct 2010. URL https://docushare.icecube.wisc.edu/dsweb/Get/Document-56270/DesignAndPerformanceOfIceCubeDeepCore_v1.0.pdf.

[86] R. Abbasi, Y. Abdou, and T. Abu-Zayyad et al. Calibration and characterization of the IceCube photomultiplier tube. *Nuclear instruments & methods in physics research. Section A, Accelerators, spectrometers, detectors and associated equipment*, 618(1-3):139–152, 2010. ISSN 0168-9002. doi: 10.1016/j.nima.2010.03.102.

[87] R. Abbasi, M. Ackermann, and J. Adams et al. The IceCube data acquisition system: Signal capture, digitization, and timestamping. *Nuclear instruments & methods in physics research. Section A, Accelerators, spectrometers, detectors and associated equipment*, 601(3):294–316, 2009. ISSN 0168-9002. doi: 10.1016/j.nima.2009.01.001.

[88] M. Ackermann, J. Ahrens, and X. Bai et al. Optical properties of deep glacial ice at the South Pole. *Journal of geophysical research*, 111(D13), 2006. ISSN 0148-0227. doi: 10.1029/2005JD006687. URL http://icecube.berkeley.edu/~bprice/publications/Optical.properties.deep.ice.South.Pole.pdf.

[89] P. Askebjer, S. Barwick, and L. Bergstrom et al. Optical properties of deep ice at the South Pole: Absorption. *Applied optics-OT*, 36(18):4168–4180, 1997. ISSN 0003-6935. doi: 10.1364/AO.36.004168. URL http://arxiv.org/abs/physics/9701025v1.

[90] J. Lynch. Antarctic muon and neutrino detector AMANDA: First data and outlook. *ROBOTIC TELESCOPES: CURRENT CAPABILITIES, PRESENT DEVELOPMENTS, AND FUTURE PROSPECTS FOR AUTOMATED ASTRONOMY*, 79: 205–220, 1995.

[91] P. Price, K. Woschnagg, and D. Chirkin. Age vs depth of glacial ice at South Pole. *Geophysical research letters*, 27(14):2129–2132, 2000. ISSN 0094-8276. doi: 10.1029/2000GL011351.

[92] P. Price, O. Nagornov, and R. Bay et al. Temperature profile for glacial ice at the South Pole: Implications for life in a nearby subglacial lake. *Proceedings of the National Academy of Sciences of the United States of America*, 99(12):7844–7847, 2002. ISSN 0027-8424. doi: 10.1073/pnas.082238999.

[93] D. Pandel. Bestimmung von Wasser- und Detektorparametern und Rekonstruktion von Myonen bis 100 TeV mit dem Baikal-Neutrinoteleskop NT-72. Master's thesis, Humboldt-Universität Berlin, DESY-Zeuthen, 1996. URL http://www.ifh.de/nuastro/publications/.

[94] R. Abbasi, M. Ackermann, and J. Adams et al. Search for point sources of high energy neutrinos with final data from AMANDA-II. *Physical review. D. Particles and fields*, 79(6), 2009. ISSN 0556-2821. doi: 10.1103/PhysRevD.79.062001. URL http://arxiv.org/abs/0809.1646.

[95] G. Cowan. *Statistical data analysis*. Oxford science publications. Clarendon Press, 1998. ISBN 9780198501565.

[96] J. Dumm and M. Baker. IC-40 Point Source Cut Variables, 5 Jan 2010. URL http://wiki.icecube.wisc.edu/index.php/IC-40_PS_Cut_Variables. IceCube internal document.

[97] T. Neunhöffer. Estimating the angular resolution of tracks in neutrino telescopes based on a likelihood analysis. *Astroparticle physics*, 25(3):220–225, 2006. ISSN 0927-6505. doi: 10.1016/j.astropartphys.2006.01.002. URL http://arxiv.org/abs/astro-ph/0403367v1.

[98] S. Barwick, J. Lynch, and R. Porrata et al. AMANDA South-Pole Neutrino Detector. *AIP conference proceedings*, 272:1250–1253, 1993. ISSN 0094-243X. doi: 10.1063/1.43263.

[99] R Abbasi, Y Abdou, and M Ackermann et al. First neutrino point-source results from the 22 string IceCube detector. *Astrophysical journal*, 701(1):L47–L51, 2009. ISSN 0004-637X. doi: 10.1088/0004-637X/701/1/L47.

[100] R. Abbasi et al. Time-Integrated Searches for Point-like Sources of Neutrinos with the 40-String IceCube Detector. paper in preparation, 2010.

[101] F. Halzen and J. Rodrigues. Detection of Supernova Explosions with IceCube. *Classical and quantum gravity*, 2010. ISSN 0264-9381. doi: 10.1088/0264-9381/27/19/194003.

[102] A. Kappes. IceCube: Neutrino Messages from GRBs. *AIP conference proceedings*, pages 234–41, 2010. ISSN 1931-3039. doi: 10.1063/1.3509273.

[103] S. Seo. Recent Results and Status of IceCube. In *DARK MATTER IN ASTROPHYSICS AND PARTICLE PHYSICS (DARK 2009)*, pages 482–493. ARRAY(0xc0c0250), 2010. ISBN 978-9-81-429378-5.

[104] R. Abbasi, Y. Abdou, and T. Abu-Zayyad et al. Measurement of the Anisotropy of Cosmic-Ray Arrival Directions With IceCube. *Astrophysical journal*, 718(2):L194–L198, 2010. ISSN 0004-637X. doi: 10.1088/2041-8205/718/2/L194.

[105] A. Gross et al. The combined AMANDA and IceCube Neutrino Telescope. In R. Caballero, International Union of Pure, and Applied Physics, editors, *Proceedings of the 30th International Cosmic Ray Conference, Mérida, México, 3-11 July 2007: SH*, pages 1253–1256. Universidad Nacional Autónoma de México, 2008. ISBN 9789703251568. URL http://indico.nucleares.unam.mx/materialDisplay.py?contribId=1013&sessionId=101&materialId=paper&confId=4.

[106] J. Bonnet-Bidaud and G. Chardin. Cygnus-X-3, A Critical-Review. *Physics Reports*, 170(6):325–404, 1988. ISSN 0370-1573. doi: 10.1016/0370-1573(88)90083-X.

[107] G. Bignami. Two Missions, One Microquasar. *Science*, 326(5959):1490–1491, 2009. ISSN 0036-8075. doi: 10.1126/science.1184534.

[108] M. Tavani, A. Bulgarelli, and G. Piano et al. Extreme particle acceleration in the microquasar Cygnus X-3. *Nature*, 462(7273):620–623, 2009. ISSN 0028-0836. doi: 10.1038/nature08578. URL http://www.nature.com/nature/journal/v462/n7273/full/nature08578.html.

[109] A. Abdo, M. Ackermann, and M. Ajello et al. Modulated High-Energy Gamma-Ray Emission from the Microquasar Cygnus X-3. *Science*, 326(5959):1512–1516, 2009. ISSN 0036-8075. doi: 10.1126/science.1182174. URL http://www.sciencemag.org/cgi/content/abstract/326/5959/1512.

[110] R. Fender. Relativistic outflows from X-ray binaries - ('Microquasars'). *Lecture notes in physics*, 589:101–122, 2002. ISSN 0075-8450. doi: 10.1007/3-540-46025-X_6.

[111] I. Félix Mirabel. Microquasars. *Comptes rendus. Physique*, 8(1):7–15, 2007. ISSN 1631-0705. doi: 10.1016/j.crhy.2006.12.001.

[112] T. Belloni. *The Jet Paradigm: From Microquasars to Quasars*. Lecture notes in physics. Springer, 2010. ISBN 9783540769361. doi: 10.1007/978-3-540-76937-8.

[113] R. Giacconi, H. Gursky, and B. Rossi et al. Evidence for X-rays from Sources Outside Solar System. *Physical review letters*, 9(11):439, 1962. ISSN 0031-9007. doi: 10.1103/PhysRevLett.9.439.

[114] R. Giacconi, G. Clark, and B. Rossi et al. 2 Sources of Cosmic X-rays in Scorpius + Sagittarius. *Nature*, 204(496):981, 1964. ISSN 0028-0836. doi: 10.1038/204981a0.

[115] D. Psaltis. Accreting neutron stars and black holes: a decade of discoveries. In W.H.G. Lewin and M. Klis, editors, *Compact stellar X-ray sources*, Cambridge astrophysics series, chapter 1. Cambridge University Press, 2004. ISBN 9780521826594. URL http://arxiv.org/abs/astro-ph/0410536v1.

[116] R. Remillard J. McClintock. Black Hole Binaries. In W.H.G. Lewin and M. Klis, editors, *Compact stellar X-ray sources*, Cambridge astrophysics series, chapter 4. Cambridge University Press, 2003. ISBN 9780521826594. URL http://arxiv.org/abs/astro-ph/0306213v4.

[117] D. Heinzeller and W. Duschl. On the Eddington limit in accretion discs. *Monthly notices of the Royal Astronomical Society*, 374(3):1146–1154, 2007. ISSN 0035-8711. doi: 10.1111/j.1365-2966.2006.11233.x.

[118] Q. Liu, J. van Paradijs, and E. van den Heuvel. Catalogue of high-mass X-ray binaries in the Galaxy (4th edition). *Astronomy and astrophysics*, 455(3):1165–1168, 2006. ISSN 0004-6361. doi: 10.1051/0004-6361:20064987.

[119] Q. Liu, J. van Paradijs, and E. van den Heuvel. A catalogue of low-mass X-ray binaries in the Galaxy, LMC, and SMC (Fourth edition). *Astronomy and astrophysics*, 469(2):807–810, 2007. ISSN 0004-6361. doi: 10.1051/0004-6361:20077303.

[120] T. M. Belloni. States and Transitions in Black-Hole Binaries. In T. Belloni, editor, *The Jet Paradigm: From Microquasars to Quasars*, Lecture notes in physics, chapter 3. Springer, 2010. ISBN 9783540769361.

[121] K. Koljonen, D. Hannikainen, and M. McCollough et al. The hardness-intensity diagram of Cygnus X-3: revisiting the radio/X-ray states. *Monthly notices of the Royal Astronomical Society*, 406(1):307–319, 2010. ISSN 0035-8711. doi: 10.1111/j.1365-2966.2010.16722.x. URL http://arxiv.org/abs/1003.4351v1.

[122] E. Gallo, R. Fender, and T. Maccarone et al. Towards a unified description of the jet-accretion coupling in stellar and super massive black holes. *Progress of theoretical physics. Supplement*, (155):83–86, 2004. ISSN 0375-9687. doi: 10.1143/PTPS.155.83.

[123] C. Shrader, L. Titarchuk, and N. Shaposhnikov. New Evidence for a Black Hole in the Compact Binary Cygnus X-3. *Astrophysical Journal*, 718(1):488–493, 2010. ISSN 0004-637X. doi: 10.1088/0004-637X/718/1/488.

[124] A. Zdziarski, A. Neronov, and M. Chernyakova. A compact pulsar wind nebula model of the gamma-ray-loud binary LS I+61 degrees 303. *Monthly notices of the Royal Astronomical Society*, 403(4):1873–1886, 2010. ISSN 0035-8711. doi: 10.1111/j.1365-2966.2010.16263.x.

[125] J. Albert, E. Aliu, and H. Anderhub et al. Variable very-high-energy gamma-ray emission from the microquasar LS I +61 303. *Science*, 312(5781):1771–1773, 2006. ISSN 0036-8075. doi: 10.1126/science.1128177.

[126] R. Manchanda. Search for pulsations in the low mass X-ray binary Sco X-1. *Proceedings of the 29th International Cosmic Ray Conference, Vol 4: OG 2.1, 2.2 & 2.3*, pages 183–186, 2005. URL http://tinyurl.sfx.mpg.de/r88r.

[127] D. Steeghs and J. Casares. The mass donor of Scorpius X-1 revealed. *Astrophysical journal*, 568(1):273–278, 2002. ISSN 0004-637X. doi: 10.1086/339224.

[128] E. Seifina and L. Titarchuk. On the Nature of the Compact Object in SS 433: Observational Evidence of X-ray Photon Index Saturation. *Astrophysical journal*, 722(1):586–604, 2010. ISSN 0004-637X. doi: 10.1088/0004-637X/722/1/586.

[129] I. F. Mirabel. Microquasars: summary and outlook. In T. Belloni, editor, *The Jet Paradigm: From Microquasars to Quasars*, Lecture notes in physics, chapter 1. Springer, 2010. ISBN 9783540769361. URL http://arxiv.org/abs/0805.2378v2.

[130] ESA, NASA, and Felix Mirabel. Fast-Flying Black Hole Yields Clues to Supernova Origin, 18 Nov 2002. URL http://hubblesite.org/newscenter/archive/releases/2002/30/image/a. accessed 28 Oct 2010.

[131] B. Margon, H. Ford, and S. Grandi et al. Enormous Periodic Doppler Shifts in SS-433. *Astrophysical journal*, 233(2):L63–L68, 1979. ISSN 0004-637X. doi: 10.1086/183077.

[132] I. Mirabel, L. Rodriguez, and B. Cordier et al. A Double-Sided Radio Jet from the Compact Galactic-Center Annihilator 1E1740.7-2942. *Nature*, 358(6383):215–217, 1992. ISSN 0028-0836. doi: 10.1038/358215a0.

[133] I. Mirabel and L. Rodriguez. A Superluminal Source in the Galaxy. *Nature*, 371 (6492):46–48, 1994. ISSN 0028-0836. doi: 10.1038/371046a0.

[134] I. Mirabel and L. Rodríguez. Microquasars in our Galaxy. *Nature*, 392(6677): 673–676, 1998. ISSN 0028-0836. doi: 10.1038/33603.

[135] R. Giacconi, H. Gursky, and J. Waters. An X-ray Survey of Cygnus Region. *Astrophysical journal*, 148(3P2):L119, 1967. ISSN 0004-637X. doi: 10.1086/180028.

[136] A. A. Watson. Ultra high energy cosmic rays and ultra high energy [gamma]-rays. *Advances in Space Research*, 4(2-3):35 – 44, 1984. ISSN 0273-1177. doi: DOI: 10.1016/0273-1177(84)90290-4. URL http://www.sciencedirect.com/science/article/B6V3S-472BD7K-JC/2/cd1262a2f5902e178e596eee61e1f35f.

[137] M. Vankerwijk, P. Charles, and T. Geballe et al. Infrared Helium Emission-Lines from Cygnus-X-3 Suggesting a Wolf-Rayet Star Companion. *Nature*, 355(6362): 703–705, 1992. ISSN 0028-0836. doi: 10.1038/355703a0.

[138] M. van Kerkwijk, T. Geballe, and D. King et al. The Wolf-Rayet counterpart of Cygnus X-3. *Astronomy and astrophysics*, 314(2):521–540, 1996. ISSN 0004-6361.

[139] V. Tudose, R. Fender, and M. Garrett et al. First e-VLBI observations of Cygnus X-3. *Monthly notices of the Royal Astronomical Society*, 375(1):L11–L15, 2007. ISSN 0035-8711. doi: 10.1111/j.1745-3933.2006.00264.x. URL http://arxiv.org/abs/astro-ph/0611054v1.

[140] A. Szostek, A. Zdziarski, and M. McCollough. A classification of the X-ray and radio states of Cyg X-3 and their long-term correlations. *Monthly notices of the Royal Astronomical Society*, 388(3):1001–1010, 2008. ISSN 0035-8711. doi: 10.1111/j.1365-2966.2008.13479.x.

[141] J. Aleksic, L. Antonelli, and P. Antoranz et al. MAGIC Constraints on Gamma-ray Emission from Cygnus X-3. *Astrophysical journal*, 721(1):843–855, 2010. ISSN 0004-637X. doi: 10.1088/0004-637X/721/1/843. URL http://arxiv.org/abs/1005.0740v2.

[142] NASA. The High Energy Astrophysics Science Archive Research Center (HEASARC). URL http://heasarc.gsfc.nasa.gov/.

[143] CDS. SIMBAD Astronomical Database. URL http://simbad.u-strasbg.fr/simbad/.

[144] R. M. Cutri, M. F. Skrutskie, and S. et al. van Dyk. *2MASS All Sky Catalog of point sources.* June 2003. URL http://cdsads.u-strasbg.fr/abs/2003tmc..book...C.

[145] A. Mioduszewski, M. Rupen, and R. Hjellming et al. A one-sided highly relativistic jet from Cygnus X-3. *Astrophysical journal*, 553(2):766–775, 2001. ISSN 0004-637X. doi: 10.1086/320965.

[146] J. Miller-Jones, K. Blundell, and M. Rupen et al. Time-sequenced multi-radio frequency observations of Cygnus X-3 in flare. *Astrophysical journal*, 600(1):368–389, 2004. ISSN 0004-637X. doi: 10.1086/379706.

[147] E. Waltman, R. Foster, and G. Pooley et al. Quenched radio emission in Cygnus X-3. *The Astronomical journal*, 112(6):2690–2698, 1996. ISSN 0004-6256. doi: 10.1086/118213. URL http://tinyurl.sfx.mpg.de/r9y2&issn=0004-6256.

[148] S. Trushkin. Multi-frequency monitoring of Galactic X-ray sources: Cygnus X-3. *Astronomy letters*, 24(1):16–21, 1998. ISSN 1063-7737. URL http://adsabs.harvard.edu/full/1998AstL...24...16T.

[149] S. Trushkin, N. Bursov, and T. Kotani et al. Recent radio monitoring of microquasars with Ratan-600 radio telescope. *6TH INTEGRAL WORKSHOP: THE OBSCURED UNIVERSE*, 622:357–360, 2007. URL http://arxiv.org/abs/astro-ph/0702393.

[150] S. A. Trushkin, N. N. Bursov, and N. A. Nizhelskij et al. What do we understand from multi-frequency monitoring of microquasars? *Proceedings VI Microquasar Workshop: Microquasars and beyond, Sept 18-22 2006, Como, Italy*, 2006. URL http://arxiv.org/abs/astro-ph/0611550v1.

[151] Hans Krimm. Scaled Map Transient Analysis for Cyg X-3, 04 Jun 2010. URL http://swift.gsfc.nasa.gov/docs/swift/results/transients/CygX-3/.

[152] NASA, J. D. Myers, and Phil Newman et al. Fermi Gamma-ray Space Telescope, 02 Nov 2010. URL http://fermi.gsfc.nasa.gov/.

[153] W. Bednarek. On the possibility of sub-TeV gamma-ray emission from Cyg X-3. *Monthly notices of the Royal Astronomical Society*, 406(1):689–700, 2010. ISSN 0035-8711. doi: 10.1111/j.1365-2966.2010.16721.x. URL http://arxiv.org/abs/1002.1563v2.

[154] W. Bednarek. TeV neutrinos from microquasars in compact massive binaries. *Astrophysical journal*, 631(1):466–470, 2005. ISSN 0004-637X. doi: 10.1086/432411. URL http://arXiv.org/abs/astro-ph/0505547v1.

[155] M. Ackermann, J. Ahrens, and X. Bai et al. Search for extraterrestrial point sources of high energy neutrinos with AMANDA-II using data collected in 2000-2002. *Physical review. D. Particles and fields*, 71(7), 2005. ISSN 0556-2821. doi: 10.1103/PhysRevD.71.077102.

[156] G. C. Hill. In C. Barthelemy, editor, *Proc. XXXVI Rencontres de Moriond: Electroweak Interactions and Unified Theories*, 2001. URL http://moriond.in2p3.fr/EW/2001/proceedings/.

[157] J. Braun, M. Baker, and J. Dumm et al. Time-dependent point source search methods in high energy neutrino astronomy. *Astroparticle physics*, 33(3):175–181, 2010. ISSN 0927-6505. doi: 10.1016/j.astropartphys.2010.01.005. URL http://arxiv.org/abs/0912.1572v1.

[158] M. Baker, J. A. Aguilar, and J. Braun et al. for the IceCube Collaboration. IceCube Time-Dependent Point Source Analysis Using Multiwavelength Information. In *Proceedings of the 31st ICRC, Lódź 2009*, 2009. URL http://pubdb.desy.de/fulltext/getfulltext.php?lid=12068&fid=30702.

[159] M. Baker et al. IC-40 Time-Dependent Analysis. IceCube Internal Document, paper in preparation, 27 July 2010. URL http://wiki.icecube.wisc.edu/index.php/IC-40_Time_Dependent_Analysis/Untriggered/Results.

[160] J. Klein and A. Roodman. Blind analysis in nuclear and particle physics. *Annual review of nuclear and particle science*, 55:141–163, 2005. ISSN 0163-8998. doi: 10.1146/annurev.nucl.55.090704.151521.

[161] A. Roodman. Blind Analysis in Particle Physics. *arXiv.org e-Print archive*, 2003. URL http://arxiv.org/abs/physics/0312102v1. arXiv:physics/0312102v1 [physics.data-an].

[162] G. G. Pooley. Radio monitoring with the Ryle Telescope. In *VI Microquasar Workshop: Microquasars and Beyond*, 2006. URL http://adsabs.harvard.edu/abs/2006smqw.confE..19P.

[163] Hale Bradt, Deepto Chakrabarty, and Wei Cui et al. ASM Light Curves - MIT X-Ray Timing Explorer Project, 11 Mar 2010. URL http://xte.mit.edu/ASM_lc.html.

[164] Guy Pooley. Radio observations of Cyg X-3 with the Ryle telescope. private communication, 23 Feb 2010.

[165] Jim Braun. 2000-2006 AMANDA Point Source Analysis – Data Sample, 19 April 2010. URL http://www.icecube.wisc.edu/~jbraun/combined_point_source/data.html.

[166] Jim Braun. 2000-2006 AMANDA Point Source Analysis – Sensitivity & Discovery Potential, 19 April 2010. URL http://www.icecube.wisc.edu/~jbraun/combined_point_source/sensitivity.html.

[167] M. Ackermann, E. Bernardini, and T. Hauschildt for the IceCube Collaboration. Search for high energy neutrino point sources in the northern hemisphere with the AMANDA-II neutrino telescope. *Proceedings of the 29th International Cosmic Ray Conference, Vol 5: OG 2.5, 2.6 & 2.7*, pages 5–8, 2005. URL http://tinyurl.sfx.mpg.de/rdfu.

[168] A. Achterberg, M. Ackermann, and J. Adams et al. Five years of searches for point sources of astrophysical neutrinos with the AMANDA-II neutrino telescope. *Physical review. D. Particles and fields*, 75(10), 2007. ISSN 0556-2821. doi: 10.1103/PhysRevD.75.102001. URL http://arxiv.org/abs/astro-ph/0611063v1.

[169] A. Gazizov and M. Kowalski. ANIS: High energy neutrino generator for neutrino telescopes. *Computer physics communications*, 172(3):203–213, 2005. ISSN 0010-4655. doi: 10.1016/j.cpc.2005.03.113. URL http://arxiv.org/abs/astro-ph/0406439.

[170] U.S. Navy. The Astronomical Almanac Online, 25 Nov 2010. URL http://asa.usno.navy.mil.

[171] J. Neyman and E. S. Pearson. On the Problem of the most Efficient Tests of Statistical Hypotheses. *Philosophical transactions - Royal Society. Mathematical, Physical and engineering sciences*, 231(694-706):289, 1933. ISSN 1364-503X. doi: 10.1098/rsta.1933.0009.

[172] J. Zwart, R. Barker, and P. Biddulph et al. The Arcminute Microkelvin Imager. *Monthly notices of the Royal Astronomical Society*, 391(4):1545–1558, 2008. ISSN 0035-8711. doi: 10.1111/j.1365-2966.2008.13953.x. URL http://arxiv.org/abs/0807.2469.

[173] Guy Pooley. Radio observations of Cyg X-3 with the AMI telescope. private communication, 13 Jan 2010.

[174] S. A. Trushkin, N. N. Nizhelskij, and J. V. Sotnikova (SAO RAS). A giant radio flare of Cygnus X-3 (ATel #1483), 18 Apr 2008. URL http://www.astronomerstelegram.org/?read=1483.

[175] J. Braun, J. Dumm, and F. De Palma et al. Methods for point source analysis in high energy neutrino telescopes. *Astroparticle physics*, 29(4):299–305, 2008. ISSN 0927-6505. doi: 10.1016/j.astropartphys.2008.02.007. URL http://arxiv.org/abs/0801.1604.

[176] F. James and M. Roos. MINUIT - System for Function Minimization and Analysis of Parameter Errors and Correlations. *Computer physics communications*, 10(6):343–367, 1975. ISSN 0010-4655. doi: 10.1016/0010-4655(75)90039-9.

[177] M. Baker et al. IC-40 Time-Dependent Analysis. IceCube Internal Document, paper in preparation, 29 April 2010. URL http://wiki.icecube.wisc.edu/index.php/IC-40_Time_Dependent_Analysis/Untriggered.

[178] G. Feldman and R. Cousins. Unified approach to the classical statistical analysis of small signals. *Physical review. D. Particles and fields*, 57(7):3873–3889, 1998. ISSN 0556-2821. doi: 10.1103/PhysRevD.57.3873.

[179] J. Ahrens, X. Bai, and G. Barouch et al. Search for point sources of high-energy neutrinos with AMANDA. *Astrophysical journal*, 583(2):1040–1057, 2003. ISSN 0004-637X. doi: 10.1086/345352.

Erklärung:

Ich versichere, dass ich diese Arbeit selbständig verfasst habe und keine anderen als die angegebenen Quellen und Hilfsmittel benutzt habe.

Heidelberg, den 01.12.2010 _____